The Chemical Vapour Deposition of $MoTe_2$ Thin Films and Their Applications

James P. Fraser

Submitted in fulfilment of the requirements of the

Degree of Doctor of Philosophy

School of Chemistry

College of Science and Engineering

October 2021

Abstract

The isolation of graphene, a single layer of graphite, in 2004 highlighted the important role dimensionality plays in determining the properties of materials. This discovery led to attention being focused on other types of two-dimensional materials, in particular the family of compounds known as the transition metal dichalcogenides (TMDCs). The chemical and structural diversity of the TMDCs means they exhibit many exotic properties that make them interesting for both fundamental science and suitable for many applications. Of the TMDCs, perhaps one of the most interesting is molybdenum ditelluride. $MoTe_2$ can exist in two polymorphs, one of which is semiconducting and the other metallic and their properties vary depending on their thickness. This polymorphism also presents a challenge towards the synthesis of phase pure $MoTe_2$ films by chemical vapour deposition (CVD), a method which shows promise for being able to produce these materials at scale and with high throughput. Both polymorphs tend to exist at the typical deposition temperatures used and as such are in competition with each other.

This work sought to develop a CVD set up that can retain control over the phase and thickness of the $MoTe_2$ product films. Following the determination of conditions that allowed for the deposition of 2H- and 1T'-$MoTe_2$, the films were characterised extensively with a variety of techniques to ensure that they were indeed phase pure. Subsequently, films of both phases with a variety of thicknesses were produced, highlighting the ability of the CVD method to accurately control the thickness and phase of $MoTe_2$. The method also allowed for the simultaneous deposition of 1T'- and 2H-$MoTe_2$ on the same substrate by taking advantage of the type of precursor layer used.

The CVD grown films of $MoTe_2$ were then trialled in two different applications. Firstly, as electrocatalytic films for the production of hydrogen from water, where the impact of the phase and film thickness on the catalytic activity was studied. Secondly, 1T'-$MoTe_2$ was applied as a surface enhanced Raman spectroscopy substrate. A preliminary study was conducted using a model analyte, rhodamine 6G, with the intention of confirming the activity of the 1T'-phase and performing brief thickness dependent measurements. Subsequently a thorough study was conducted using a clinically relevant biomolecule, β-sitosterol, as an analyte. This highlighted the potential applications of the TMDCs as SERS substrates with the achieved limit of detection of 10^{-9} M being one of the lowest reported so far for sterol-like lipophilic molecules. Furthermore, the mechanism of Raman enhancement was determined to be related to the formation of a surface complex between the analyte and 1T'-film, which was then characterised extensively.

Finally, the $Mo_3Sb_{7-x}Te_x$ (where x = 0, 1, 1.6 and 2) group of compounds were synthesised and investigated. These materials offer an interesting opportunity to see how varying the tellurium amount impacts their performance as hydrogen evolution catalysts. It was found that increasing the amount of tellurium led to increased catalytic performance as well as improving the stability of the materials. Efforts were made to utilise the previously developed CVD system to try and deposit thin films of Mo_3Sb_7 and $Mo_3Sb_{5.4}Te_{1.6}$ as there are no literature reports of this being achieved. This was somewhat successful but overall hampered by the difficulty in characterising the product films.

Acknowledgements

Firstly, I would like to thank Dr. Alexey Ganin for his guidance and support throughout this process. I'm extremely grateful for everything you have done and the opportunities you've afforded me. I could not have wished for a better supervisor and will greatly miss working with you.

I would also like to thank the wonderful collaborators I've been privileged to work with over the course of my PhD. In particular, Professor Thomas Pichler for accommodating me in his lab on several occasions, making me feel incredibly welcome in his group and taking an interest in my work. Also, Dr. Olga Guselnikova for the incredibly productive collaboration and for teaching me about surface enhanced Raman spectroscopy. Finally, I'd like to thank Dr. David Moran and the members of his group, particularly Dr. David MacDonald and Jingyi "Zoey" Zhang for their help and support in the JWNC, and the numerous Chinese snacks given to me over the past 4 years.

I'm extremely grateful to the members of the Ganin group, past and present, who have made my time in C2-02 such an enjoyable experience. So, thank you to Jessica, Liudvika, Youyi and Yuanshen for your friendship and support, especially over the very strange period of time that has been the last ~18 months.

I'd like to thank my amazing girlfriend Emma for her love, support and encouragement over the course of my PhD, I genuinely would not have got through it without you. I'm sure those holidays to Vienna were worth having to occasionally sit and listen to me practice presentations pretending to understand what I was talking about.

Of course, I'm grateful for the support and encouragement I've received from my parents and over the years as I wouldn't have got where I am today without it. I'd also like to thank them for always taking an interest in my work and for the help in proofreading this thesis.

Lastly, I'd like to thank my friends, in particular Blair, Ryan and Gary for keeping me sane over the last 4 years. The countless hours spent playing Xbox, going for pints or attending gigs have been some of the most enjoyable experiences over the course of this PhD and made getting through some of the tougher parts much more bearable.

Abbreviations

AFM	Atomic Force Microscopy
ALD	Atomic Layer Deposition
CM	Chemical Enhancement Mechanism
CT	Charge Transfer
CVD	Chemical Vapour Deposition
CV	Cyclic Voltammetry
DFT	Density Functional Theory
EBPVD	Electron Beam Physical Vapour Deposition
EDX	Energy Dispersive X-Ray Spectroscopy
EM	Electromagnetic Enhancement Mechanism
FTIR	Fourier Transform Infrared Spectroscopy
HER	Hydrogen Evolution Reaction
HOMO	Highest Occupied Molecular Orbital
LOD	Limit of Detection
LSV	Linear Sweep Voltammetry
LUMO	Lowest Unoccupied Molecular Orbital
MBE	Molecular Beam Epitaxy
NHE	Normal Hydrogen Electrode
PXRD	Powder X-Ray Diffraction
R6G	Rhodamine 6G
SAED	Selected Area Electron Diffraction
SEM	Scanning Electron Microscopy
SERS	Surface Enhanced Raman Spectroscopy
TEM	Transmission Electron Microscopy
TMDC	Transition Metal Dichalcogenide
WCA	Water Contact Angle
XPS	X-Ray Photoelectron Spectroscopy
2D	Two Dimensional

Thesis Contributions

Some of the work undertaken in this thesis was performed in collaboration with others. The details of collaboration are listed below.

- Raman mapping of 2H- and 1T'-$MoTe_2$ films was performed by Dr. Stacey Laing at the University of Strathclyde.
- XPS spectra of 2H-$MoTe_2$ were recorded by Dr. Juan Carlos Moreno-López at the University of Vienna.
- XPS spectra of 1T'-$MoTe_2$ were recorded by Dr. Petr Sajdl at the University of Chemistry and Technology Prague.
- TEM images and EDX spectra of 2H- and 1T'-$MoTe_2$ were obtained by Dr. Donald A. MacLaren at the University of Glasgow.
- WCA measurements were performed by Dr. Olga Guselnikova at the University of Chemistry and Technology Prague.
- SERS measurements of β-sitosterol on 1T'-$MoTe_2$ were performed by Dr. Olga Guselnikova at the University of Chemistry and Technology Prague.
- DFT calculations were performed by Dr. Rashid Valiev at the University of Helsinki
- UV-vis spectra were recorded by Dr. Olga Guselnikova at the University of Chemistry and Technology Prague.
- FTIR spectra were obtained by Dr. Olga Guselnikova at the University of Chemistry and Technology Prague.
- CV measurements of β-sitosterol on 1T'-$MoTe_2$ were performed by Elena Miliutina at the University of Chemistry and Technology Prague.

Author’s Declaration

I declare that, except where explicit reference is made to the contribution of others, that this dissertation is the result of my own work and has not been submitted for any other degree at the University of Glasgow or any other institution.

Printed name: James Fraser

Signature:

Publications and Conferences

The following manuscripts were published as a result of work undertaken over the course of this PhD:

- **Fraser, J. P**., Postnikov, P., Miliutina, E., Kolska, Z., Valiev, R., Švorčík, V., Lyutakov, O., Ganin, A. Y. & Guselnikova, O. *ACS Appl. Mater. Interfaces* **15**, 54 (2020).
- **Fraser, J. P**., Masaityte, L., Zhang, J., Laing, S., Moreno-Lopez, J. C., McKenzie, A. F., McGlynn, J. C., Panchal, V., Graham, D., Kazakova, O., Pichler, T., MacLaren, D. A., Moran, D. A. J. & Ganin, A. Y. *Commun Mater* **1,** 48 (2020).
- McGlynn, J. C., Dankwort, T., Kienle, L., Bandeira, N. A. G., **Fraser, J. P**., Gibson, E. K., Cascallana-Matías, I., Kamarás, K., Symes, M. D., Miras, H. N. & Ganin, A. Y. *Nat. Commun.* **10**, 4916 (2019).
- McGlynn, J. C., Cascallana-Matias, I., **Fraser, J. P**., Roger, I., McAllister, J., Miras, H. N., Symes, M. D. & Ganin, A. Y. *Energy Technol.* **6**, 345–350 (2018).

The following conferences were attended over the course of this PhD:

- Chemistry of 2-dimensional materials: beyond graphene Faraday Discussion 2020 (Online) – Poster presentation.
- Graphene 2020 (Online) – Oral presentation.
- RSC Solid State Chemistry Group ECR Meeting 2020 (Online) – Oral Presentation.
- Universities of Scotland Inorganic Conference 2019 (Glasgow, UK) – Poster presentation.
- RSC Solid State Chemistry Group Meeting 2018 (London, UK) – Poster presentation
- Energy Technology Partnership Annual Conference 2018 (Glasgow, UK) – Oral presentation.

Table of Contents

1. Introduction

The isolation of graphene in 2004 by Andre Geim and Konstantin Novoselov highlighted that it is not only the composition and crystal structure of a material that dictates its properties, but dimensionality also plays a key role. Graphene, a single layer of graphite, exhibits properties that are different to those of the bulk material, such as a significantly higher electron mobility and tensile strength.[1–3] Graphene has been shown to be a promising material for the design of next generation energy storage, sensing, and electronic and catalytic devices amongst a host of other applications.[4–6] The metallic properties of graphene, however, mean it is not suited to some applications like logic devices, without significant modification to achieve the required semiconducting properties.[7,8] This fact coupled with the rapid development of graphene and the methods used for preparing ultrathin layers subsequently led to the exploration of other two-dimensional materials. The most prominent of these include the transition metal dichalcogenides (TMDCs) (MoS_2, WS_2, etc.), hexagonal boron nitride (h-BN), black phosphorus, MXenes (Ti_2C, Mo_2TiC_2, etc.) and Xenes (silicene, germanene, etc.) (Figure 1-1).[9–13]

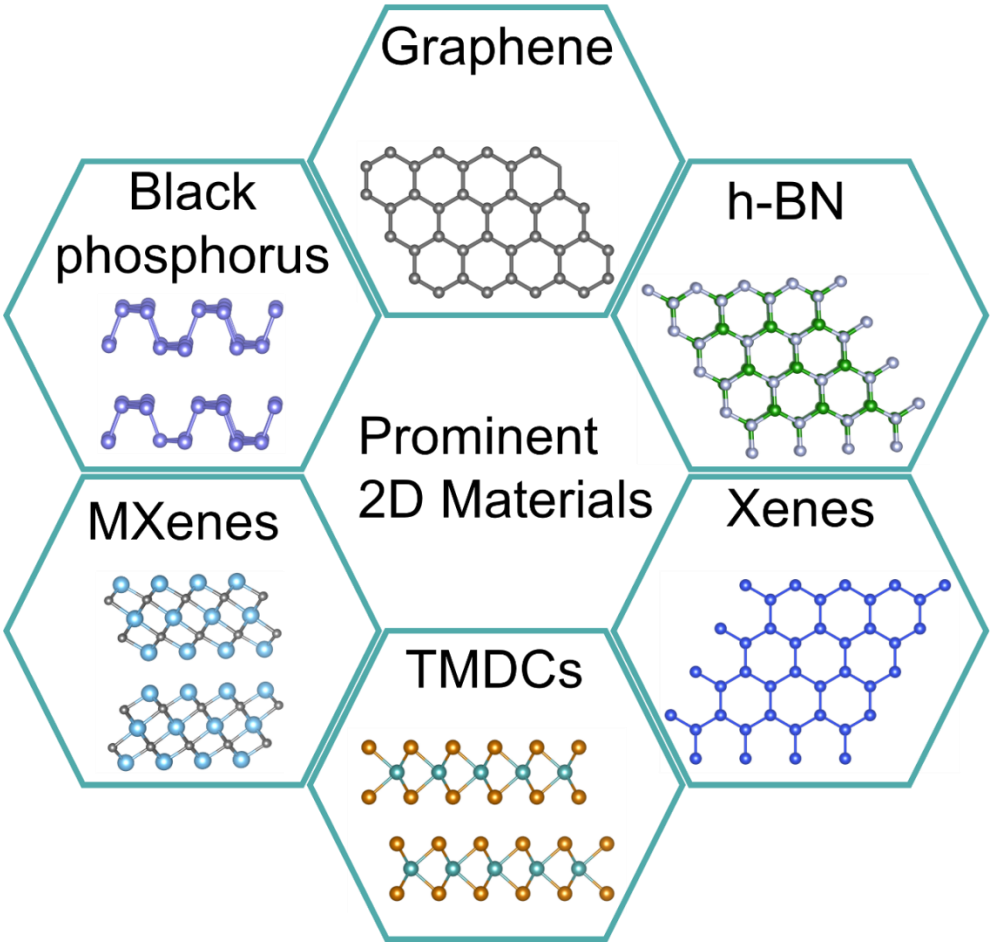

Figure 1-1: Prominent types of 2D materials.

Of the 2D materials listed above it is perhaps the TMDCs that have provoked the most interest from researchers owing to the diverse array of structures and properties exhibited by these materials. A plot of the number of publications containing the phrase “transition metal dichalcogenide” in either the title or abstract against publication year reveals how the study of these materials has rapidly grown over the previous decade (Figure 1-2). One of the most important works in this regard was the study conducted by Mak *et al.* in 2010 where they discovered that the bandgap of MoS_2 nanosheets varied in respect to the thickness of the nanosheets. More importantly they observed a transition from an indirect bandgap of ~1.3 eV in bulk MoS_2 to a direct bandgap of ~1.9 eV when MoS_2 was thinned to a monolayer. A direct bandgap provides stronger and more efficient light emission compared to an indirect bandgap, making monolayer MoS_2 an exciting material for various electronic and optoelectronic applications.[14]

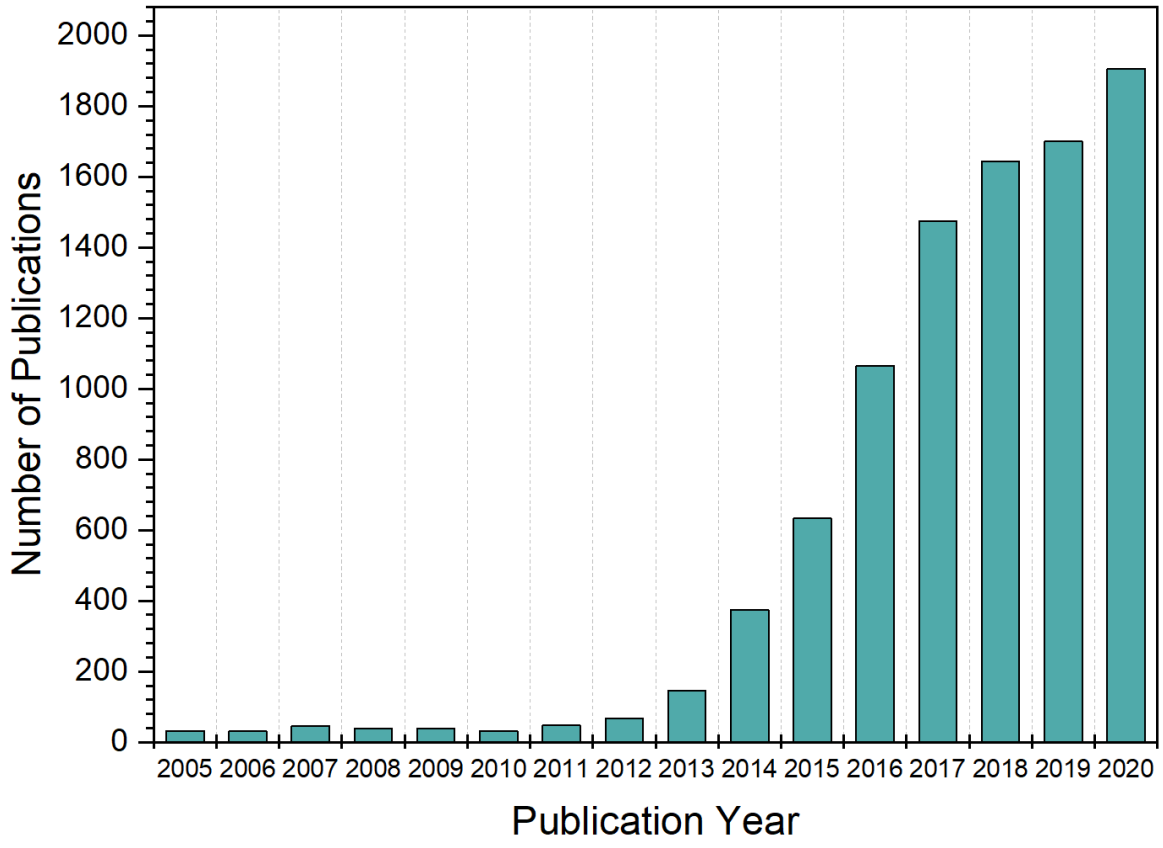

Figure 1-2: Plot showing the number of publications with "transition metal dichalcogenide" featured as a keyword in the title or abstract plotted against publication year. The data was obtained from Web of Science.

1.1. Transition Metal Dichalcogenides

The transition metal dichalcogenides are a group of materials with the general formula MX_2, where M refers to a transition metal atom from groups 4-10 and X is a chalcogen. Around 40 of the TMDC compounds exist as layered materials which are highlighted on the periodic table in Figure 1-3. Only some of the compounds formed by Co, Rh, Ir and Ni exhibit a layered structure, hence the partial highlight, for example NiS_2 has a pyrite structure whereas $NiTe_2$ has a layered structure.[15,16]

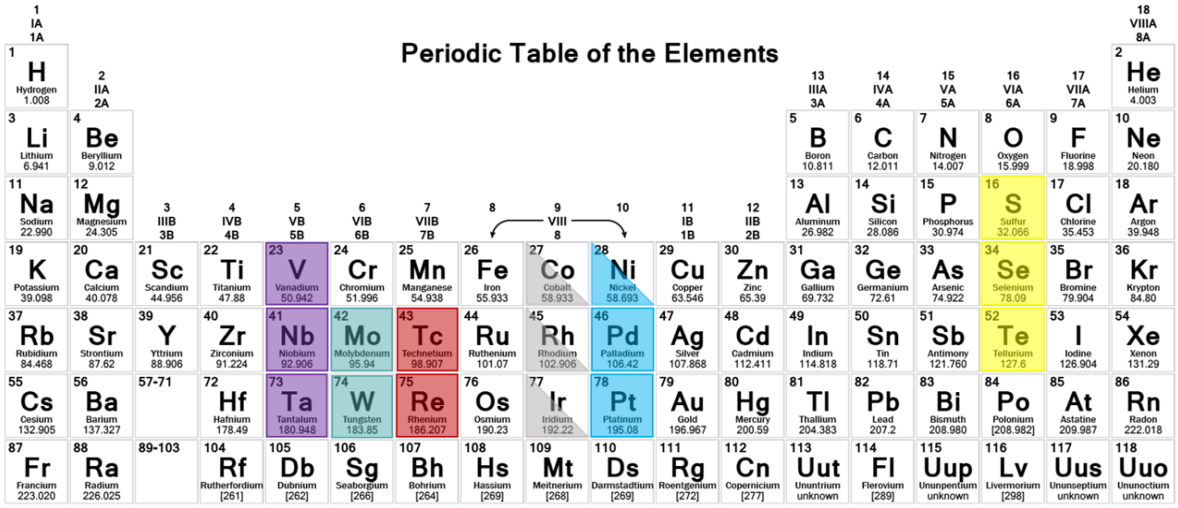

Figure 1-3: The periodic table highlighting the transition metal atoms and chalcogens that predominantly form layered structures. Adapted from [13].

There are several structural phases in which the TMDCs can exist and are a result of differing coordination geometries of the metal atom. Three of the most common are the 2H, 1T and 1T' phases where the metal atoms are coordinated in a trigonal prismatic, octahedral or distorted octahedral manner by six chalcogen atoms (Figure 1-4).[17] Each layer consists of strong, covalently bonded X-M-X stacks, which are then bonded *via* van der Waals interactions to other layers above and below.

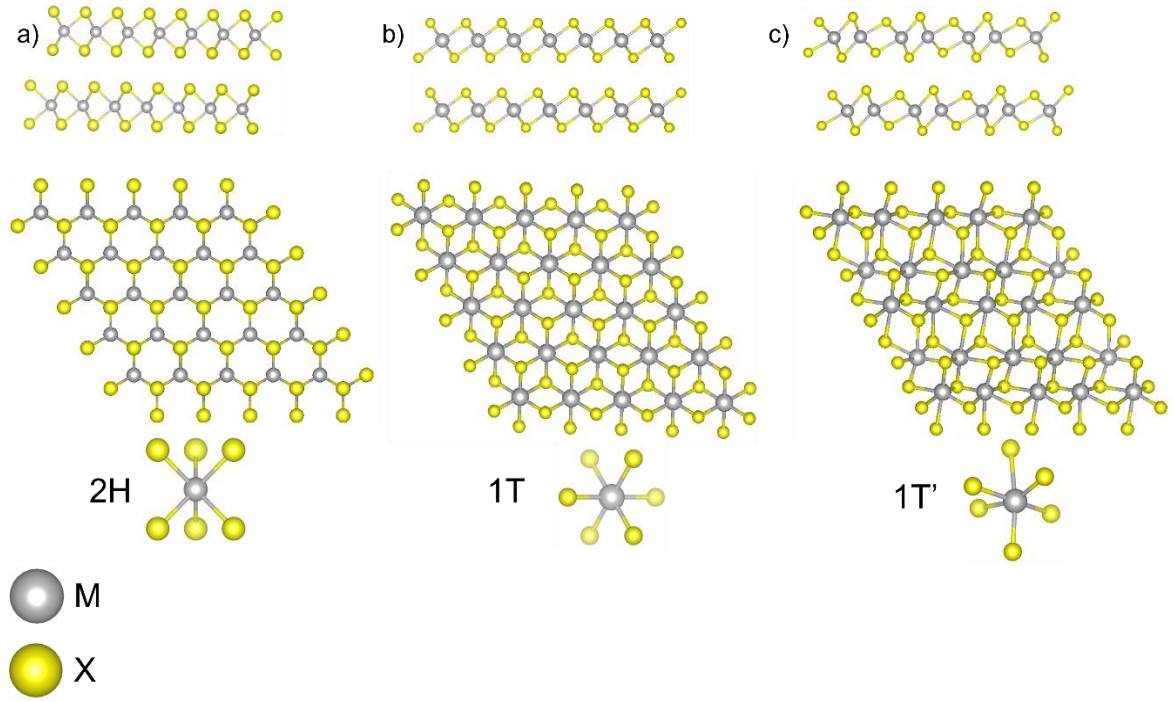

Figure 1-4: Depiction of three of the most common structures exhibited by the layered TMDCs: 2H (a), 1T (b) and 1T' (c). The metal and chalcogen atoms are represented by grey and yellow spheres, respectively.

The variety of chemical compositions and structural phases possible in the TMDCs results in a broad spectrum of electronic properties, covering metallic conductors, semiconductors and insulators.[13] In this regard, the TMDCs formed by the group 6 transition metal Mo and the chalcogens S, Se and Te are particularly interesting. In their thermodynamically stable 2H-phases, MoS_2, $MoSe_2$ and $MoTe_2$ are all semiconducting. As discussed earlier for MoS_2, these materials also exhibit thickness-dependent bandgaps, allowing for a degree of control over the bandgap width.[18] This coupled with the transition from an indirect to direct bandgap upon thinning from few-layers to monolayers makes the molybdenum TMDCs attractive for applications in electronic devices.[18,19] The Mo TMDCs can also exist in octahedral 1T (MoS_2 and $MoSe_2$) or distorted octahedral 1T' ($MoTe_2$) phases, which exhibit metallic conductivity. In the case of MoS_2 and $MoSe_2$ the 1T phases are unstable and are not able to be synthesised directly. However, this is not true for 1T'-$MoTe_2$ which can be synthesised directly and is more stable than 1T-MoS_2 and 1T-$MoSe_2$.[13] The ability to exploit the polymorphism of $MoTe_2$ is an exciting opportunity and makes it, arguably, a more interesting material than its sulfide and selenide cousins.

1.2. Molybdenum Ditelluride

1.2.1. Structure and Properties of 2H-$MoTe_2$

2H-$MoTe_2$ is characterised by its hexagonal structure in which an atomic plane of closely packed Mo atoms are strongly bonded to and sandwiched between two layers of Te atoms.

The Te-Mo-Te layers are weakly bonded by van der Waals forces to other Te-Mo-Te layers and are stacked in the *c* direction resulting in a hexagonal structure. In this polymorph each Mo atom is coordinated to six Te atoms in a trigonal prismatic fashion (Figure 1-5a).

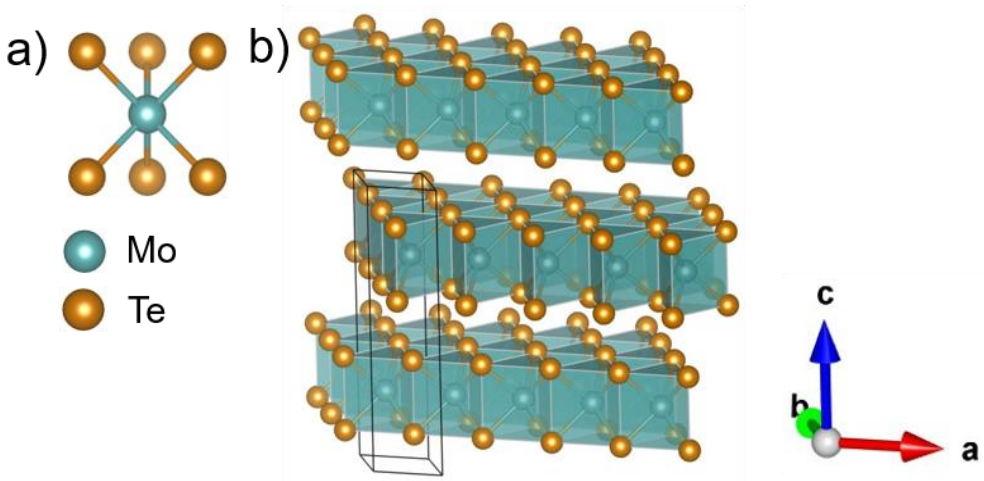

Figure 1-5: Depiction of the trigonal prismatic coordination of Mo by Te in 2H-$MoTe_2$ (a); and crystal structure of 2H-$MoTe_2$ showing the unit cell and highlighting the flat, Te terminated terraces of each Te-Mo-Te layer (b). Mo atoms are represented by teal spheres, whilst Te atoms are represented by orange spheres.

This results in the formation of infinite two dimensional layers of edge-sharing {$MoTe_6$} trigonal prisms. Within a prism each Te atom is stacked directly on top of another, whilst the Mo atoms in successive layers are shifted slightly giving 2H-$MoTe_2$ its characteristic flat terraces terminated by Te atoms (Figure 1-5b). The Ramsdell notation used to describe this $MoTe_2$ polymorph arises from its hexagonal structure symbolised by the capital letter "H" and the preceding digit "2" describes the number of van der Waals layers in the unit cell.[20,21] The crystallographic data of 2H-$MoTe_2$ is summarised in Table 3-1.[22]

Table 1-1: Summary of the crystallographic data of 2H-$MoTe_2$ as determined by Puotinen and Newnham.[22]

Crystal System	Hexagonal
Space Group	$P6_3/mmc$
Lattice Parameters	a = 3.519 Å, c = 13.964 Å $\alpha=\beta=90°$, $\gamma=120°$
Z	2

In the bulk form 2H-$MoTe_2$ is a semiconductor with an indirect bandgap of ~0.9 eV with a valence band maximum at the K point and a conduction band minimum at the midpoint along

Γ-K symmetry lines (Figure 1-6a). Upon decreasing the number of layers in a sample the width of the band gap increases to a maximum of ~1.10 eV for a monolayer of 2H-$MoTe_2$.[23,24] Furthermore, an isolated monolayer possesses a direct bandgap with the valence band maximum and conduction band minimum coinciding at the K point (Figure 1-6b).

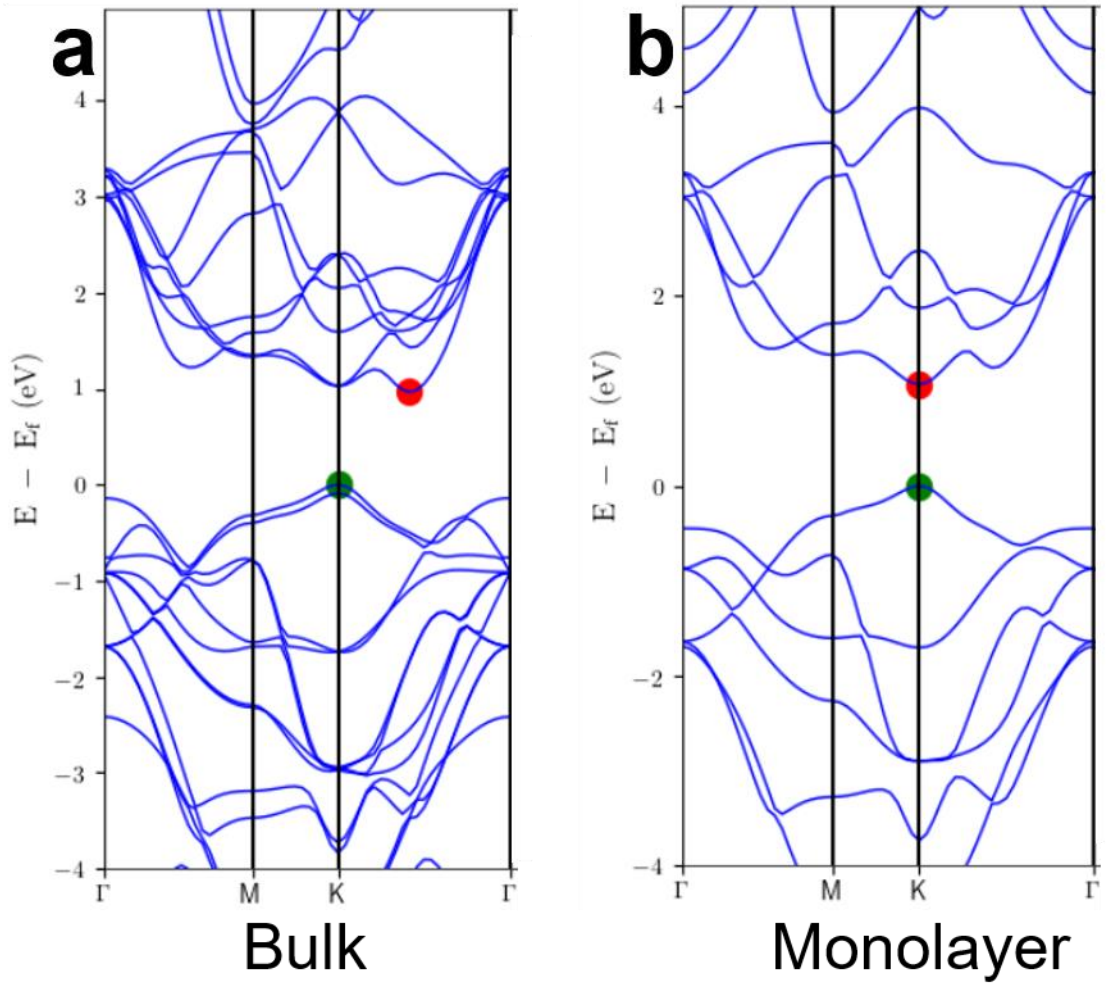

Figure 1-6: Band structures of bulk 2H-$MoTe_2$ (a); and monolayer 2H-$MoTe_2$ (b). Diagrams produced from [25].

This indirect-to-direct bandgap transition on going from bulk to a monolayer is why 2H-$MoTe_2$ is such an attractive target for optoelectronic applications. With its bandgap of ~1.1 eV, monolayer 2H-$MoTe_2$ has a similar bandgap width as silicon but has the advantage of being direct as opposed to the indirect gap of crystalline silicon. Direct band gap materials can more efficiently emit and absorb photons as both electrons and holes have the same crystal momentum so a photon can be directly emitted or absorbed. Whereas, in an indirect band gap material a photon cannot be directly emitted as an electron must pass through an intermediate state and transfer momentum to the crystal lattice.[26]

The size and layer-dependent nature of the band gap of 2H-$MoTe_2$ makes it a particularly interesting material for electronic and optoelectronic applications. For example, there are several reports of few-layered 2H-$MoTe_2$ being utilised to fabricate photodetectors.[27–29] Aside from photodetectors, 2H-$MoTe_2$ has also found a use in silicon photonics. There has been a growing interest in the integration of 2D materials with silicon to produce gain materials and light emitters.[30] Fang *et al* were able to achieve a silicon laser-like emission whilst using few layer 2H-$MoTe_2$ as a gain material, emitting at 1305 nm which is in the middle of the technologically important "O-band" of fibre optical communication, indicating that 2H-$MoTe_2$ may have a bright future in this field.[31]

1.2.2. Structure and Properties of 1T'-$MoTe_2$

$MoTe_2$ can also crystallise in the monoclinic 1T'-phase which consists of Mo atoms strongly bonded to and sandwiched by two layers of Te atoms with these atomic trilayers separated from each other by van der Waals forces. However, instead of the trigonal prismatic coordination of Mo by Te seen in 2H-$MoTe_2$, there is distorted octahedral coordination of Mo by six Te atoms (Figure 1-7a). In this coordination geometry Mo atoms are displaced from the centre of each {$MoTe_6$} octahedra, resulting in the buckling of the tellurium sheets (Figure 1-7b).

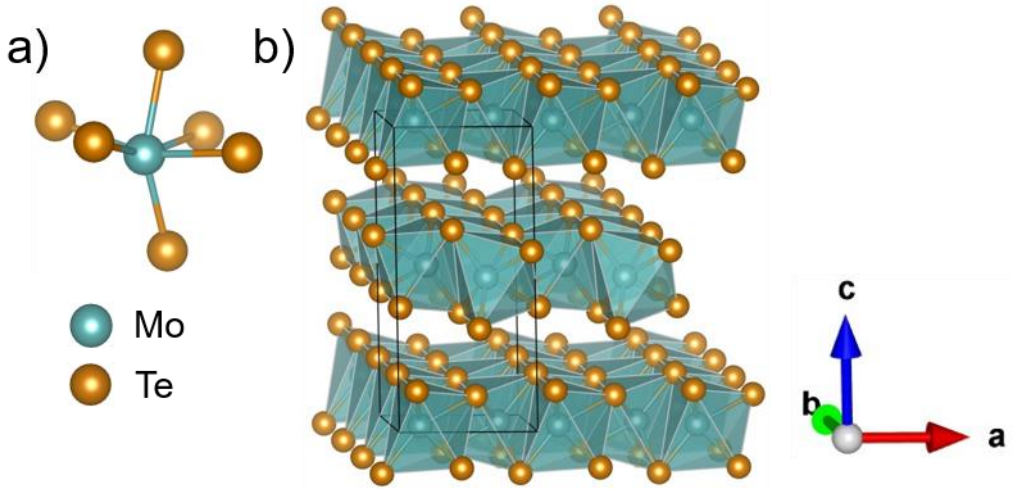

Figure 1-7: Depiction of the distorted octahedral coordination of Mo by Te in 1T'-$MoTe_2$ (a); and crystal structure of 1T'-$MoTe_2$ showing the unit cell and highlighting the buckled nature of the Te sheets in this polymorph (b). Mo atoms are represented by teal spheres, whilst Te atoms are represented by orange spheres.

The Ramsdell notation used to describe this $MoTe_2$ polymorph arises from its distorted octahedral structure symbolised by "T'" and the preceding digit "1" describes the number of full van der Waals layers in the unit cell.[20,21] The crystallographic data of 1T'-$MoTe_2$ is summarised in Table 1-2.

Table 1-2: Summary of the crystallographic data of 1T'-$MoTe_2$ as determined by Brown.[32]

Crystal System	Monoclinic
Space Group	$P2_1/m$
Lattice Parameters	a = 6.330 Å, b = 3.469 Å c = 13.860 Å, β = 93°
Z	4

Due to the change in crystal symmetry 1T'-$MoTe_2$ exhibits vastly different electronic properties to the semiconducting 2H phase.[33] It is a Weyl semi-metal in the bulk form and also displays other exotic properties such as topological superconductivity and a large magnetoresistance.[34–37] Moreover, the metallic conductivity of 1T'-$MoTe_2$ means it has found uses in energy storage and conversion applications such as replacing platinum as a counter electrode in a dye sensitised solar cell as well as an electrocatalyst for the production of hydrogen from water.[38–40] Finally, the conductivity of 1T'-$MoTe_2$ coupled with its atomically flat surface has made it an interesting target for use in surface enhanced Raman spectroscopy (SERS).[41]

1.3. Synthesis Methods for $MoTe_2$

The key to widespread adoption of $MoTe_2$ in the applications mentioned in the previous section is the ability to produce, large area, high quality samples at scale whilst having great control over the phase and thickness of the $MoTe_2$. A variety of methods have been used for the synthesis of few- and mono-layered $MoTe_2$ flakes/films including exfoliation from bulk crystals and vapour deposition methods.[24,42–44]

1.3.1. Mechanical Exfoliation from Bulk Crystals

The mechanical exfoliation of bulk crystals results in very high quality, crystalline flakes of $MoTe_2$ and is able to produce monolayer and few-layer materials, although lacking in precise control.[24,43] First, bulk $MoTe_2$ crystals must be synthesised, which can be achieved using a chemical vapour transport method. This involves the sealing of $MoTe_2$ powder and a transport agent (typically Br_2 or I_2) in a quartz ampoule under vacuum and then heating in a tube furnace featuring a temperature gradient. Single crystals of $MoTe_2$ subsequently form at the colder end of the ampoule with phase selectivity achieved by differing the cooling rates of the furnace. For example, slower cooling rates favour the formation of 2H-$MoTe_2$, whilst rapid cooling rates form 1T'-$MoTe_2$.[45,46]

To exfoliate few- and monolayer flakes from the bulk $MoTe_2$ crystal there are several methods that can be used such as mechanical exfoliation, chemical intercalation and exfoliation and liquid phase exfoliation.[47] Only mechanical exfoliation shall be discussed here, namely due to its simplicity and the fact that it was the method used by Geim and Novoselov to first isolate graphene.[1] Also known as the "Scotch Tape method" it involves placing adhesive tape onto the bulk TMDC crystal and peeling off successive layers. So, for $MoTe_2$ the tape would be placed onto the basal plane of the crystal and then peeled off, leaving a slice of $MoTe_2$ crystal around ~1 μm thick on the tape. Another piece of tape is then placed on the exposed $MoTe_2$ flake forming a Tape/$MoTe_2$/Tape stack. The two pieces of tape are then pulled apart and because the adhesive forces of the tape are stronger than the van der Waals forces the flake is thinned further. This process of folding and unfolding the tape is then repeated until the exfoliated layers are barely visible to the naked eye. The flakes are pressed onto a silicon substrate with a defined thickness of oxide layer, and gentle pressure is applied to the back of the tape, before being peeled off leaving the $MoTe_2$ flakes adhered to the SiO_2/Si substrate. The residues left by the tape can then be washed off using a solvent like isopropanol.[24,48] The flakes can then be identified using an optical microscope and characterised further using techniques such as Raman spectroscopy or atomic force microscopy (AFM).

The mechanical exfoliation of bulk crystals can produce incredibly high quality, few- and monolayer flakes of $MoTe_2$ which are suited to fundamental research and prototyping electronic devices. However, the size of the flakes is limited by the size of the bulk crystals that can be grown and the method is not suited to large scale, high throughput production.

1.3.2. Vapour Deposition Methods

$MoTe_2$ thin films have been successfully grown by a variety of vapour deposition methods such as chemical vapour deposition (CVD),[44] pulsed laser deposition,[49] atomic layer deposition (ALD)[50] and molecular beam epitaxy (MBE).[51] Of these methods CVD has been the most widely used for the production of atomically thin $MoTe_2$ films. In simple terms, CVD involves exposing a substrate to one or more volatile precursors, which can react or decompose to deposit a solid material onto the substrate. In addition, any volatile by-products that form are subsequently removed from the reaction chamber by a flow of carrier gas.[52] There are many types of chemical vapour deposition with their names often describing operating conditions like atmospheric pressure CVD or ultrahigh vacuum CVD, the type of substrate heating such as hot or cold wall CVD or the type of precursors used such as

metalorganic CVD.[53] This work will utilise an atmospheric pressure, hot-wall CVD setup for the deposition of $MoTe_2$ thin films and as such will be the only type discussed further.

Atmospheric pressure CVD is probably the simplest CVD set up, and therefore quite widely used. All that is required for this kind of setup is a tube furnace, a reaction chamber, usually a quartz tube due to its ability to withstand high temperatures as well as rapid heating and cooling, a carrier gas with a controllable flow rate and a substrate coupled with suitable precursor materials (Figure 1-8). Regarding the CVD of $MoTe_2$ in this setup, there are two widely used approaches which vary only in the type of precursors used. The first involves the direct tellurisation of a pre-deposited precursor film which is usually either Mo or MoO_3. The benefits of this method include its simplicity and the ability to grow large films, which are only limited by the size of the substrate and reaction chamber used. However, there are also limitations to this method such as the quality and thickness of the product $MoTe_2$ film is related directly to the quality and thickness of the precursor layer.[47] This is the method utilised in this work and an in depth discussion on how various CVD parameters can impact the reaction outcome can be found in Chapter 3.

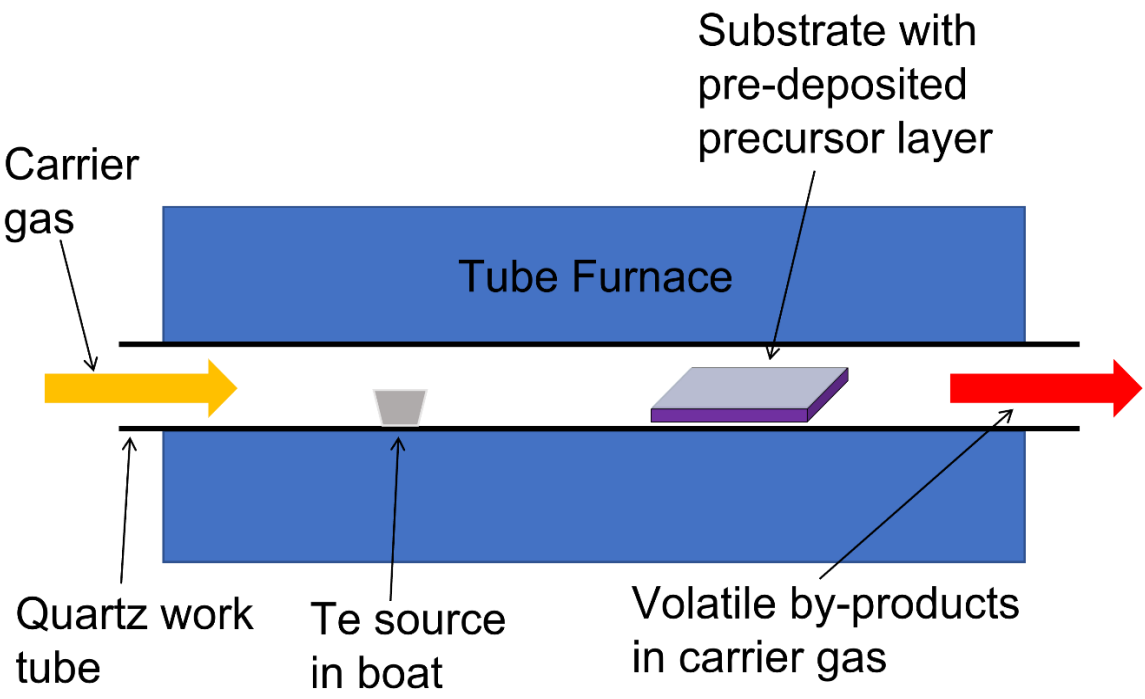

Figure 1-8: Schematic illustration of a hot-wall atmospheric pressure CVD setup for the tellurisation of a pre-deposited molybdenum precursor layer.

The other important route to the CVD of $MoTe_2$ films involves the vapourisation and direct reaction of molybdenum and tellurium powder precursors in the vapour phase. With this method MoO_3 powder is typically used as the source of molybdenum, due to its lower

evaporation temperature compared to molybdenum metal.[54,55] Again, elemental Te is used overwhelmingly as the tellurium source in literature procedures. There is very little research into alternatives to elemental tellurium even though large amounts must be used due to the low evaporation temperature of Te. Therefore, finding different precursor materials with the aim of reducing the amount of Te consumed is an important area of research that should be explored. The direct reaction of molybdenum and tellurium powder precursors in the vapour phase can produce crystalline flakes and films. However, controlling the number of layers accurately can be difficult and requires extensive optimisation of the reaction conditions.

CVD offers numerous parameters that can be varied to affect the outcome of the deposition process. For example, the dwell temperature and time can have a large influence on the CVD process. The growth temperature impacts the evaporation rates of the precursors and therefore their concentration and diffusion rate at the substrate, whilst longer growth times result in higher nucleation densities and the eventual formation of continuous thin films from individual crystalline domains.[56]

The carrier gas composition is an important parameter that must be considered. The inclusion of hydrogen in the carrier gas is necessary in case of $MoTe_2$ as it increases the reactivity of Te through the formation of hydrogen telluride and produces a reductive atmosphere which can reduce MoO_3 to a more reactive suboxide species.[57]

The choice of substrate is another parameter that can have a significant impact on the CVD process as it can influence the shape and orientation of $MoTe_2$ islands during growth. This was illustrated to great effect by Hynek *et al*. who converted ALD deposited MoO_3 precursor layers into few- and monolayer $MoTe_2$ films. They found that the choice of substrate played an important role in deciding the quality of their films, with sapphire substrates promoting the growth of continuous films whilst amorphous SiO_2 substrates encouraged the formation of $MoTe_2$ islands.[57,58]

1.4. The Characterisation of $MoTe_2$

The layer dependent nature of the properties of $MoTe_2$ make it important to be able to accurately characterise the thickness of produced films or flakes. Moreover, the ability to accurately characterise the phase of $MoTe_2$ is incredibly important due to the differing electronic properties of the 2H- and 1T'-phases, respectively. A way of defining the crystallinity of a sample is also required as potential applications may need highly crystalline material with large domains and fewer grain boundaries such as optoelectronic applications.[31,59] Whereas polycrystalline films may be sufficient in some cases. Finally, a

method for confirming that the films are free from impurities or that a precursor layer has been fully converted to $MoTe_2$, in the case of direct tellurisation, is quite important. Some of the most common characterisation methods used to answer these questions are optical microscopy, Raman spectroscopy, X-ray photoelectron spectroscopy (XPS) and transmission electron microscopy (TEM).

1.4.1. Characterisation of $MoTe_2$ using Optical Microscopy

As $MoTe_2$ exhibits thickness dependent properties it is obviously extremely important to identify the thickness of any exfoliated flakes or thin films. As well as identifying the location of exfoliated flakes, optical microscopy can also be used to gauge the number of layers in a sample. When placed on a silicon substrate with an optimised thickness of oxide layer, $MoTe_2$ flakes (and other 2D materials) exhibit vastly different optical contrasts depending on their thickness.[60] An example of this is shown in Figure 1-9 from work conducted by Chang *et al*. showing the extreme contrast difference between flakes of 1-6 layers, which is only a thickness difference of 3.5 nm, when placed onto a 90 nm SiO_2/Si substrate.[61]

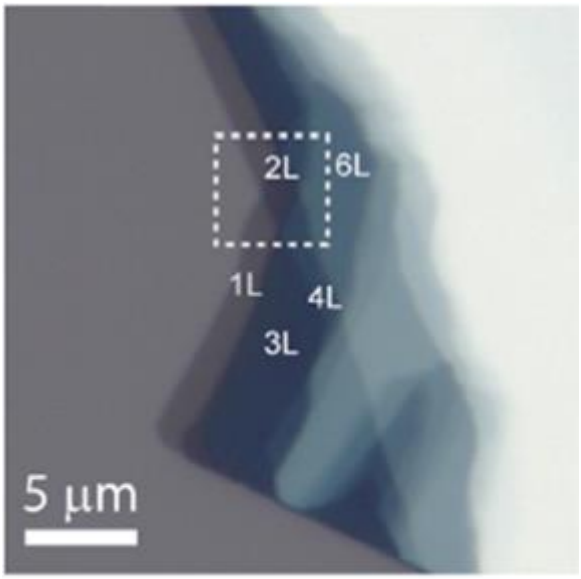

Figure 1-9: Optical image of 1–6-layer $MoTe_2$ on a 90 nm SiO_2/Si substrate. From Chang et al. [61]

This phenomenon is a result of the fact that the $MoTe_2$ flakes absorb an appreciable amount of incident light, roughly a few percent for each monolayer, despite their atomic thickness.[47] This method offers a rapid, non-destructive method of assessing the thickness of flakes and films, but only relative to each other. A library of reference samples whose thicknesses are definitively known through AFM, for example, can be created and then used to benchmark new samples going forward using optical contrast.[61]

1.4.2. Characterisation of $MoTe_2$ using Raman Spectroscopy

Raman spectroscopy is one of the most powerful analytical tools for the characterisation of $MoTe_2$. Due to the differing structures of the two polymorphs Raman spectroscopy can easily distinguish between them, allowing for the rapid, non-destructive characterisation of both 2H- and 1T'-$MoTe_2$ samples (Figure 1-10).

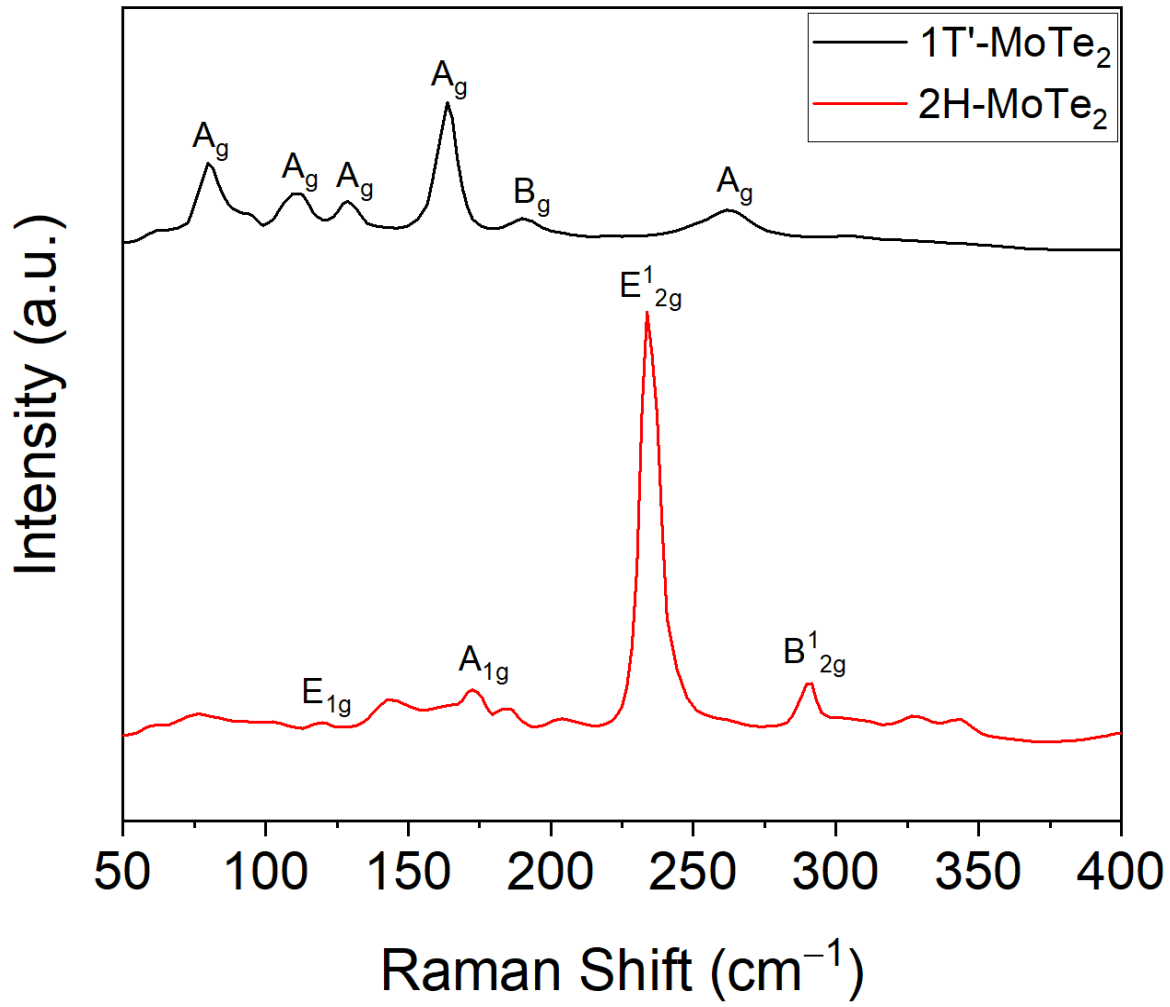

Figure 1-10: Raman spectra of few-layer 1T'- and 2H-$MoTe_2$ with their respective Raman modes highlighted.

The Raman spectrum of a few-layer 2H-$MoTe_2$ film will typically feature 4 Raman modes, which are the in-plane E_{1g} mode at ~119 cm^{-1}, the out-of-plane A_{1g} mode at ~171 cm^{-1}, the in-plane E^1_{2g} mode at ~234 cm^{-1} and the out-of-plane B^1_{2g} mode at ~289 cm^{-1}.[48] In contrast, the Raman spectrum of a few-layer 1T'-$MoTe_2$ film typically features numerous Raman modes, which include A_g modes at ~80, ~108, ~125, ~161, ~251 and ~265 cm^{-1}, whilst a B_g mode usually appears at ~190cm^{-1}.[62]

The labels for the Raman modes are the Mulliken symbols which describe the symmetry of the specific vibrations. For example, in the case of 2H-$MoTe_2$ the A_{1g} mode features out-of-plane, out-of-phase vibrations of the Te planes (Figure 1-11). The "A" symbol signifies that

this vibration is symmetric with respect to the principal rotation axis of 2H-$MoTe_2$, whilst the subscript "1" indicates that it is symmetric to the two-fold rotation that is perpendicular to the principal axis. Finally, the subscript "g" means that this vibration is symmetric with respect to an inversion centre. The B^1_{2g} mode involves out-of-plane vibrations of Mo and Te atoms in opposite directions, with the "B" signifying that this vibration is antisymmetric with respect to the principal rotation axis of 2H-$MoTe_2$. The superscript "1" indicates that this mode is symmetric with respect to reflection in the horizontal plane. The subscript "2" indicates that it is antisymmetric with respect to the two-fold rotation that is perpendicular to the principal axis. The E_{1g} mode involves the in-plane, out-of-phase vibration of Te planes whilst the E^1_{2g} modes involves the in-plane vibration of the Mo and Te planes against each other.[48] The "E" in the case of these two modes indicates that they are both degenerate vibrations, whilst the remaining symbols for these modes have been discussed above.

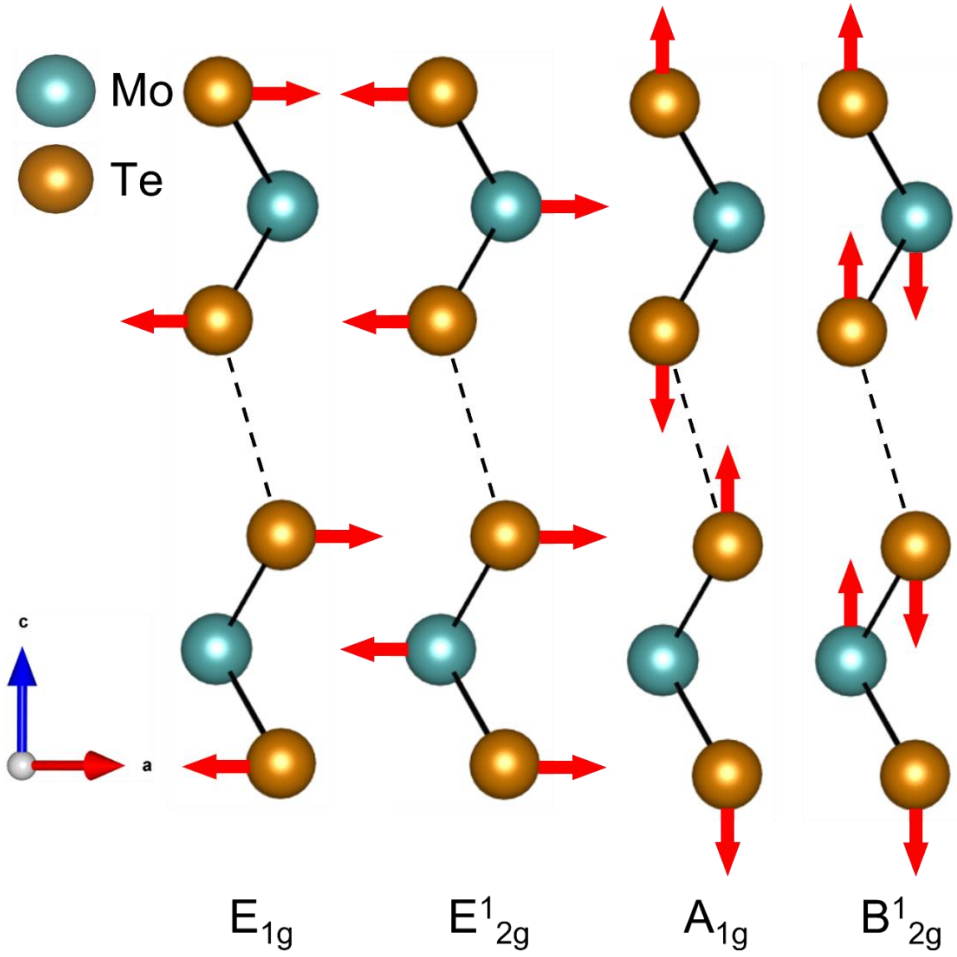

Figure 1-11: Schematic of the vibrational modes of 2H-$MoTe_2$, with their respective Mulliken symbols. Adapted from [48].

As well as being able to distinguish between the two $MoTe_2$ phases easily, Raman spectroscopy can also give information about the number of layers in a 2H-$MoTe_2$ sample. For example, due to differing symmetries of bulk, few-layer and monolayer 2H-$MoTe_2$ the

intensity of the B^1_{2g} mode varies with the number of layers. This mode is inactive in both monolayer and bulk form and as such is an excellent way of rapidly determining if the studied exfoliated flake or CVD grown film is few-layered in nature (Figure 1-12).[48]

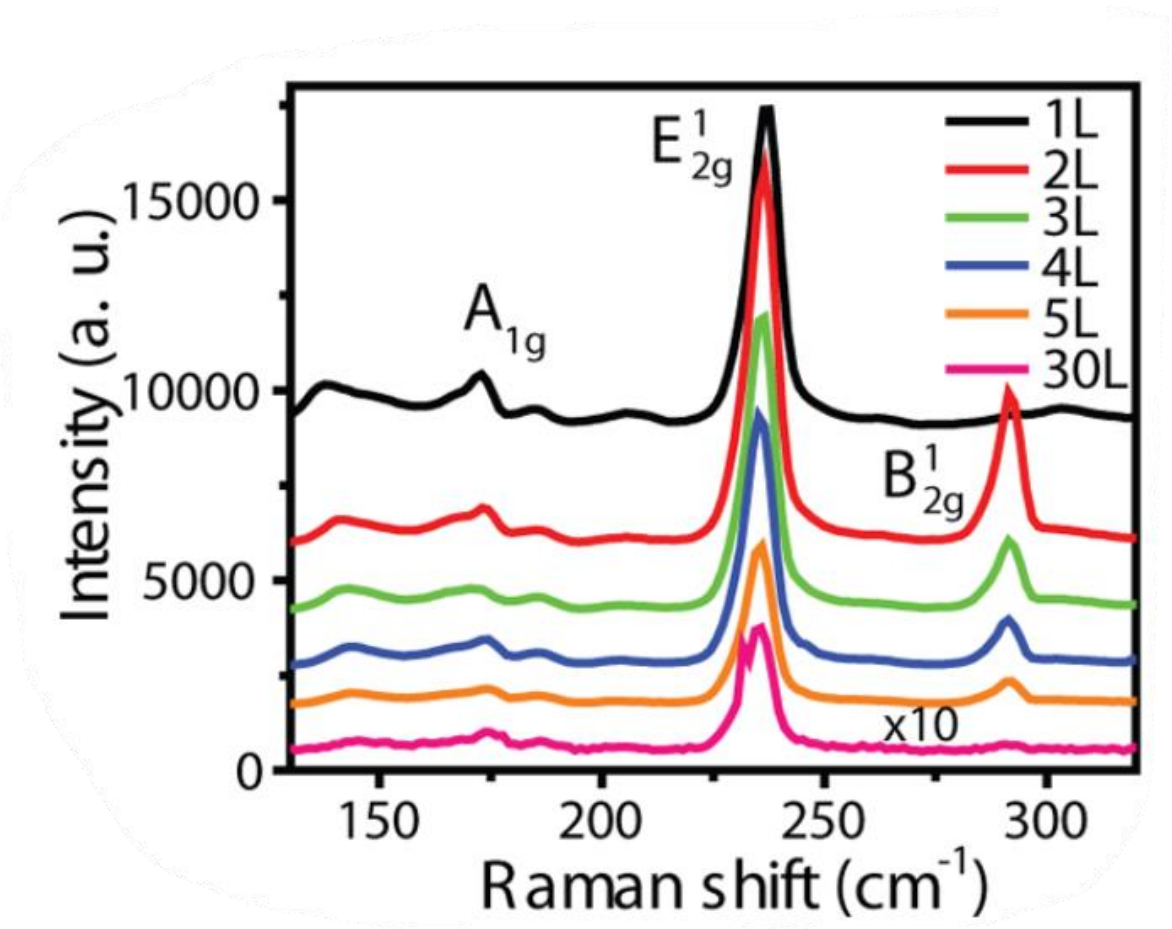

Figure 1-12: Raman spectra obtained from 1-5 and 30 layer exfoliated 2H-$MoTe_2$ flakes by Yamamoto et al.[48] illustrating how the intensity of the B^1_{2g} mode at ~289 cm^{-1} varies with the number of layers.

Calculating the intensity ratio of the B^1_{2g}/E^1_{2g} peaks and plotting against the accurately known number of layers in the 2H-$MoTe_2$ samples results in a plot that can then be used to rapidly benchmark the thicknesses of any flakes or films produced in the future, similar to the optical contrast measurements discussed above.

1.4.3. Characterisation of $MoTe_2$ using X-ray Photoelectron Spectroscopy

Ensuring that exfoliated flakes or CVD deposited thin films of $MoTe_2$ are free from impurities potentially related to the synthesis method is extremely important. XPS is one such technique that is often used to probe the elemental composition and chemical environment of the elements present in a material and due to its ability to only probe the outermost 10 nm or so of a solid surface it is ideal for studying atomically thin films and flakes.[63]

Typically, high resolution XPS spectra are recorded of the Mo and Te 3d areas where in a pristine material it would be expected to find a single spin-orbit doublet in each spectrum, corresponding to Mo^{4+} $3d_{5/2}$ and $3d_{3/2}$ and Te^{2-} $3d_{5/2}$ and $3d_{3/2}$ peaks, respectively. Due to the differing chemical environments of Mo in $MoTe_2$ and MoO_3 for example, any oxidation of the $MoTe_2$ will manifest as a second doublet corresponding to Mo^{6+} $3d_{5/2}$ and $3d_{3/2}$, making the presence of oxidation immediately clear.[64] Similarly, if attempting to synthesise $MoTe_2$ through tellurisation of a Mo precursor layer and for some reason full conversion did not occur, it would be immediately clear due to the presence of an elemental Mo band.

Due to the differing lattice symmetries of 1T'- and 2H-$MoTe_2$ there are small differences in the XPS spectra of the two polymorphs, There is a small binding energy shift of the Mo and Te 3d peaks on the order of ~0.5 eV between the two phases, which is distinct enough to be able distinguish between the two phases and can be used for additional confirmation of Raman results for example.[65]

1.4.4. Characterisation of $MoTe_2$ using Transmission Electron Microscopy

TEM is one of the most used techniques for observing the crystallographic structure of samples of interest. Again, due to the differing structures of the $MoTe_2$ polymorphs it is possible to distinguish between the two phases as the crystal structures can be observed directly (Figure 1-13).[24]

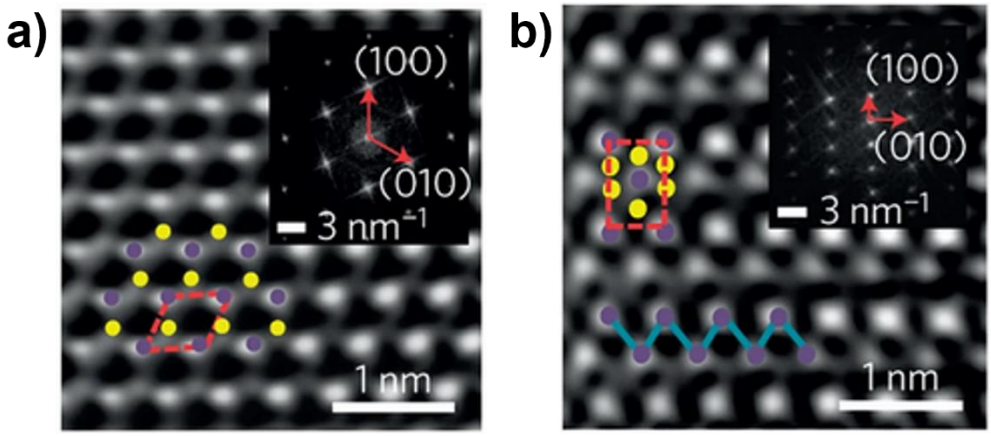

Figure 1-13: TEM images of 2H-$MoTe_2$ (a) and 1T'-$MoTe_2$ (b) single crystals grown by Keum et al.[24] with selected-area electron diffraction patterns inset. Mo atoms are represented by purple spheres, whilst Te atoms are represented by yellow spheres.

To perform TEM measurements, the material of interest must first be transferred onto a TEM grid. In the case of thin films, this requires the sample to be transferred from the growth substrate to the grid. One of the most common substrates used for the growth of $MoTe_2$ thin films is SiO_2/Si. In order to free the $MoTe_2$ film from the substrate, the SiO_2 layer is typically

etched with a solution of hydrofluoric (HF) acid, before submerging the substrate in water, which causes the $MoTe_2$ to float on the surface where it can be easily scooped up with a TEM grid. These conditions are quite harsh and it is possible for the transfer process to damage the film.[57]

TEM measurements are usually coupled with selected-area electron diffraction (SAED), a technique which allows for the qualitative analysis of crystal structure from a spot diffraction pattern. The pattern is acquired through illumination of the sample with the TEM's electron beam parallel to the sample. The SAED pattern of a single crystalline sample will manifest as a series of spots that correspond to the crystal structure of that material, whereas polycrystalline materials will produce a series of diffraction rings, owing to the numerous orientations of the crystals in the material.[66] In the case of crystalline 2H-$MoTe_2$ a diffraction pattern corresponding to the hexagonal structure would be expected (Figure 1-13a inset), and for 1T'-$MoTe_2$ a pattern corresponding to its monoclinic structure would be expected (Figure 1-13b inset).[24]

1.5. Challenges in the Production and Applications of $MoTe_2$

There are still some challenges in the production of large-area phase pure $MoTe_2$ thin films, for instance the polymorphism exhibited by the material can present a challenge in the vapour deposition of phase pure films. The layer dependent properties of $MoTe_2$ also present a challenge with certain applications requiring a specific thickness $MoTe_2$ to perform optimally. Furthermore, the degradation of $MoTe_2$ devices in ambient conditions has led to research into passivation strategies to protect them from environmental damage.

1.5.1. Polymorphism

The advantage that $MoTe_2$ has over MoS_2 and $MoSe_2$ is that its metallic 1T' phase can be synthesised directly and is more stable than 1T-MoS_2/$MoSe_2$. However, this polymorphism does present a challenge for the CVD of $MoTe_2$ thin films. There is only a small energy difference of around ~35 meV per formula unit between 2H- and 1T'-$MoTe_2$ and as such both tend to exist at the typical deposition temperatures used (600-700 °C).[42] This can make finding the conditions for the deposition of phase pure films somewhat tricky and due to the differing properties of the two polymorphs it is extremely important to have phase control over the produced film. For example, in the electrocatalytic production of hydrogen, 1T'-$MoTe_2$ has been shown to significantly outperform 2H-$MoTe_2$ when both materials were utilised as catalysts.[39] Fortunately, there are CVD parameters that can be exploited to favour a particular phase and will be discussed in significant detail in Chapter 3.

Although the polymorphism of $MoTe_2$ presents a challenge in terms of synthesis, it also provides an interesting opportunity for device applications. 2H-$MoTe_2$ electronic devices contacted with the metallic 1T' phase have been shown to outperform those contacted with noble metals due to lower contact resistances in these devices.[67,68] There have been several different methods utilised to induce phase changes in $MoTe_2$ to produce 1T'-2H junctions. A method for this was suggested by Cho *et al.* where the authors claim that laser irradiation could induce a phase change from 2H-$MoTe_2$ to 1T'-$MoTe_2$ and could therefore pattern 1T' contacts into a 2H flake. They attributed the phase change to the creation of tellurium vacancies caused by laser heating which is thought to stabilise the 1T' phase over 2H.[68] This method has been reported by several more groups, but the Raman spectra obtained from the phase converted 1T'-$MoTe_2$ look significantly different to spectra from bulk crystals or CVD grown films.[69,70] In these spectra there is no presence of the A_g mode at ~161 cm^{-1} which is the most prominent mode of 1T'-$MoTe_2$, and they bear a striking resemblance to the Raman spectrum of elemental tellurium. This was investigated further by Sakanashi *et al.* who provided compelling evidence that the laser irradiation does not cause a phase change, but instead causes the decomposition of 2H-$MoTe_2$ into Mo and Te. They showed that similar Raman spectra were obtained after irradiating both 2H- and 1T'-$MoTe_2$ flakes, which match with the spectrum of elemental tellurium (Figure 1-14).[71] Nevertheless, reliable methods for creating 1T'-2H junctions such as patterning followed by a second CVD step and inducing a phase change through electrostatic doping have been demonstrated.[72,73]

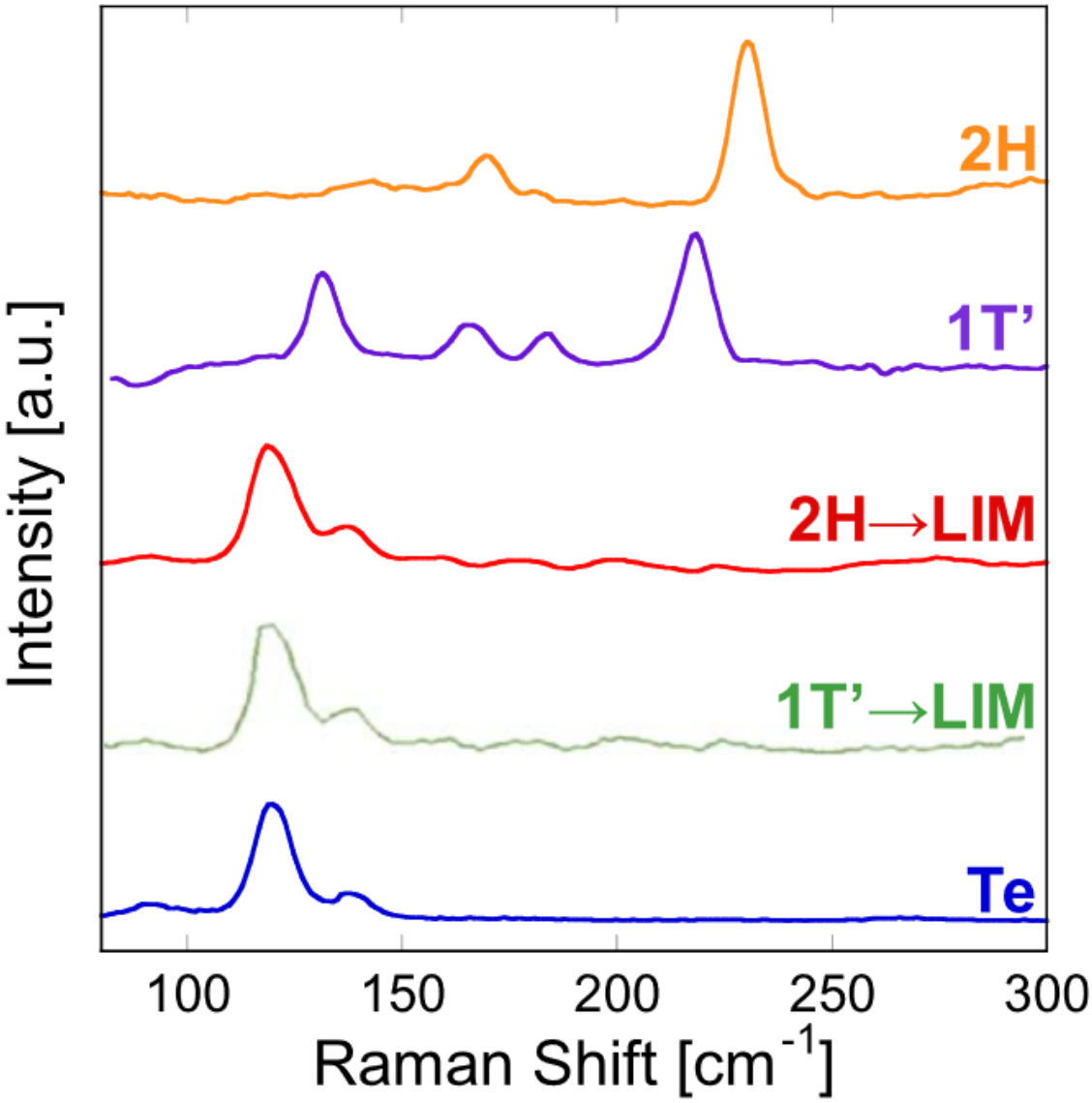

Figure 1-14: Raman spectra of bulk crystal 2H- and 1T'-$MoTe_2$, flakes from these crystals that had been irradiated with a laser and elemental tellurium obtained by Sakanashi et al.[71]

1.5.2. Control Over Number of Layers

The layer dependent properties of $MoTe_2$ are most evident in the semiconducting 2H phase, which experiences a transition from an indirect band gap to a direct band gap when the thickness is reduced from few-layered to monolayered. This transition is particularly evident in the photoluminescence spectra of 2H-$MoTe_2$ as demonstrated by Ruppert *et al.* who measured exfoliated 2H flakes ranging in thickness from 1-5 layers and bulk flakes. From Figure 1-15 it is immediately clear that the photoluminescence intensity is the highest for the monolayer flake and rapidly decreases with increasing thickness. Moreover, there is an appreciable shift in the emission wavelength when the number of layers is increased, further highlighting the thickness dependent properties of the material.[74]

Although it does not exhibit such pronounced thickness dependent properties, there are still some applications where being able to precisely control the thickness of 1T'-$MoTe_2$ is required. For instance, in the case of using 2D materials as surface enhanced Raman spectroscopy substrates. It has been shown for graphene and some TMDCs that the enhancement of the Raman signal of the analyte is heavily dependent on the thickness of the 2D material substrate.[41,75]

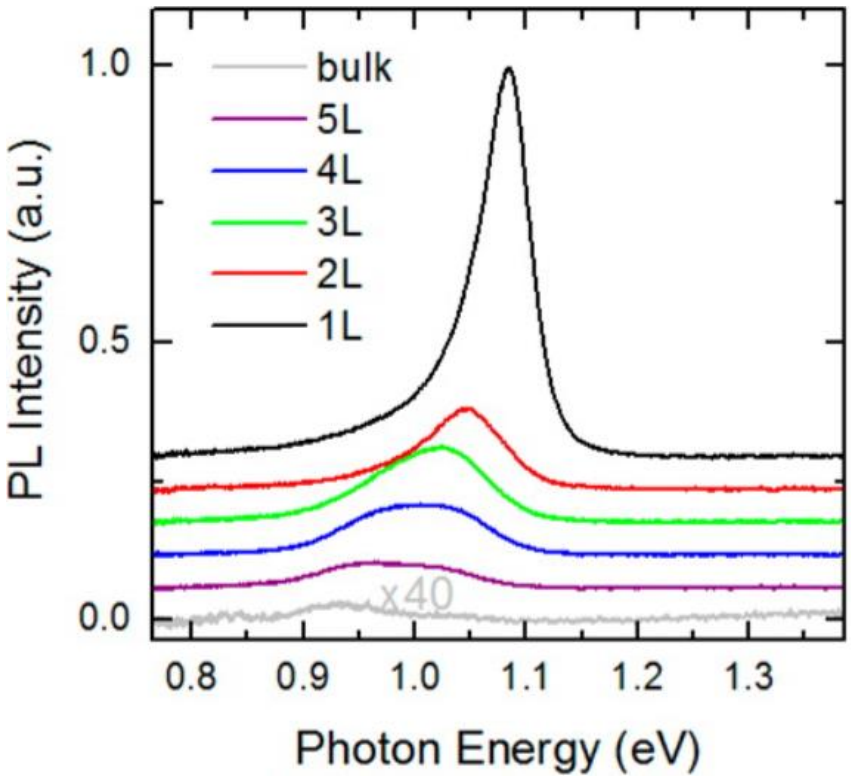

Figure 1-15: Photoluminescence spectra of 1-5 layer and bulk 2H-$MoTe_2$ exfoliated flakes obtained by Ruppert et al.[74]

Being able to accurately control the thickness of any CVD grown $MoTe_2$ films is therefore extremely important. This is where using a predeposited Mo or MoO_3 film as the precursor layer for direct tellurisation has significant advantages. If the thickness of the precursor layer can be controlled precisely then so can the resultant $MoTe_2$ film. An excellent example of this can be found in work published by Hynek *et al.* where the authors synthesised various thicknesses of 2H-$MoTe_2$ films. They used an ALD system to deposit MoO_3 precursor layers, which affords a huge degree of control over the thickness by either increasing or decreasing the number of ALD cycles. Cross-sectional TEM images of the resultant 2H films (Figure 1-16) reveals how much control this method gives with the group able to increase/decrease the thickness by as small an amount as one layer.[57]

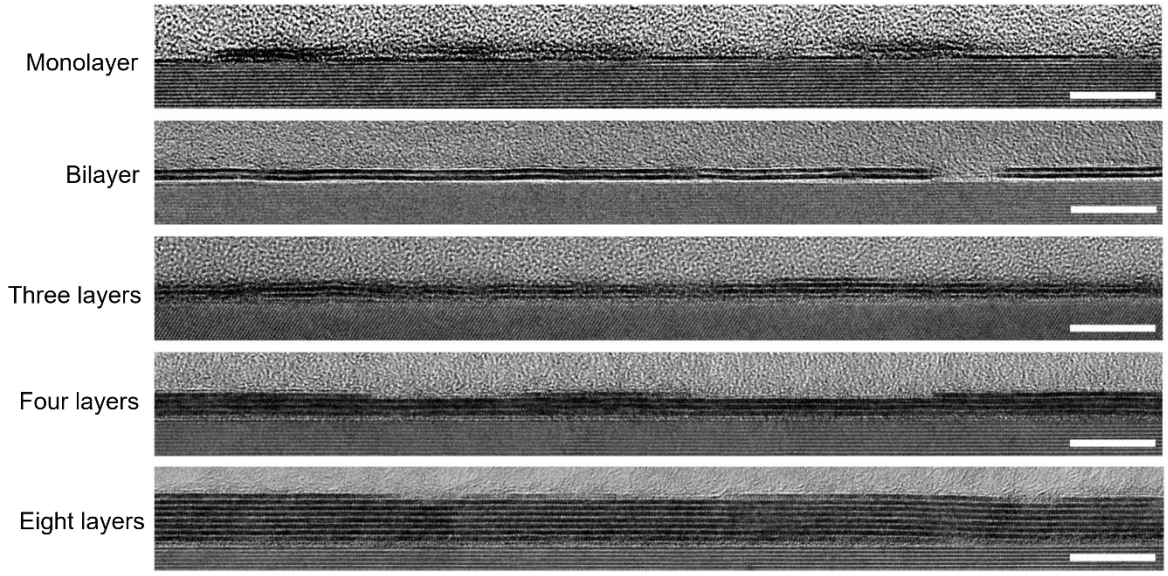

Figure 1-16: Cross-sectional TEM images of CVD grown 2H-$MoTe_2$ films on sapphire substrates converted from ALD deposited MoO_3 precursor films by Hynek et al.[57] The thicknesses of the films range from monolayered to 8 layers.

1.5.3. Oxidation

One of the biggest challenges towards the widespread adoption of $MoTe_2$ in various applications is its propensity to oxidise in ambient conditions. It has been shown that exfoliated 2H-$MoTe_2$ flakes degrade rapidly, of the order of days to a week, with a decrease in their photoluminescence intensity observed, coupled with a blue-shift of the emission wavelength. Interestingly, this rapid decay is not observed in MoS_2 or $MoSe_2$ and can be attributed to the oxidative properties of tellurium which readily forms TeO_2 upon contact with O_2.[76]

Similarly, a study on the stability of 1T'-$MoTe_2$ in ambient conditions conducted by Yang *et al.* found that this polymorph was even more prone to oxidation than the 2H phase. The group found that Mo surface atoms were preferentially oxidised compared to Te and the oxidation led to the formation of an ultrathin MoO_x-TeO_2 surface film that possessed a self-limiting thickness.[77] Concerningly, the authors showed that the formation of the surface oxides significantly impacted the electrical transport characteristics of the film, which is not ideal for devices featuring $MoTe_2$.

The oxidation of $MoTe_2$ in air has led to the investigation of strategies to protect the material from damage in ambient conditions. So far encapsulation has proved to be the most popular passivation strategy for $MoTe_2$, with polymers, ALD deposited Al_2O_3 films and other 2D materials like graphene and h-BN used as encapsulants.[78] The encapsulation of 2H-$MoTe_2$ with h-BN has shown particular promise in optoelectronic applications. For example, Fang

et al. witnessed no decline in performance of their silicon photonic laser using h-BN encapsulated 2H-$MoTe_2$ as a gain material when stored in ambient conditions for the period of one week. The authors note that unencapsulated devices must be stored under vacuum to retain their performance, confirming the observations of Bie *et al.* who had previously fabricated similar devices.[59,79] However, the long term impact that encapsulation has on the stability of $MoTe_2$ films is yet to be fully investigated.

1.6. Aims

This thesis aims to develop a chemical vapour deposition method for $MoTe_2$ that allows for phase selectivity and precise control over the thickness of the resultant films. Furthermore, the use of iron telluride as an alternative tellurium precursor will be explored in the deposition of the $MoTe_2$ films. These produced films will be thoroughly characterised to determine their phase using techniques such as Raman spectroscopy, XPS and TEM, whilst Raman spectroscopy, AFM and optical microscopy will be used to determine their thickness. Subsequently, the CVD grown films will be applied in two different applications, namely as hydrogen evolution catalysts and SERS substrates, with their thickness related performance evaluated.

1.7. References

1. Novoselov, K. S., Geim, A. K., Morozov, S. V., Jiang, D., Zhang, Y., Dubonos, S. V., Grigorieva, I. V. & Firsov, A. A. Electric Field Effect in Atomically Thin Carbon Films. *Science* **306**, 666-669 (2004).

2. Geim, A. K. Graphene: Status and Prospects. *Science* **324**, 1530-1534 (2009).

3. Castro Neto, A. H., Guinea, F., Peres, N. M. R., Novoselov, K. S. & Geim, A. K. The electronic properties of graphene. *Rev. Mod. Phys.* **81**, 109–162 (2009).

4. Shen, J., Zhu, Y., Yang, X. & Li, C. Graphene quantum dots: emergent nanolights for bioimaging, sensors, catalysis and photovoltaic devices. *Chem. Commun.* **48**, 3686–3699 (2012).

5. Pumera, M. Graphene-based nanomaterials for energy storage. *Energy Environ. Sci.* **4**, 668–674 (2011).

6. Zhu, Y., Murali, S., Cai, W., Li, X., Suk, J. W., Potts, J. R. & Ruoff, R. S. Graphene and Graphene Oxide: Synthesis, Properties, and Applications. *Adv. Mater.* **22**, 3906–3924 (2010).

7. Han, M. Y., Özyilmaz, B., Zhang, Y. & Kim, P. Energy Band-Gap Engineering of Graphene Nanoribbons. *Phys. Rev. Lett.* **98**, 206805 (2007).

8. Ni, Z. H., Yu, T., Lu, Y. H., Wang, Y. Y., Feng, Y. P. & Shen, Z. X. Uniaxial Strain on Graphene: Raman Spectroscopy Study and Band-Gap Opening. *ACS Nano* **2**, 2301–2305 (2008).

9. Zhang, K., Feng, Y., Wang, F., Yang, Z. & Wang, J. Two dimensional hexagonal boron nitride (2D-hBN): synthesis, properties and applications. *J. Mater. Chem. C* **5**, 11992–12022 (2017).

10. Qiu, M., Ren, W. X., Jeong, T., Won, M., Park, G. Y., Sang, D. K., Liu, L.-P., Zhang, H. & Kim, J. S. Omnipotent phosphorene: a next-generation, two-dimensional nanoplatform for multidisciplinary biomedical applications. *Chem. Soc. Rev.* **47**, 5588–5601 (2018).

11. Molle, A., Goldberger, J., Houssa, M., Xu, Y., Zhang, S.-C. & Akinwande, D. Buckled two-dimensional Xene sheets. *Nat. Mater.* **16**, 163–169 (2017).

12. Vahidohammadi, A., Rosen, J. & Gogotsi, Y. The world of two-dimensional carbides and nitrides (Mxenes). *Science* **372**, (2021).

13. Chhowalla, M., Shin, H. S., Eda, G., Li, L.-J., Loh, K. P. & Zhang, H. The chemistry of two-dimensional layered transition metal dichalcogenide nanosheets. *Nat Chem* **5**, 263–275 (2013).

14. Mak, K. F., Lee, C., Hone, J., Shan, J. & Heinz, T. F. Atomically Thin MoS_2: A New Direct-Gap Semiconductor. *Phys. Rev. Lett.* **105**, 136805 (2010).

15. Yao, X. & Honig, J. M. Growth of nickel dichalcogenides crystals with pyrite structure from tellurium melts [NiS_2, $NiS_{2-x}Se_x$ ($x \leq 0.7$)]. *Mater. Res. Bull.* **29**, 709–716 (1994).

16. Yang, E., Ji, H. & Jung, Y. Two-Dimensional Transition Metal Dichalcogenide Monolayers as Promising Sodium Ion Battery Anodes. *J. Phys. Chem. C* **119**, 26374–26380 (2015).

17. Manzeli, S., Ovchinnikov, D., Pasquier, D., Yazyev, O. V & Kis, A. 2D transition metal dichalcogenides. *Nat. Rev. Mater.* **2**, 17033 (2017).

18. Mann, J., Ma, Q., Odenthal, P.M., Isarraraz, M., Le, D., Preciado, E., Barroso, D., Yamaguchi, K., von Son Palacio, G., Nguyen, A., Tran, T., Wurch, M., Nguyen, A., Klee, V., Bobek, S., Sun, D., Heinz, T.F., Rahman, T.S., Kawakami, R. & Bartels, L.. 2-Dimensional Transition Metal Dichalcogenides with Tunable Direct Band Gaps: $MoS_{2(1-x)}Se_{2x}$ Monolayers. *Adv. Mater.* **26**, 1399–1404 (2014).

19. Radisavljevic, B., Radenovic, A., Brivio, J., Giacometti, V. & Kis, A. Single-layer MoS_2 transistors. *Nat. Nanotechnol.* **6**, 147–150 (2011).

20. Trigunayat, G. C. & Verma, A. R. Polytypism and Stacking Faults in Crystals with Layer Structure. in *Crystallography and Crystal Chemistry of Materials with Layered Structures* 269–340 (Springer Netherlands, 1976).

21. Rao, G. V. S. & Shafer, M. W. Intercalation in Layered Transition Metal Dichalcogenides. in *Intercalated Layered Materials* 99–199 (Springer Netherlands, 1979).

22. Puotinen, D. & Newnham, R. E. The crystal structure of $MoTe_2$. *Acta Crystallogr.* **14**, 691–692 (1961).

23. Lezama, I. G., Ubaldini, A., Longobardi, M., Giannini, E., Renner, C., Kuzmenko, A. B. & Murpurgo, A. F. Surface transport and band gap structure of exfoliated 2H-$MoTe_2$ crystals. *2D Mater.* **1**, 21002 (2014).

24. Keum, D. H., Cho, S., Kim, J. H., Choe, D.-H., Sung, H.-J., Kan, M., Kang, H., Hwang, J.-Y., Kim, S. W., Yang, H., Chang, K. J. & Lee, Y. H. Bandgap opening in few-layered monoclinic $MoTe_2$. *Nat Phys* **11**, 482–486 (2015).

25. Jain, A., Ong, S. P., Hautier, G., Chen, W., Richards, W. D., Dacek, S., Cholia, S., Gunter, D., Skinner, D., Ceder, G. & Persson, K. A. The Materials Project: A materials genome approach to accelerating materials innovation. *APL Mater.* **1**, 11002 (2013).

26. Simon, S. H. *The Oxford Solid State Basics*. (Oxford University Press, 2013).

27. Kuiri, M., Chakraborty, B., Paul, A., Das, S., Sood, A. K. & Das, A. Enhancing photoresponsivity using $MoTe_2$-graphene vertical heterostructures. *Appl. Phys. Lett.* **108**, 063506 (2016).

28. Pezeshki, A., Shokouh, S. H. H., Nazari, T., Oh, K. & Im, S. Electric and Photovoltaic Behavior of a Few-Layer α-$MoTe_2$ /MoS_2 Dichalcogenide Heterojunction. *Adv. Mater.* **28**, 3216–3222 (2016).

29. Octon, T. J., Nagareddy, V. K., Russo, S., Craciun, M. F. & Wright, C. D. Fast High-Responsivity Few-Layer $MoTe_2$ Photodetectors. *Adv. Opt. Mater.* **4**, 1750–1754 (2016).

30. Youngblood, N. & Li, M. Integration of 2D materials on a silicon photonics platform for optoelectronics applications. *Nanophotonics* **6**, 1205–1218 (2017).

31. Fang, H., Liu, J., Li, H., Zhou, L., Liu, L., Li, J., Wang, X., Krauss, T. F. & Wang, Y. 1305 nm Few-Layer $MoTe_2$-on-Silicon Laser-Like Emission. *Laser Photonics Rev.* **12**, 1800015 (2018).

32. Brown, B. E. The crystal structures of WTe_2 and high-temperature $MoTe_2$. *Acta Crystallogr.* **20**, 268 (1966).

33. Vellinga, M. B., de Jonge, R. & Haas, C. Semiconductor to metal transition in $MoTe_2$. *J. Solid State Chem.* **2**, 299–302 (1970).

34. Qi, Y., Naumov, P. G., Ali, M. N., Rajamathi, C. R., Schnelle, W., Barkalov, O., Hanfland, M., Wu, S.-C., Shekhar, C., Sun, Y., Süß, V., Schmidt, M., Schwarz, U., Pippel, E., Werner, P., Hillebrand, R., Förster, T., Kampert, E., Parkin, S., Cava, R. J., Felser, C., Yan, B. & Medvedev, S. A. Superconductivity in Weyl semimetal candidate $MoTe_2$. *Nat. Commun.* **7**, 11038 (2016).

35. Yan, B. & Felser, C. Topological Materials: Weyl Semimetals. *Annu. Rev. Condens. Matter Phys. is* **8**, 337–54 (2017).

36. Jiang, J., Liu, Z. K., Sun, Y., Yang, H. F., Rajamathi, C. R., Qi, Y. P., Yang, L. X., Chen, C., Peng, H., Hwang, C.-C., Sun, S. Z., Mo, S.-K., Vobornik, I., Fujii, J., Parkin, S. S. P., Felser, C., Yan, B. H. & Chen, Y. L. Signature of type-II Weyl semimetal phase in $MoTe_2$. *Nat. Commun.* **8**, 13973 (2017).

37. Yuan, S., Luo, X., Chan, H. L., Xiao, C., Dai, Y., Xie, M. & Hao, J. Room-temperature ferroelectricity in $MoTe_2$ down to the atomic monolayer limit. *Nat. Commun.* **10**, 1775 (2019).

38. Hussain, S., Patil, S. A., Vikraman, D., Mengal, N., Liu, H., Song, W., An, K.-S., Jeong, S. H., Kim, H.-S. & Jung, J. Large area growth of $MoTe_2$ films as high performance counter electrodes for dye-sensitized solar cells. *Sci. Rep.* **8**, 29 (2018).

39. McGlynn, J. C., Cascallana-Matias, I., Fraser, J. P., Roger, I., McAllister, J., Miras, H. N., Symes, M. D. & Ganin, A. Y. Molybdenum Ditelluride Rendered into an Efficient and Stable Electrocatalyst for the Hydrogen Evolution Reaction by Polymorphic Control. *Energy Technol.* **6**, 345–350 (2018).

40. McGlynn, J. C., Dankwort, T., Kienle, L., Bandeira, N. A. G., Fraser, J. P., Gibson, E. K., Cascallana-Matías, I., Kamarás, K., Symes, M. D., Miras, H. N. & Ganin, A. Y. The rapid electrochemical activation of $MoTe_2$ for the hydrogen evolution reaction. *Nat. Commun.* **10**, 1–9 (2019).

41. Tao, L., Chen, K., Chen, Z., Cong, C., Qiu, C., Chen, J., Wang, X., Chen, H., Yu, T., Xie, W., Deng, S. & Xu, J.-B. 1T′ Transition Metal Telluride Atomic Layers for Plasmon-Free SERS at Femtomolar Levels. *J. Am. Chem. Soc.* **140**, 8696–8704 (2018).

42. Park, J. C., Yun, S. J., Kim, H., Park, J.-H., Chae, S. H., An, S.-J., Kim, J.-G., Kim, S. M., Kim, K. K. & Lee, Y. H. Phase-Engineered Synthesis of Centimeter-Scale 1T′- and 2H-Molybdenum Ditelluride Thin Films. *ACS Nano* **9**, 6548–6554 (2015).

43. Seok, J., Lee, J.-H., Cho, S., Ji, B., Kim, H. W., Kwon, M., Kim, D., Kim, Y.-M., Oh, S. H., Kim, S. W., Lee, Y. H., Son, Y.-W. & Yang, H. Active hydrogen evolution through lattice distortion in metallic $MoTe_2$. *2D Mater.* **4**, 025061 (2017).

44. Zhou, L., Xu, K., Zubair, A., Liao, A. D., Fang, W., Ouyang, F., Lee, Y-H., Ueno, K., Saito, R., Palacios, T., Kong, J. & Dresselhaus, M. S. Large-Area Synthesis of High-Quality Uniform Few-Layer $MoTe_2$. *J. Am. Chem. Soc.* **137**, 11892–11895 (2015).

45. Ueno, K. & Fukushima, K. Changes in structure and chemical composition of α-$MoTe_2$ and β-$MoTe_2$ during heating in vacuum conditions. *Appl. Phys. Express* **8**, 95201 (2015).

46. Ueno, K. Introduction to the Growth of Bulk Single Crystals of Two-Dimensional Transition-Metal Dichalcogenides. *J. Phys. Soc. Japan* **84**, 121015 (2015).

47. Samadi, M., Sarikhani, N., Zirak, M., Zhang, H., Zhang, H.-L. Moshfegh, A. Z. Group 6 transition metal dichalcogenide nanomaterials: Synthesis, applications and future perspectives. *Nanoscale Horizons* vol. 3 90–204 (2018).

48. Yamamoto, M., Wang, S. T., Ni, M., Lin, Y.-F., Li, S.-L., Aikawa, S., Jian, W.- B., Ueno, K., Wakabayashi, K. & Tsukagoshi, K.. Strong Enhancement of Raman Scattering from a Bulk-Inactive Vibrational Mode in Few-Layer $MoTe_2$. *ACS Nano* **8**, 3895–3903 (2014).

49. Lu, Z. J., Xu, Y., Yu, Y. Q., Xu, K. W., Mao, J., Xu, G. B., Ma, Y. M., Wu, D. & Jie, J. S. Ultrahigh Speed and Broadband Few-Layer $MoTe_2$/Si 2D–3D Heterojunction-Based Photodiodes Fabricated by Pulsed Laser Deposition. *Adv. Funct. Mater.* **30**, 1907951 (2020)

50. Zazpe, R., Sopha, H., Charvot, J., Krumpolec, R., Rodriguez-Pereira, J., Michalicka, J., Mistrik, J., Baca, D., Motola, M., Bures, F. & Macak, J. M. 2D $MoTe_2$ nanosheets by atomic layer deposition: Excellent photo- electrocatalytic properties. *Appl. Mater. Today* **23**, 101017 (2021).

51. Ogorzałek, Z., Seredynski, B., Kret, S., Kwiatkowski, A., Korona, K. P., Grzeszczyk, M., Mierzejewski, J., Wasik, D., Pacuski, W., Sadowski, J. & Gryglas-Borydiewicz, M. Charge transport in MBE-grown 2H-$MoTe_2$ bilayers with enhanced stability provided by an AlO_x capping layer. *Nanoscale* **12**, 16535–16542 (2020).

52. Sun, L., Yuan, G., Gao, L., Yang, J., Chhowalla, M., Gharahcheshmeh, M. H., Gleason, K. K., Choi, Y. S., Hong, B. H. & Liu, Z. Chemical vapour deposition. *Nat. Rev. Methods Prim.* **1**, 5 (2021).

53. Jonesm A. C. & Hitchman, M. L. Chapter 1 Overview of Chemical Vapour Deposition. in *Chemical Vapour Deposition: Precursors, Processes and Applications* (eds. Jones, A. C. & Hitchman, M. L.) 1–36 (The Royal Society of Chemistry, 2009).

54. Empante, T. A., Zhou, Y., Klee, V., Nguyen, A. E., Lu, I.-H., Valentin, M. D., Naghibi Alvillar, S. A., Preciado, E., Berges, A. J., Merida, C. S., Gomez, M., Bobek, S., Isarraraz, M., Reed, E. J. & Bartels, L. Chemical Vapor Deposition Growth of Few-Layer $MoTe_2$ in the 2H, 1T′, and 1T Phases: Tunable Properties of $MoTe_2$ Films. *ACS Nano* **11**, 900–905 (2017).

55. Zhou, J., Liu, F., Lin, J., Huang, X., Xia, J., Zhang, B., Zeng, Q., Wang, H., Zhu, C., Niu, L., Wang, X., Fu, W., Yu, P., Chang, T.-R., Hsu, C-H., Wu, D., Jeng, H-T., Huang, Y., Lin, H., Shen, S., Yang, C., Suenaga, K., Zhou, W., Pantelides, S. T., Liu, G. & Liu, Z. Large-Area and High-Quality 2D Transition Metal Telluride. *Adv. Mater.* **29**, 1603471 (2017).

56. Brent, J. R., Savjani, N. & O'Brien, P. Synthetic approaches to two-dimensional transition metal dichalcogenide nanosheets. *Prog. Mater. Sci.* **89**, 411–478 (2017).

57. Hynek, D. J., Singhania, R. M., Xu, S., Davis, B., Wang, L., Yarali, M., Pondick, J. V., Woods, J. M., Strandwitz, N. C. & Cha, J. J. cm^2-Scale Synthesis of $MoTe_2$ Thin Films with Large Grains and Layer Control. *ACS Nano* **15**, 410–418 (2021).

58. Hynek, D. J., Singhania, R. M., Hart, J. L., Davis, B., Wang, M., Strandwitz, N. C. & Cha, J. J. Effects of growth substrate on the nucleation of monolayer $MoTe_2$. *CrystEngComm* (2021) doi:10.1039/D1CE00275A.

59. Fang, H., Liu, J., Lin, Q., Su, R., Wei, Y., Krauss, T. F., Li, J., Wang, Y. & Wang, X. Laser-Like Emission from a Sandwiched $MoTe_2$ Heterostructure on a Silicon Single-

Mode Resonator. *Adv. Opt. Mater.* **7**, 1900538 (2019).

60. Li, H., Wu, J., Huang, X., Lu, G., Yang, J., Lu, X., Xiong, Q. & Zhang, H. Rapid and Reliable Thickness Identification of Two-Dimensional Nanosheets Using Optical Microscopy. *ACS Nano* **7**, 10344–10353 (2013).

61. Chang, Y.-M., Lin, C.-Y., Lin, Y.-F. & Tsukagoshi, K. Two-dimensional $MoTe_2$ materials: From synthesis, identification, and charge transport to electronics applications. *Jpn. J. Appl. Phys.* **55**, 1102A1 (2016).

62. Zhou, L., Huang, S., Tatsumi, Y., Wu, L., Guo, H., Bie, Y.-Q., Ueno, K., Yang, T., Zhu, Y., Kong, J., Saito, R. & Dresselhaus, M. S. Sensitive Phonon-Based Probe for Structure Identification of 1T′ $MoTe_2$. *J. Am. Chem. Soc.* **139**, 8396–8399 (2017).

63. Van der Heide, P. *X-ray photoelectron spectroscopy : an introduction to principles and practices*. (Wiley-Blackwell, 2012).

64. Fleisch, T. H. & Mains, G. J. An XPS study of the UV reduction and photochromism of MoO_3 and WO_3. *J. Chem. Phys.* **76**, 780–786 (1982).

65. Zhou, L., Xu, K., Zubair, A., Zhang, X., Ouyang, F., Palacios, T., Dresselhaus, M. S., Li, Y. & Kong, J. Role of Molecular Sieves in the CVD Synthesis of Large-Area 2D $MoTe_2$. *Adv. Funct. Mater.* **27**, 1603491 (2017).

66. Williams, D. B. & Carter, C. B. Transmission electron microscopy: A textbook for materials science. *Transm. Electron Microsc. A Textb. Mater. Sci.* 1–760 (2009)

67. Ma, R., Zhang, H., Yoo, Y., Degregorio, Z. P., Jin, L., Golani, P., Azadani, J. G., Low, T., Johns, J. E., Bendersky, L. A., Davydov, A. V. & Koester, S. J. $MoTe_2$ Lateral Homojunction Field-Effect Transistors Fabricated using Flux-Controlled Phase Engineering. *ACS Nano* **13**, 8035–8046 (2019).

68. Cho, S., Kim, S., Kim, J. H., Zhao, J., Seok, J., Keum, D. H., Baik, J., Choe, D-H., Chang, K. J., Suenaga, K., Kim, S. W., Lee, Y. H. & Yang, H. Phase patterning for ohmic homojunction contact in $MoTe_2$. *Science* **349**, 625 (2015).

69. Tan, Y., Luo, F., Zhu, M., Xu, X., Ye, Y., Li, B., Wang, G., Luo, W., Zheng, X., Wu, N., Yu, Y., Qin, S. & Zhang, X.-A. Controllable 2H-to-1T′ phase transition in few-layer $MoTe_2$. *Nanoscale* **10**, 19964–19971 (2018).

70. Si, C., Choe, D., Xie, W., Wang, H., Sun, Z., Bang, J. & Zhang, S. Photoinduced Vacancy Ordering and Phase Transition in $MoTe_2$. *Nano Lett.* **19**, 3612–3617 (2019).

71. Sakanashi, K., Ouchi, H., Kamiya, K., Kruger, P., Miyamoto, K., Omatsu, T., Ueno, K., Watanabe, K., Taniguchi, T., Bird, J. P. & Aoki, N. Investigation of laser-induced-metal phase of $MoTe_2$ and its contact property via scanning gate microscopy. *Nanotechnology* **31**, 205205 (2020).

72. Wang, Y., Xiao, J., Zhu, H., Li, Y., Alsaid, Y., Fong, K. Y., Zhou, Y., Wang, S., Shi, W., Wang, Y., Zettl, A., Reed, E. J. & Zhang, X. Structural phase transition in monolayer $MoTe_2$ driven by electrostatic doping. *Nature* **550**, 487–491 (2017).

73. Yoo, Y., DeGregorio, Z. P., Su, Y., Koester, S. J. & Johns, J. E. In-Plane 2H-1T′ $MoTe_2$ Homojunctions Synthesized by Flux-Controlled Phase Engineering. *Adv. Mater.* **29**, 1605461 (2017).

74. Ruppert, C., Aslan, O. B. & Heinz, T. F. Optical Properties and Band Gap of Single- and Few-Layer $MoTe_2$ Crystals. *Nano Lett.* **14**, 6231–6236 (2014).

75. Qiu, C., Zhou, H., Yang, H., Chen, M., Guo, Y. & Sun, L. Investigation of *n* -Layer Graphenes as Substrates for Raman Enhancement of Crystal Violet. *J. Phys. Chem. C* **115**, 10019–10025 (2011).

76. Chen, B., Sahin, H., Suslu, A., Ding, L., Bertoni, M. I., Peeters, F. M. & Tongay, S. Environmental Changes in $MoTe_2$ Excitonic Dynamics by Defects-Activated Molecular Interaction. *ACS Nano* **9**, 5326–5332 (2015).

77. Yang, L., Wu, H., Zhang, W., Chen, Z., Li, J., Lou, J., Xie, Z., Zhu, R. & Chang, H. Anomalous oxidation and its effect on electrical transport originating from surface chemical instability in large-area, few-layer 1T′-$MoTe_2$ films. *Nanoscale* **10**, 19906–19915 (2018).

78. Li, Q., Zhou, Q., Shi, L., Chen, Q. & Wang, J. Recent advances in oxidation and degradation mechanisms of ultrathin 2D materials under ambient conditions and their passivation strategies. *J. Mater. Chem. A* **7**, 4291–4312 (2019).

79. Bie, Y.-Q., Grosso, G., Heuck, M., Furchi, M. M., Cao, Y., Zheng, J., Bunandar, D., Navarro-Moratalla, E., Zhou, L., Efetov, D. K., Taniguchi, T., Watanabe, K., Kong, J., Englund, D. & Jarillo-Herrero, P. A $MoTe_2$-based light-emitting diode and photodetector for silicon photonic integrated circuits. *Nat. Nanotechnol.* **12**, 1124 (2017).

2. Experimental Methods

2.1. Substrate Cleaning and Precursor Deposition

All substrates used in this work were cleaned using the following procedure. Substrates were first cleaned by sonication in acetone for 10 minutes, followed by sonication in isopropyl alcohol (IPA) for a further 10 minutes before being dried under a stream of nitrogen gas. Substrates used in this work include: SiO_2/Si (100) (10×10 mm^2, 300 nm), Sapphire (10×10 mm^2) and Si (111) (20×8 mm^2) all purchased from Inseto.

Specified thicknesses of molybdenum (99.95%) were deposited on to the cleaned substrates via electron beam physical vapour deposition (EBPVD) using a Plassys MEB550s. Deposition occurred under a vacuum of 1×10^{-6} mbar at a rate of 0.07 nm s^{-1}, with the electron beam gun emission current at 220 mA. The thicknesses of the Mo films were controlled by a quartz crystal microbalance.

Varied-thickness molybdenum trioxide films were deposited by thermal evaporation of MoO_3 pellets (99.99%, Pi-Kem) in a Plassys MEB400 under a vacuum of 2×10^{-6} mbar at a rate of 0.2 nm s^{-1}. Again, the thicknesses of the MoO_3 films were controlled by a quartz crystal microbalance.

2.2. Synthesis of $FeTe_2$ Precursor

Stoichiometric amounts of elemental iron (Alfa Aesar, 99+%) and tellurium (Alfa Aesar, 99.999%) powders were ground together with a pestle and mortar. The resulting powder was placed into a silica boat which then was placed into the hot zone of a Lenton tube furnace. The furnace was ramped to the dwell temperature of 500 °C at a rate of 10 °C min^{-1} and held for 14 hours before cooling to room temperature at a rate of 10 °C min^{-1}. 5% H_2/Ar was flowed through the furnace at a rate of 300 sccm for the duration of the reaction. The resulting powder was again ground in a pestle and mortar before being analysed by powder x-ray diffraction.

2.3. Chemical Vapour Deposition of $MoTe_2$ Thin Films

2.3.1. Closed CVD Setup

This CVD setup was designed in such a way as to minimise the turbulence inside the reactor (Figure 2-1). Firstly, into a 31.5 cm quartz ampoule (**A,** inside diameter: 12 mm, outside diameter: 15 mm) was placed a 13.5 cm quartz tube (**B,** inside diameter: 9 mm, outside diameter: 11 mm) until it was resting against the end of the larger ampoule. Then the substrate was placed into the quartz ampoule until it rested against the quartz tube. Subsequently 30–33 mg of $FeTe_2$ powder was placed into a 7 cm long quartz ampoule (**C**,

inside diameter: 9 mm, outside diameter: 11 mm), which was inserted into the large quartz ampoule until the open end rested against the substrate. The 31.5 cm ampoule was placed into a 43.5 cm quartz work tube (**D,** inside diameter: 17 mm, outside diameter: 20 mm) which itself resides inside a Lenton tube furnace.

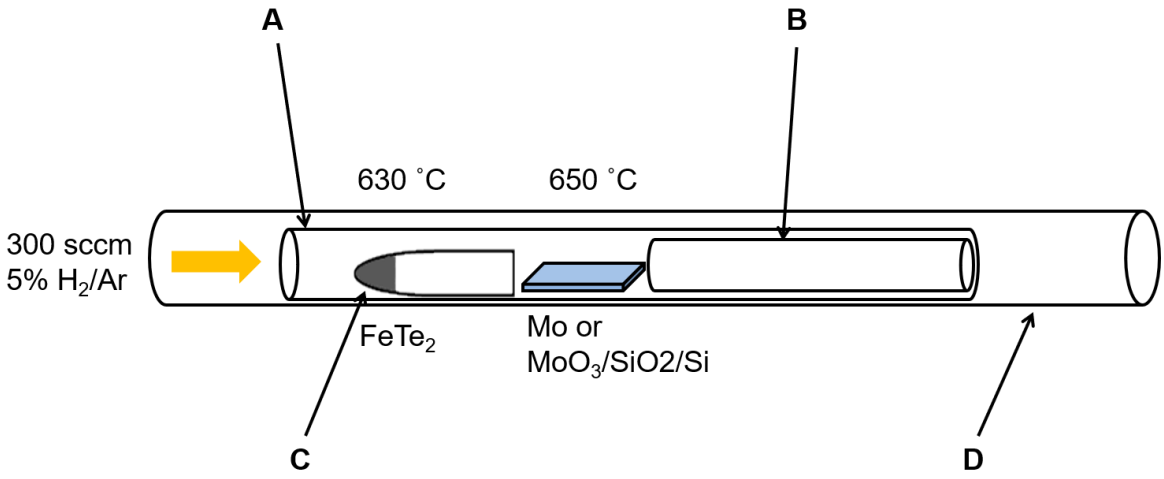

Figure 2-1: Schemetic of the closed CVD reactor.

One end of the work tube was connected to a cylinder of 5% H_2/Ar carrier gas, whilst the other end was connected to a vacuum pump through which the system could be evacuated. Before the CVD process began the system was evacuated to a pressure of 1×10^{-2} mbar, before being refilled with the carrier gas, this procedure was carried out a total of three times to ensure an oxygen free environment for the reaction. The substrate temperature was set to 650 °C and source temperature with $FeTe_2$ precursor at 630 °C. The ramping rate was at 5 °C min^{-1} with a dwell time of 4 hours, before cooling to room temperature at 5 °C min^{-1}. A commercially available and safe carrier gas mixture containing only 5 vol. % of H_2 in Ar was used at a flow rate of 300 sccm.

2.3.2. Flow CVD Setup

Further CVD experiments were conducted in an open "flow" style CVD setup (Figure 2-2). A SiO_2/Si substrate with Mo or MoO_3 deposited onto it was placed into a 14.5 cm quartz tube (inside diameter: 12 mm, outside diameter: 15 mm) a 300 mg pellet of Te or $FeTe_2$ was then placed 5 cm upstream of the substrate. The quartz tube was then loaded into 50.5 cm quartz work tube (inside diameter: 22 mm, outside diameter: 25 mm) of a Lenton tube furnace so that the substrate was positioned in the hot zone of the furnace. The setup was again connected to a vacuum pump as well as a cylinder of 5% H_2/Ar carrier gas. Before the deposition process began the system was evacuated to a pressure of $1x10^{-2}$ mbar before being refilled with carrier gas, this process was repeated for a total of three times to ensure an oxygen free environment. The substrate temperature was set to 650 °C and source

temperature with Te or $FeTe_2$ precursor at 630 °C. The ramping rate was set at 5 °C min^{-1} with a variable dwell time, before cooling to room temperature at 5 °C min^{-1}. Again, the 5% H_2/Ar carrier gas was flowed at a rate of 300 sccm.

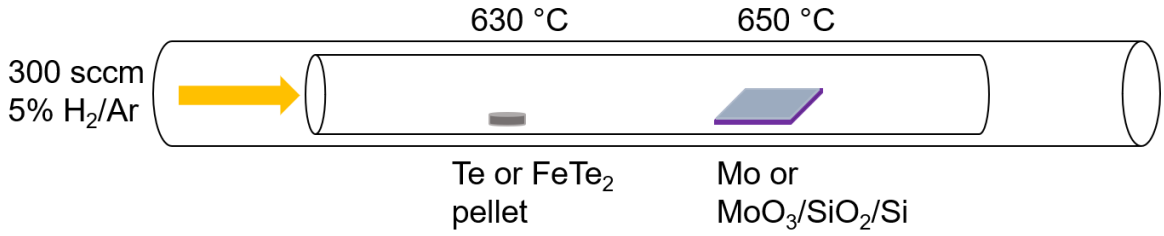

Figure 2-2: Schematic of the flow CVD reactor.

2.4. Solid State Synthesis of Mo_3Sb_7 and $Mo_3Sb_{7-x}Te_x$

Elemental powders of molybdenum (Sigma Aldrich, 99.95%), antimony (Alfa Aesar, 99.999%) and tellurium (Alfa Aesar, 99.999%) were ground together in the correct stoichiometric ratios in a pestle and mortar. The powders were sealed in quartz ampoules under a vacuum pressure of 1×10^{-3} mbar. Mo_3Sb_7 was heated in a Lenton furnace to 700 °C with a heating rate of 5 °C min^{-1} for 100 hours before cooling to room temperature naturally, whilst $Mo_3Sb_{7-x}Te_x$ compounds were heated to 750 °C with a heating rate of 5 °C min^{-1} for 100 hours before cooling to room temperature naturally.

2.5. Raman Spectroscopy

Raman scattering, along with infrared absorption are the processes behind the main spectroscopies used to probe vibrations in molecules. They are extensively used to provide information on chemical structures, identify substances from characteristic spectral peaks and to quantitatively determine the amount of a chosen substance in a sample. Infrared (IR) spectroscopy has been the most widely used of the two due to the issues Raman spectroscopy faced with fluorescence and sample degradation. Recent advances in instrument technology have simplified the required equipment and substantially reduced the problems mentioned previously. This coupled with the ability of Raman spectroscopy to probe aqueous solutions, samples inside of glass containers and samples without any preparation has led to a rapid rise in the application of the technique.

The ways in which light can interact with matter is key to Raman spectroscopy: photons can be absorbed, scattered or can pass straight through a material without interacting at all. In Raman spectroscopy a monochromatic source is used to irradiate the sample and the photons scattered from the molecule are detected. The incident light interacts with the molecule by polarizing the cloud of electrons around the nucleus to form a very unstable, short-lived state

known as a “virtual state”. Due to the instability of virtual states the photon is quickly re-radiated.

The energy changes detected in vibrational spectroscopy are those required to produce nuclear motion. If only electron cloud distortion is involved in the scattering process, the photons will be scattered with very small changes in frequency. This process is regarded as elastic and is known as Rayleigh scattering. If nuclear motion is induced during scattering, then energy will be transferred from the incident photon to the molecule or from the molecule to the scattered photon. These cases involve inelastic scattering and as such the energy of the scattered photon is different from that of the incident photon. This is Raman scattering. It is a fairly weak process with only one in every scattered 10^6-10^8 photons being Raman scattered. The scattering processes are illustrated in Figure 2-3.

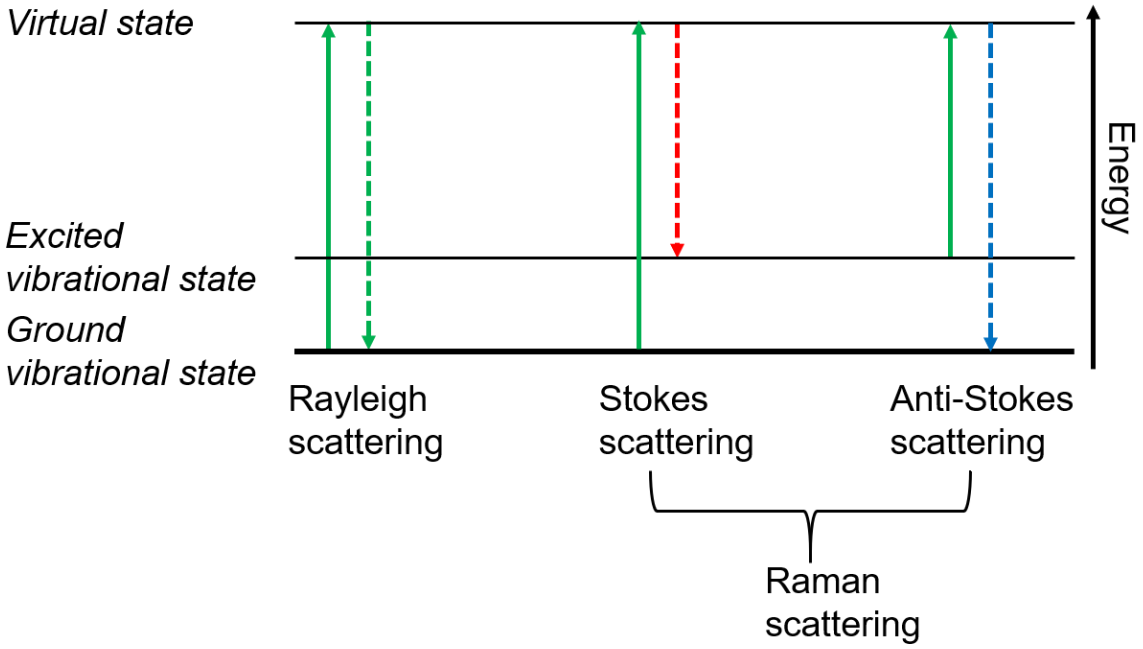

Figure 2-3: Diagram depicting Rayleigh, Stokes and anti-Stokes scattering processes. Adapted from [1].

At room temperature the vast majority of molecules exist in the ground vibrational state. For Rayleigh scattering the molecule returns to this ground vibrational state from the virtual state and is the most intense process as most photons scatter this way. There are two types of Raman scattering that can occur. Firstly, Stokes scattering involves a molecule from the ground vibrational state absorbing energy and subsequently being promoted to a higher energy excited state. Secondly, due to thermal energy some molecules may exist in an excited vibrational state. Scattering from this state to the ground state is known as anti-Stokes scattering and involves transfer of energy to the scattered photon. As most molecules prior

to interaction with the laser at room temperature will exist in the ground vibrational state, Stokes Raman scattering is by far the more common of the two.[1,2]

Raman spectra of $MoTe_2$ films were collected in a backscattering configuration on a Horiba JY HR800 spectrometer with a 532 nm laser excitation wavelength (laser power at sample, 10 mW) and a 600 g/mm grating. The spectra were acquired using a 50×objective with a 10 second accumulation time and were repeated 10 times.

Raman mapping was performed using a WITec alpha 300R spectrometer using 532 nm laser excitation. Spectra were collected using a 50× objective with a 1 second integration time and 1 μm spatial resolution. Background subtraction of the spectra was carried out on WITec Project 4.1 software and maps were generated based on the intensity of the peaks. Raman mapping was carried out by Dr. Stacey Laing at the University of Strathclyde.

2.6. Surface Enhanced Raman Spectroscopy

Surface enhanced Raman spectroscopy (SERS) is a technique in which the Raman signal of a specific molecule is enhanced by bringing it into contact with surface with a well-defined morphology, particularly noble metals like gold and silver.[1] This effect was observed by Fleischman *et al* in 1974, where they reported that pyridine adsorbed from solution onto a roughened silver electrode resulted in particularly strong Raman scattering.[3] Since SERS was experimentally discovered lots of theories were proposed in the infancy of the technique. Now however, there are two main theories of surface enhancement that are currently accepted which are known as the electromagnetic and chemical enhancement methods.[4]

The electromagnetic enhancement mechanism relies upon the analyte being adsorbed or in close proximity to a metal nanoparticle surface. The local electric field around the nanoparticle is enhanced through resonant excitation of plasmons in the nanostructure by the incident Raman laser light. This leads to an interaction between the surface plasmons and the adsorbed analyte increasing the polarisation of the analyte, enhancing its Raman signal. Typically, gold or silver nanoparticles are used as SERS substrates as their plasmon resonance frequency lies in the visible and near infrared region where several wavelengths of lasers commonly used for Raman spectroscopy are found.[1,2,4,5]

The chemical enhancement mechanism relies upon the formation of a bond between the analyte molecule and metal substrate surface. Charge transfer between the metal substrate and analyte molecule can lead to an increased polarisability of the molecule and thus, increase its Raman cross section. The chemical enhancement mechanism does not provide

as great an enhancement factor as the electromagnetic enhancement mechanism but it does have benefits such as simpler synthesis methods of the substrates that can be used.[1,2,4,6]

Analyte solutions of rhodamine 6G (R6G) were prepared by dissolution of R6G in ethanol to a concentration of 10 mM before subsequent dilution in water to the desired concentration.

Raman spectra of R6G on $MoTe_2$ films for the preliminary study were collected in a backscattering configuration on a Horiba JY HR800 spectrometer with a 532 nm laser excitation wavelength (laser power at sample, 10 mW) and a 600 g/mm grating. The spectra were acquired using a 50×objective with a 10 second accumulation time and were repeated 10 times.

Analyte solutions of β-sitosterol were prepared by dissolution of the respective solid to varying concentrations (10^{-4}, 10^{-5}, 10^{-6}, 10^{-7}, 10^{-8}, 10^{-9} M) in water/methanol (1:2) and spin-coated onto the 1T'-$MoTe_2$ film (300 rpm, 10 min).

Raman spectra of β-sitosterol on 1T'-$MoTe_2$ were collected on a ProRaman-L (laser power at sample, 70 mW, excitation wavelength, 785 nm) Raman spectrometer. The spectra were measured 100 times, each of them with 1 second accumulation time. Raman spectra were used for chemical mapping with a surface area of 1.4×0.8 mm^2, having 70×12 points spaced by a gap of 0.05 mm. The same Raman spectrometer fitted with a source shining at 785 nm and 70 mW power was used for the mapping. The spectra were recorded at a resolution of 2 cm^{-1} in the 2000−500 cm^{-1} wavenumber range with an exposure time of 100 seconds for 1 exposure. SERS measurements were performed by Dr. Olga Guselnikova at the University of Chemistry and Technology Prague.

2.7. Atomic Force Microscopy

Atomic force microscopy (AFM) is a type of scanning probe microscopy and has a demonstrated resolution of the order of fractions of a nanometre, more than 1000 times greater than the optical diffraction limit. AFM was used in this work to study the topography and measure the thickness of the $MoTe_2$ films. A typical atomic force microscope consists of a small, spring-like cantilever attached to a support and fixed at the free end of the cantilever is a sharp tip. A detector then monitors the deflection of the cantilever, this is achieved by reflecting a laser beam off the flat top of the cantilever. Any deflection of the cantilever will cause slight changes in direction of the reflected beam. These changes are monitored by a position-sensitive photodiode (Figure 2-4)

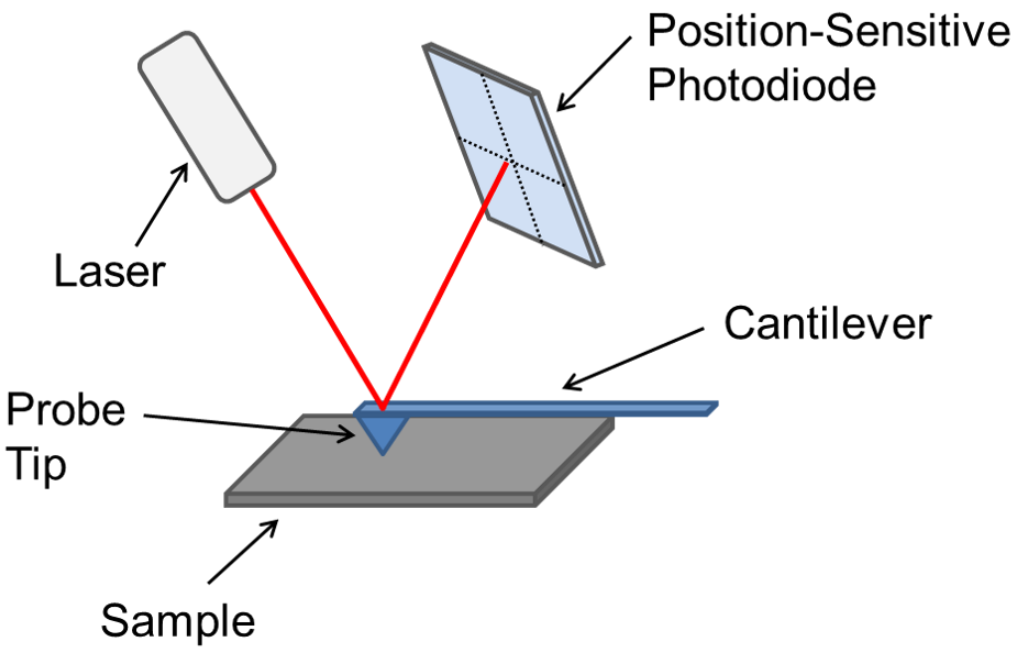

Figure 2-4 Schematic of a simple AFM setup. Adapted from [7]

AFM images the topography of a sample surface by scanning the cantilever over an area of interest. The deflection of the cantilever is influenced by the topography of the sample and is monitored by the position-sensitive photodiode. A feedback loop is used to control the height of the tip above the surface and maintain a constant laser position, accurate topographical maps of the surface features can be generated.[7,8]

AFM measurements in this work were carried out on a Bruker Dimension Icon AFM using ScanAsyst mode. Surface roughness measurements were obtained from a scan area of 5×5 μm^2. $MoTe_2$ Film thicknesses were measured relative to bare SiO_2/Si substrate over an area of 3×3 μm^2. To create the step between the $MoTe_2$ film and SiO_2/Si substrate, the following procedure was utilised and is depicted in Figure 2-5.

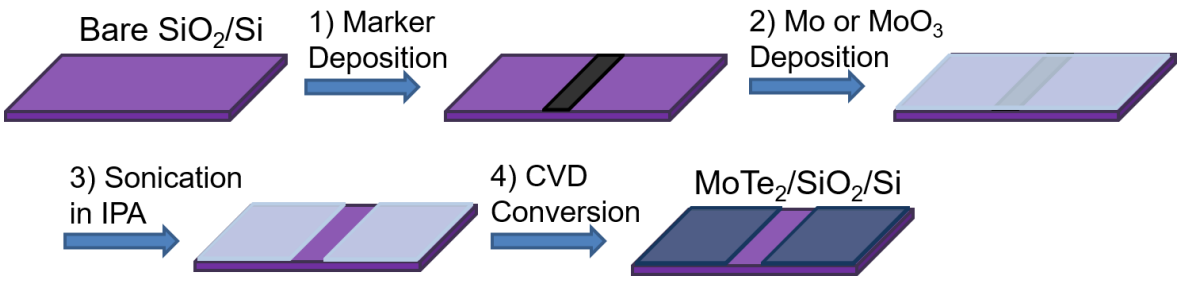

Figure 2-5: Method used for creation of a step between $MoTe_2$ film and SiO_2/Si substrate for AFM thickness measurements.

(1) A marker pen was used to draw a ~3 mm thick line across a cleaned SiO_2/Si substrate. (2) Mo or MoO_3 was deposited onto the substrate using the same procedure as described in Section 2.1. (3) The substrate with Mo or MoO_3 deposited was then sonicated in isopropyl

alcohol for 30 seconds, removing the marker pen and taking a strip of Mo or MoO_3 with it, leaving bare SiO_2/Si. (4) The substrate was then subjected to the CVD process described in Section 2.3.1. resulting in the formation of $MoTe_2$ with a strip of bare SiO_2/Si that could be measured by AFM giving the thickness of the $MoTe_2$ film.

2.8. X-ray Photoelectron Spectroscopy

X-ray photoelectron spectroscopy (XPS) is an invaluable tool in the field of material science for probing the elemental composition and the electronic states of these elements in a sample of interest. It is an extremely popular technique due to its ability to identify and quantify the elemental composition of the outer 10 nm or less of a solid surface, with all elements from lithium through to uranium detectable. Both hydrogen and helium are unable to be detected due to their low photoelectron cross sections and the fact that XPS is optimised to analyse core electrons. Furthermore, it provides information about the chemical environment that the respective elements exist in. This information can be obtained with relative ease and limited sample preparation.

The physical basis behind XPS revolves around photoelectron production, this is when an electron bound to an atom or ion is ejected by an incident photon. As photons are massless, chargeless packages of energy they are destroyed during photon-electron interactions with a complete transfer of energy. If there is sufficient energy the electron will be ejected from the atom/ion. XPS measures the kinetic energy that remains on these emitted electrons (Figure 2-6).

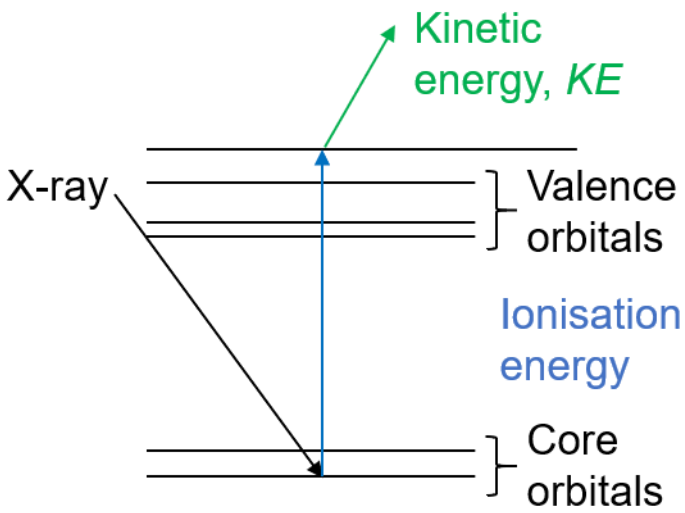

Figure 2-6: Diagram of an X-ray ejecting a core electron from its orbital with kinetic energy KE. Adapted from [9].

This is useful as the kinetic energy can be related to the binding energy of the electrons, which is element and environment specific. They are related by the following equation:

$$KE = E_{ph} - \phi_{XPS} - BE$$

Where KE is the kinetic energy of the electrons detected, E_{ph} is the energy of the incoming photons, ϕ_{XPS} is the work function of the instrument and BE is the binding energy.

The surface sensitivity of XPS arises from the limited inelastic mean free path of electrons within a solid before some of their energy is lost. If energy is lost, then the signal becomes hidden in the spectral background. Almost all photoelectrons produced from atoms or ions situated ~10 nm or more below the surface will lose a fraction of their energy, meaning the discrete signals that remain are from the surface region only. Ultra-high vacuum conditions (UHV, $<10^{-9}$ mbar) must be used for XPS analysis as this controls the density of molecules in the gas phase. Limiting the number of molecules present in the gas phase between the sample and detector with UHV maximises the chance of electrons emitted from the sample making it to the detector.[9–11]

XPS spectra of 2H-$MoTe_2$ were collected on a system consisting of a Scienta MX650 X-ray source (Al Kα,1486.6 eV) coupled with a Scienta RS4000 hemispherical analyser. A pass energy of 200 eV was used for the measurements. The XPS set-up was kept at a pressure of $1x10^{-10}$ mbar and samples were attached to a copper holder and annealed at 100 ˚C for an hour before XPS spectra were recorded to remove surface contaminants. These measurements were performed by Dr. Juan Carlos Moreno-López at the University of Vienna.

XPS spectra of 1T'-$MoTe_2$ were collected using an Omicron Nanotechnology ESCAProbeP spectrometer fitted with a monochromated Al Kα X-ray source working at 1486.6 eV. The samples were clipped on a sample holder and outgassed in the fast entry lock several hours before transfer to the analysis chamber. The survey and narrow regions were recorded using a pass energy of 200 and 50 eV, respectively. Dwell time was set to 100 ms and step sizes of 1 and 0.1 eV for the survey and the narrow regions were used. These measurements were performed by Dr. Petr Sajdl at the University of Chemistry and Technology Prague.

2.9. Transmission Electron Microscopy coupled with Energy Dispersive X-ray Spectroscopy

Transmission electron microscopy operates in a slightly different manner to SEM, in that the electron beam passes through the thin sample and is imaged on a phosphorescent screen. This makes sample preparation for TEM more difficult than is required for SEM.[9]

To remove $MoTe_2$ films from SiO_2/Si substrates, they were submersed in 10% hydrofluoric acid solution for ~30 seconds before being placed into a beaker filled with deionised water where the $MoTe_2$ films separated from the substrate and floated to the surface. The films were then scooped up with Carbon on 200 mesh Au grids.

Transmission electron microscopy was conducted on a JEOL CFEG ARM instrument operated at 200 kV, using samples supported by holey carbon films and Au grids. Selected area electron diffraction patterns were typically collected from a 20 or 50 micrometre diameter area. Beam damage was evident for the 1T' samples but not for the 2H sample after prolonged exposure to the electron beam.

Energy dispersive X-ray spectroscopy (EDX) data was collected in (probe-corrected) scanning transmission electron microscopy mode, employing a Bruker X-Flash detector.

TEM and EDX measurements were performed by Dr. Donald A. MacLaren at the University of Glasgow.

2.10. Scanning Electron Microscopy coupled with Energy Dispersive X-ray Spectroscopy

Scanning electron microscopy (SEM) coupled with energy dispersive X-ray spectroscopy (EDX) is a powerful tool for observing the morphology of a sample as well as determining its elemental composition and stoichiometry. In SEM an electron beam is scanned over the sample and the scattered beam is collected by the detector resulting in an image. The electron beam causes the production of X-rays from the sample, which have characteristic energies of the elements present in the material meaning EDX can determine the elemental composition of the sample.[9,12]

Scanning Electron Microscopy (SEM) of Mo_3Sb_7 and $Mo_3Sb_{7-x}Te_x$ was performed on a Phillips XL30 ESEM instrument coupled with an Oxford Instruments X-act spectrometer for EDX measurements. The EDX was calibrated using INCA software with Cu as the calibration standard.

2.11. Powder X-Ray Diffraction and Rietveld Refinement

Diffraction techniques, including those using X-rays, are some of the most important tools available for the determination of inorganic structures.

Diffraction is the interference between waves that occurs due to an object in their path. Electrons in atoms scatter X-rays elastically and diffraction can occur for a periodic structure of atoms as they are separated by distances similar to the wavelength of the X-rays (~100 pm). If we imagine scattering as being reflection from two parallel planes of atoms separated by a distance, *d*, then constructive interference between waves of wavelength, λ, will occur at an angle given by Bragg's equation:

$$2d\ sin\theta = n\lambda$$

Where *n* is an integer. Therefore, an X-ray interacting with a crystalline material with an ordered set of atoms will produce a diffraction pattern with each reflection occurring at an angle, θ, corresponding to a different separation of planes of atoms, *d*, in the sample (Figure 2-7).

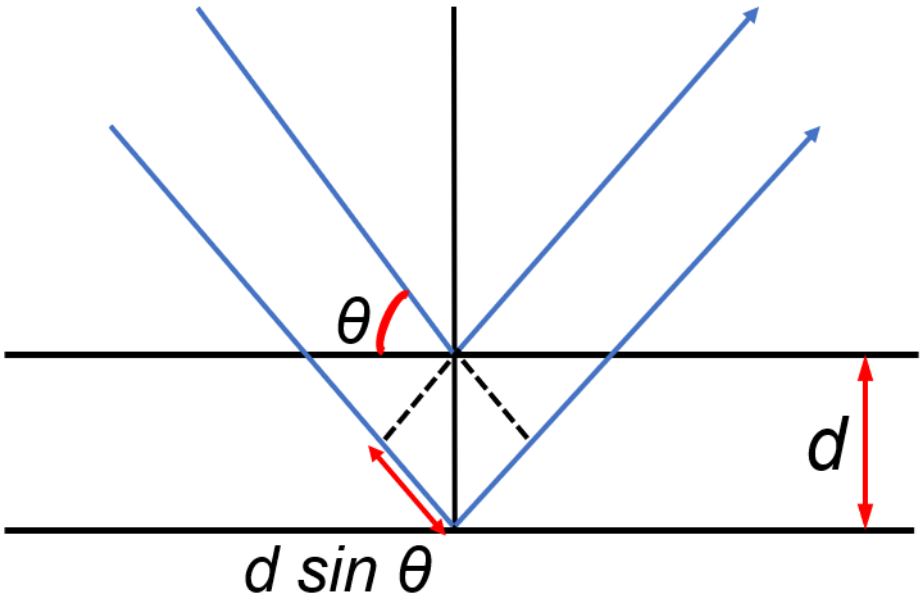

Figure 2-7: An illustration of Bragg's law, constructive interference between X-rays will occur when the additional path length 2d sin θ is equal to an integral multiple of the wavelength λ. Adapted from [9].

Atoms scatter X-rays proportionally to the number of electrons they contain, meaning that a diffraction pattern is characteristic of the types of atoms and their positions in a material. Whilst the diffractions angles and intensities provide structural information.[13]

Powder X-Ray Diffraction (PXRD) was performed on a PANalytical X'pert Pro diffractometer with Cu K_α (λ = 1.54178 Å) operating in Bragg-Brentano geometry.

Rietveld refinement was used for the analysis of Mo_3Sb_7 and $Mo_3Sb_{7-x}Te_x$ compounds. The method was first published by Hugo Rietveld in 1969.[14] It relies upon fitting a calculated model (containing structural and instrument parameters) to the experimentally obtained diffraction data using the non-linear least squares method to refine the theoretical line profile until it matches the experimentally obtained one. Rietveld refinement requires a crystal structure model and is unable to produce such a model on its own. Although, it is able to find structural details missing from a partial structure solution including parameters such as unit cell dimensions, phase fractions, atomic coordinates, bond lengths, micro strain in the lattice and vacancies. The successful outcome of a refinement in highly dependent upon the quality of both the diffraction data and the model used.[13]

Rietveld refinements were performed using the GSAS-II software package.[15] Crystallographic information files (.cif) used for Rietveld refinements were obtained from the Inorganic Crystal Structure Database.

2.12. Optical Microscopy

An Olympus BX41 microscope integrated into the Horiba-JY HR800 spectrometer was used for optical imaging. All images were captured using a 50× objective. The intensity of the light source (Euromex fiber optic light source EK-1, equipped with 12 V, 100W halogen lamp) was adjusted to level 8 when capturing images for contrast measurements and to level 8.5 when capturing images for the colour palette. The white balance was adjusted to R: B = 0.91: 1.21 via the source settings section in LabSpec5 software when capturing contrast images. White balance was adjusted to imitate different colour temperature white light sources when capturing images for the colour palette. The optical contrast difference was measured using ImageJ software. Colour optical images were split into RGB channels using "Split Channels" function. Contrast profiles were obtained by selecting an area of the images and then pressing "K".

2.13. Fourier Transform Infrared (FTIR) Spectroscopy

FTIR spectra were recorded using a Nicolet 6700 spectrometer (Thermo Scientific, France) with a Smart ATR accessory device (2000 scans and 4 cm^{-1} resolution). FTIR measurements were performed by Dr. Olga Guselnikova at the University of Chemistry and Technology Prague.

2.14. UV-Vis Spectroscopy

UV−Vis spectra were measured using a Spectrometer Lambda 25 (PerkinElmer) in 200−1100 nm wavelength range and were obtained by Dr. Olga Guselnikova at the University of Chemistry and Technology Prague.

2.15. Density Functional Theory (DFT) Calculations

The optimization geometry of the ground electronic state of β-sitosterol was performed using FIREFLY[16] software at the density functional level of theory[17] (DFT) with B3LYP functional[18] 6-31G** basis set.[19] 52 Also, the energies of highest occupied molecular orbital (HOMO) and lowest unoccupied molecular orbital (LUMO) were calculated at the same level of theory. The schematic description of HOMO and LUMO was performed using Chemcraft software.[20] DFT calculations were performed by Dr. Rashid Valiev at the University of Helsinki.

2.16. Water Contact Angle Measurements

Water contact angles (WCA) were measured by a DropShape Analyzer−DSA100 (Kruss, Germany) at 10 positions (drop volume, 2 μL) at room temperature. The measurements were processed using the software package ADVANCE (Kruss, Germany). WCA measurements were performed by Dr. Olga Guselnikova at the University of Chemistry and Technology Prague.

2.17. Electrochemical Measurements

2.17.1. Electrode Preparation

Electrochemical measurements of $MoTe_2$ thin films were performed using a silicon substrate. The deposition of precursor and CVD conversion used the process described in Section 2.1, except a 20×8 mm silicon substrate was used instead. Clear nail polish was used to mark off an area of each film to ensure the active geometric surface areas of the films were 0.56 cm^2 to ensure consistency between the 1T'- and 2H-phases.

Electrochemical measurements of Mo_3Sb_7 and $Mo_3Sb_{7-x}Te_x$ compounds were performed using a glassy carbon working electrode (IJ Cambria) with a surface area of 0.071 cm^2. The electrode was cleaned prior to use with diamond polish and alumina pad (IJ Cambria), before being cycled electrochemically in 1 M H_2SO_4 between +1 V and -1.2 V vs. the normal hydrogen electrode (NHE).

For the electrochemical characterisation of Mo_3Sb_7 and the $Mo_3Sb_{7-x}Te_x$ compounds, they were prepared as catalyst inks and deposited onto the glassy carbon working electrode. This

involved sonicating 10 mg of catalyst powder in 0.8 ml dimethylformamide with 80 µL of Nafion, which acts as a conductive binder to the substrate. 30 µL of the catalyst ink was then drop-cast onto a glassy carbon electrode and allowed to dry for several hours.

2.17.2. Electrochemical Setup

Electrochemical measurements were performed on a Biologic SP-150 potentiostat utilising a single cell, three-electrode setup in 1 M H_2SO_4, shown below in Figure 2-8. It consisted of a three-necked flask filled with 1 M H_2SO_4 as the electrolyte, carbon felt (Alfa Aesar) as the counter electrode and Ag/AgCl in 3 M NaCl as the reference electrode (IJ Cambria). For Mo_3Sb_7 and the $Mo_3Sb_{7-x}Te_x$ compounds a glassy carbon electrode with the deposited catalyst was used as the working electrode. In the case of 2H- and 1T'-$MoTe_2$ the silicon substrate with respective $MoTe_2$ thin film was used as the working electrode.

Figure 2-8: The single cell, three-electrode setup used for electrochemical measurements. The glassy carbon working electrode, carbon felt counter electrode and Ag/AgCl in 3 M NaCl reference electrode are immersed in 1 M H_2SO_4.

Electrode potentials were converted to the NHE scale using the following equation:

$$E(NHE) = E(Ag/AgCl) + 0.209\,V$$

2.17.3. Voltammetry

Cyclic voltammetry (CV) is a technique used to determine the current produced at a working electrode over a fixed potential range. The voltage is swept in both oxidative and reductive directions between two fixed potential values. As the potential is swept to increasingly negative potentials a current will flow as a species undergoes reduction. Once the fixed potential value is reached, the potential is then swept in the positive direction. Again, current will flow when a species undergoes oxidation. Linear sweep voltammetry (LSV) also involves the sweeping of potentials in a fixed, but only in one direction. Lower scan rates can be used with LSV, allowing for more accurate readings of the currents achieved at a specific potential.[21]

Usually, a three-electrode setup is used for both CV and LSV measurements. The setup consists of working, counter and reference electrodes which are immersed in an electrolyte. The oxidation and reduction reactions occur at the working electrode, with the counter electrode balancing the charge that is produced. The reference electrode controls the balancing of charge and has a known reduction potential.[21]

Linear sweep voltammetry was used to test the performance of the 2H- and 1T'-$MoTe_2$ films as hydrogen evolution catalysts, using the setup described above in Section 2.17.2. A scan rate of 2 mV s^{-1} was used for the measurements and internal resistance was compensated for using the iR function of the potentiostat.

Cyclic voltammetry was used to test the performance of the Mo_3Sb_7 and $Mo_3Sb_{7-x}Te_x$ powders as hydrogen evolution catalysts. The setup used was described above in Section 2.17.2. A scan rate of 100 mV s^{-1} was used for the measurements and internal resistance was compensated for using the iR function of the potentiostat.

Cyclic voltammetry measurements of β-sitosterol on 1T'-$MoTe_2$ were performed with a Palm Sens 4 potentiostat by PSTrace 5.3 software, within a potential range of 0−2000 mV and a linear potential sweep rate of 100 mV/s using Pt as a counter electrode and Ag/AgCl (3 M KCl) as a reference electrode. Before the measurements, the Pt electrode was polished with 0.05−0.01 μm Al_2O_3 powder on a wet pad and washed in water. The measurement used 5 mL of the supporting electrolyte consisting of 1 M sitosterol/0.1 M NaClO4 solution in ethanol. Light-emitting diode irradiation was done for 10 min continuously with 780 nm, 7 μW/mm^2, and 530 nm, 9 μW/mm^2 sources by Thorlabs. These measurements were performed by Elena Miliutina at the University of Chemistry and Technology Prague.

2.18. References

1. Smith, E. & Dent, G. *Modern Raman spectroscopy : a practical approach*. (J. Wiley, 2005).

2. Vandenabeele, P. *Practical Raman Spectroscopy - An Introduction*. (John Wiley & Sons, Ltd, 2013). doi:10.1002/9781119961284.

3. Fleischmann, M., Hendra, P. J. & McQuillan, A. J. Raman spectra of pyridine adsorbed at a silver electrode. *Chem. Phys. Lett.* **26**, 163–166 (1974).

4. Schlücker, S. Surface-Enhanced Raman Spectroscopy: Concepts and Chemical Applications. *Angew. Chemie Int. Ed.* **53**, 4756–4795 (2014).

5. Ding, S. Y., Yi, J., Li, J.-F., Ren, B., Wu, D.-Y., Panneerselvam, R. & Tian, Z.-Q. Nanostructure-based plasmon-enhanced Raman spectroscopy for surface analysis of materials. *Nature Reviews Materials* **1**, 16021 (2016).

6. Tao, L., Chen, K., Chen, Z., Cong, C., Qiu, C., Chen, J., Wang, X., Chen, H., Yu, T., Xie, W., Deng, S. & Xu, J.-B. 1T′ Transition Metal Telluride Atomic Layers for Plasmon-Free SERS at Femtomolar Levels. *J. Am. Chem. Soc.* **140**, 8696–8704 (2018).

7. Eaton, P. & West, P. *Atomic Force Microscopy*. (Oxford University Press, 2010).

8. Binnig, G., Quate, C. F. & Gerber, C. Atomic Force Microscope. *Phys. Rev. Lett.* **56**, 930–933 (1986).

9. Atkins, P., Overton, T., Rourke, J., Weller, M. & Armstrong, F. *Shriver & Atkins' Inorganic Chemistry*. (Oxford Universtiy Press, 2010).

10. Van der Heide, P. *X-ray photoelectron spectroscopy : an introduction to principles and practices*. (Wiley-Blackwell, 2012).

11. Guo, J. *X-Rays in nanoscience : spectroscopy, spectromicroscopy, and scattering techniques*. (Wiley-VCH, 2010).

12. Goldstein, J. I., Newbury, D. E., Joy, D. C., Lyman, C. E., Echlin, P., Lifshin, E., Sawyer, L. & Michael, J. R. *Scanning Electron Microscopy and X-ray Microanalysis*. (Springer US, 2003).

13. Pecharsky, V. K. & Zavalij, P. Y. *Fundamentals of powder diffraction and structural characterization of materials*. *Fundamentals of Powder Diffraction and*

Structural Characterization of Materials (Springer US, 2005).

14. Rietveld, H. M. A profile refinement method for nuclear and magnetic structures. *J. Appl. Crystallogr.* **2**, 65–71 (1969).

15. Toby, B. H. & Von Dreele, R. B. GSAS-II: The genesis of a modern open-source all purpose crystallography software package. *J. Appl. Crystallogr.* **46**, 544–549 (2013).

16. Granovsky, A. A. Firefly.

17. Casida, M. E. & Chong, D. P. Recent Advances in Density Functional Methods. *Recent Advances in Density Functional Methods, Part 1* vol. 1 155 (1995).

18. Lee, C., Yang, W. & Parr, R. G. Development of the Colle-Salvetti correlation-energy formula into a functional of the electron density. *Phys. Rev. B* **37**, 785–789 (1988).

19. Rassolov, V. A., Ratner, M. A., Pople, J. A., Redfern, P. C. & Curtiss, L. A. 6-31G* basis set for third-row atoms. *J. Comput. Chem.* **22**, 976–984 (2001).

20. https://www.chemcraftprog.com.

21. Browne, W. R. *Electrochemistry*. (Oxford Universtiy Press, 2018).

3. Chemical Vapour Deposition of 2H- and 1T'-$MoTe_2$ Thin Films

3.1. Introduction

A key step towards the practical application of $MoTe_2$ in the fields mentioned in the introductory chapter is the production of high-quality, large area, atomically thin $MoTe_2$ films. Early research on $MoTe_2$ tended to rely on flakes obtained from top-down exfoliation methods. Although high quality, exfoliation produces small flakes that have arbitrary shapes and would be randomly distributed on a surface, making production for large scale applications difficult.[1,2] Therefore, if $MoTe_2$ is to be implemented into any future technologies other methods of production must be explored.

3.1.1. CVD Synthesis of $MoTe_2$

One of the most promising methods suited to large scale production is chemical vapour deposition. The apparatus required is relatively inexpensive and can be readily scaled to industry levels. It has also already been proven to be capable of producing high-quality atomically-thin TMDC films.[3–5] Whilst the other molybdenum based TMDCs, MoS_2 and $MoSe_2$, only tend to exhibit the hexagonal structure when grown by CVD, this is not the case for $MoTe_2$. The two polymorphs of $MoTe_2$ are in direct competition with each other at typical deposition temperatures (~650 °C) used in CVD due to the small energy difference per formula unit between the two (~35 meV), as depicted in Figure 3-1.[6]

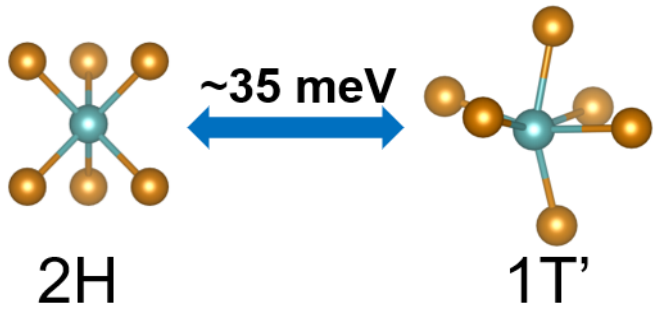

Figure 3-1: Depiction of the energy difference between the $MoTe_2$ polymorphs per formula unit.

This polymorphism presents both a challenge and an exciting opportunity in the utilisation of $MoTe_2$. For example, to produce phase pure thin films of 1T'- or 2H-$MoTe_2$ several of the CVD parameters can be exploited. Table 3-1 highlights the parameters used in several literature reports of the chemical vapour deposition of 2H-$MoTe_2$, whilst Table 3-2 shows the conditions utilised for the chemical vapour deposition of 1T'-$MoTe_2$.

Table 3-1: Conditions used for the CVD of 2H-$MoTe_2$ broken down into the controllable variables.

Mo Source	Te Source (Amount, g)	Substrate	Substrate Temp, °C	Source Temp, °C	Time, min	Heating/Cooling Rate, °C min^{-1}	Gas, flow rate , sccm	Ref.
Mo film (50 nm)	Te (2g)	SiO_2/Si	650	650	180	30/5	H_2/Ar 100/500	[6]
MoO_3 film (1nm)	Te/Molecular sieves (-)	SiO_2/Si	700	700	60	45/140	H_2/Ar 4/3	[7]
MoS_2 film (0.7 nm)	Na_2Te (1g)	SiO_2/Si	525-675	600	30	17.5-22.5/-	H_2/Ar 25/500	[8]
MoO_3 film (1 nm)	Te/Molecular sieves (0.18g)	SiO_2/Si	700	700	60	45/-	H_2/Ar 4/3	[9]
MoO_3 film (-)	Te (0.1g)	SiO_2/Si	650	650	30	-/natural cooling to 500 °C then open furnace.	H_2/Ar 4/3	[10]
Mo film (1-3 nm)	Te (0.8g)	SiO_2/Si	635	635	60	40.6/open furnace after growth period	H_2/Ar 5/5	[11]
MoO_3:$MoCl_5$ powders	Te (0.5g)	SiO_2/Si	780	-	5-15	52/natural cooling	H_2/Ar 15/200	[12]
MoO_3 powder	Te (-)	SiO_2/Si	650	450	15	32.5/natural cooling	H_2/Ar 24/24	[13]
MoO_2 film (30 nm)	Te (-)	SiO_2/Si	700	600	60	17.5/-	H_2/Ar -	[14]
MoO_3 powder	Te (0.06g)	SiO_2/Si	700	-	60	70/natural cooling to 600 °C then open furnace	H_2/Ar 4/3	[15]
MoO_3 film (Thick)	Te (-)	SiO_2/Si	650	650	30	-/natural cooling to 500 °C then open furnace	H_2/Ar 4/3	[16]
Mo film (1-3 nm)	Te (0.8g)	SiO_2/Si	635	635	60	40.6/ open furnace after growth period	H_2/Ar 5/5	[17]
Mo film (3 nm)	Te (-)	SiO_2/Si	700	-	120	50/ natural cooling to 500 °C then open furnace	H_2/Ar 7.5/42.5	[18]

Table 3-2: Conditions used for the CVD of 1T'-$MoTe_2$ broken down into the controllable variables.

Mo Source	Te Source (Amount, g)	Substrate	Substrate Temp, °C	Source Temp, °C	Time, min	Heating/Cooling Rate, °C min^{-1}	Gas, flow rate , sccm	Ref.
Mo film (50 nm)	Te (2g)	SiO_2/Si	650	650	20	30/5	H_2/Ar 100/500	[6]
Mo film (1nm)	Te/Molecular sieves (-)	SiO_2/Si	700	700	60	45/140	H_2/Ar 4/3	[7]
Mo film (1nm)	Te/Molecular sieves (0.18g)	SiO_2/Si	700	700	60	45/-	H_2/Ar 4/3	[9]
MoO_3 film (-)	Te (0.1g)	SiO_2/Si	650	650	30	-/open furnace after growth period	H_2/Ar 4/3	[10]
Mo film (1-3nm)	Te (0.8g)	SiO_2/Si	635	535	60	40.6/ open furnace after growth period	H_2/Ar 5/5	[11]
MoO_3:$MoCl_5$ powders	Te (0.5g)	SiO_2/Si	780	-	5-15	52/ natural cooling	H_2/Ar 15/200	[12]
MoO_3 powder	Te (-)	SiO_2/Si	680	450	15	32.5/ natural cooling to 350 °C, then open furnace	H_2/Ar 24/24	[13]
MoO_2 film (30 nm)	Te (-)	SiO_2/Si	800	600	60	20/-	H_2/Ar -	[14]
MoO_3 powder	Te (0.06g)	SiO_2/Si	700	-	5	70/ natural cooling to 600 °C then open furnace	H_2/Ar 4/3	[15]
MoO_3 film (Thin)	Te (-)	SiO_2/Si	650	650	30	-/natural cooling to 500 °C then open furnace	H_2/Ar 4/3	[16]
Mo film (1-3 nm)	Te (0.8 g)	SiO_2/Si	635	535	60	40.6/ open furnace after growth period	H_2/Ar 5/5	[17]
Mo film (3 nm)	Te (-)	SiO_2/Si	800	-	120	50/ natural cooling to 500 °C then open furnace	H_2/Ar 7.5/42.5	[18]

The most commonly utilised molybdenum precursors for the CVD of $MoTe_2$ are Mo and MoO_3 thin films pre-deposited onto target substrates which are then converted to $MoTe_2$ through direct tellurisation. These precursor films can be deposited *via* several methods such as, thermal evaporation, electron beam evaporation, atomic layer deposition or sputter deposition. The ability to grow large films that are only limited by the size of the substrate and the simplicity are the major benefits of this method. The thickness of the product $MoTe_2$ film is directly related to the thickness of the precursor film and as such can be controlled quite accurately depending on the quality of the deposition method used.[3] The choice between Mo or MoO_3 films can dictate the phase of the product $MoTe_2$ film, with Zhou *et al* finding that in their setup MoO_3 would preferentially convert into 2H-$MoTe_2$ whilst Mo would form 1T'-$MoTe_2$. They theorise that this is due to the large increase in volume when converting each Mo unit (15.6 $Å^3$) into $MoTe_2$ (74.9 $Å^3$) inducing strain and 1T'-$MoTe_2$ has been shown to be stabilised by the application of strain. Whereas the volume increase from MoO_3 (50.8 $Å^3$) to $MoTe_2$ (74.9 $Å^3$) is much lower and therefore forms 2H-$MoTe_2$, which is more stable in the absence of strain.[7] It should be noted that other parameters can be manipulated to achieve phase pure 1T'- and 2H-$MoTe_2$ films from both Mo and MoO_3 precursor films.

The overwhelming majority of the procedures highlighted in Tables 3-1 and 3-2 utilise elemental tellurium as the tellurium source for their CVD reactions. However, the relatively low sublimation temperature of tellurium (~450 °C) compared to the temperatures required for the deposition of $MoTe_2$ (~650 °C) mean that the tellurium evaporates rapidly and as such large amounts are required to sustain tellurium flux throughout the deposition. The amounts of Te used ranges from ~0.1-2 g for a single deposition of typically a 1 cm^2 $MoTe_2$ film and with the low natural abundance of tellurium, which is similar to that of platinum, it is important to utilise it responsibly.[19] Moreover, the toxicity of tellurium is of concern so if $MoTe_2$ finds widespread use in any of its potential applications then minimising the amount used in an industrial setting will be imperative.[20] Therefore, searching for alternative tellurium sources, that ideally have higher sublimation temperatures and can provide a constant stream of tellurium throughout the deposition whilst minimising the amount of the precursor required, is an area that needs to be explored.

One parameter where there is little contention in the literature is the type of substrate used to grow $MoTe_2$ on, with SiO_2/Si being the unanimous choice for the methods presented in Tables 3-1 and 3-2. SiO_2/Si is one of the most used substrates for the growth and investigation of 2D materials. Utilising a known thickness of SiO_2 (typically 90 or 300 nm)

allows for the use of optical microscopy to determine the thickness of 2D materials, in a rapid and non-destructive manner, due to optical contrast caused by light interference.[21,22] Furthermore, they remain stable under typical growth conditions including elevated temperatures between 600-1000 °C in the presence of various chemical species. Finally, SiO_2/Si is heavily used in the semiconductor industry and is compatible with state-of-the art fabrication techniques, allowing for $MoTe_2$ to be easily integrated into this field.

The dwell temperature of the tellurium source and the substrate are parameters that can have a large impact on the deposition of $MoTe_2$. A higher source temperature results in a higher vapour pressure of tellurium throughout deposition, which has been shown to favour 2H-$MoTe_2$. Whereas a lower source temperature and lower Te vapour pressure favours the 1T'-$MoTe_2$ phase. A higher vapour pressure of Te tends to produce stoichiometric $MoTe_2$ and a previous study using density functional theory calculations (DFT) predicted that the 2H phase is more thermodynamically stable in stoichiometric $MoTe_2$. Conversely, a lower vapour pressure of Te often produces tellurium deficient $MoTe_2$ and the same study found that 1T'-$MoTe_2$ becomes more stable as the concentration of Te vacancies increases.[23] The temperature of the substrate can also be used to influence the phase of the $MoTe_2$ film. A higher dwell temperature favours the formation of 1T'-$MoTe_2$ whilst 2H-$MoTe_2$ can be stabilised by utilising a lower dwell temperature. Again, this has been attributed to the concentration of tellurium vacancies obtained for the different dwell temperatures.[18]

The duration of growth for $MoTe_2$ is another parameter that varies widely across the literature procedures and can be exploited to synthesise a preferred phase. For example, 1T'-$MoTe_2$ is generally favoured by shorter reaction times, while the opposite is true for 2H-$MoTe_2$. A time dependent tellurisation study conducted by Park *et al* discovered that 1T'-$MoTe_2$ initially formed after a 20-minute deposition and upon increasing the reaction time a gradual phase transition to 2H-$MoTe_2$ occurred. This observation was explained by the increased tellurisation time relaxing the tensile strain of the material favouring the formation of 2H-$MoTe_2$.[6]

The heating and cooling rates of the CVD apparatus used for the deposition of $MoTe_2$ are highly varied across the literature methods highlighted in Tables 3-1 and 3-2. The cooling rates of the furnace in particular can be used to achieve a desired phase of $MoTe_2$. One such example is shown in the work of Empante *et al.* where to achieve 1T'-$MoTe_2$ the furnace is allowed to cool naturally to 350 °C before the film growth is quenched by opening the furnace and cooling with a fan. In order to obtain 2H-$MoTe_2$ the furnace is allowed to cool naturally to temperatures below 100 °C before being opened. They attribute the phase

selectivity of their method to the thermodynamic stability of the respective polymorphs. Computational calculations by the group showed that at lower temperatures the 2H phase is favoured whereas above temperatures of ~310 °C 1T'-$MoTe_2$ is favoured, so quenching above this temperature preserves the 1T' phase.[13] The issue with employing cooling rates for phase selectivity is that they will vary between different furnaces, making reproduction of literature procedures difficult. As such, methods that avoid this should be investigated.

The choice of carrier gas and its flow rate are the final parameters that can be varied for the CVD of $MoTe_2$. The unanimous choice for the carrier gas is a combination of H_2/Ar. This gas mixture provides a reductive atmosphere and is essential for the growth of $MoTe_2$, due to the lower chemical reactivity of tellurium compared to other chalcogens, like sulfur.[7,24,25] Unlike the choice of carrier gas there is no consensus in the procedures outlined in Tables 3-1 and 3-2 for the flow rates of the gas, with the values seemingly set arbitrarily. The ways in which the aforementioned parameters can be exploited to achieve a desired phase of $MoTe_2$ are summarised in Table 3-3 below.

Table 3-3: A summary of the CVD parameters that can be exploited to grow a preferential $MoTe_2$ phase.

CVD Parameter	**Exploit**	**Ref.**
Choice of molybdenum precursor	Mo→1T'-$MoTe_2$, MoO_3→2H-$MoTe_2$	[7,9]
Tellurium source temperature	Lower T→1T', Higher T→2H	[11,17]
Substrate temperature	Lower T→2H, Higher T→1T'	[13,14,18]
Duration of deposition	Shorter duration→1T', Longer duration→2H	[6,15]
Heating and cooling rates	Slow ramping→2H, Rapid ramping→1T'	[10,13]

One of the most interesting applications for the polymorphism of $MoTe_2$ is the use of both phases in a single electronic device. These devices require metal-semiconductor contacts to allow for the injection of charge. The barrier to charge injection can be quite low if the metallic and semiconductor materials are two phases of the same material, resulting in the formation of minimally resistive ohmic contacts.[23,26] Research has consistently shown that 2H-$MoTe_2$ devices contacted with the metallic 1T' phase outperform devices contacted with noble metals.[15,17,18,23] However, the optimisations in CVD conditions (Table 3-3) used to achieve phase pure films do not lend themselves to synthesising both 1T'- and 2H-$MoTe_2$ on the same substrate in a single reaction. Instead, to achieve this, post-growth modification must be utilised. Methods for this vary greatly such as, patterning followed by a second CVD

step, electrostatic doping, or the application of strain.[11,17,23,27,28] Multiple-step procedures are unpractical from an industrial point of view and therefore, finding a simple method for the preferential growth of both $MoTe_2$ polymorphs on the same substrate and through a single step procedure is an interesting and important area of research.

3.2. Aims

The aims of this chapter are to utilise iron telluride in place of the commonly used elemental tellurium precursor in the CVD of $MoTe_2$. Then, conditions that allow for the phase pure synthesis of 1T'- and 2H-$MoTe_2$ using $FeTe_2$ will be investigated and the thin films produced will be extensively characterised using techniques such as Raman spectroscopy, atomic force microscopy, X-ray photoelectron spectroscopy and transmission electron microscopy. Finally, conditions that allow for the simultaneous deposition of 1T'- and 2H-$MoTe_2$ on the same substrate in a single deposition will be explored.

3.3. Results and Discussion

3.3.1. The Use of $FeTe_2$ as a Novel Precursor

As discussed in the introduction to this chapter there are some issues with using elemental tellurium in the CVD of $MoTe_2$ thin films. The main concern being the large amount required for each deposition and therefore, in this work an alternative precursor was employed. Iron telluride was chosen as the alternative for several reasons. Firstly, it can be synthesised through a simple solid-state method, which is described in detail in Chapter 2.2. Figure 3-2 shows the PXRD pattern of the synthesised $FeTe_2$ compared to a calculated pattern from the ICSD (card number 42727). The experimental pattern matches the simulated pattern to a great extent, indicating that phase pure $FeTe_2$ has been synthesised. Secondly, thermogravimetric analysis (Figure 3-3) reveals that the decomposition of $FeTe_2$ only occurs around ~600 °C and shows a relatively low mass loss of around ~6.5% at a maximum temperature of 900°C. This indicates that there will be constant and consistent mass loss from the precursor which will result in tellurium vapour being supplied throughout the duration of the deposition process. Furthermore, the low amount of mass loss suggests that it is only Te that is evaporating from the precursor, as a much higher percentage would be expected if iron was also evaporating, especially considering its high melting point. Finally, there are currently no reports of compounds containing Mo, Fe and Te existing and as such there should be no issues with iron contamination of the product $MoTe_2$ films.

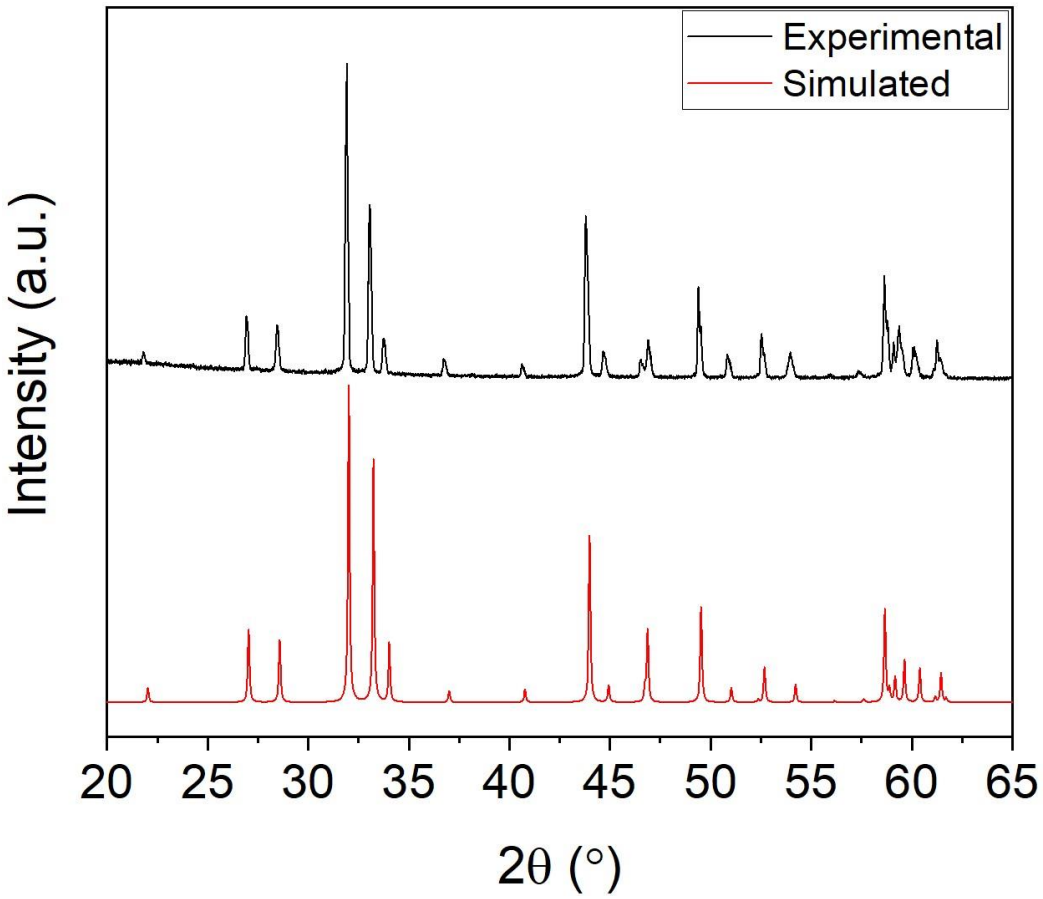

Figure 3-2: PXRD patterns of synthesised $FeTe_2$ and simulated $FeTe_2$ from the ICSD, card number 42727.

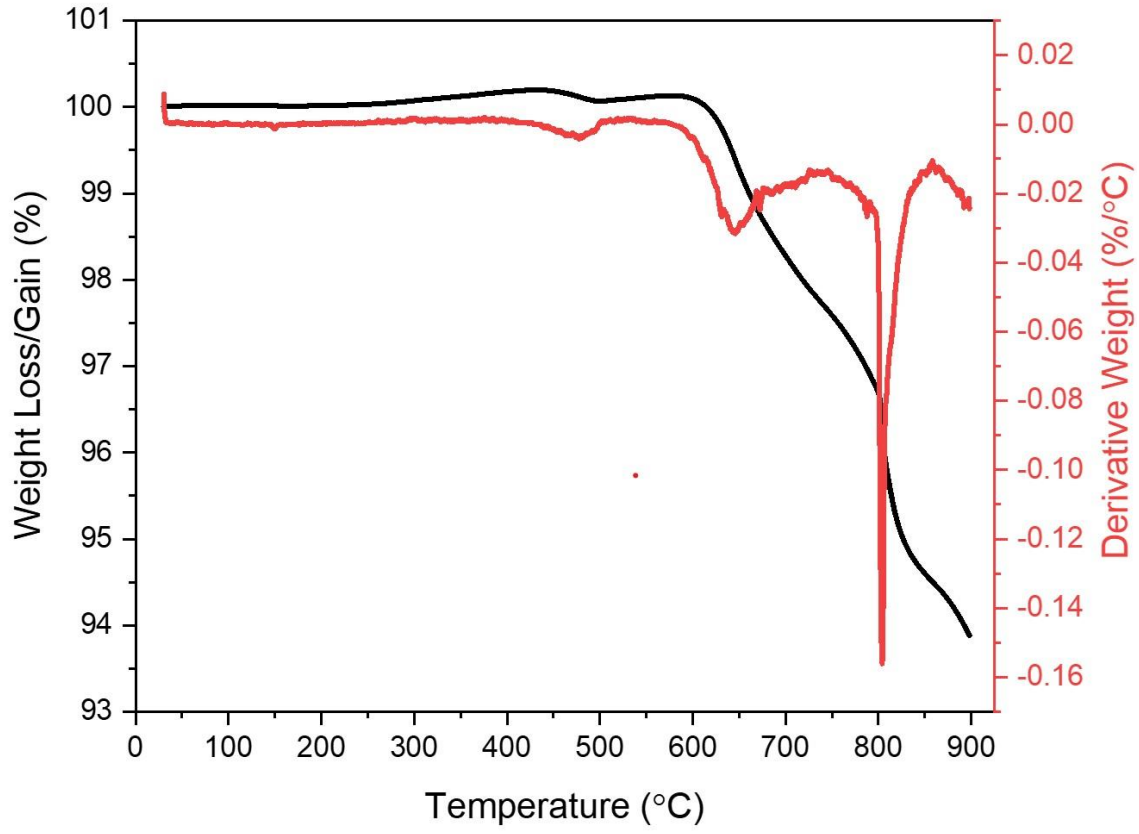

Figure 3-3: TGA data for $FeTe_2$ precursor heated in N_2 atmosphere.

3.3.2. Determination of Initial CVD Parameters

After a review of literature procedures for the chemical vapour deposition of $MoTe_2$, several CVD parameters were chosen due to their consistent presence in the methods highlighted in Tables 3-1 and 3-2. Firstly, 300 nm SiO_2/Si was chosen as the substrate material due to its compatibility with various fabrication techniques and the fact it is stable at the temperatures likely to be used during depositions. Precursor films of molybdenum deposited on SiO_2/Si were chosen initially due to the simplicity of operation of the Plassys MEB550s and the high-quality nature of the molybdenum films obtained through electron-beam physical vapour deposition. A readily available and inexpensive carrier gas of 5% H_2/Ar was selected to provide a reducing and oxygen free environment and the flow rate was arbitrarily set at 300 sccm. Due to reproducibility issues with rapid heating and cooling rates, it was decided to set these at a very low value of 5 °C min^{-1} for both in the hope that it would be reproducible across a variety of furnaces. A relatively long dwell time of 4 hours was selected to ensure that the molybdenum precursor would fully convert into $MoTe_2$ and the dwell temperature of the substrate was set at 650 °C as it is in the middle of the range of temperatures used in the literature methods. Due to the high decomposition temperature of the $FeTe_2$ source, its dwell temperature was set at 630 °C and only a small amount (30 mg) was used for each deposition.

Due to the use of the novel $FeTe_2$ precursor and its high decomposition temperature, a closed CVD reactor was designed to ensure that there would be a sufficient vapour pressure of tellurium in the reactor chamber. This consisted of a large quartz ampoule into which a quartz stopper tube was placed, followed by the Mo/SiO_2/Si substrate before another small ampoule containing the $FeTe_2$ precursor was inserted until it rested against the substrate. The large quartz ampoule was then inserted into the work tube of a Lenton tube furnace ensuring that the Mo/SiO_2/Si substrate resided in the hot zone, with the $FeTe_2$ precursor 7cm upstream. Figure 3-4 contains a photograph and a schematic illustrating the setup.

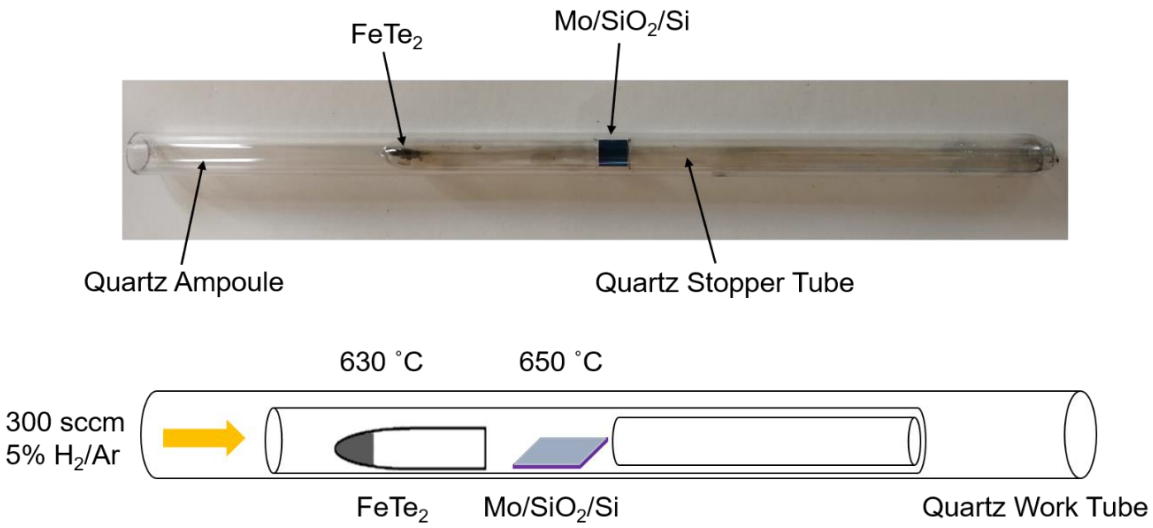

Figure 3-4: Photograph and schematic showing the closed CVD reactor tube designed to ensure a sufficient vapour pressure of Te throughout the duration of a deposition.

An initial test reaction was then performed using a 1 nm $Mo/SiO_2/Si$ film utilising the conditions described above and discussed in detail in Chapter 2.3.1. As Raman spectroscopy is a powerful tool for the characterisation of $MoTe_2$, it was chosen as a means of assessing the reaction outcome. The structural differences between the 1T'- and 2H-$MoTe_2$ phases mean they have vastly different Raman spectra, making Raman an ideal technique for differentiating between the two polymorphs. Figure 3-5 shows the Raman spectrum of the product film obtained from this initial CVD reaction.

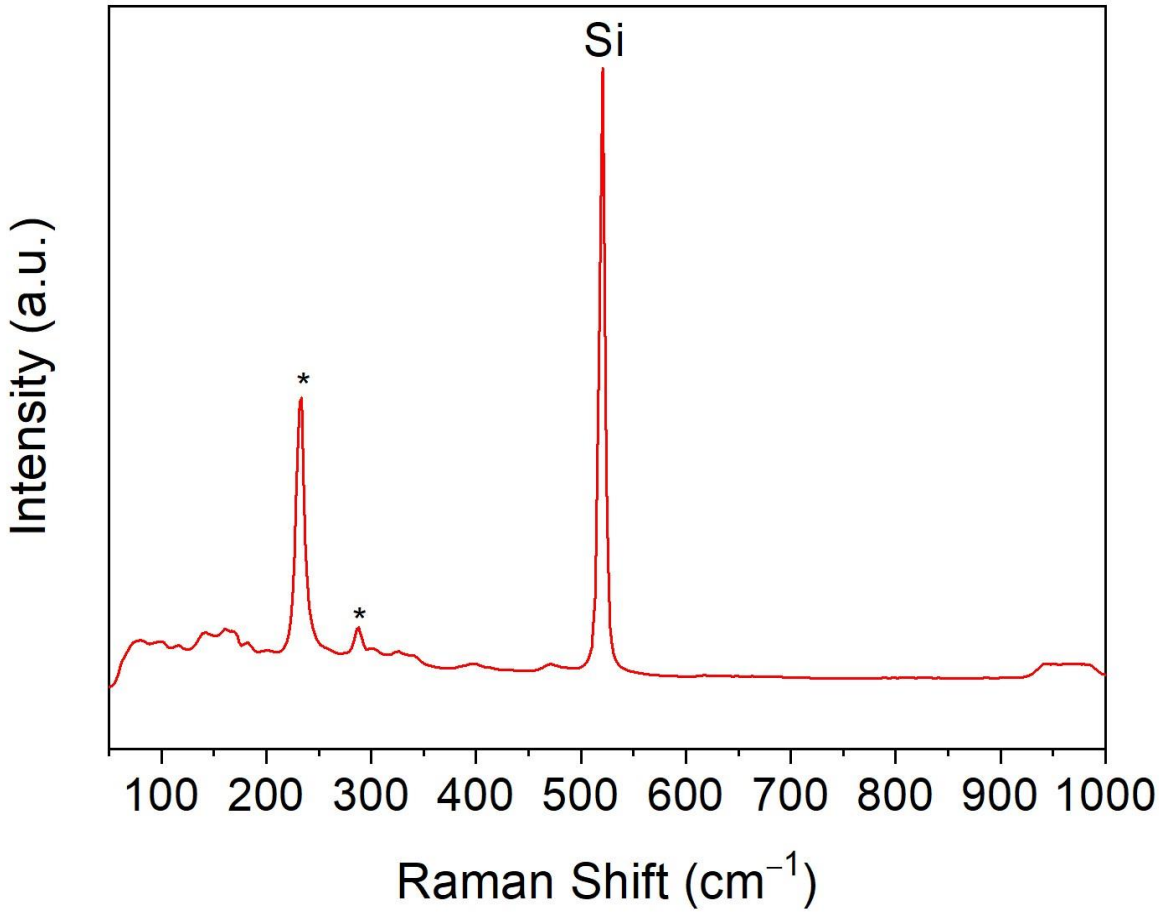

*Figure 3-5: 532 nm Raman spectrum of the product film obtained from the initial CVD reaction with a 4-hour dwell time. Peaks associated with 2H-$MoTe_2$ are marked with * and the peak belonging to the substrate denoted with "Si".*

Interestingly, peaks belonging to 2H-$MoTe_2$ are clearly observed at ~234 and ~289 cm^{-1} along with a large peak at 520 cm^{-1} belonging to the silicon substrate, which helpfully can be used as an internal standard for peak positions.[29,30] In an effort to produce highly crystalline films an increased dwell time of 8 hours was then trialled. The Raman spectrum of the resulting film is shown in Figure 3-6. The spectrum again features peaks belonging to 2H-$MoTe_2$ at ~171, ~234 and ~289 cm^{-1}, but the increased dwell time also led to the formation of a small amount of 1T'-$MoTe_2$ in the product film. With peaks belonging to the metallic phase present at ~78 and ~161 cm^{-1}, respectively.[31] The conversion of 2H-$MoTe_2$ into 1T'-$MoTe_2$ with prolonged reaction times is something that had been previously observed by Zhang *et al*, which they attributed to the formation of Te vacancies with increased reaction time leading to the stabilisation of 1T'-$MoTe_2$.[32] Therefore, for future CVD reactions the dwell time was maintained at 4 hours.

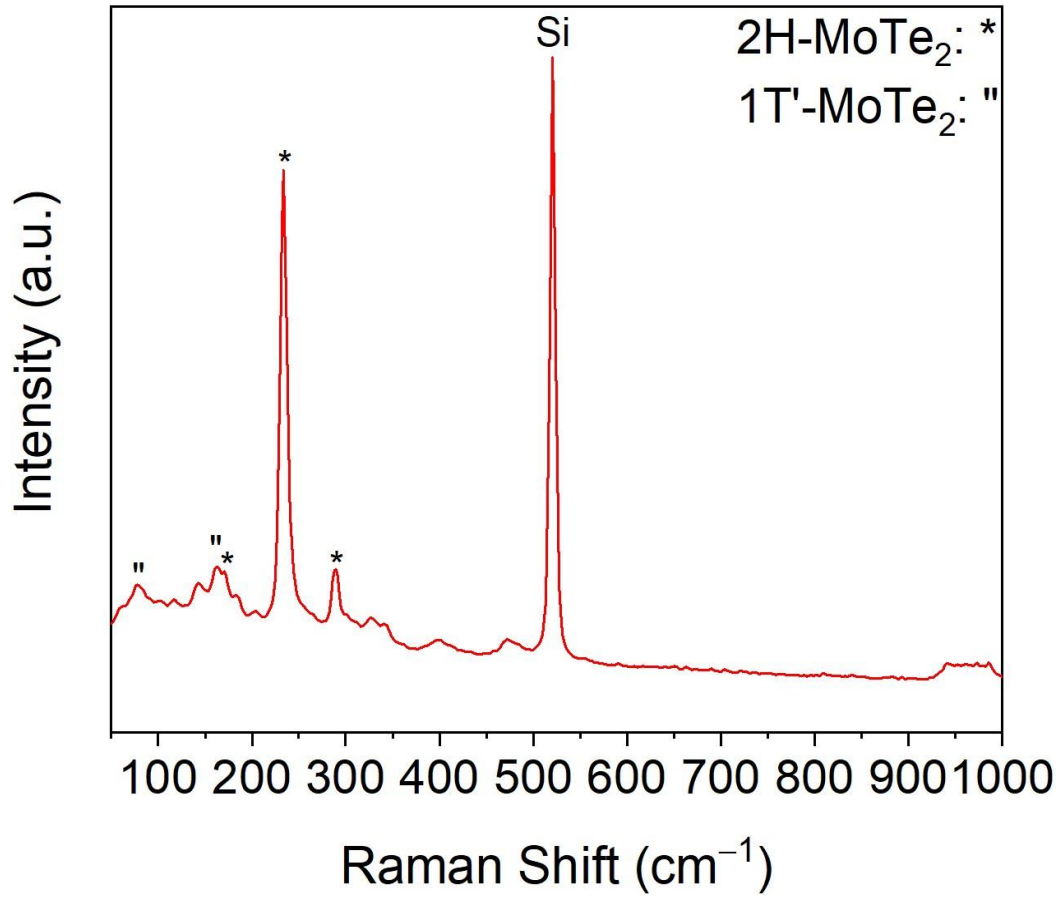

*Figure 3-6: 532 nm Raman spectrum of the product film obtained from the initial CVD reaction with an 8-hour dwell time. Peaks associated with 2H-$MoTe_2$ are marked with *, peaks associated with 1T'-$MoTe_2$ are marked with ", and the peak belonging to the substrate denoted with "Si".*

3.3.3. Characterisation of 2H-$MoTe_2$

With parameters that led to the successful deposition of 2H-$MoTe_2$ determined, attention was then turned into fully characterising these films using techniques such as Raman spectroscopy and mapping, XPS, TEM and AFM. Furthermore, a series of 2H-$MoTe_2$ films with varying thicknesses was also produced and three different methods for assessing their thicknesses were explored.

3.3.3.1. Raman Spectroscopy

The Raman spectra of a 2H-$MoTe_2$ film grown *via* the CVD method as discussed in Section 3.3.1 is shown below in Figure 3-7.

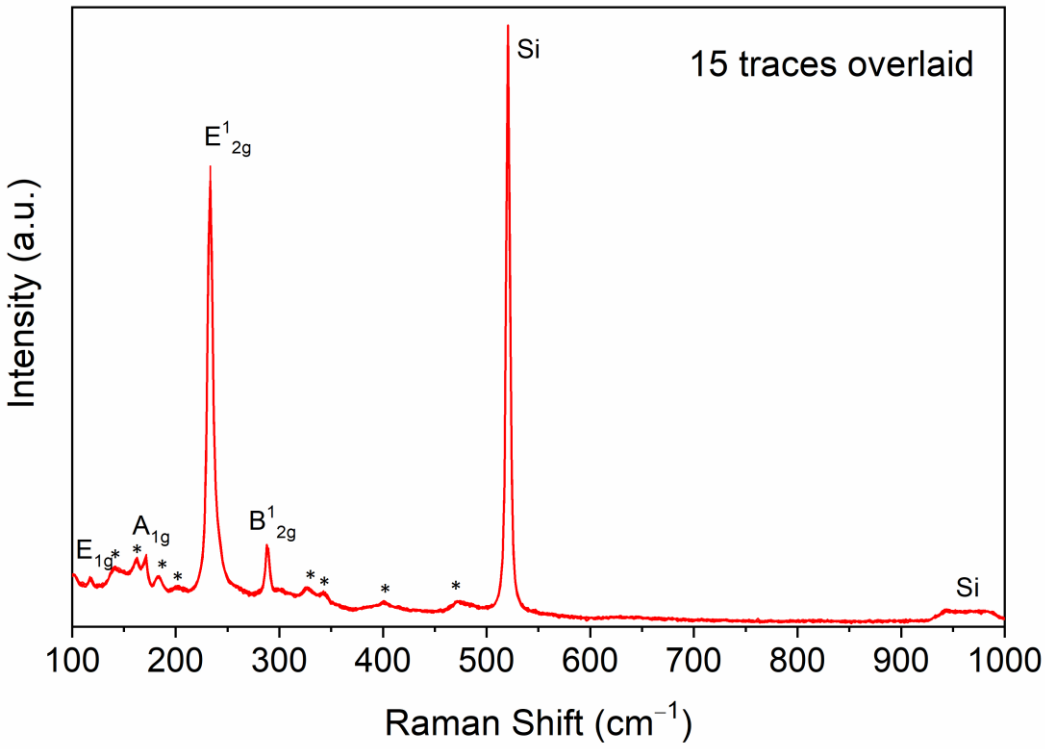

Figure 3-7: 532 nm Raman spectrum of a 2H-$MoTe_2$ film on a SiO_2/Si substrate. Modes associated with $MoTe_2$ are highlighted, second order peaks are marked with "" and peaks belonging to silicon in the substrate are denoted "Si".*

The presence of E_{1g}, A_{1g} and E^1_{2g} modes at ~119 cm^{-1}, ~171 cm^{-1} and 234 cm^{-1} respectively, confirm that the $MoTe_2$ thin film is the 2H phase. Furthermore, the few-layer character of the film is evident from the appearance of the phonon-active out of plane mode at ~289 cm^{-1} as this mode is inactive in monolayer and bulk samples. Additionally, weak peaks at 138, 185, 200, 326, 342, 400 and 470 cm^{-1} (*) are observed which have been confirmed as second-order resonant peaks, further adding to the evidence that phase pure 2H-$MoTe_2$ has been formed.[29,33] The wide ranging spectra also shows no presence of MoO_2 or MoO_3 impurities that have prominent peaks at 225, 740 and 820 cm^{-1} respectively.[34,35] The film is single

phased and uniform across the entirety of the substrate as indicated by the near perfect overlap of the 15 spectra collected from the film at various locations.

To further confirm the uniformity of the film Raman mapping was employed. The intensity of the most prominent Raman mode of 2H-$MoTe_2$ (E^1_{2g}, 234 cm^{-1}) was mapped across the area highlighted in the white square in Figure 3-8a. The resulting colour map (Fig. 3-8b) shows little variation in colour, further highlighting the homogeneity of the 2H-$MoTe_2$ grown film.

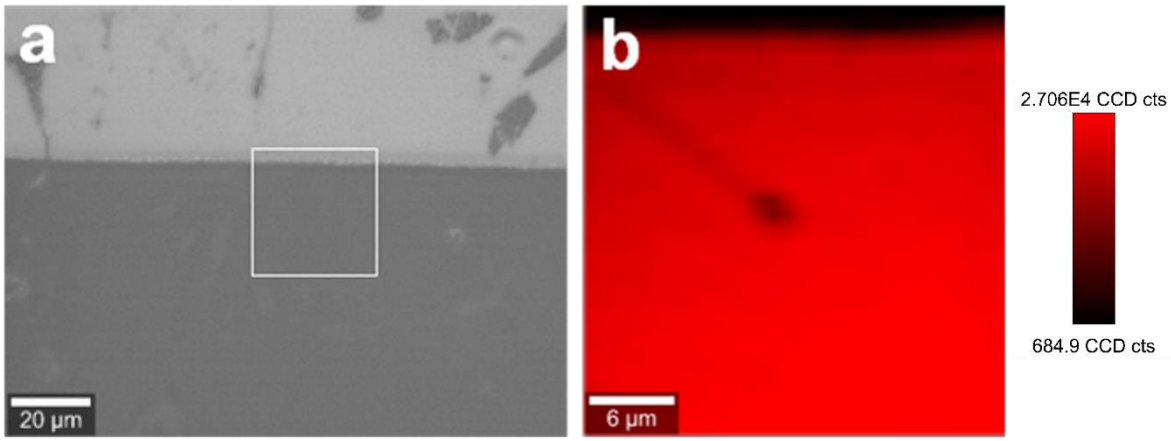

Figure 3-8: White light image of 2H-$MoTe_2$ film, map collected from area highlighted (a); map of same area based on the intensity of the E^1_{2g} mode at 234 cm^{-1} (b).

The Raman data collected confirmed that using $FeTe_2$ and Mo films as precursor materials leads to the formation of highly uniform single phase 2H-$MoTe_2$ films.

In order to investigate the optical properties of the $MoTe_2$ films SiO_2/Si substrates cannot be used. Therefore, Mo was deposited onto a sapphire substrate and the same CVD conversion process was used to convert it into 2H-$MoTe_2$. Sapphire substrates can be used for optical measurements as they transmit a large proportion of visible and infrared light. Figure 3-9 shows the Raman spectra collected from a 2H-$MoTe_2$ film grown on a sapphire substrate. The positions and relative intensities of the peaks for the Raman spectrum on sapphire are similar to those grown on SiO_2/Si. However, the absolute peak intensities were found to be weaker relative to the baseline. For instance, the peak associated with the E_{1g} mode at 119 cm^{-1} is unresolved in this case due to the higher background. This is in keeping with previous observations for a 2.1 nm 2H-$MoTe_2$ film grown on sapphire by physical vapour deposition.[36,37] Furthermore, this has also been observed in other 2D materials. For example, Calizo *et al* found that the spectra acquired from graphene on glass and sapphire substrates featured much noisier backgrounds compared to graphene measured on SiO_2/Si.[38]

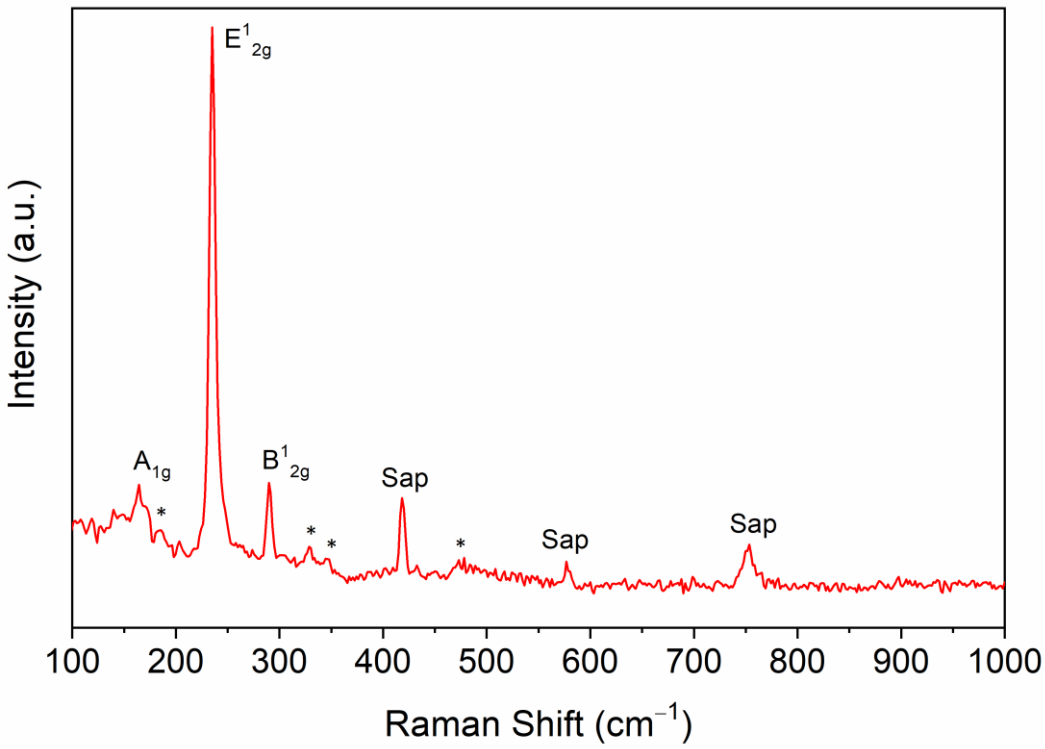

Figure 3-9: *532 nm Raman spectrum from a 2H-$MoTe_2$ film on a sapphire substrate. The modes associated with 2H-$MoTe_2$ are highlighted, second order peaks are marked with "*" and peaks belonging to the sapphire substrate are denoted "Sap".*

3.3.3.2. X-ray Photoelectron Spectroscopy

X-ray photoelectron spectroscopy is an invaluable tool in the field of material science for probing the elemental composition and the electronic states of these elements in a sample of interest. It is an extremely popular technique due to its ability to identify and quantify the elemental composition of the outer 10 nm or less of a solid surface, with all elements from lithium through to uranium detectable.[39]

High resolution XPS spectra were obtained for a 6-layer 2H-$MoTe_2$ film grown on a SiO_2/Si substrate in the Mo and Te 3d regions, and a wide-ranging survey spectrum was also collected as shown in Figure 3-10. The Mo 3d region (Figure 3-10a) exhibits spin-orbit doublets for two oxidation states. The dominant doublet peaks at E_B = 228.12 eV and E_B = 231.2 eV can be assigned to Mo^{4+} $3d_{5/2}$ and Mo^{4+} $3d_{3/2}$ oxidation states for 2H-$MoTe_2$, respectively. Whilst the doublet upshifted to higher binding energies includes a weak shoulder at E_B = 232.5 eV (Mo $3d_{5/2}$) and a broad feature at E_B = 235.71 eV (Mo $3d_{3/2}$). These are consistent with the expected binding energies for the molybdenum oxidation states in MoO_3.[40,41] The peaks consistent with MoO_3 have been observed in other literature work and may originate from surface oxidation in ambient conditions during transfer to the XPS instrument.[42] The high resolution spectrum of the Te 3d region shows only a single doublet

at E_B = 572.75 eV (Te $3d_{5/2}$) and E_B = 583.12 eV (Te $3d_{3/2}$) corresponding to $MoTe_2$ only (Figure 3-10b). Furthermore, upon comparison of our measurements with reference values, we witness an upshift to higher binding energies of 0.12eV for Mo $3d_{5/2}$ and a downshift of 0.35 eV for Te $3d_{5/2}$ peaks. This suggests a net electron transfer from Mo to Te atoms.[43] Given the very small difference in electronegativity between Mo and Te ($\chi_{Te-Mo} = 0.3$) this is in line with expectation.

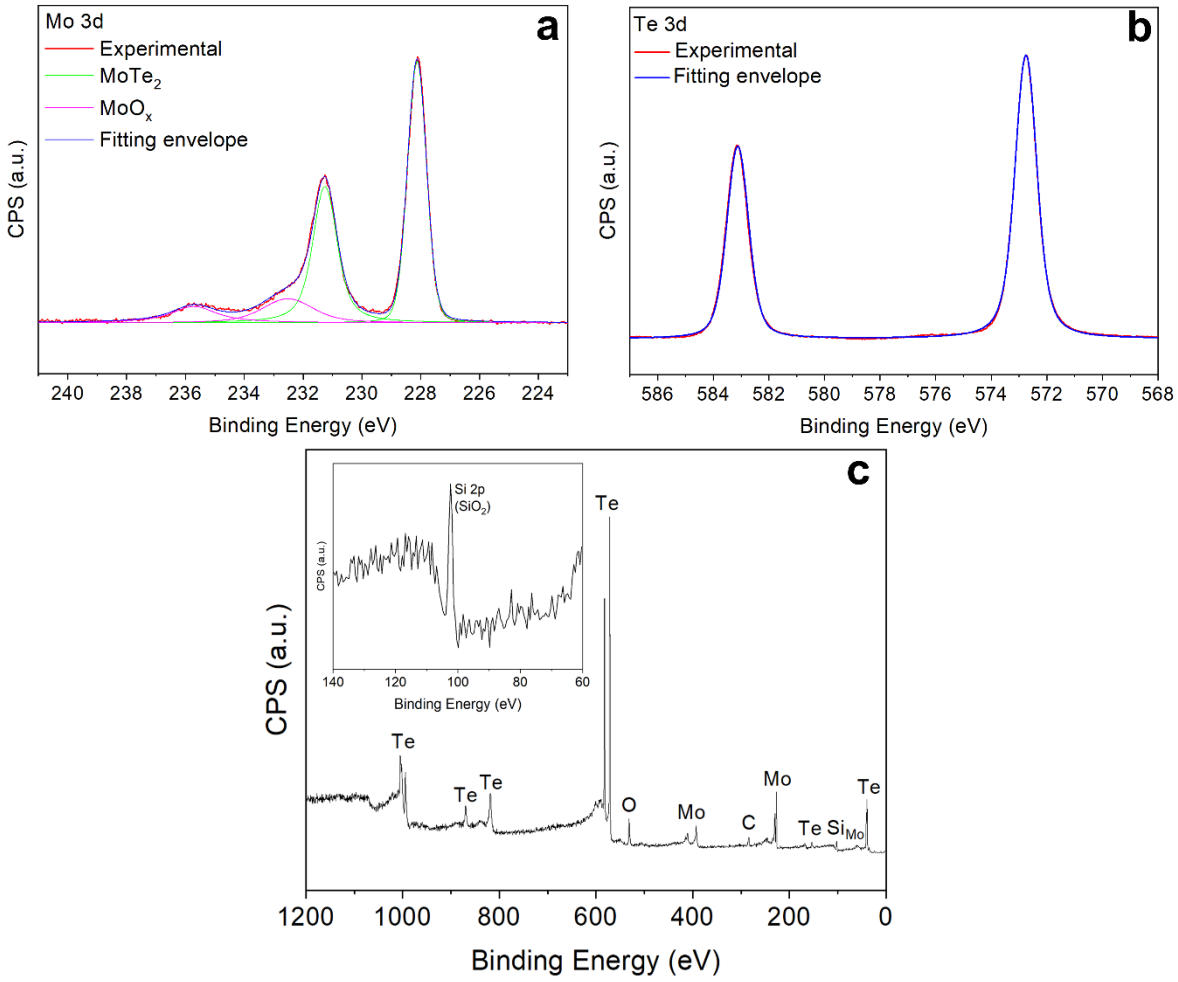

Figure 3-10: High resolution X-ray photoelectron spectroscopy spectrum obtained from six-layered 2H-$MoTe_2$ on 300 nm SiO_2/Si in the Mo 3d region (a); and in the Te 3d region (b); The XPS survey spectrum of few-layered 2H-$MoTe_2$ on SiO_2/Si substrate. The inset shows a zoom into the Si 2p region associated with SiO_2 from the substrate (c).

An interesting feature in the survey spectrum (Figure 3-10c) is the presence of a peak belonging to silicon at E_B = 102.4 eV. The inset of Figure 3-10c shows a zoomed in view of the Si 2p region. The peak originates from SiO_2 in the substrate and confirms that the $MoTe_2$ film is few-layered, as photoelectrons ejected from SiO_2 are able to escape through it and make it to the detector without a change in kinetic energy meaning a discrete signal is observed. A review of the available XPS survey spectra for $MoTe_2$ films on SiO_2/Si revealed

only one example of a 0.96 nm thick film where the Si 2p peak was visible.[44] Therefore, as well as revealing information about elemental composition and oxidation states, XPS could also be used for determining the thickness of the $MoTe_2$ film.[45] Furthermore, there is no evidence of any Mo-metal bands in the high resolution XPS, suggesting the precursor Mo film was converted to $MoTe_2$ in its entirety.

3.3.3.3. Transmission Electron Microscopy

High Resolution Transmission Electron Microscopy (HRTEM) was used to assess the crystallinity of a 6-layer 2H-$MoTe_2$ film transferred to a gold TEM grid. The transfer method involved submerging the 2H-$MoTe_2$/SiO_2/Si substrate in 10% HF diluted with deionised water for 30 seconds. The substrate was then transferred to a beaker of pure deionised water, causing the $MoTe_2$ film to float to the surface. It was then carefully scooped up with the TEM grid and placed into the microscope.

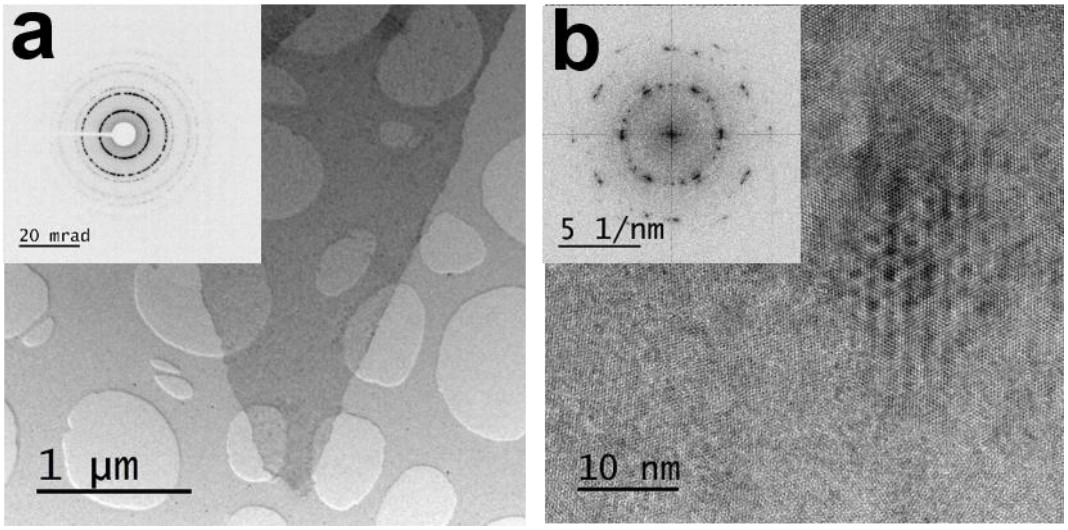

Figure 3-11: TEM of a 6-layered 2H-$MoTe_2$ film supported by holey carbon on Au, the support appears as a network of holes and the darker region in the centre of the image is the $MoTe_2$ flake, a few layers thick; (inset) selected area diffraction (25cm camera length) confirms the flake's polycrystallinity, which manifests as a sequence of diffraction rings rather than spots (a); Higher magnification TEM with the crystal structure is evident, including a moiré fringe effect between crystal layers lying towards the centre of the image, and indicating a polycrystalline structure that is confirmed by (inset) a Fourier transform with multiple sets of hexagonal spots (b).

The selected area electron diffraction confirms that the film is polycrystalline, as it exhibits a sequence of diffraction rings rather than spots (Fig 3-11a inset). At higher magnifications, the crystal structure of the sample is evident (Fig 3-11b). Furthermore, there is a moiré fringe effect between the crystal layers towards the centre of the image. This indicates a polycrystalline structure and is further confirmed by a Fourier transform (Fig 3-11b inset)

which shows multiple sets of hexagonal spots. The extremely harsh conditions in which the films are transferred onto the TEM grids may have an impact upon the crystallinity of the films so ideally, a gentler route to transferral will be found.

Whilst the sample was in the TEM microscope the opportunity was taken to perform Energy Dispersive X-ray Spectroscopy to investigate whether there was any iron contamination from the $FeTe_2$ precursor in the $MoTe_2$ sample.

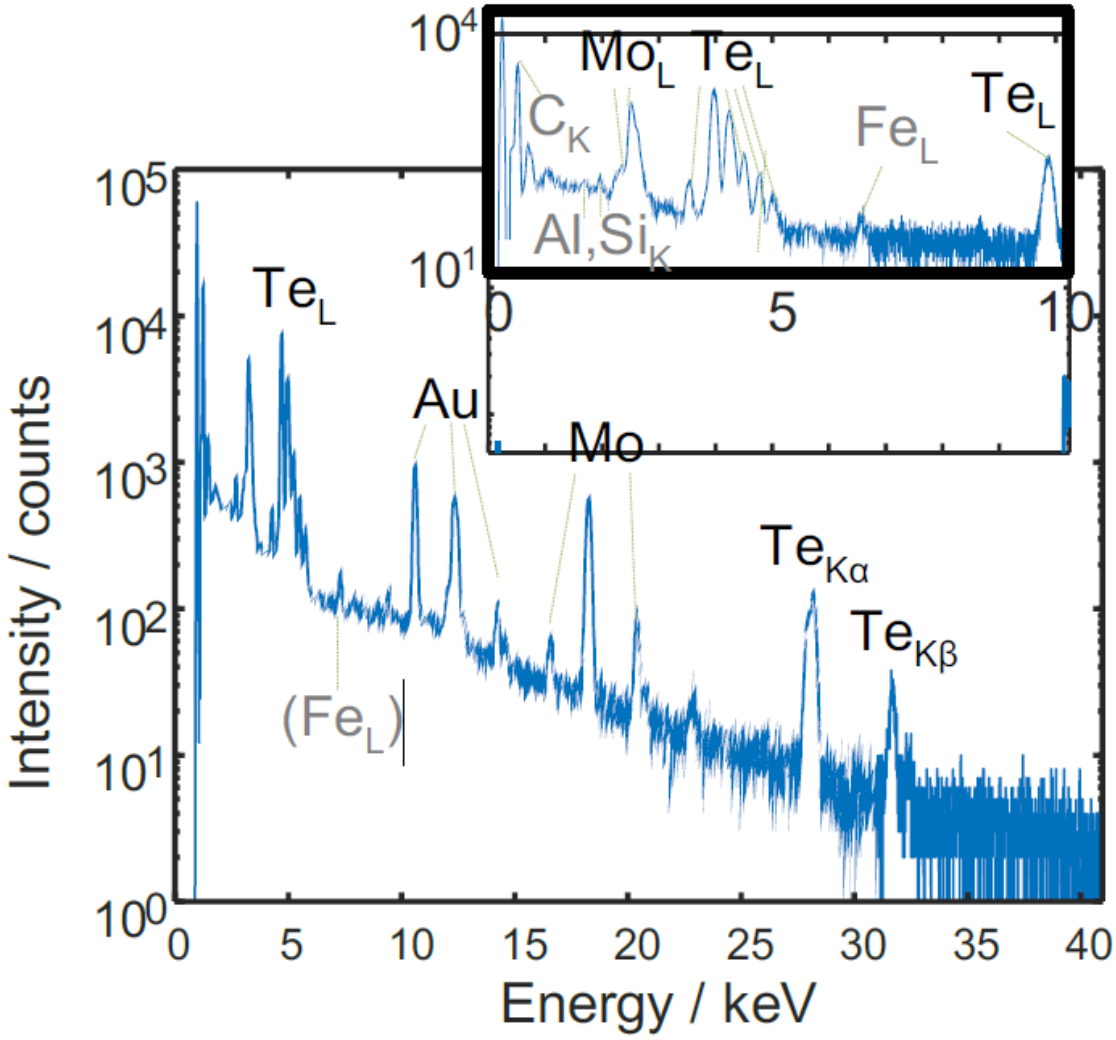

Figure 3-12: EDX spectrum of a representative 6-layered film which is dominated by Mo, Te and Au (support grid) peaks. Very weak Fe, C, Al and Si peaks are visible, at trace levels consistent with secondary scattering within the microscope.

The EDX spectrum (Fig. 3-12) is dominated by peaks corresponding to Mo, Te and Au (support grid). Very weak peaks belonging to Fe, C, Al and Si are also visible, but these are at trace levels consistent with secondary scattering within the microscope. Therefore, it does not appear that using $FeTe_2$ as a precursor has any negative impacts regarding Fe contamination of the product $MoTe_2$ film.

3.3.3.4. AFM Surface Roughness

Atomic force microscopy is a useful technique that images the topography of a sample surface. It can provide information about the height of features on a surface as well as other information such as surface roughness.[46] The root mean square surface roughness (R_q) was measured across an area or 5x5 µm on a pristine SiO_2/Si substrate, a 1 nm thick layer of Mo/SiO_2/Si and finally a 2H-$MoTe_2$ film converted from the 1 nm Mo/SiO_2/Si. The two-dimensional topographic profiles for the aforementioned surfaces are represented in Figure 3-13.

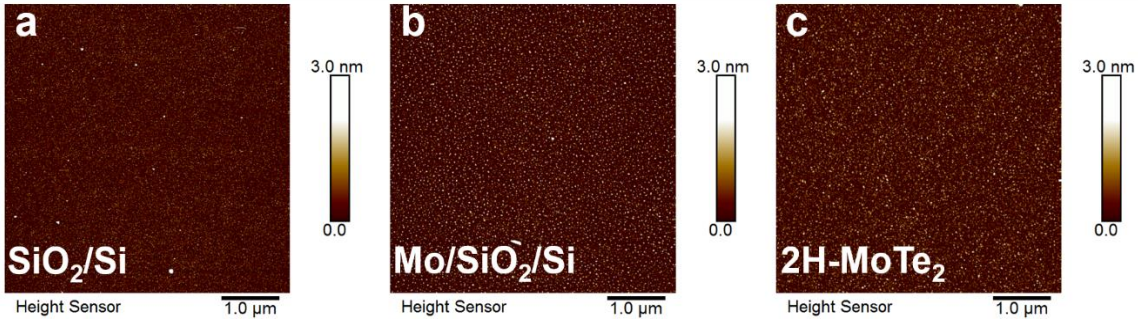

Figure 3-13: 2D topographic profiles of 5 µm × 5 µm area of the surfaces of 300 nm SiO_2/Si pristine substrate (a), 1 nm Mo/SiO_2/Si (b) and a few-layered $MoTe_2$ film on SiO_2/Si substrate (c).

The measured R_q values of both the deposited Mo precursor film and the resultant 2H-$MoTe_2$ film are identical at 0.6 nm. These values are also only marginally higher than that obtained from a pristine SiO_2/Si substrate which had an R_q of 0.45 nm. These values are summarised in Table 3-4.

Table 3-4: A summary of the R_q values of the surfaces presented in Figure 3-13.

Surface	**R_q (nm)**
SiO_2/Si	0.45
1 nm Mo/SiO_2/Si	0.60
2H-$MoTe_2$	0.60

The similarities in morphology of the 1nm Mo/SiO_2/Si and 2H-$MoTe_2$ films suggest that an isomorphic transformation of the molybdenum layer into $MoTe_2$ occurs. This contrasts with a recent literature report that exhibited a substantial increase in the surface roughness of 2H-$MoTe_2$ compared to the precursor Mo film when elemental tellurium was used.[47] It is possible that the retention of morphology is aided by the slow heating and cooling rates of 5 °C min^{-1} utilised in this method. The low rates may suppress any differences in thermal

coefficients between the film and substrate that would otherwise lead to rupturing of the film.

3.3.4. Film Thickness Evaluation of 2H-$MoTe_2$

The main characteristic of 2H-$MoTe_2$ that makes it such an attractive material for electronic and optoelectronic applications are its layer dependent electronic properties. As discussed in Chapter 1.2.1 the bandgap of 2H-$MoTe_2$ changes from indirect to direct and widens from ~0.9 eV to ~1.1 eV going from bulk to monolayer. Furthermore, the vast majority of previous reports on CVD grown $MoTe_2$ have focused on one-off few-layered samples and with only one report available where films with different thicknesses were able to be grown in the same CVD setup.[48] Therefore, we attempted the deposition process with all reaction parameters kept consistent, except for the thickness of the initial molybdenum precursor layer. Mo films with thicknesses of 0.75, 1.00, 1.25, 1.50, and 1.75 nm were deposited by EBPVD and then converted to $MoTe_2$. The thicknesses of the resulting 2H-$MoTe_2$ were then investigated by several different techniques.

3.3.4.1 AFM

As well as being useful for measuring the surface roughness of thin films, AFM is an excellent technique for measuring the height of features ranging from nanometres to micrometres in size. A simple lift off procedure was used (discussed in greater detail in Chapter 2.7) to create a step between the SiO_2/Si substrate and the 2H-$MoTe_2$ film. This step was then measured using AFM and the thickness of the film obtained.

The relevant two-dimensional topological images of the interface between the films and the substrates are shown in Figure 3-14. Whilst the corresponding height profiles of these images are displayed in Figure 3-15.

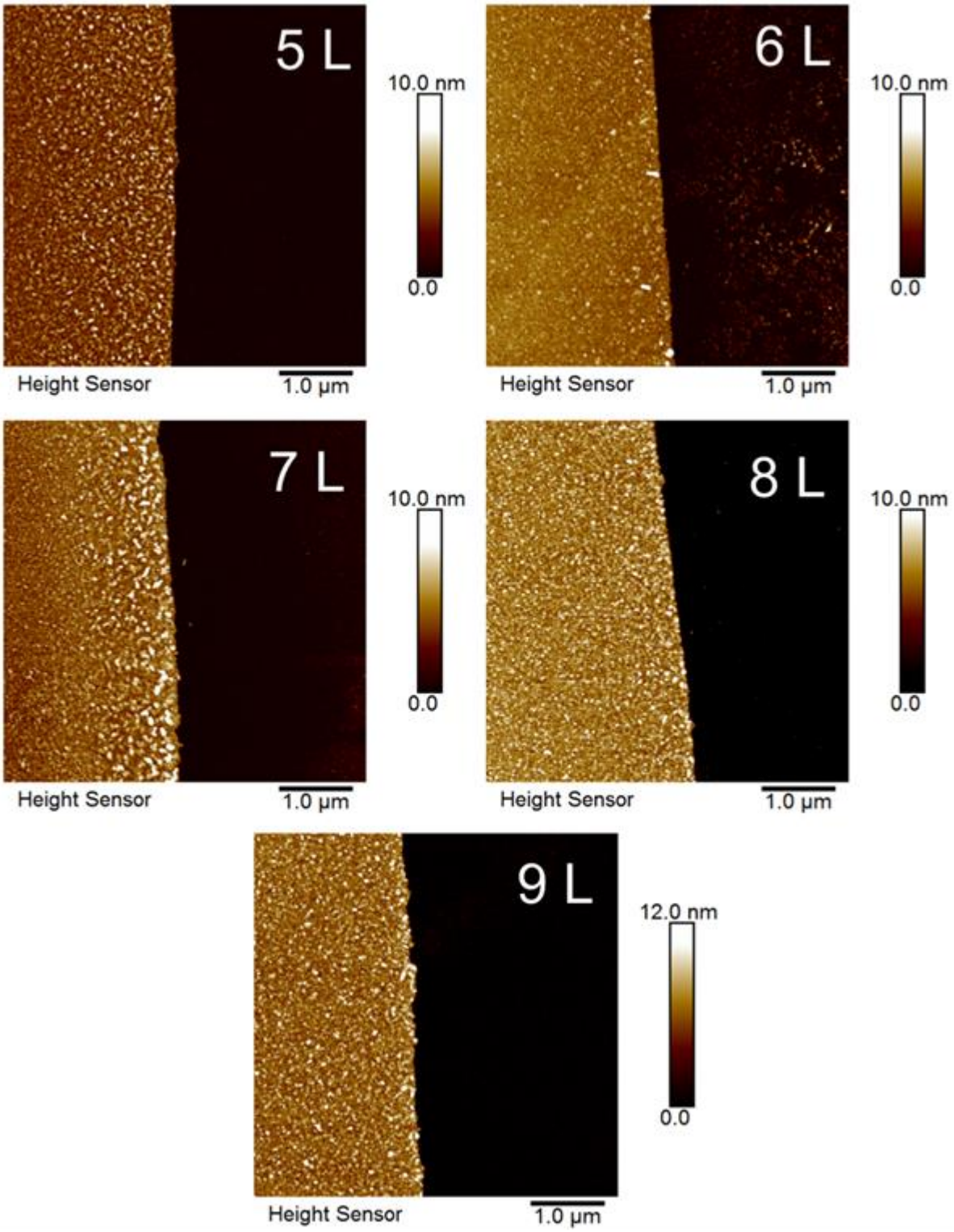

Figure 3-14: 2D topographic profiles of the interface between few-layered 2H-$MoTe_2$ films ranging from 5-9 layers in thickness and SiO_2/Si substrates.

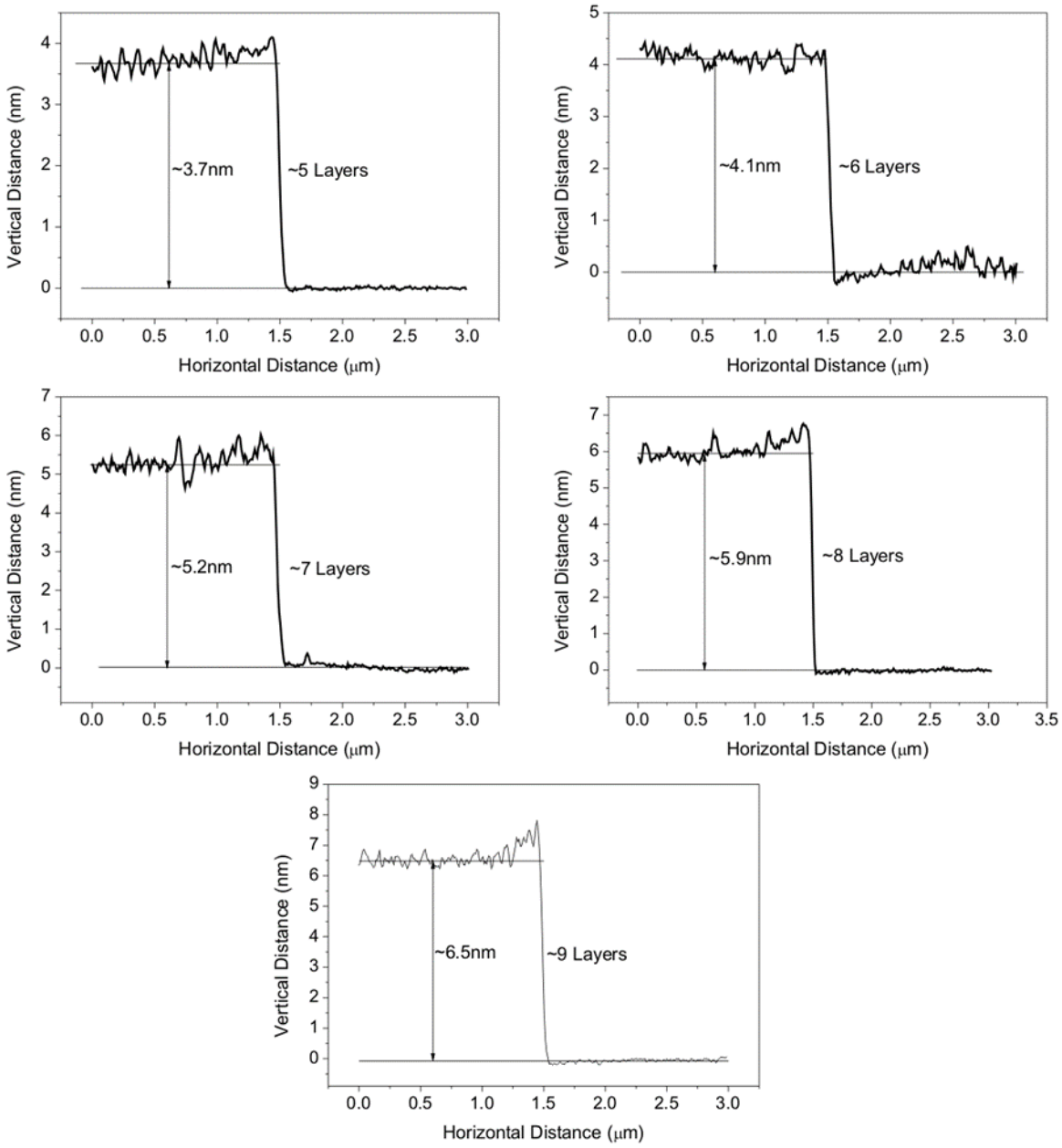

Figure 3-15: The variation in height between 2H-$MoTe_2$ films (corresponding to images in Figure 3-14) and their substrates from AFM measurements.

From synchrotron X-ray diffraction studies, it has been found that the length of the *c*-parameter of $MoTe_2$ is 0.7 nm, meaning that a monolayer of $MoTe_2$ should be ~0.7 nm thick.[49] It is then possible to use the height profiles measured by AFM and convert into the number of $MoTe_2$ layers formed. From these height profiles, it is evident that the precursor Mo film converted to 2H-$MoTe_2$ films with thicknesses of 5, 6, 7, 8 and 9-layers respectively. This shows that the number of 2H-$MoTe_2$ layers increases with the increasing thickness of the precursor Mo films, as would be expected. Unfortunately, due to limitations with the evaporation system used for deposition of the Mo precursor it was not possible to

synthesise monolayer 2H-$MoTe_2$ films. Depositing a single layer of Mo using atomic layer deposition and then converting to $MoTe_2$ may offer a route to monolayer CVD grown 2H-$MoTe_2$ films.

3.3.4.2. Raman Spectroscopy

Raman spectroscopy was again used to characterise the nature of the CVD grown $MoTe_2$ films, the spectra collected from the films with a range of thicknesses are shown below in Figure 3-16.

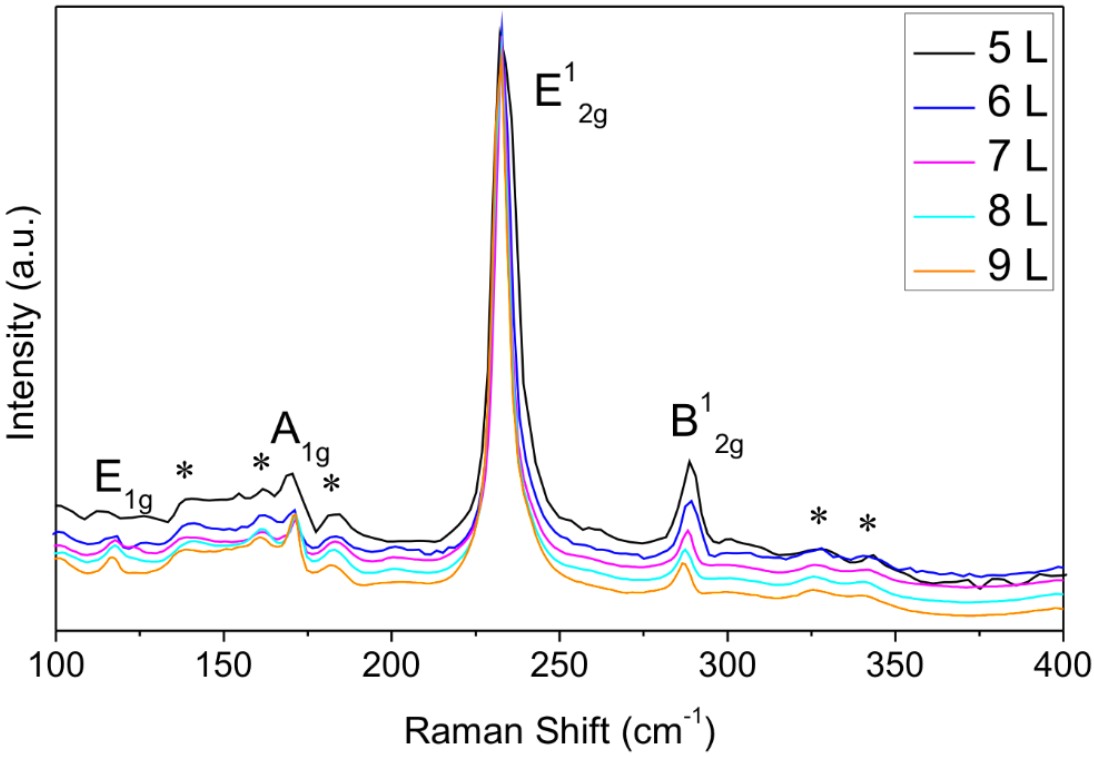

Figure 3-16: 532 nm Raman spectra of 2H-$MoTe_2$ films on 300nm SiO_2/Si substrates with varying thicknesses ranging from 5-9 layers.

The spectra confirm that all the produced films are 2H-$MoTe_2$ in nature. As well as determining the phase of the resultant films, Raman spectroscopy was also used to estimate the thickness of the films. Previous work on characterising the thickness of exfoliated 2H-$MoTe_2$ flakes by Yamamoto *et al* showed that the B^1_{2g}/E^1_{2g} peak intensity ratio could be used to gauge the number of layers in the studied flakes.[29] Although the presence of the B^1_{2g} peak in the Raman spectra of CVD-grown few-layered 2H-$MoTe_2$ films has been shown by various groups, to the best of our knowledge there are currently no reports where the B^1_{2g}/E^1_{2g} peak heights ratio *vs*. film thickness has been systematically investigated for CVD-grown few-layered $MoTe_2$ films. The peak intensity ratios of the B^1_{2g} and E^1_{2g} modes against film thickness are plotted in Figure 3-17a. The relationship between film thickness and the peak positions of the B^1_{2g} and E^1_{2g} modes were also studied and are plotted in Figure 3-17b.

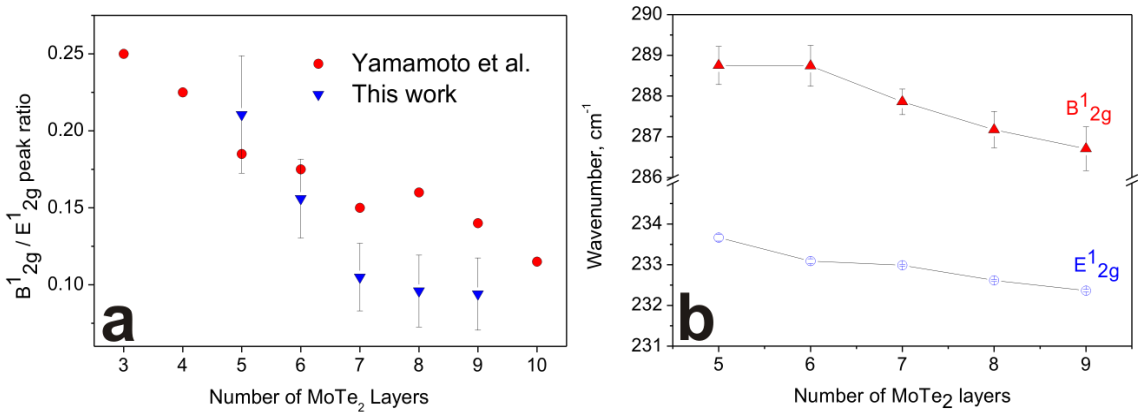

Figure 3-17: Raman data assessment of B^1_{2g}/E^1_{2g} ratio for $MoTe_2$ films on 300 nm SiO_2/Si depending on the number of layers (blue triangles). The data (red circles) for exfoliated $MoTe_2$ samples adopted from Ref. 29 are plotted for comparison. (a); Raman data assessment of the positions of B^1_{2g} and E^1_{2g} peaks depending upon the number of layers (b).

The peak intensity ratios decrease with the increasing thickness of the 2H-$MoTe_2$ film. This is also witnessed for the peak positions for the B^1_{2g} and E^1_{2g} modes, which experience a blue shift when the number of layers is increased. Both metrics show a distinctive trend with increasing number of layers of 2H-$MoTe_2$ and are in good agreement with the previously obtained AFM thickness data and the literature work of Yamamoto *et al.* However, as the thickness of the films and number of layers increase the intensity of the B^1_{2g} peak tends to decrease, with the B^1_{2g}/E^1_{2g} peak heights ratio then plateauing for films with 7 or more layers making it a relatively insensitive measure for thicker films. Raman spectroscopy can be a useful, rapid and non-invasive way of estimating the thickness of 2H-$MoTe_2$ films, especially those with 7 layers or less.

3.3.4.3. Optical Contrast Microscopy

Another technique that has been used for determining the number of layers in exfoliated samples of various 2D materials is optical contrast microscopy. This technique relies upon the contrast difference between a 2D nanosheet and the substrate it was grown on or transferred onto. It is a simple, efficient and non-destructive technique that enables rapid characterisation of 2D materials over a large area. It can provide a rapid, non-destructive assessment of the thickness of the CVD grown 2H-$MoTe_2$ thin films. Again, to the best of my knowledge there have been no systematic investigations on CVD grown $MoTe_2$ films with varying thicknesses using optical contrast microscopy. Therefore, the optical contrast difference (C_d) between the substrate (C_s) and the $MoTe_2$ film (C_f) was investigated by measuring a range of $MoTe_2$ films using a cut-off filter. Figure 3-18 shows the outcome of this study with the normalised contrast difference plotted against film thickness.

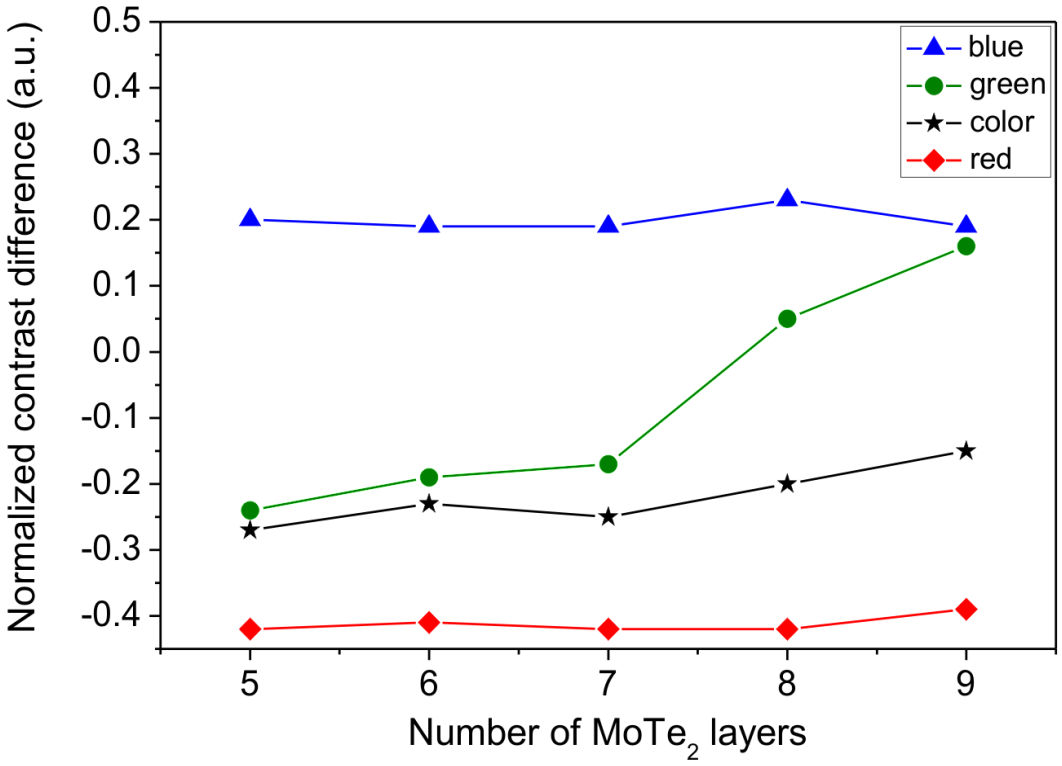

Figure 3-18: Measured normalized contrast (C_d) values depending on the number of layers of few-layered 2H-$MoTe_2$ on 300 nm SiO_2/Si substrates.

It was necessary to split the full colour image into its respective R, B, G channels in order to observe a trend with thickness. The green channel shows the best correlation between C_d and increasing thickness, whilst the red and blue channels saturate quickly. This may be due to a Bayer filter being used in the colour sensor of the camera used for these measurements. In this type of filter 50% of the pixels are green, 25% are red and 25% are blue. This would result in having half as much noise in the green channel and possibly better observed contrast because of this. The representative colour optical images showing the interface between the 300 nm SiO_2/Si substrate and all $MoTe_2$ films together with the corresponding grayscale images of RGB channels are summarised in Figure 3-19.

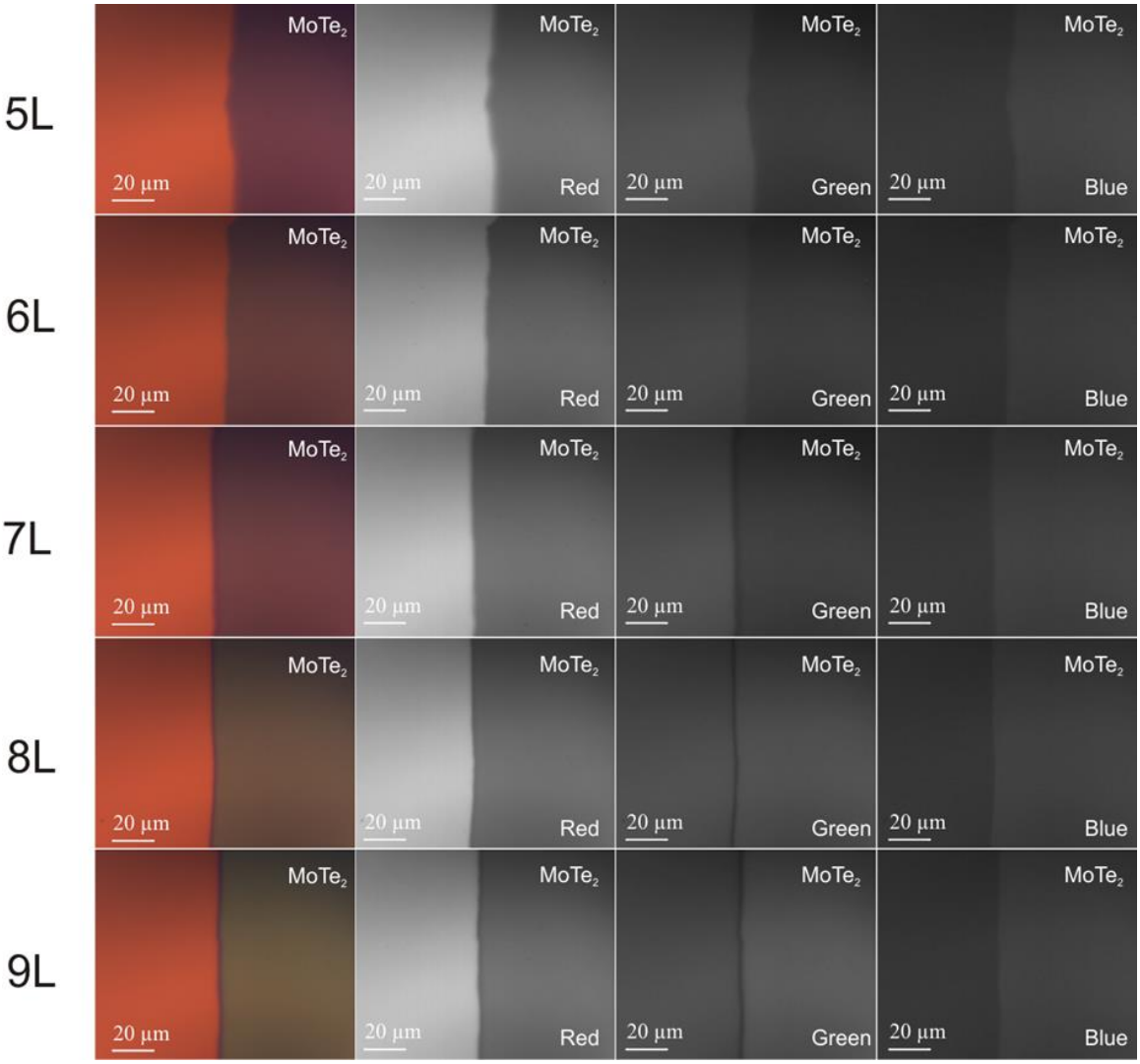

Figure 3-19: Optical colour and grayscale images of the corresponding RGB channels depending on the number of layers for CVD-grown 2H-$MoTe_2$ films on 300 nm SiO_2/Si substrates.

It also appears that optical microscopy is a complimentary technique to Raman spectroscopy for thickness measurements. The C_d values show large differences between the films with 7, 8 and 9 layers, whereas there was very little variation in the measurements for these taken using Raman spectroscopy.

Whilst the contrast between the substrate and film gives good results in the case of the CVD-grown films, it may not always be ideal to measure contrast compared to the substrate. Other molybdenum based TMDCs have been shown to possess thickness dependent refractive indexes, and as such it would be expected that $MoTe_2$ would show a variation in colour depending on the number of layers.[50] Therefore, a colour palette that could be used to rapidly assess the thickness of 2H-$MoTe_2$ films was developed (Figure 3-20).

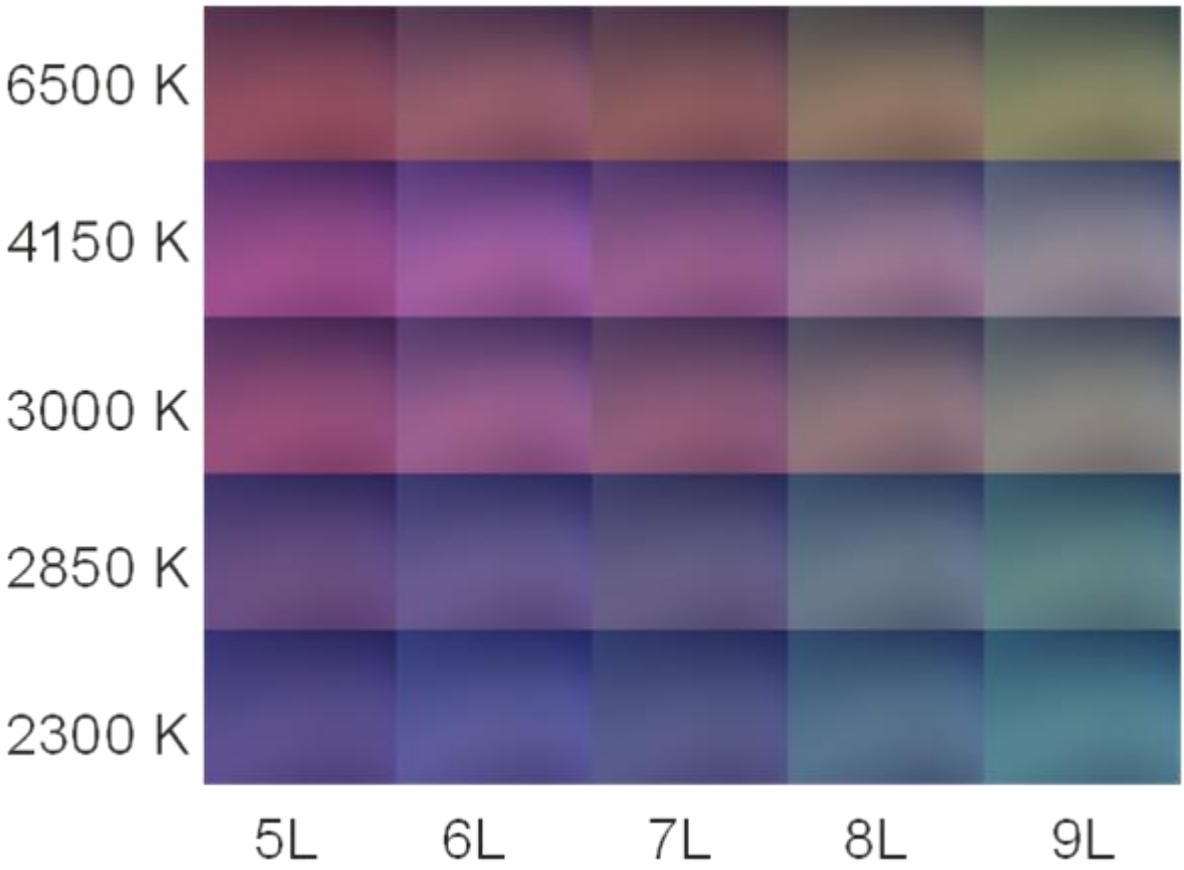

Figure 3-20: A colour palette collated from the optical images of the films with different thicknesses depending on the temperature of the irradiated light which is shown on the left hand side of the image.

Depending on film thickness and temperature of the irradiated light ranging from "incandescent" 2300 K to "daylight" 6500 K, there is a strong colour difference exhibited by films of different thicknesses. Consequently, using the intensity of the green channel, a simple numerical plot was able to be produced which shows a good correlation with the number of layers within the $MoTe_2$ samples (Figure 3-21).

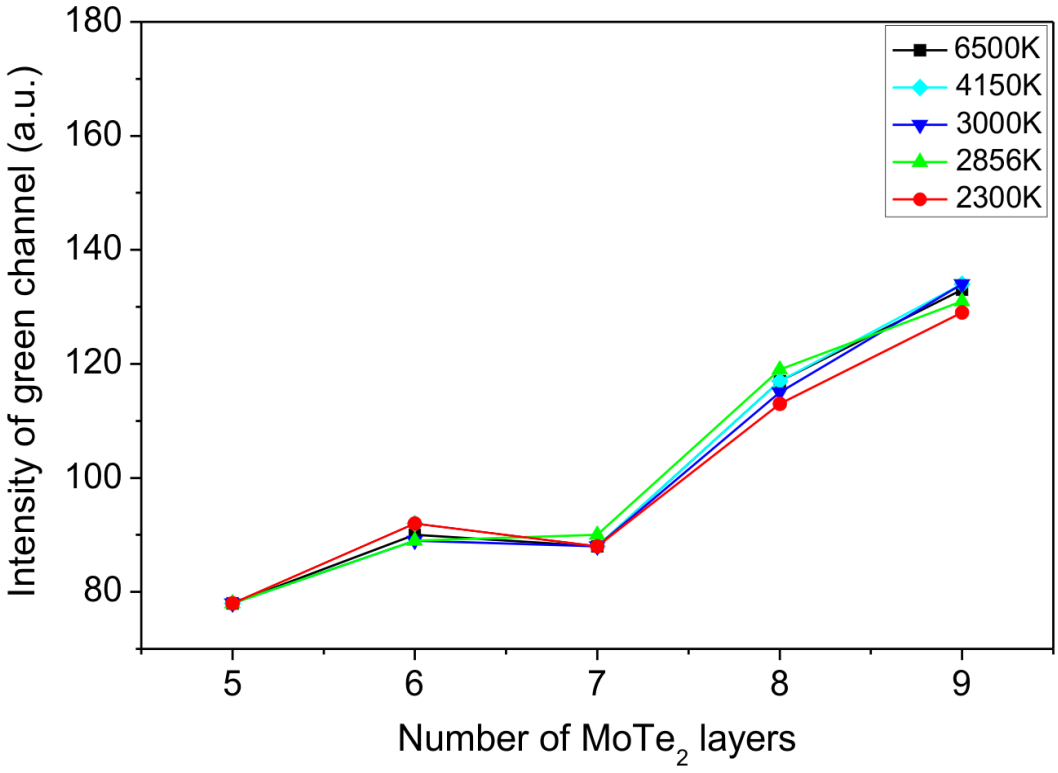

Figure 3-21: The dependence of film thickness on the intensity read from the green channel with various temperatures of irradiated light.

It should be mentioned that although contrast microscopy is a quick and convenient tool for evaluating the thickness of thin film materials, the measurements are only valid for a specific, calibrated system. There are many factors that can affect the result of the measurements, including: the camera system, the thickness of the SiO_2 layer and the microscope objective used. However, once the system has been calibrated, this technique is a quick and convenient way of measuring the thickness of 2D systems.

3.3.5. Synthesis and Characterisation of 1T'-$MoTe_2$

An interesting observation was made upon the conversion of $Mo/SiO_2/Si$ films that had not been stored in an inert atmosphere. Due to oxidation, it is possible that these films were now some MoO_x species rather than pure Mo and the resultant $MoTe_2$ film was a mix of the 2H and 1T' phases as seen from the Raman spectrum in Figure 3-22.

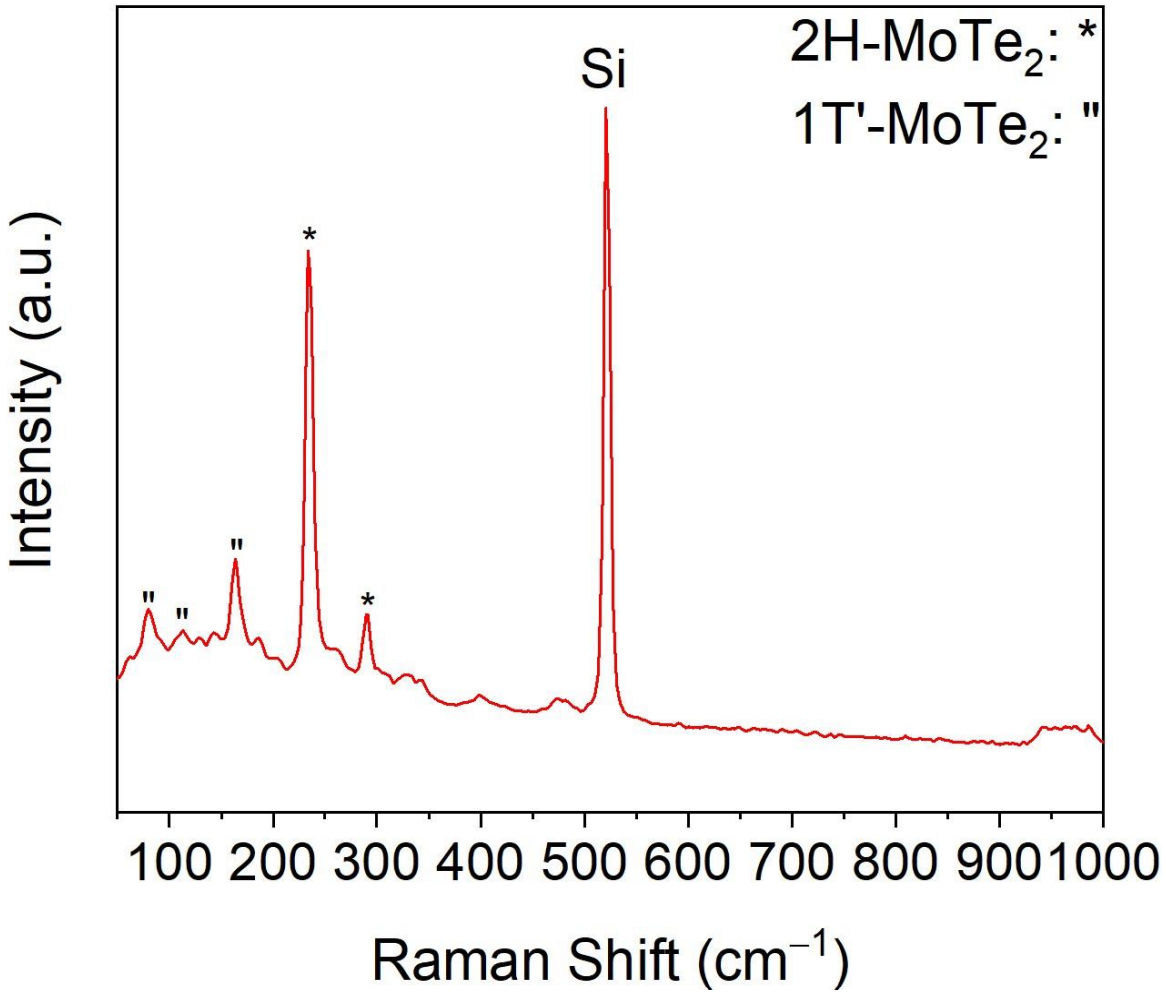

*Figure 3-22: 532 nm Raman spectrum of the product film obtained from a partially oxidised Mo film. Peaks associated with 2H-$MoTe_2$ are marked with *, peaks associated with 1T'-$MoTe_2$ are marked with ", and the peak belonging to the substrate denoted with "Si".*

The spectrum highlights the presence of 2H-$MoTe_2$ with peaks at ~234 and ~289 cm^{-1} as well as a significant amount of 1T'-$MoTe_2$, with peaks belonging to the metallic phase present at ~78, ~110 and ~161 cm^{-1}. One of the exploits in the CVD parameters to achieve phase pure films discussed in the introduction of this chapter was selection of the molybdenum precursor to influence the phase of the product $MoTe_2$ film. Therefore, it is not unrealistic to expect a partially oxidised Mo film to produce a mixed phase $MoTe_2$ film. To investigate this further pure $MoO_3/SiO_2/Si$ films were obtained and converted using the same conditions and set up as used for the deposition of 2H-$MoTe_2$ (Figure 3-23).

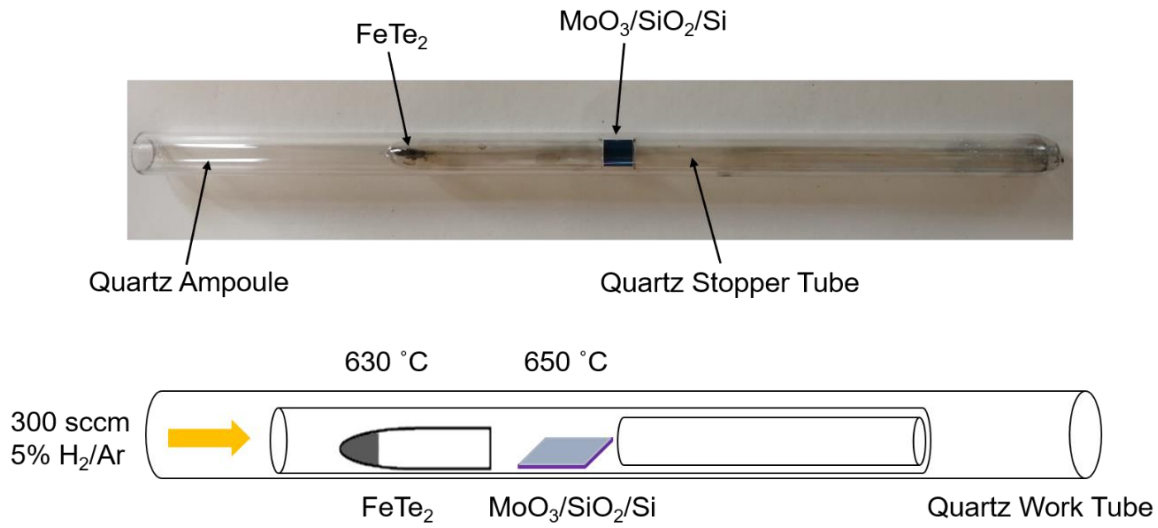

Figure 3-.23: Photograph and schematic showing the same closed CVD reactor used for the deposition of 2H-$MoTe_2$, except in this case $MoO_3/SiO_2/Si$ replaces the previously used $Mo/SiO_2/Si$.

3.3.5.1 Raman Spectroscopy

Raman spectroscopy was again used to characterise the product film and confirms that 1T'-$MoTe_2$ has been successfully grown, with the characteristic Raman peaks of the 1T' phase present between 50 and 400 cm^{-1} (Figure 3-24).

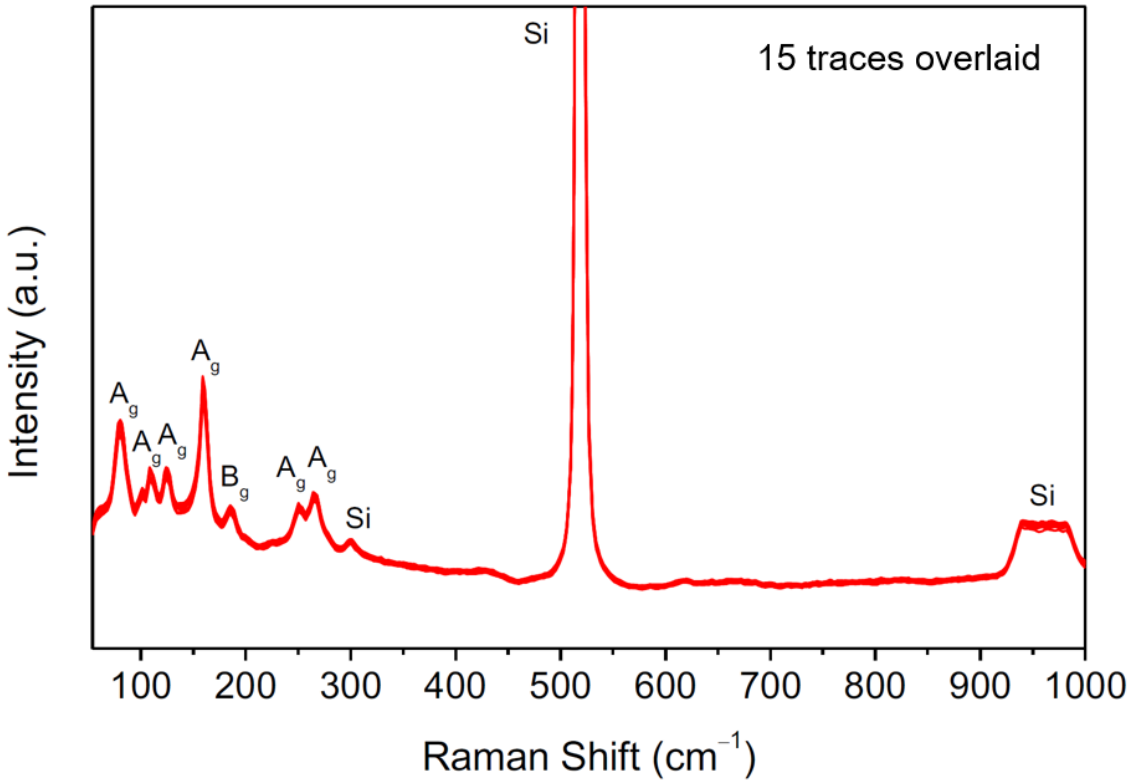

Figure 3-24: 532 nm Raman spectrum of a 1T'-$MoTe_2$ film on a SiO_2/Si substrate. Modes associated with 1T'-$MoTe_2$ are highlighted and peaks belonging to silicon in the substrate are denoted "Si".

A_g modes are present at ~80, ~108, ~125, ~161, ~251 and ~265 cm^{-1} and one B_g mode at ~186 cm^{-1} is present also.[31] Furthermore, the lack of peaks around 225, 740 or 820 cm^{-1} indicate that the entire MoO_3 seeding layer was converted to 1T'-$MoTe_2$ as these peaks are associated with MoO_3 and MoO_2.[34,35] The near identical peak positions and intensities of the peaks in the spectra taken from 15 different locations across the film highlight the uniformity and quality of the film. This uniformity was reaffirmed by Raman mapping. The intensity of the most prominent Raman mode of 1T'-$MoTe_2$ (A_g, 161 cm^{-1}) was mapped across the area highlighted, on the edge of the $MoTe_2$ film, in the white square in Figure 3-25a. The resulting colour map (Figure 3-25b) shows little variation in colour, further highlighting the homogeneity of the 1T'-$MoTe_2$ grown film.

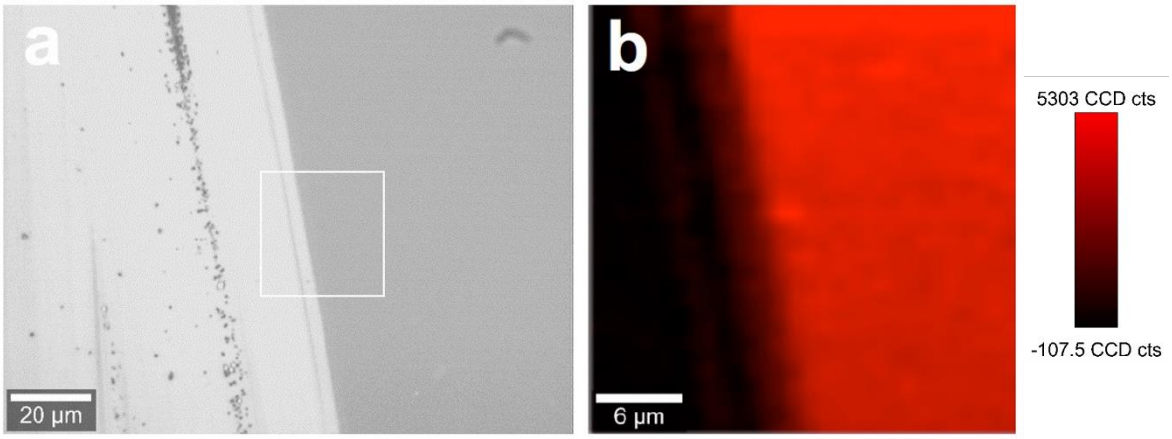

Figure 3-25: White light image of 1T'-$MoTe_2$ film, map collected from area highlighted (a); map of same area based on the intensity of the Ag mode at 161 cm^{-1} (b).

For consistency, utilising sapphire as a substrate for 1T'-$MoTe_2$ was also trialled. A precursor film of MoO_3 was deposited on sapphire and converted using the same reaction conditions as before. The Raman spectrum collected from the resulting film is shown in Figure 3-26 and clearly indicates that 1T'-$MoTe_2$ has been successfully grown. The positions and relative intensities of the peaks for the Raman spectrum on sapphire are similar to those grown on SiO_2/Si. However, the two A_g modes at ~251 and ~265 cm^{-1} appear broadened to the extent that they have merged in the spectrum recorded on the sapphire substrate.

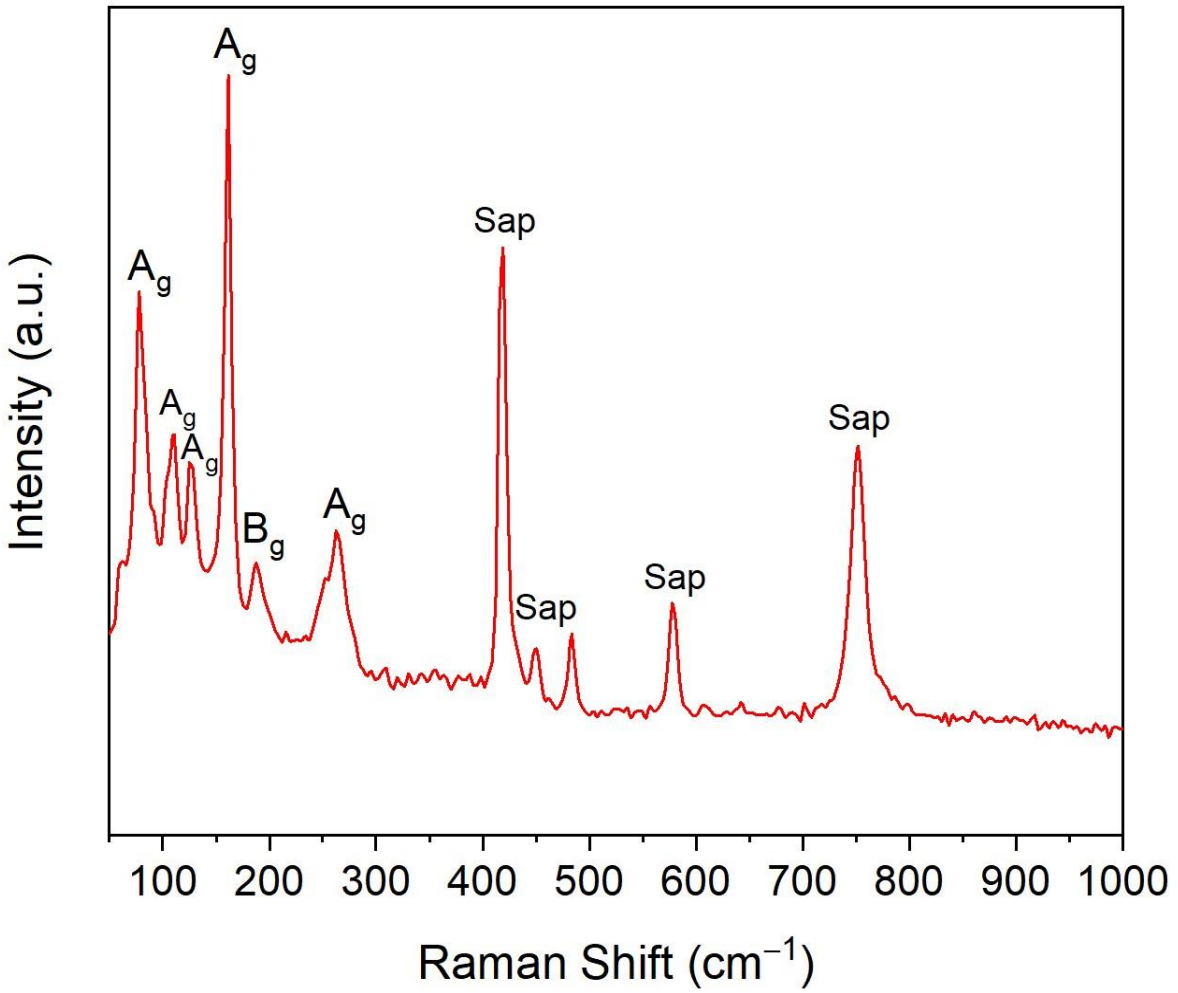

Figure 3-26: 532 nm Raman spectrum from a 1T'-$MoTe_2$ film on a sapphire substrate. The modes associated with 1T'-$MoTe_2$ are highlighted and peaks belonging to the sapphire substrate are denoted "Sap".

3.3.5.2. XPS

High resolution XPS spectra were obtained for a 7-layer 1T'-$MoTe_2$ film grown on a SiO_2/Si substrate in the Mo and Te 3d regions, and a wide-ranging survey spectrum was also collected as shown in Figure 3-27. The Mo 3d region (Figure 3-27a) exhibits a single doublet at E_B = 227.61 eV and E_B = 230.76 eV which can be assigned to the Mo^{4+} $3d_{5/2}$ and Mo^{4+} $3d_{3/2}$ oxidation states for $MoTe_2$, respectively. The 1T' sample measured appears oxide free, with no second doublet appearing around E_B = 233 eV (Mo $3d_{5/2}$) and E_B = 236 eV (Mo $3d_{3/2}$) which is where peaks associated with molybdenum trioxide would be expected to manifest.[40,41] The Te 3d region (Figure 3-27b) contains a single doublet at E_B = 572.36 eV and E_B = 582.76 eV corresponding to the Te^{2-} $3d_{5/2}$ and Te^{2-} $3d_{3/2}$ oxidation states for $MoTe_2$, respectively. Interestingly, downshifts of 0.51 eV and 0.44 eV are observed for the Mo and Te $3d_{5/2}$ peaks in 1T'-$MoTe_2$ compared to the 2H phase. Downshifts of the 1T'-$MoTe_2$ peaks compared to 2H-$MoTe_2$ have been witnessed by several other groups.[7,11,23,42] The broad survey spectrum (Figure 3-27c) is dominated by peaks corresponding to Mo and Te, as

expected, as well as C and O signals arising from surface contamination. A peak belonging to silicon at E_B = 102.7 eV originating from SiO_2 in the substrate also features in the survey. This indicates that the 1T'-$MoTe_2$ film is few-layered in nature as photoelectrons ejected from the SiO_2 layer were able to be detected as a discrete signal. Furthermore, the absence of any bands belonging to elemental Mo or Mo oxides confirm that the entire precursor MoO_3 layer was converted to $MoTe_2$.

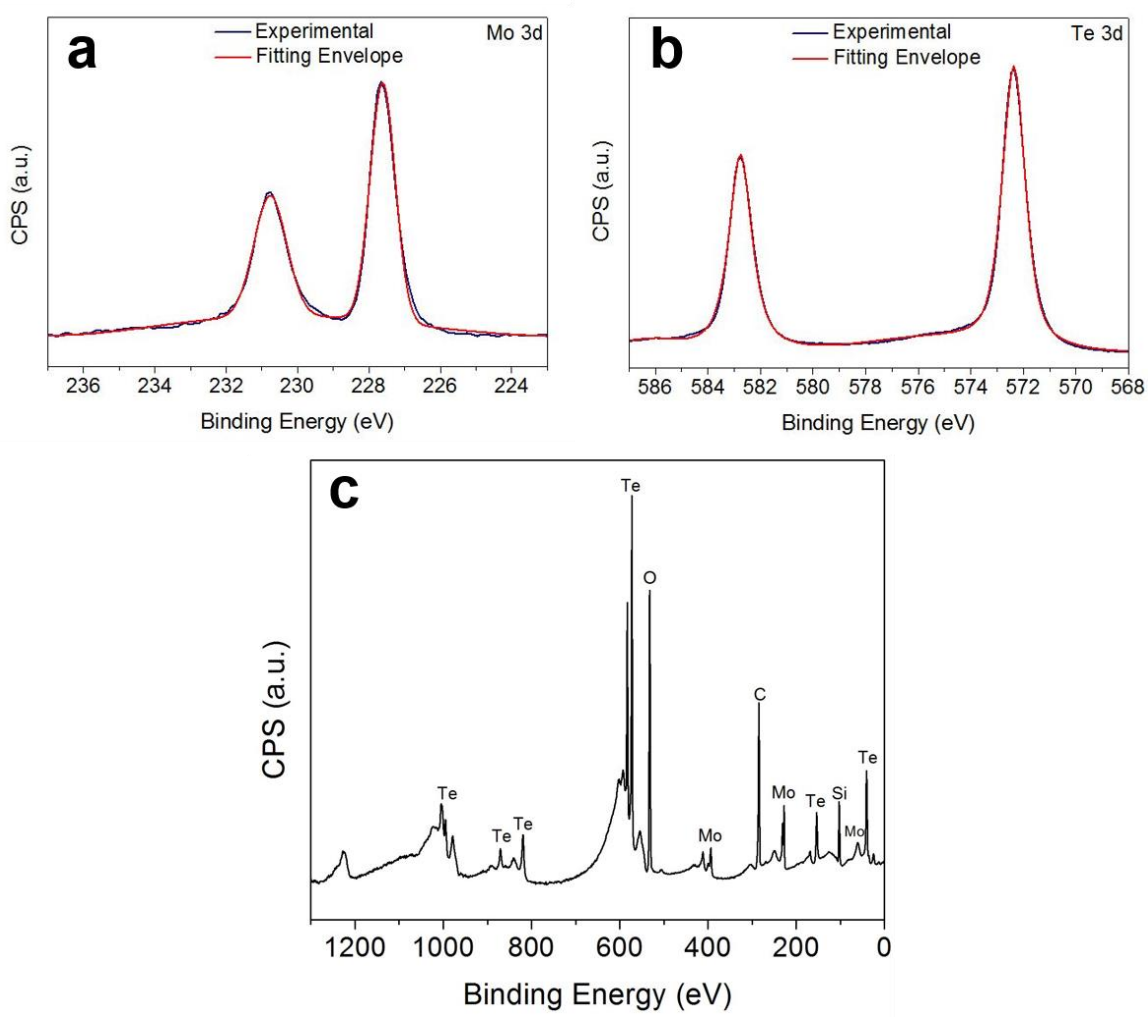

Figure 3-27: High resolution X-ray photoelectron spectroscopy spectrum obtained from 7-layer 1T'-$MoTe_2$ on 300 nm SiO_2/Si in the Mo 3d region (a); the Te 3d region (b); and survey spectrum of few-layered 1T'-$MoTe_2$ on SiO_2/Si substrate (c).

3.3.5.3. TEM

The crystallinity of the 1T'-$MoTe_2$ film was probed using HRTEM and SAED. The same transfer method for removing the 2H-$MoTe_2$ film from the substrate and transferring to the TEM grid was also used in this instance. The images (Figure 3-28) reveal that the studied film was polycrystalline in nature with domain sizes of around 10 nm. This is confirmed by the selected area electron diffraction, manifesting as a sequence of diffraction rings rather than spots. The results of the HRTEM studies are consistent with a recent literature report on a 1T'-$MoTe_2$ film grown at a similar temperature of 650 °C.[51]

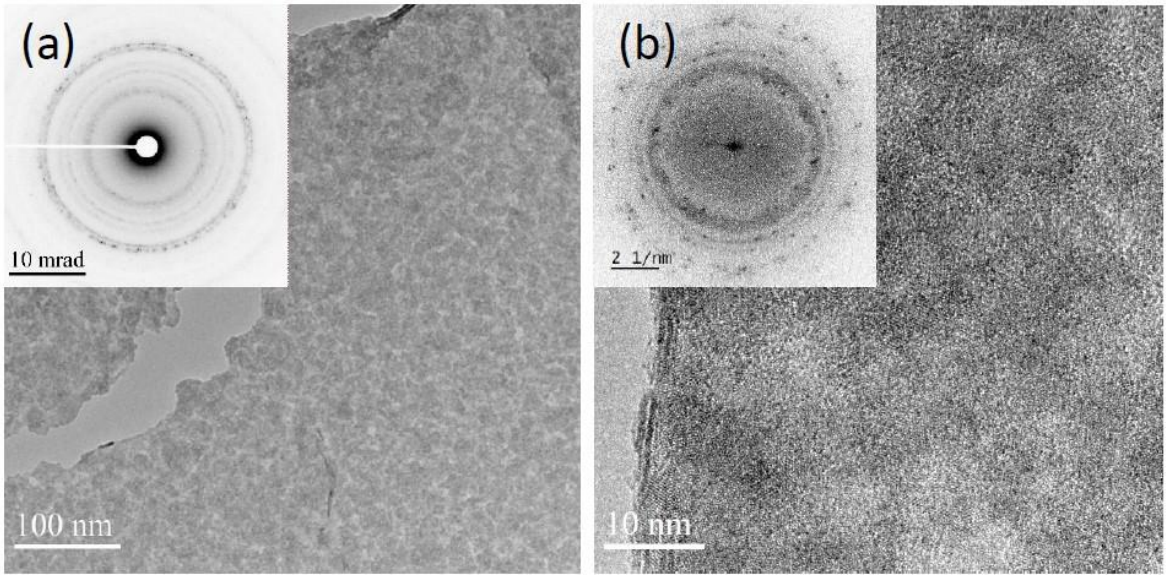

Figure 3-28: TEM images of 1T'-$MoTe_2$ inset with selected area electron diffraction (collected with a nominal 40 cm cameral length) (a); and Fourier transform of the image (b).

3.3.5.4. AFM

AFM was once again used to monitor the surface roughness of the precursor MoO_3 layer and the converted 1T'-$MoTe_2$ film. The surface roughness of the initial MoO_3 film (R_q = 0.480) (Figure 3-29a) and the converted 1T'-$MoTe_2$ film (R_q = 0.484) (Figure 3-29b) are almost identical when compared over a 5×5 μm scan area. This indicates an isomorphic transformation of MoO_3 into 1T'-$MoTe_2$ and means that the quality of the product film is dependent on the quality of the precursor layer and the deposition method.

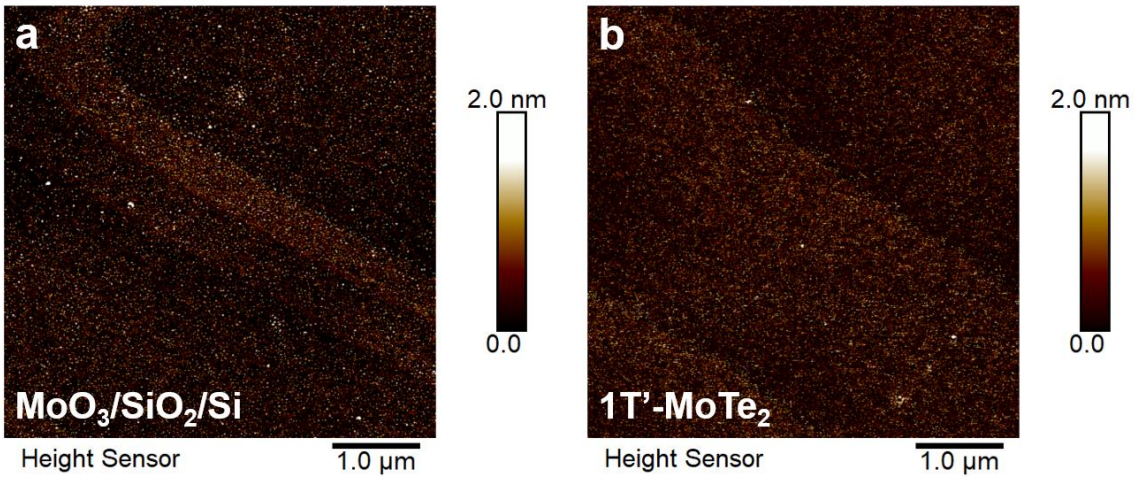

Figure 3-29: 2D topographic profiles of 5 µm×5 µm area of the surfaces of $MoO_3/SiO_2/Si$ (a); and 1T'-$MoTe_2/SiO_2/Si$ (b).

Although 1T'-$MoTe_2$ does not exhibit drastic band structure changes with decreasing thickness like 2H-$MoTe_2$, it is still important to have control over the thickness of the CVD produced films. For example, in the field of surface enhanced Raman spectroscopy, it has been discovered that metallic TMDCs show thickness dependent SERS performance, with few-layer films generally outperforming many-layered films.[52–54] Through the deposition of the precursor MoO_3 layers it is possible to control the thickness of the product 1T'-$MoTe_2$ films, identically to how this was achieved for 2H-$MoTe_2$. MoO_3 films with thicknesses of 1.5, 3, 4.5 and 6 nm were deposited *via* thermal evaporation and then converted to 1T'-$MoTe_2$ using the previously discussed reaction conditions. The same procedure for creating steps, described in Chapter 2.7, between the 1T'-$MoTe_2$ films and SiO_2/Si substrates was used, allowing for the thicknesses of the films to be recorded by AFM. These MoO_3 films were converted into 1T'-$MoTe_2$ films with thicknesses of 5, 7, 8 and 10 layers respectively, assuming that a monolayer of $MoTe_2$ is 0.7 nm in thickness. Figures 3-30 and 3-31 show the relevant two-dimensional topological images of the interface between these films and the substrates and the corresponding height profiles of the images. Once again, as the thicknesses of the precursor layers increase, so do the thicknesses of the resultant 1T'-$MoTe_2$ films.

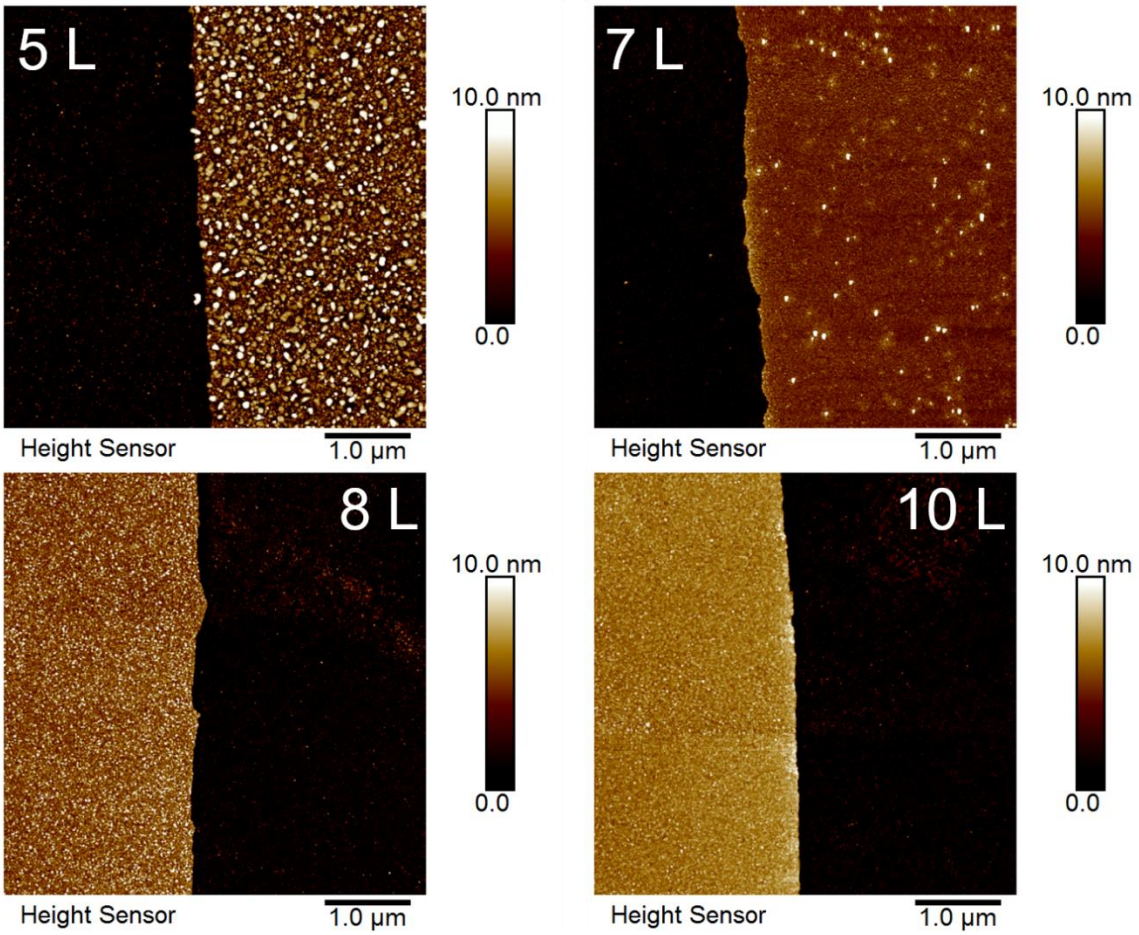

Figure 3-30: 2D topographic profiles of the interface between few-layered 1T'-$MoTe_2$ films ranging from 5-10 layers in thickness and SiO_2/Si substrates.

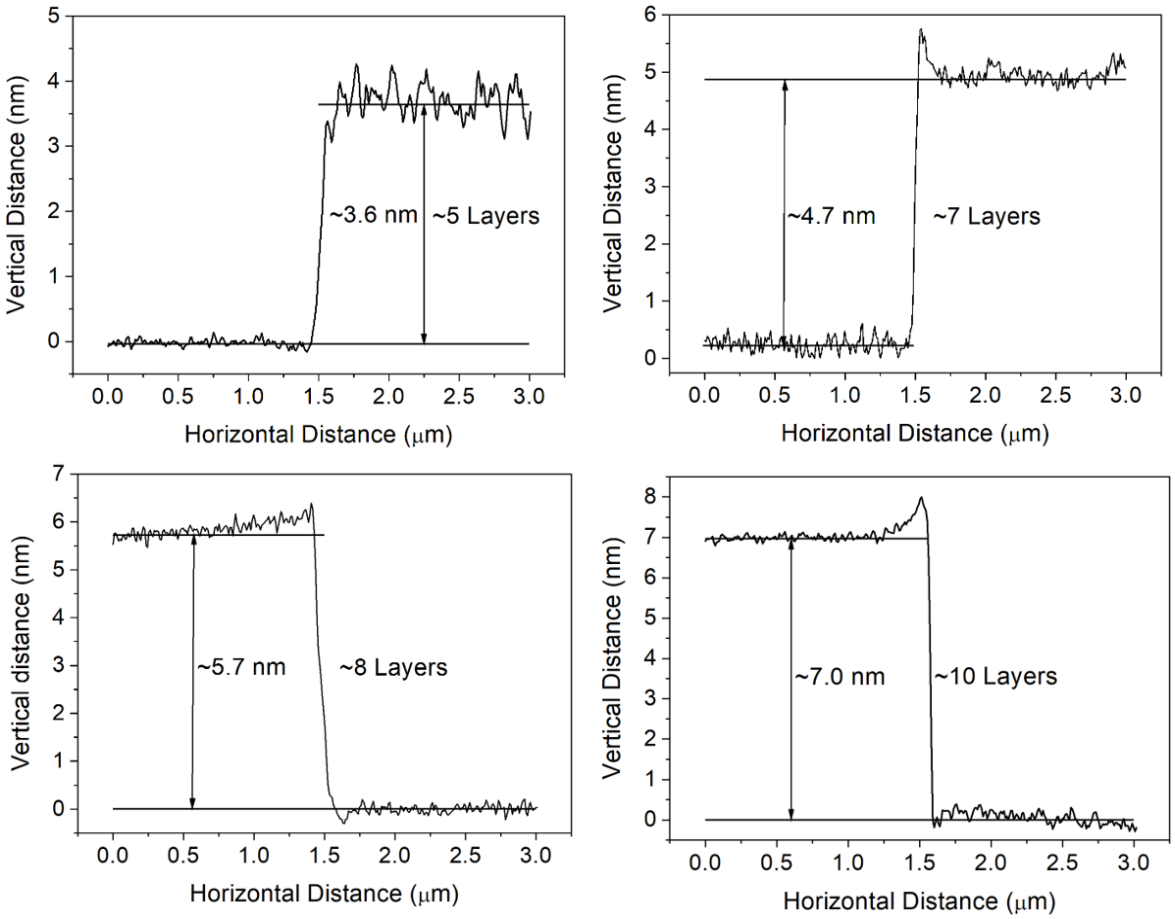

Figure 3-31: The variation in height between 1T'-$MoTe_2$ films (corresponding to images in Figure 3-30) and their substrates from AFM measurements.

Raman spectroscopy was used to ensure that the films of varying thickness produced from MoO_3 were phase pure 1T'-$MoTe_2$. Figure 3-32 shows the spectra collected from these films. The presence of A_g modes at ~109, ~127, ~161 and ~257 and a B_g mode at ~189 cm^{-1} confirm that all films are phase pure 1T'-$MoTe_2$.[31] Due to limitations with the thermal evaporation system used for deposition of the MoO_3 precursor, it was not possible to synthesise monolayer 1T'-$MoTe_2$ films. Depositing a single layer of MoO_3 using atomic layer deposition and then converting to 1T'-$MoTe_2$ may offer a route to monolayer CVD grown 1T'-$MoTe_2$ films.

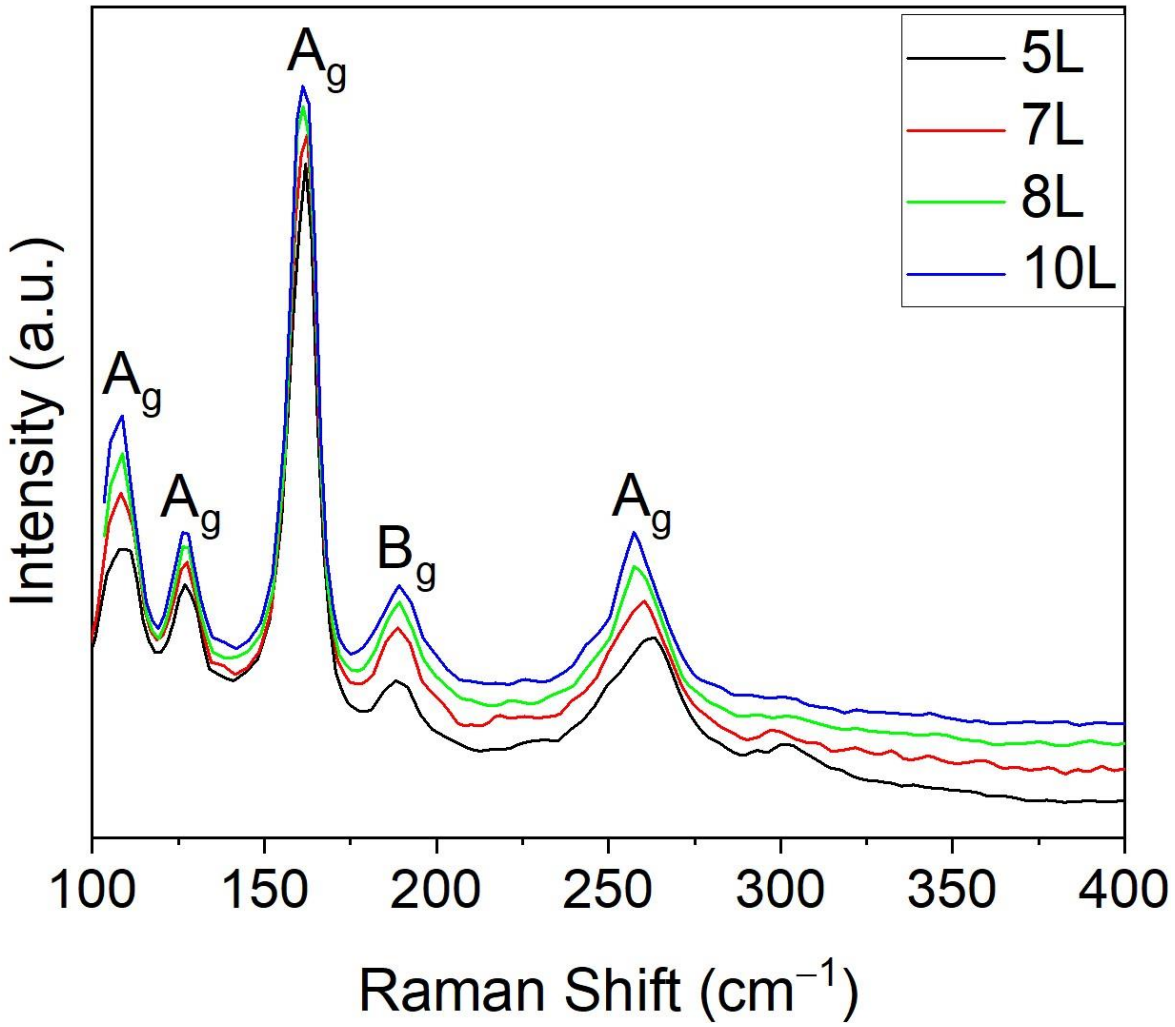

Figure 3-32: 532 nm Raman spectra of 1T'-$MoTe_2$ films on 300 nm SiO_2/Si substrates with varying thicknesses ranging from 5-10 layers.

3.3.6. Simultaneous Deposition of 1T'- and 2H-$MoTe_2$

The fact that the phase selectivity in the CVD system used in this work is dependent upon the type of precursor layer means that there is an opportunity to exploit this for the simultaneous deposition of 2H- and 1T'-$MoTe_2$. A simple mask was used to deposit both Mo and MoO_3 on one substrate, with each precursor covering half of a SiO_2/Si substrate. This substrate was then subjected to the same CVD conditions used previously. The successful simultaneous growth of 2H- and 1T'-$MoTe_2$ on the same substrate was confirmed by Raman spectroscopy, with Mo converting to 2H-$MoTe_2$ and MoO_3 converting to 1T'-$MoTe_2$ respectively (Figure 3-33a). An image taken of the sample shows the two phases separated by a 20-micron strip of bare SiO_2/Si substrate (Figure 3-33b).

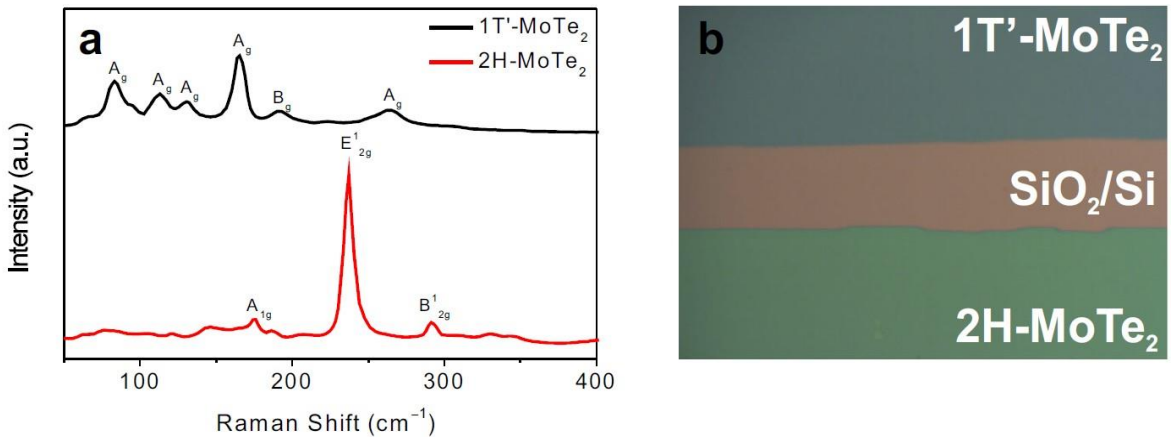

Figure 3-33: 532 nm Raman spectra from 1T'- and 2H-$MoTe_2$ grown simultaneously on 300 nm SiO_2/Si substrate (a) and an optical image of the two $MoTe_2$ phases separated by a ~20 µm strip of bare SiO_2/Si substrate for a better optical contrast (b).

Achieving simultaneous growth in a single step reaction is an important development as this method does not rely upon post growth modification for the creation of 1T'-2H junctions. Furthermore, this method retains spatial control of the phases as it is decided by the deposition of the precursor layers. Access to a single step method may prove to be beneficial in the wider adoption of future $MoTe_2$ applications.

To try and understand why a specific phase is formed from differing precursors, the solid-solid transformation process was investigated by using Mo and MoO_3 powders. Bulk powders were used to achieve slower reaction rates and would hopefully allow any intermediate products to be identified. Around 5 mg each of Mo and MoO_3 were placed onto bare SiO_2/Si substrates and were then subjected to the same CVD conditions as the thin film precursors. Raman spectroscopy was then used to monitor the progress of these reactions. Figure 3-34a reveals that MoO_3 is first reduced to MoO_2 with no formation of 1T'-$MoTe_2$ after a 4-hour dwell. It is only after 8 hours that the Raman spectrum is dominated by peaks belonging to 1T'-$MoTe_2$. Mo powder, however, converted to 2H-$MoTe_2$ irrespective of reaction time and without any intermediate products (Figure 3-34b).

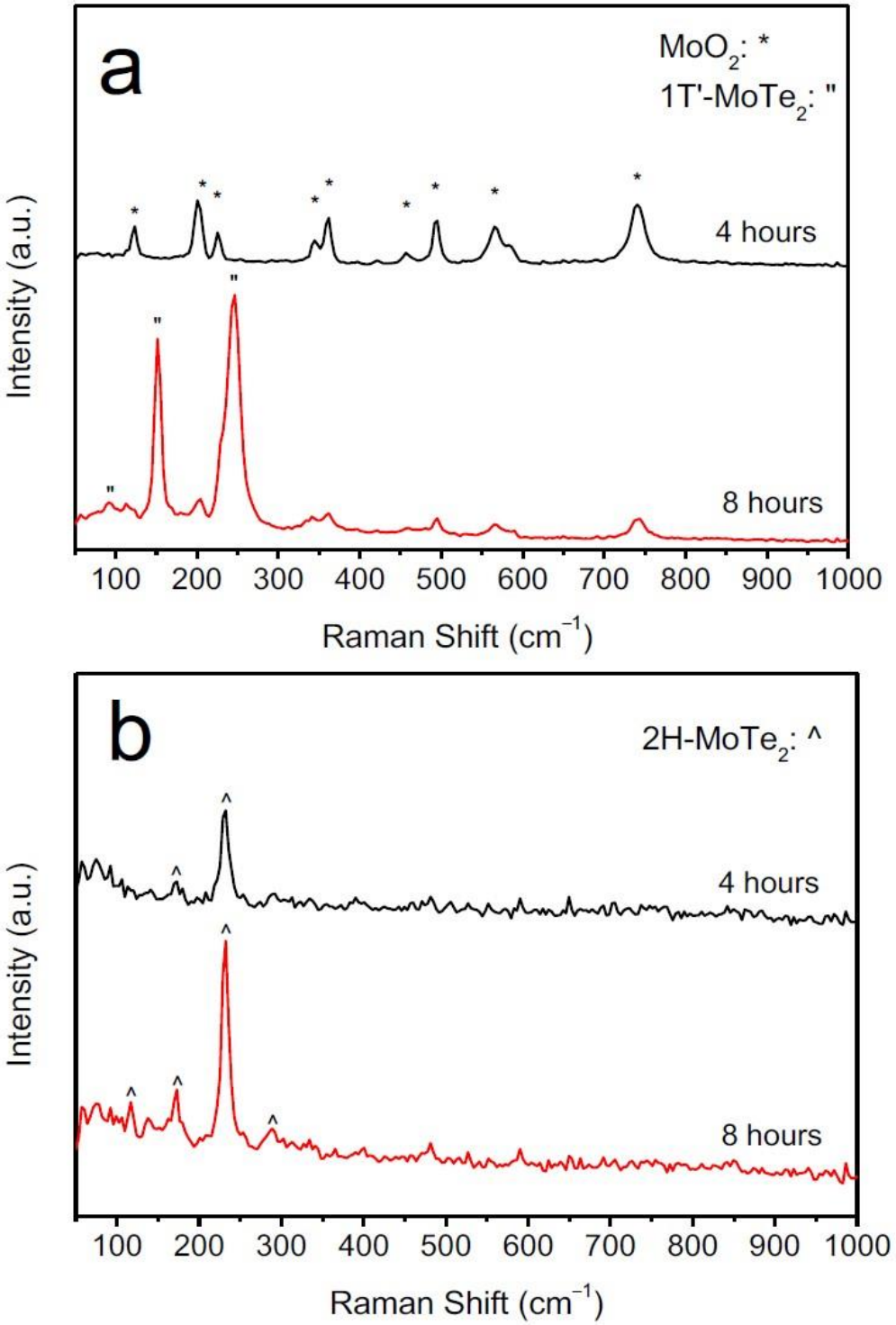

Figure 3-34: Raman spectra of MoO3 powder (a) and Mo powder (b) tellurised in the CVD setup at 650 °C using FeTe2 for varying durations.

The use of $FeTe_2$ as a precursor as opposed to elemental Te means that the Te vapour pressure throughout the CVD process is much lower. This is due to the higher evaporation temperature of Te from $FeTe_2$ compared to elemental Te. Research by Yoo *et al* illustrated that 1T'-$MoTe_2$ is kinetically stable at the substrate when the Te vapour pressure is low, which is the case for $FeTe_2$.[11] This coupled with the observations from Xu *et al* that during their CVD process 1T'-$MoTe_2$ forms initially before conversion to 2H-$MoTe_2$ with increased

reaction time may give the reasons for the phase selectivity in the CVD system employed in this work.[51] The low vapour pressure of Te in the system coupled with the initial reduction of MoO_3 to MoO_2 before conversion to 1T'-$MoTe_2$ means there is not sufficient Te vapour to convert this kinetically stable phase to 2H-$MoTe_2$. However, the Mo precursor does not go through any oxide intermediate so there is sufficient Te vapour pressure in this case to convert the film fully to 2H-$MoTe_2$. If this hypothesis is accurate then in theory it should be possible to find the optimal Te vapour pressure from elemental Te to achieve the same outcome as using $FeTe_2$. However, there are no literature examples of any group being able to achieve this.

3.4. Conclusions

In conclusion, a CVD method has been developed that allows for the phase selective deposition of 2H- or 1T'-$MoTe_2$ thin films using a novel $FeTe_2$ precursor. The phase selectivity arises from the choice of molybdenum precursor, with Mo converting to 2H-$MoTe_2$ and MoO_3 converting to 1T'-$MoTe_2$. This meant that the simultaneous deposition of both phases on the same substrate in one CVD reaction was possible. The method gives spatial control of where the phases are located and allows for control over the number of layers, meaning the properties of the $MoTe_2$ films can be tuned. Furthermore, the $MoTe_2$ films were characterised extensively *via* Raman spectroscopy, atomic force microscopy, X-ray photoelectron spectroscopy and transmission electron microscopy, ensuring their quality and consistency of the method developed. Finally, three methods for determining the thickness of the product $MoTe_2$ films were trialled and evaluated. It was found that optical microscopy and Raman spectroscopy were complimentary methods to AFM for rapidly determining the thickness of the $MoTe_2$ films.

3.5. References

1. Lin, Y.-F., Yong, X., Wang, S-T., Li, S-L., Yamamoto, M., Aparecido-Ferrerira, A., Li, W., Sun, H. Nakaharai, S., Jian, W-B., Ueno, K. & Tsukagoshi, K. Ambipolar $MoTe_2$ Transistors and Their Applications in Logic Circuits. *Adv. Mater.* **26**, 3263–3269 (2014).

2. Pradhan, N. R., Rhodes, D., Feng, S., Xin, Y., Memaran, S., Moon, B-H., Terrones, H. Terrones, M., & Balicas, L. Field-Effect Transistors Based on Few-Layered α-$MoTe_2$. *ACS Nano* **8**, 5911–5920 (2014).

3. Manzeli, S., Ovchinnikov, D., Pasquier, D., Yazyev, O. V & Kis, A. 2D transition metal dichalcogenides. *Nat. Rev. Mater.* **2**, 17033 (2017).

4. Zhou, J. Lin, J., Huang, X., Zhou, Y., Chen, Y., Xia, J., Wang, H., Xie, Y., Yu, H., Lei, J., Wu, D., Liu, F., Fu, Q., Zeng, Q., Hsu, C-H., Yang, C., Lu, L., Yu, T., Shen, Z., Lin, H., Yakobson, B. I., Liu, Q., Suenaga, K., Liu, G., & Liu, Z. A library of atomically thin metal chalcogenides. *Nature* **556**, 355–359 (2018).

5. Zhang, Y., Yao, Y., Sendeku, M. G., Yin, L., Zhan, X., Wang, F., Wang, Z., & He, J. Recent Progress in CVD Growth of 2D Transition Metal Dichalcogenides and Related Heterostructures. *Adv. Mater.* **31**, 1901694 (2019).

6. Park, J. C. Yun, S. J., Kim, H., Park, J-H., Chae, S. H., An, S.-J., Kim, J.-G., Kim, S. M., Kim, K. K. & Lee, Y. H. Phase-Engineered Synthesis of Centimeter-Scale 1T′- and 2H-Molybdenum Ditelluride Thin Films. *ACS Nano* **9**, 6548–6554 (2015).

7. Zhou, L., Xu, K., Zubair, A., Liao, A. D., Fang, W., Ouyang, F., Lee, Y-H., Ueno, K., Saito, R., Palacios, T., Kong, J. & Dresselhaus, M. S. Large-Area Synthesis of High-Quality Uniform Few-Layer $MoTe_2$. *J. Am. Chem. Soc.* **137**, 11892–11895 (2015).

8. Yun, S. J., Han, G. H., Kim, H., Duong, D. L., Shin, B. G., Zhao, J., Vu, Q. A., Lee, J., Lee, S. M. & Lee, Y. H. Telluriding monolayer MoS_2 and WS_2 via alkali metal scooter. *Nat. Commun.* **8**, 2163 (2017).

9. Zhou, L., Zubair, A., Wang, Z., Zhang, X., Ouyang, F., Xu, K., Fang, W., Ueno, K., Li, J., Palacious, T., Kong, J. & Dresselhaus, M. S. Synthesis of High-Quality Large-Area Homogenous 1T′ $MoTe_2$ from Chemical Vapor Deposition. *Adv. Mater.* **28**, 9526–9531 (2016).

10. Cheng, S., Yang, L., Li, J., Liu, Z., Zhang, W. & Chang, H. Large area, phase-

controlled growth of few-layer, two-dimensional $MoTe_2$ and lateral 1T′-2H heterostructures by chemical vapor deposition. *CrystEngComm.* **19**, 1045-1051 (2017).

11. Yoo, Y., DeGregorio, Z. P., Su, Y., Koester, S. J. & Johns, J. E. In-Plane 2H-1T′ $MoTe_2$ Homojunctions Synthesized by Flux-Controlled Phase Engineering. *Adv. Mater.* **29**, 1605461 (2017).

12. Zhou, J., Liu, F., Lin, J., Huang, X., Xia, J., Zhang, B., Zeng, Q., Wang, H., Zhu, C., Niu, L., Wang, X., Fu, W., Yu, P., Chang, T.-R., Hsu, C-H., Wu, D., Jeng, H-T., Huang, Y., Lin, H., Shen, S., Yang, C., Suenaga, K., Zhou, W., Pantelides, S. T., Liu, G. & Liu, Z. Large-Area and High-Quality 2D Transition Metal Telluride. *Adv. Mater.* **29**, 1603471 (2017).

13. Empante, T. A., Zhou, Y., Klee, V., Nguyen, A. E., Lu, I.-H., Valentin, M. D., Naghibi Alvillar, S. A., Preciado, E., Berges, A. J., Merida, C. S., Gomez, M., Bobek, S., Isarraraz, M., Reed, E. J. & Bartels, L. Chemical Vapor Deposition Growth of Few-Layer $MoTe_2$ in the 2H, 1T′, and 1T Phases: Tunable Properties of $MoTe_2$ Films. *ACS Nano* **11**, 900–905 (2017).

14. Xu, X. Li, X., Liu, K., Li, J., Feng, Q., Zhou, L., Cui, F., Liang, X., Lei, Z., Liu, Z. & Xu, H. Thermodynamics and Kinetics Synergetic Phase-Engineering of Chemical Vapor Deposition Grown Single Crystal $MoTe_2$ Nanosheets. *Cryst. Growth Des.* **18**, 2844–2850 (2018).

15. Zhu, X., Li, A., Wu, D., Zhu, P., Xiang, H., Liu, S., Sun, J., Ouyang, F., Zhou, Y. & Xiong, X. Tunable large-area phase reversion in chemical vapor deposited few-layer $MoTe_2$ films. *J. Mater. Chem. C* **7**, 10598–10604 (2019).

16. Sun, L., Ding, M., Li, J., Yang, L., Lou, X., Xie, Z., Zhang, W. & Chang, H. Phase-controlled large-area growth of $MoTe_2$ and $MoTe_{2-x}O_x/MoTe_2$ heterostructures for tunable memristive behavior. *Appl. Surf. Sci.* **496**, 143687 (2019).

17. Ma, R., Zhang, H., Yoo, Y., Degregorio, Z. P., Jin, L., Golani, P., Azadani, J. G., Low, T., Johns, J. E., Bendersky, L. A., Davydov, A. V. & Koester, S. J. $MoTe_2$ Lateral Homojunction Field-Effect Transistors Fabricated using Flux-Controlled Phase Engineering. *ACS Nano* **13**, 8035–8046 (2019).

18. Zhang, X., Jin, Z., Wang, L., Hatchtel, J. A., Vilarreal, E., Wang, Z., Ha, T., Nakanishi, Y., Tiwary, C. S., Lai, J., Dong, L., Tang, J., Vajtai, R., Ringe, E., Idrobo,

J. C., Yakobson, B. I., Lou, J., Gambin, V., Koltun, R. & Ajayan, P. M. Low Contact Barrier in 2H/1T′ $MoTe_2$ In-Plane Heterostructure Synthesized by Chemical Vapor Deposition. *ACS Appl. Mater. Interfaces* **11**, 12777–12785 (2019).

19. Yanhe, L. I., Yimin, W., Hebin, S. & Guoliang, Y. U. E. Extreme Enrichment of Tellurium in Deep-Sea Sediments. *Acta Geol. Sin. - English Ed.* **79**, 547–551 (2010).

20. CDC-NIOSH Pocket Guide to Chemical Hazards-Tellurium. https://www.cdc.gov/niosh/npg/npgd0587.html.

21. Ni, Z. H., Wang, H. M., Kasim, J., Fan, H. M., Yu, T., Wu, Y. H., Feng, Y. P. & Shen, Z. X. Graphene Thickness Determination Using Reflection and Contrast Spectroscopy. *Nano Lett.* **7**, 2758–2763 (2007).

22. Li, H., Wu, J., Huang, X., Lu, G., Yang, J., Lu, X., Xiong, Q. & Zhang, Hua. Rapid and Reliable Thickness Identification of Two-Dimensional Nanosheets Using Optical Microscopy. *ACS Nano* **7**, 10344–10353 (2013).

23. Cho, S., Kim, S., Kim, J. H., Zhao, J., Seok, J., Keum, D. H., Baik, J., Choe, D-H., Chang, K. J., Suenaga, K., Kim, S. W., Lee, Y. H. & Yang, H. Phase patterning for ohmic homojunction contact in $MoTe_2$. *Science* **349**, 625-628 (2015).

24. Huang, J.-K., Pu, J., Hsu, C.-L., Chiu, M.-H., Juang, Z.-Y., Chang, Y.-H., Chang, W.-H., Iwasa, Y., Takenobu, T. & Li, L.-J. Large-Area Synthesis of Highly Crystalline WSe_2 Monolayers and Device Applications. *ACS Nano* **8**, 923–930 (2014).

25. Wang, X., Gong, Y., Shi, G., Chow, W. L., Keyshar, K., Ye, G., Vajtai, R., Lou, J., Zheng, L., Ringe, E., Tay, B. K. & Ajayan, P. M. Chemical Vapor Deposition Growth of Crystalline Monolayer $MoSe_2$. *ACS Nano* **8**, 5125–5131 (2014).

26. Kappera, R., Voiry, D., Yalcin, S. E., Branch, B., Gupta, G., Mohite, A. D. & Chhowalla. M. Phase-engineered low-resistance contacts for ultrathin MoS_2 transistors. *Nat. Mater.* **13**, 1128–1134 (2014).

27. Song, S., Keum, D. H., Cho, S., Perello, D., Kim, Y., Lee, Y. H. Room Temperature Semiconductor–Metal Transition of $MoTe_2$ Thin Films Engineered by Strain. *Nano Lett.* **16**, 188–193 (2016).

28. Wang, Y., Xiao, J., Zhu, H., Li, Y., Alsaid, Y., Fong, K. Y., Zhou, Y., Wang, S., Shi, W., Wang, Y., Zettl, A., Reed, E. J. & Zhang, X. Structural phase transition in monolayer $MoTe_2$ driven by electrostatic doping. *Nature* **550**, 487–491 (2017).

29. Yamamoto, M., Wang, S. T., Ni, M., Lin, Y.-F., Li, S.-L., Aikawa, S., Jian, W.- B., Ueno, K., Wakabayashi, K. & Tsukagoshi, K. Strong Enhancement of Raman Scattering from a Bulk-Inactive Vibrational Mode in Few-Layer $MoTe_2$. *ACS Nano* **8**, 3895–3903 (2014).

30. Parker, J. H., Feldman, D. W. & Ashkin, M. Raman Scattering by Silicon and Germanium. *Phys. Rev.* **155**, 712–714 (1967).

31. Zhou, L., Huang, S., Tatsumi, Y., Wu, L., Guo, H., Bie, Y.-Q., Ueno, K., Yang, T., Zhu, Y., Kong, J., Saito, R. & Dresselhaus, M. S. Sensitive Phonon-Based Probe for Structure Identification of 1T′ $MoTe_2$. *J. Am. Chem. Soc.* **139**, 8396–8399 (2017).

32. Zhang, X., Jin, Z., Wang, L., Hatchtel, J. A., Vilarreal, E., Wang, Z., Ha, T., Nakanishi, Y., Tiwary, C. S., Lai, J., Dong, L., Tang, J., Vajtai, R., Ringe, E., Idrobo, J. C., Yakobson, B. I., Lou, J., Gambin, V., Koltun, R. & Ajayan, P. M. Low Contact Barrier in 2H/1T′ $MoTe_2$ In-Plane Heterostructure Synthesized by Chemical Vapor Deposition. *ACS Appl. Mater. Interfaces* **11**, 12777–12785 (2019).

33. Guo, H., Yang, T., Yamamoto, M., Zhou, L., Ishikawa, R., Ueno, K., Tsukagoshi, K., Zhang, Z., Dresselhaus, M. S. & Saito, R. Double resonance Raman modes in monolayer and few-layer $MoTe_2$. *Phys. Rev. B - Condens. Matter Mater. Phys.* **91**, 205415 (2015).

34. Jin, Y. & Shen, P. K. Nanoflower-like metallic conductive MoO_2 as a high-performance non-precious metal electrocatalyst for the hydrogen evolution reaction. *J. Mater. Chem. A* **3**, 20080–20085 (2015).

35. Wang, T., Li, J. & Zhao, G. Synthesis of MoS_2 and MoO_3 hierarchical nanostructures using a single-source molecular precursor. *Powder Technol.* **253**, 347–351 (2014).

36. Ruppert, C., Aslan, O. B. & Heinz, T. F. Optical Properties and Band Gap of Single- and Few-Layer $MoTe_2$ Crystals. *Nano Lett.* **14**, 6231–6236 (2014).

37. Huang, J.-H., Deng, K.-Y., Liu, P.-S., Wu, C.-T., Chou, C.-T., Chang, W.- H., Lee, Y.-J. & Hou, T-.H. Large-Area 2D Layered $MoTe_2$ by Physical Vapor Deposition and Solid-Phase Crystallization in a Tellurium-Free Atmosphere. *Adv. Mater. Interfaces* **4**, 1700157 (2017).

38. Calizo, I., Bao, W., Miao, F., Lau, C. N. & Balandin, A. A. The Effect of Substrates on the Raman Spectrum of Graphene: Graphene- on-Sapphire and Graphene-on-Glass. *Appl. Phys. Lett.* **91**, 201904 (2007).

39. Van der Heide, P. *X-ray photoelectron spectroscopy : an introduction to principles and practices*. (Wiley-Blackwell, 2012).

40. Fleisch, T. H. & Mains, G. J. An XPS study of the UV reduction and photochromism of MoO_3 and WO_3. *J. Chem. Phys.* **76**, 780–786 (1982).

41. Plyuto, Y. V., Babich, I. V., Plyuto, I. V., Van Langeveld, A. D. & Moulijn, J. A. XPS studies of MoO_3/Al_2O_3 and MoO_3/SiO_2 systems. *Appl. Surf. Sci.* **119**, 11–18 (1997).

42. Naylor, C. H., Parkin, W. M., Ping, J., Gao, Z., Zhou, Y. R., Kim, Y., Streller, F., Carpick, R. W., Rappe, A. M., Drndic, M., Kikkawa, J. M. & Charlie Johnson, A. T. Monolayer Single-Crystal 1T′-$MoTe_2$ Grown by Chemical Vapor Deposition Exhibits Weak Antilocalization Effect. *Nano Lett.* **16**, 4297–4304 (2016).

43. Wagner, C. D. *Handbook of x-ray photoelectron spectroscopy: a reference book of standard data for use in x-ray photoelectron spectroscopy, Physical Electronics Division, Perkin-Elmer Corp.* (Physical Electronics Division Perkin-Elmer Corp., 1979).

44. Zhou, J., Liu, F., Lin, J., Huang, X., Xia, J., Zhang, B., Zeng, Q., Wang, H., Zhu, C., Niu, L., Wang, X., Fu, W., Yu, P., Chang, T.-R., Hsu, C-H., Wu, D., Jeng, H-T., Huang, Y., Lin, H., Shen, S., Yang, C., Suenaga, K., Zhou, W., Pantelides, S. T., Liu, G. & Liu, Z. Large-Area and High-Quality 2D Transition Metal Telluride. *Adv. Mater.* **29**, 1603471 (2017).

45. Cumpson, P. J. The Thickogram: A Method for Easy Film Thickness Measurement in XPS. *Surf. Interface Anal.* **29**, 403–406 (2000).

46. Eaton, P. & West, P. *Atomic Force Microscopy*. (Oxford University Press, 2010).

47. Zhou, L., Xu, K., Zubair, A., Zhang, X., Ouyang, F., Palacios, T., Dresselhaus, M. S., Li, Y. & Kong, J. Role of Molecular Sieves in the CVD Synthesis of Large-Area 2D $MoTe_2$. *Adv. Funct. Mater.* **27**, 1603491 (2017).

48. Cui, J., Li, P., Zhou, J., He, W.-Y., Huang, X., Yi, J., Fan, J., Ji, Z., Jing, X., Qu, F., Cheng, Z. G., Yang, C., Lu, L., Suenaga, K., Liu, J., Law, K. T., Lin, J., Liu, Z. & Liu, G. Transport evidence of asymmetric spin–orbit coupling in few-layer superconducting 1T d -$MoTe_2$. *Nat. Commun.* **10**, 2044 (2019).

49. McGlynn, J. C., Dankwort, T., Kienle, L., Bandeira, N. A. G., Fraser, J. P., Gibson, E. K., Cascallana-Matías, I., Kamarás, K., Symes, M. D., Miras, H. N. & Ganin, A.

Y. The rapid electrochemical activation of $MoTe_2$ for the hydrogen evolution reaction. *Nat. Commun.* **10**, 4916 (2019).

50. Hsu, C., Frisenda, R., Schmidt, R., Arora, A., de Vasconcellos, S. M., Bratschitsch, R., van der Zant, H. S. J. & Castellanos-Gomez, A. Thickness-Dependent Refractive Index of 1L, 2L, and 3L MoS_2 , $MoSe_2$, WS_2 , and WSe_2. *Adv. Opt. Mater.* **7**, 1900239 (2019).

51. Xu, X., Chen, S., Liu, S., Cheng, X., Wanjin, X., Li, P., Wan, Y., Yang, S., Gong, W., Yuan, K., Gao, P., Ye, Y. & Dai, L. Millimeter-Scale Single-Crystalline Semiconducting $MoTe_2$ via Solid-to-Solid Phase Transformation. *J. Am. Chem. Soc.* **141**, 2128–2134 (2019).

52. Song, X., Wang, Y., Zhao, F., Li, Q., Ta, H. Q., Rummeli, M. H., Tully, C. G., Li, Z., Y, W.-J., Yang, L., Lee, K.-B., Yang, J., Bozkurt, I., Liu, S., Zhang, W. & Chhowalla. M. Plasmon-Free Surface-Enhanced Raman Spectroscopy Using Metallic 2D Materials. *ACS Nano* **13**, 8312–8319 (2019).

53. Tao, L., Chen, K., Chen, Z., Cong, C., Qiu, C., Chen, J., Wang, X., Chen, H., Yu, T., Xie, W., Deng, S. & Xu, J.-B. 1T′ Transition Metal Telluride Atomic Layers for Plasmon-Free SERS at Femtomolar Levels. *J. Am. Chem. Soc.* **140**, 8696–8704 (2018).

54. Lv, Q., Wu, X., Tan, J., Liu, B., Gan, L., Li, J., Huang, Z.-H. Kang, F. & Lv R. Ultrasensitive molecular sensing of few-layer niobium diselenide. *J. Mater. Chem. A* **9**, 2725–2733 (2021).

4. Chemical Vapour Deposition of 2H- and 1T'-$MoTe_2$ Thin Films in a Flow CVD Setup

4.1. Introduction

In the previous chapter the phase selective chemical vapour deposition of 1T'- and 2H-$MoTe_2$ using a novel $FeTe_2$ precursor was explored. Phase selectivity was achieved through varying the type of molybdenum precursor layer used. This is in keeping with several literature reports that made similar observations. However, the studies conducted by Zhou *et al.* found that MoO_3 converted to 2H-$MoTe_2$, whilst Mo converted to 1T'-$MoTe_2$, differing from the results obtained in this work.[1,2] In the previous chapter a closed ampoule was utilised as the reaction chamber to ensure a significant vapour pressure of Te from $FeTe_2$ could be obtained, due to the lower vapour pressure of Te over $FeTe_2$ compared to the commonly used elemental Te precursor. To discover whether it was the type of reactor used or the different precursor that was responsible for this discrepancy, it was decided to test $FeTe_2$ in a more conventional "flow CVD" setup. This allows for a more valid comparison between $FeTe_2$ and literature examples using Te as the precursor, as the types of setups used are more similar. Another parameter that is often varied in literature procedures to achieve phase selectivity is the dwell time, with increasing dwell time favouring the formation of 2H-$MoTe_2$.[3,4] Due to the higher evaporation temperature of $FeTe_2$ compared to Te, it should allow for the use of extended dwell times without being depleted. This may offer a route to overcoming the phase selectivity enforced by the choice of molybdenum precursor and should therefore be explored using $FeTe_2$.

4.2. Aims

The aims of this chapter are to apply the previously used $FeTe_2$ precursor for the CVD of $MoTe_2$ in a conventional "flow" CVD setup. The impact that varying CVD parameters have on the reaction outcome will be investigated by varying reaction time and type of molybdenum source. The results will be monitored using Raman spectroscopy. Finally, the commonly used elemental tellurium precursor will be tested and the results obtained will be compared to those obtained when using $FeTe_2$.

4.3. Results and Discussion

4.3.1. CVD Using Molybdenum Films Whilst Varying Reaction Time

For this series of experiments the $FeTe_2$ powder precursor was replaced by $FeTe_2$ pellets for ease of handling. This required an increase to the quantity used to 300 mg so that a pellet could be formed. Initially, reaction duration was chosen as the variable parameter and for the preliminary test reaction all parameters were kept identical to the optimised closed CVD parameters. A 1 nm $Mo/SiO_2/Si$ substrate was placed into a quartz tube and the $FeTe_2$ pellet positioned 5 cm upstream. This tube was then placed into the work tube of a Lenton tube furnace so that the substrate resided in the hot zone of the furnace. The dwell temperature of the substrate was set at 650 °C, whilst the temperature of the $FeTe_2$ pellet was maintained at 630 °C for a dwell of 4 hours. Once again, slow heating and cooling rates of 5 °C min^{-1} were utilised, and the carrier gas and flow rate were identical to those used in Chapter 3 (Figure 4-1).

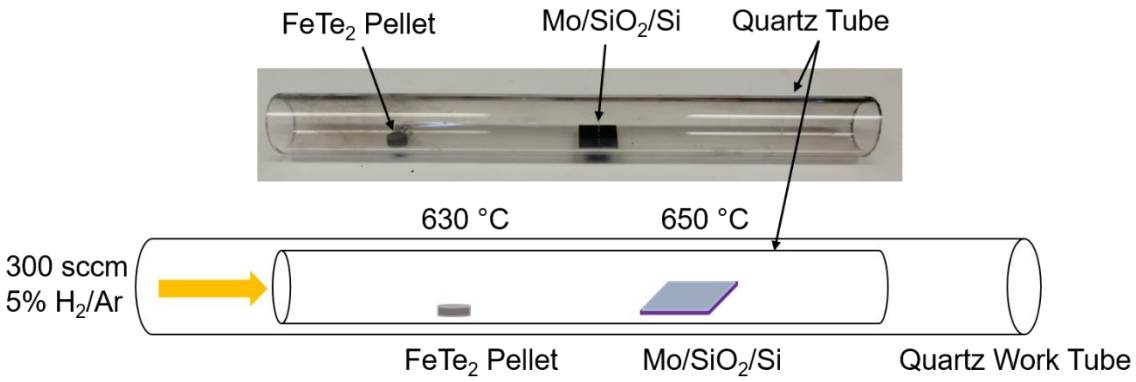

Figure 4-1: Photograph and schematic illustrating the flow CVD reactor setup for Mo films reacted with $FeTe_2$ at 650 °C.

The Raman spectra from the initial reaction are shown in Figure 4-2.

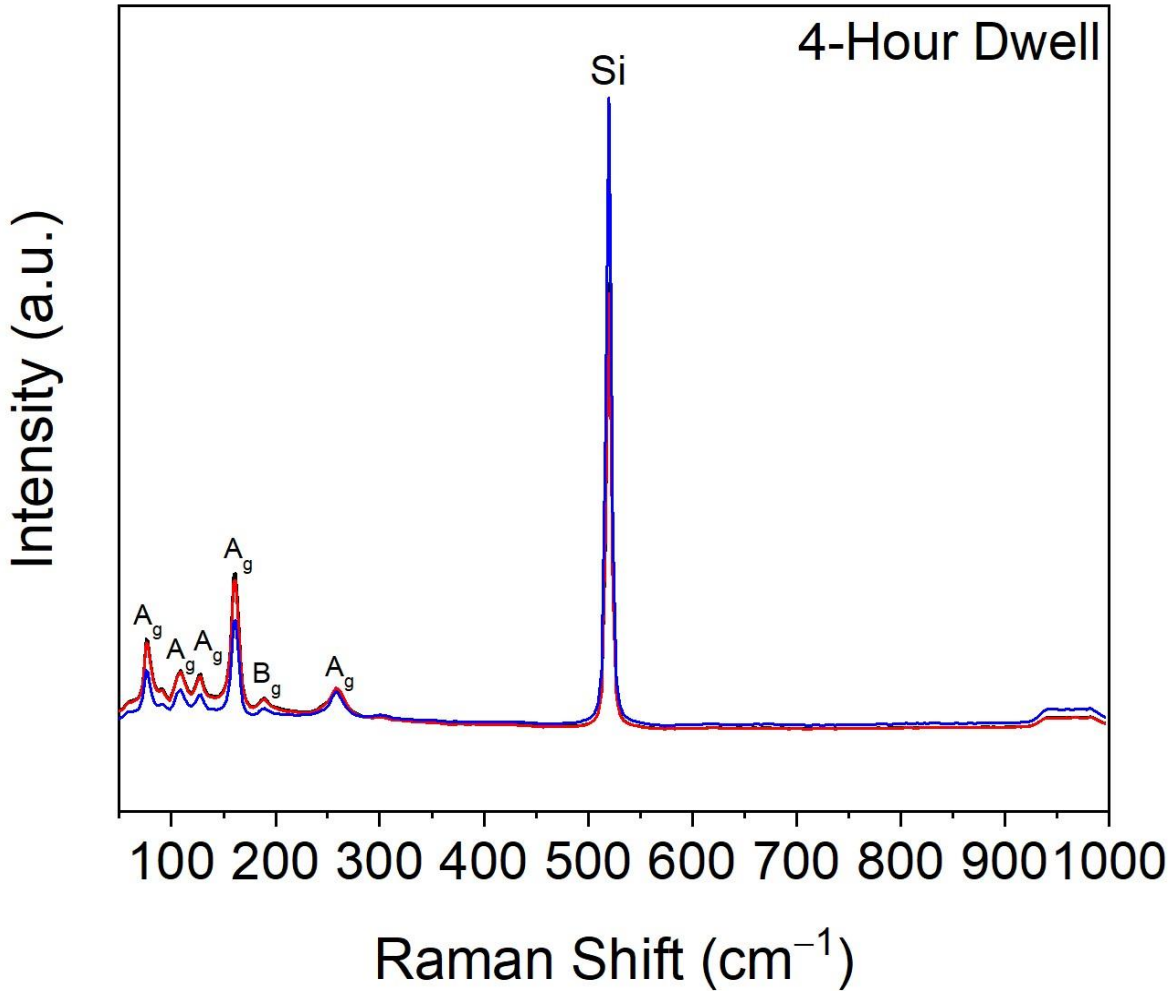

Figure 4-2: 532 nm Raman spectra obtained from a 1T'-$MoTe_2$ film converted from a 1 nm Mo/SiO_2/Si film with $FeTe_2$ at 650 °C with a 4-hour dwell.

From the three Raman spectra recorded across the product film it is clear that the aforementioned conditions resulted in the formation of 1T'-$MoTe_2$, with characteristic peaks present between 50 and 300 cm^{-1}. A_g modes are present at ~76, ~108, ~126, ~161 and ~257 cm^{-1} whilst there is one B_g mode present at ~187 cm^{-1}.[5] As was the case with 1T' films produced in the closed CVD setup there is also no presence of MoO_2 or MoO_3 impurities in the spectra obtained from the film converted in the flow setup.[6,7] In order to see if dwell time has any impact on the phase of $MoTe_2$ obtained, it was decided to increase it to 8 hours with all other parameters remaining the same. The Raman spectra from this film are displayed in Figure 4-3.

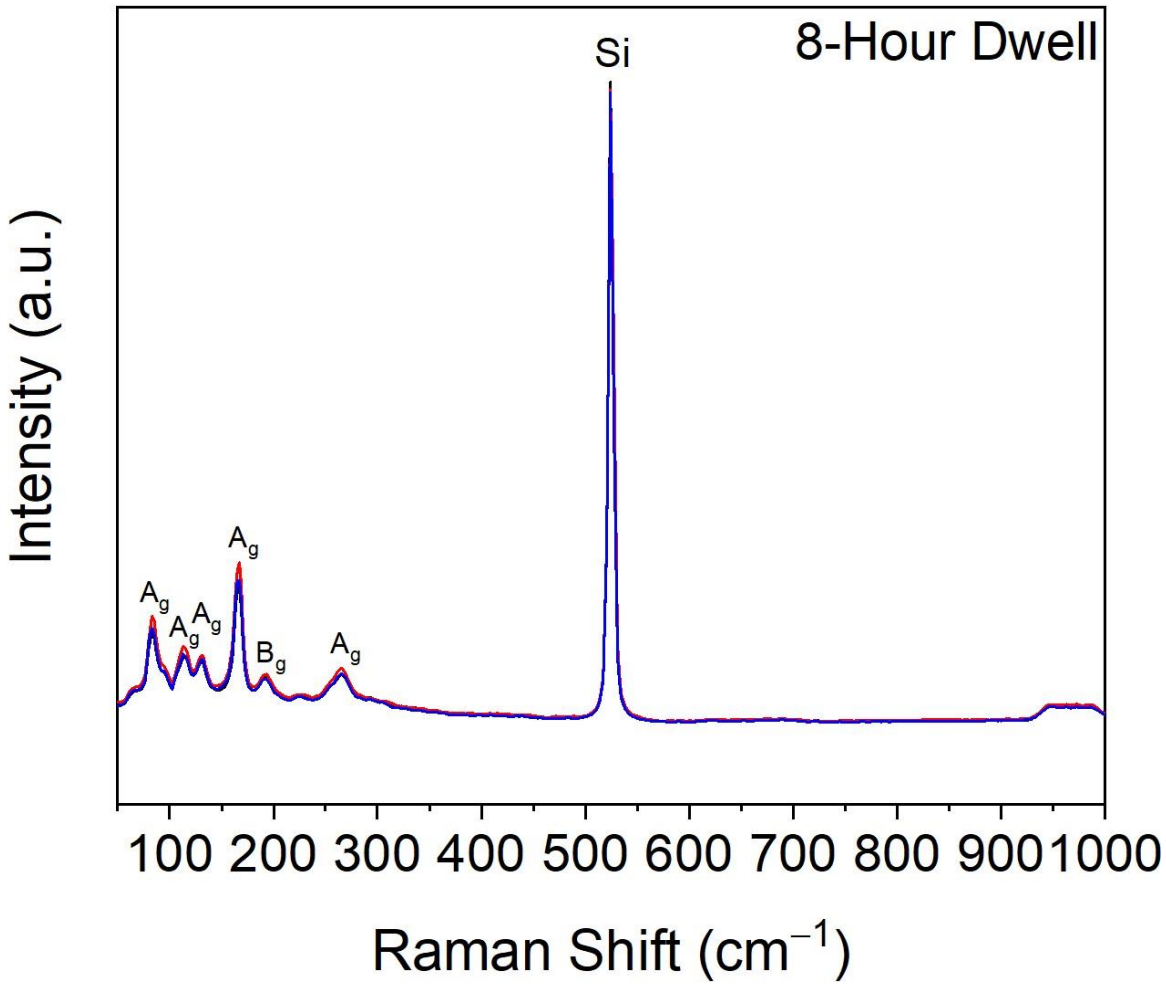

Figure 4-3: 532 nm Raman spectra obtained from a 1T'-$MoTe_2$ film converted from a 1 nm Mo/SiO_2/Si film with $FeTe_2$ at 650 °C with an 8-hour dwell.

Interestingly, an 8-hour dwell also resulted in the formation of 1T'-$MoTe_2$, with the same characteristic peaks present as the previous deposition. Increasing the duration of the deposition of $MoTe_2$ has been shown to favour the formation of 2H-$MoTe_2$ in literature work, so this result is quite surprising.[3,4] One possible explanation is that the vapour pressure of Te from $FeTe_2$ in this flow setup is too low to convert the 1T' phase into 2H-$MoTe_2$ even with extended dwell times. To further test this an extreme dwell time of 16 hours was then trialled and Raman spectra recorded from the resultant film (Figure 4-4).

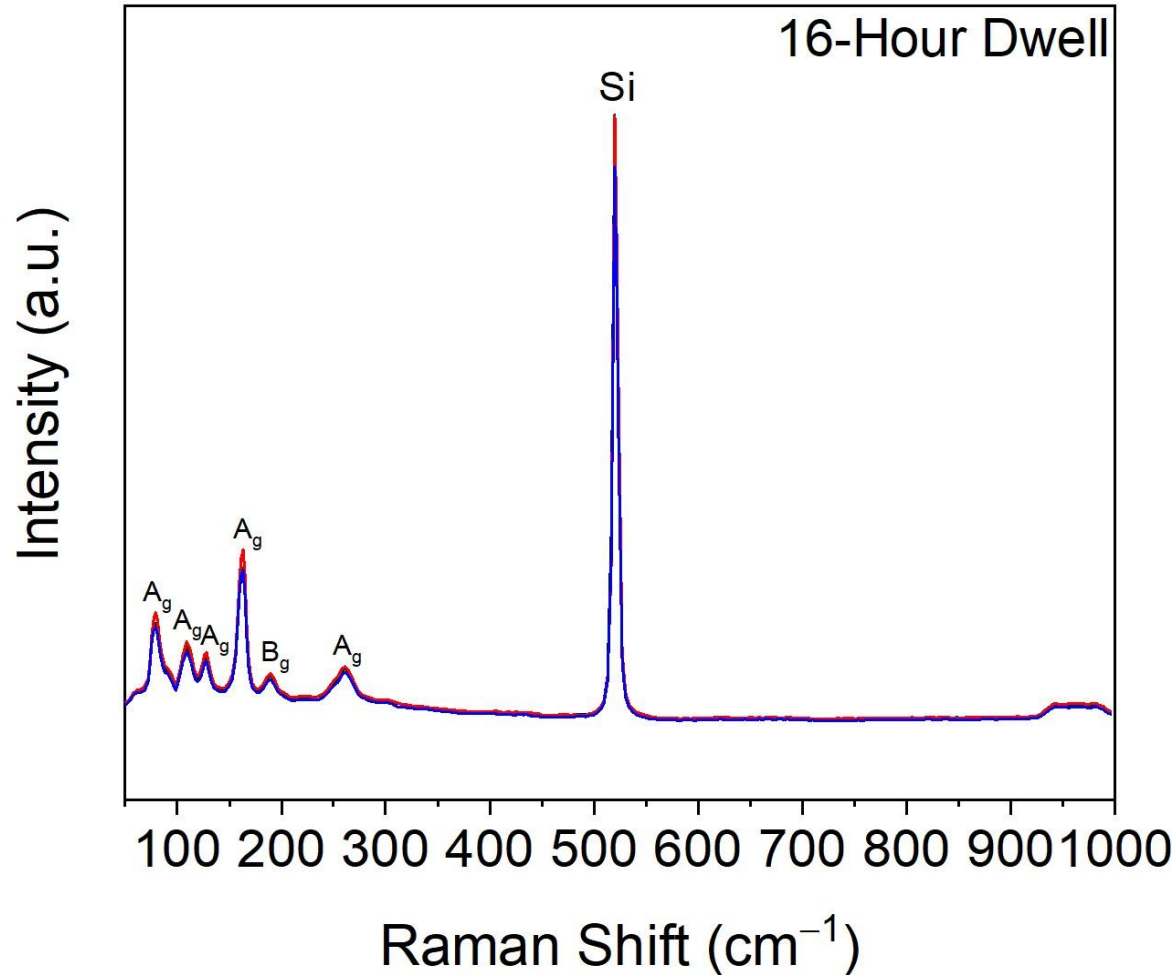

Figure 4-4: 532 nm Raman spectra obtained from a 1T'-$MoTe_2$ film converted from a 1 nm Mo/SiO_2/Si film with $FeTe_2$ at 650 °C with a 16-hour dwell.

Once again the product film is phase pure 1T'-$MoTe_2$ with no presence of any molybdenum oxides in the wide-ranging spectra. There is also no indication that a phase change has started to occur which is remarkable considering the dwell time of 16 hours, almost four times as long as the longest dwell used in the literature procedures in Tables 3-1 and 3-2. It would seem that the low vapour pressure of Te from $FeTe_2$ combined with the experimental setup is responsible for the stability of the 1T'-$MoTe_2$ film under extremely long dwell times. Finally, the other extreme of dwell duration was investigated for these reaction conditions with a particularly short dwell time of 1 minute tested. Figure 4-5 shows the Raman spectra recorded from the resulting film converted under these conditions.

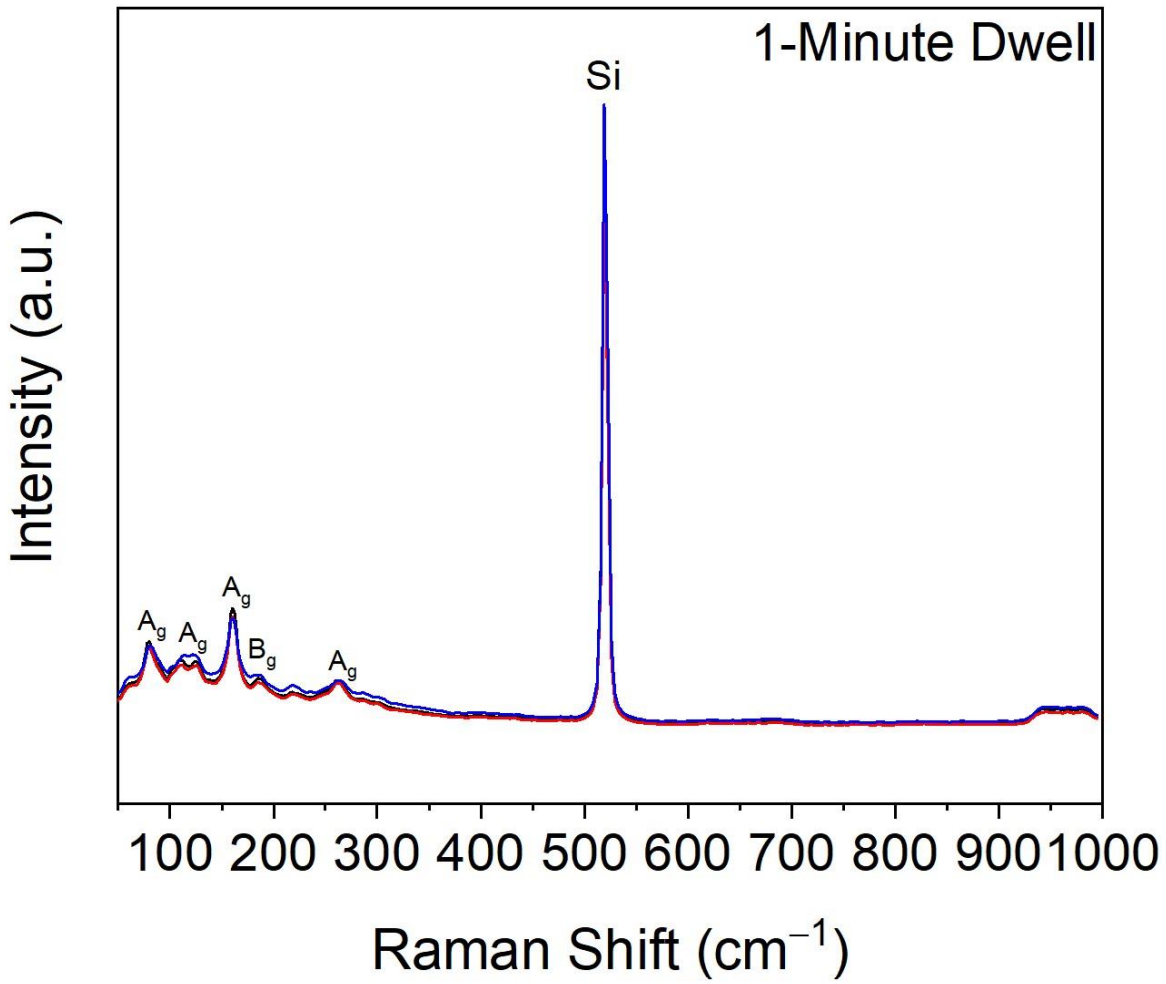

Figure 4-5: 532 nm Raman spectra obtained from a 1T'-$MoTe_2$ film converted from a 1 nm Mo/SiO_2/Si film with $FeTe_2$ at 650 °C with a 1-minute dwell.

The 1-minute dwell time still resulted in the formation of 1T'-$MoTe_2$, but the Raman peaks appear less intense than those in the other experiments conducted. This would suggest that the Mo precursor layer had not been fully converted to $MoTe_2$ which is understandable considering the shortness of the dwell time used. To try and quantify which dwell duration produced the best results the peak area of the most intense Raman mode of 1T'-$MoTe_2$ (A_g, 161 cm^{-1}) was divided by the normalised peak area of silicon for each film. The higher the resulting A_g/Si ratio, the higher the quality of the film, and this ratio can also be used to monitor the consistency of the films. A plot of this ratio against dwell time is shown in Figure 4-6.

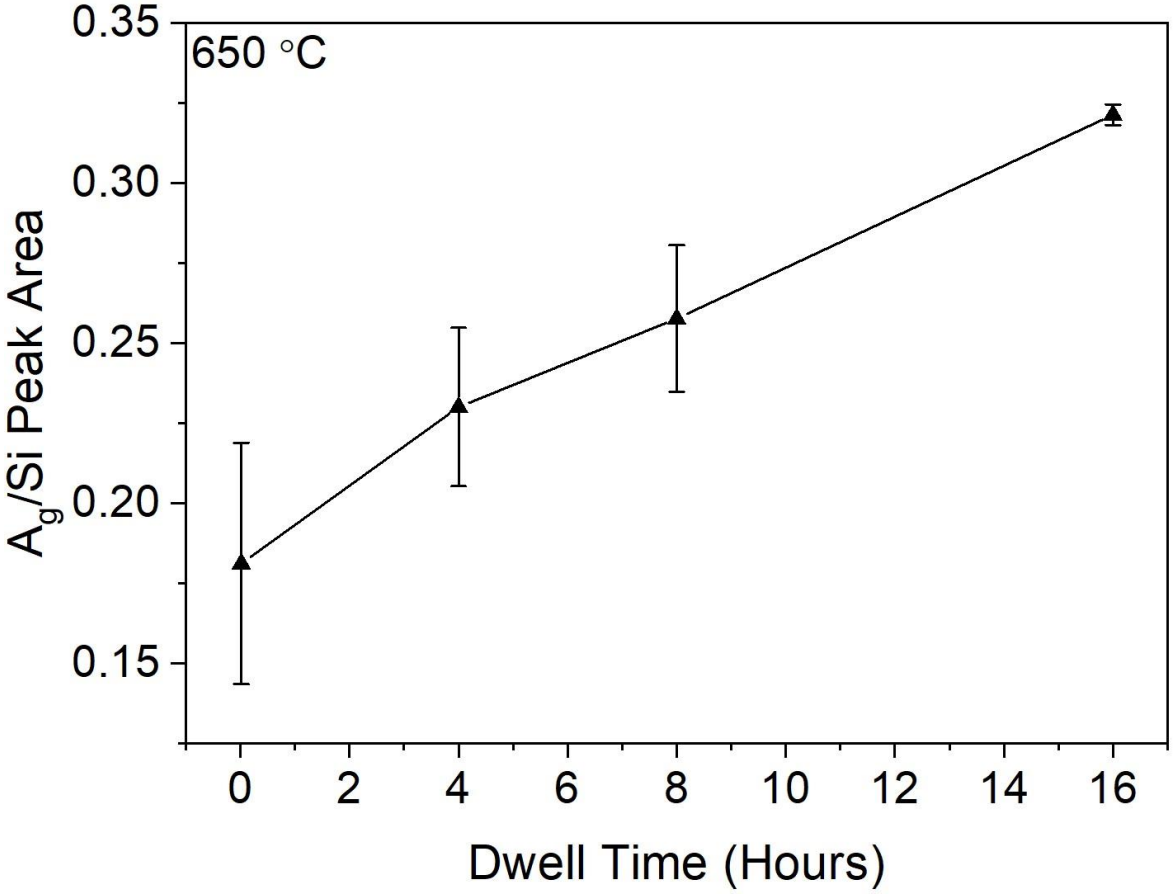

Figure 4-6: Plot of the A_g (161 cm^{-1}) peak area divided by the Si peak area against the dwell time of the CVD reactions for Mo films reacted at 650 °C with $FeTe_2$.

From this plot it is immediately clear that a dwell duration of 16 hours produces the highest quality film, with it generating the highest A_g/Si peak area ratio as well as the most consistent values across the film. This plot also confirms that although a dwell time of 1 minute does produce 1T'-$MoTe_2$, it is a very inhomogeneous film. The $FeTe_2$ pellets were weighed before and after each deposition to record how much mass was lost in the form of evaporated tellurium. Figure 4-7 shows a plot of the mass lost from the $FeTe_2$ pellets against the dwell time of the depositions. From this plot it is clear that Te vapour is constantly generated throughout the course of the depositions as the mass of Te lost increases with increasing dwell time and does not level off even after 16 hours.

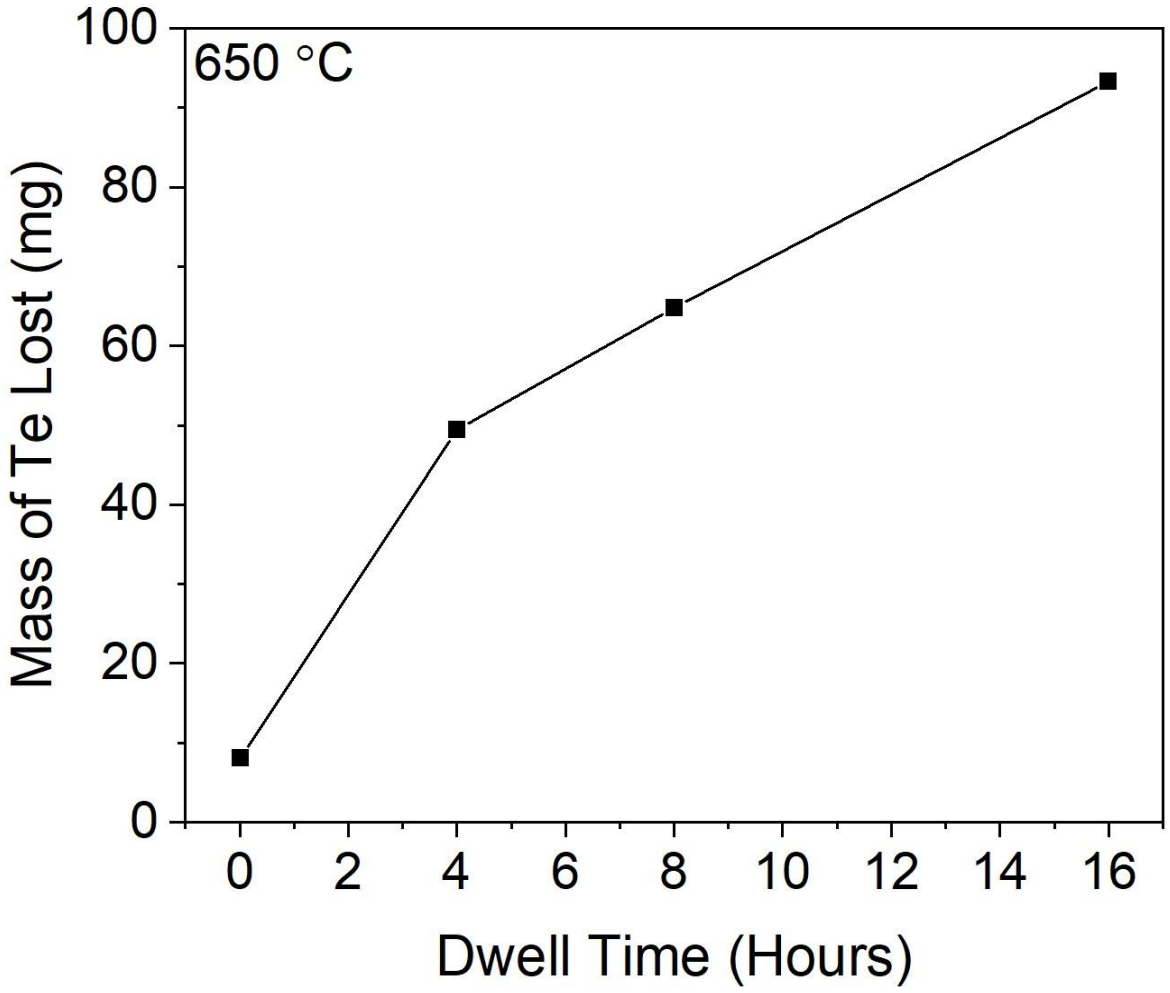

Figure 4-7: Plot of the mass lost from the $FeTe_2$ precursor pellets against the dwell time of the CVD reactions for Mo films reacted at 650 °C.

Overall, the results obtained in this section were slightly surprising in that the Mo precursor films converted to 1T'-$MoTe_2$, as in the closed CVD setup they converted to 2H-$MoTe_2$. However, this is in line with the observations made by Zhou *et al* where Mo preferentially converted to 1T'-$MoTe_2$. This was attributed to the large unit cell expansion upon transitioning from Mo to 1T'-$MoTe_2$ inducing strain and stabilising the 1T' phase.[1] The fact that 1T'-$MoTe_2$ was still formed after a 16 hour dwell suggests that $FeTe_2$ cannot produce sufficient Te vapour in this setup to induce a phase transition to 2H-$MoTe_2$.

4.3.2. CVD Using Molybdenum Trioxide Films Whilst Varying Reaction Time

In order to see what impact changing the molybdenum precursor to molybdenum trioxide films would have the previous experiments were repeated using 3 nm $MoO_3/SiO_2/Si$ substrates under the same conditions (Figure 4-8).

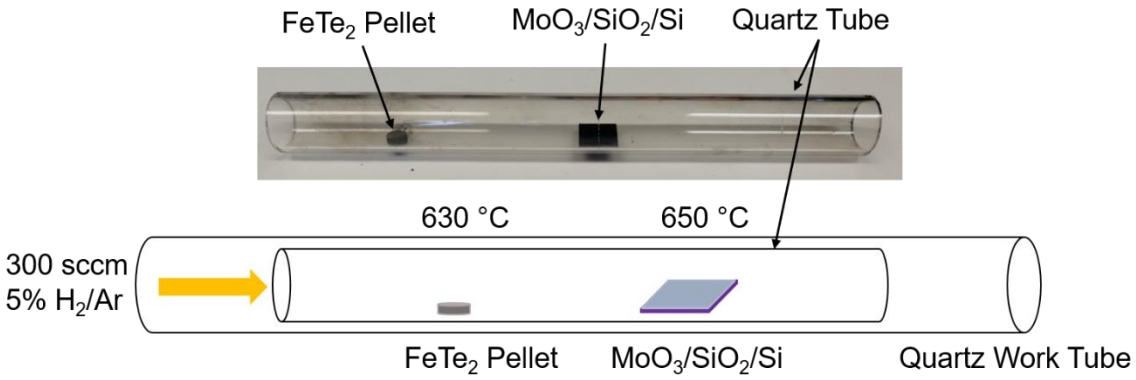

Figure 4-8: Photograph and schematic illustrating the flow CVD reactor setup for MoO_3 films reacted with $FeTe_2$ at 650 °C.

An initial reaction was conducted with a dwell time of 1 minute and the Raman spectra recorded from the product film are shown in Figure 4-9.

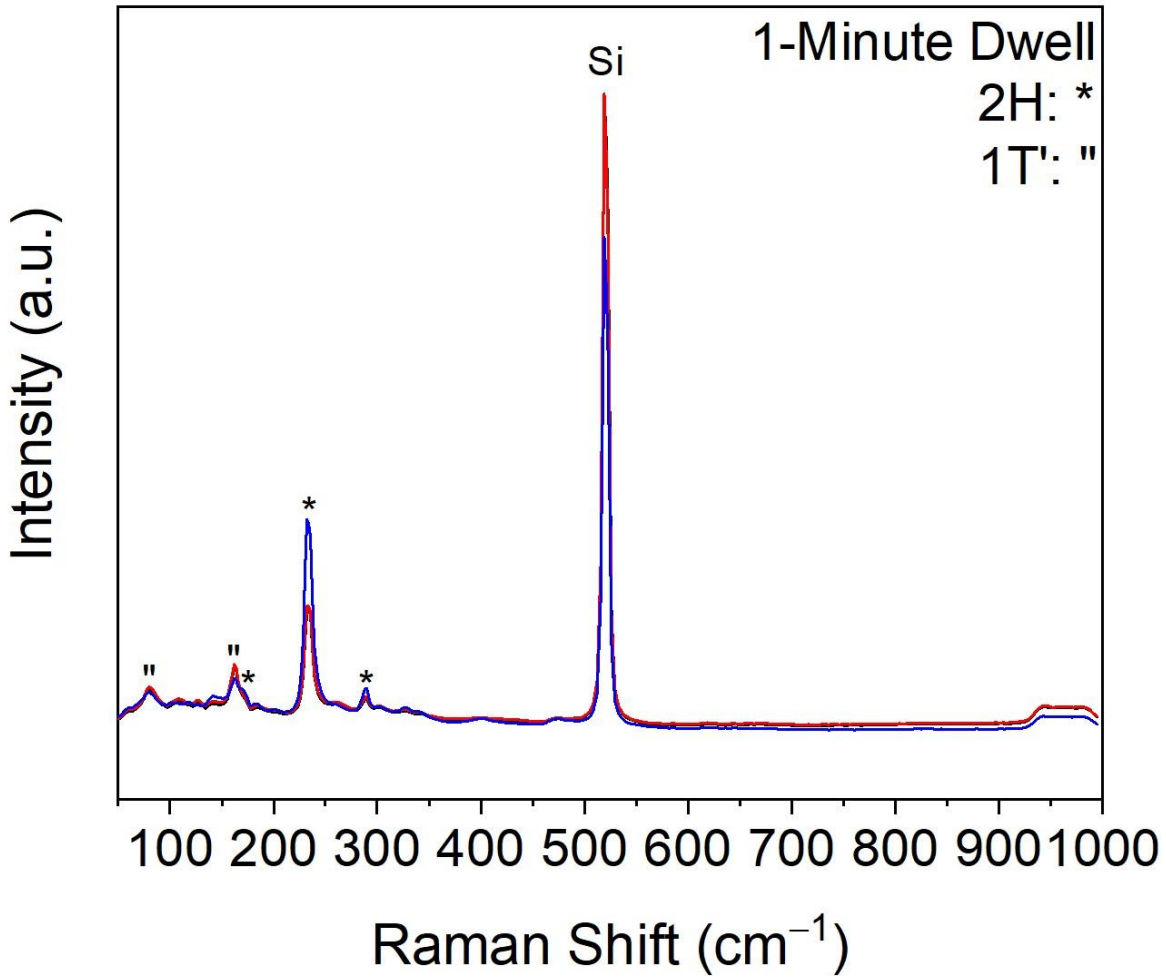

*Figure 4-9: 532 nm Raman spectra obtained from a $MoTe_2$ film converted from a 3 nm $MoO_3/SiO_2/Si$ film with $FeTe_2$ at 650 °C with a 1-minute dwell. Peaks belonging to 2H-$MoTe_2$ are marked with * whilst those belonging to 1T'-$MoTe_2$ are marked with ".*

From these spectra it is clear that the product film is mixed phase. Peaks associated with 1T'-$MoTe_2$ are present at ~80 and ~161 cm^{-1}, whilst those indicative of 2H-$MoTe_2$ are present at ~171, ~234 and ~289 cm^{-1} respectively. This result suggests that the dwell time was not sufficient enough to convert the initially formed 1T' phase fully to 2H-$MoTe_2$ and therefore, longer dwell times should produce 2H-$MoTe_2$ with less of the 1T' impurity or completely phase pure 2H-$MoTe_2$. So, a dwell time of 4 hours was then trialled, and the resulting Raman spectra are presented in Figure 4-10.

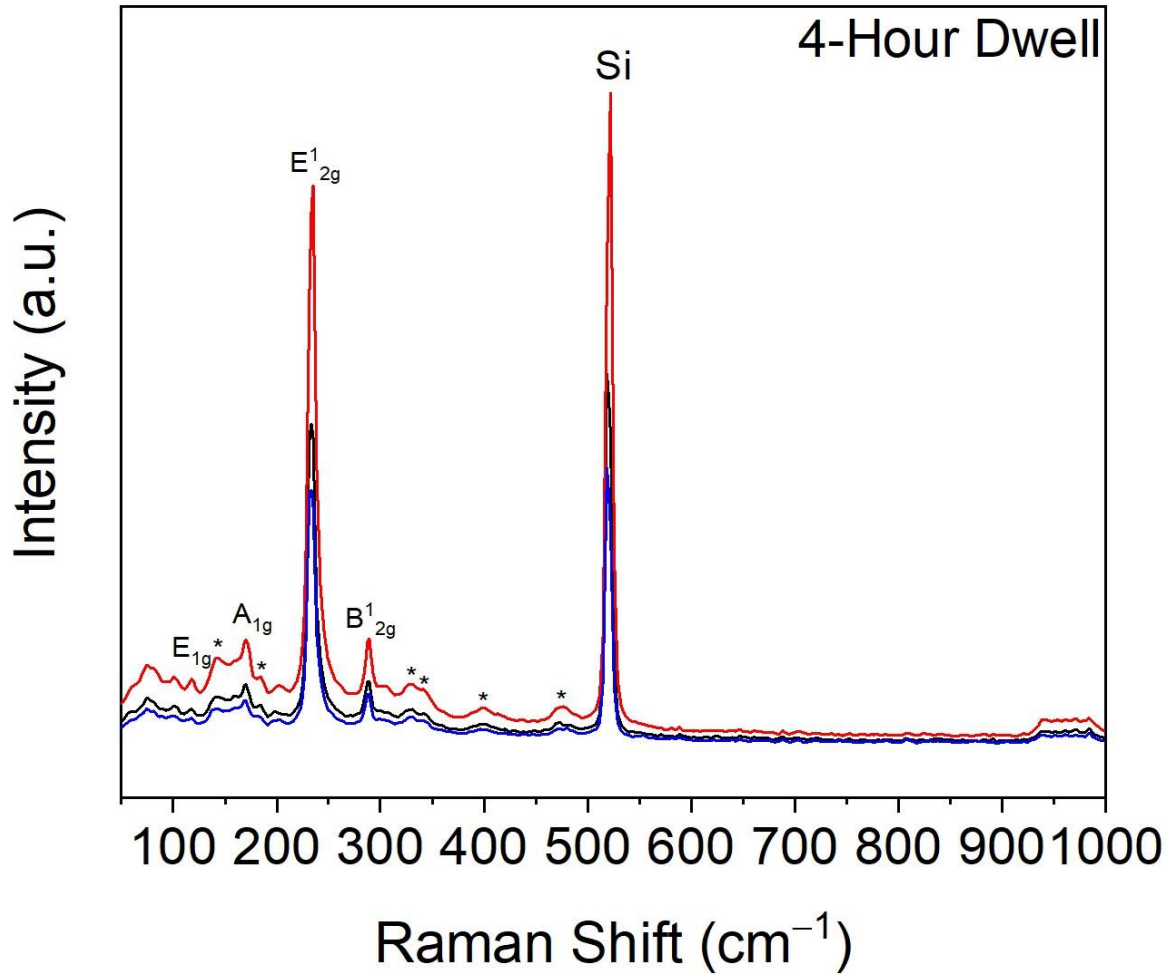

Figure 4-10: 532 nm Raman spectra obtained from a 2H-$MoTe_2$ film converted from a 3 nm MoO_3/SiO_2/Si film with $FeTe_2$ at 650 °C with a 4-hour dwell.

In this case the resultant film appears to be phase pure 2H-$MoTe_2$, with E_{1g}, A_{1g} and E^1_{2g} modes appearing at ~119 cm^{-1}, ~171 cm^{-1} and ~234 cm^{-1}, respectively. In addition to these modes there are also weak peaks that are known second order resonant peaks at 138, 185, 326, 342, 400 and 470 cm^{-1} (marked with *).[8,9] Furthermore, the few-layer nature of this film is confirmed by the presence of the B^1_{2g} mode at 289 cm^{-1}, which is to be expected as a 3 nm MoO_3/SiO_2/Si precursor film produced a 7-layered $MoTe_2$ film in the closed CVD setup used in Chapter 3.

Two further reactions were conducted utilising extended 8- and 16-hour dwell periods, the Raman spectra obtained from the product films are shown in Figures 4-11 and 4-12. Both films are also phase pure 2H-$MoTe_2$, with the same modes and second order resonant peaks present as the film produced from a 4-hour dwell. These results are again different from those obtained using the closed CVD setup, where MoO_3 preferentially converted to 1T'-$MoTe_2$. However, they are consistent with the observations of Zhou *et al* where MoO_3 precursor films would convert to 2H-$MoTe_2$, which they credit to the small unit cell volume

expansion upon transitioning from MoO_3 to $MoTe_2$ favouring the 2H phase, which is stable in the absence of strain, unlike 1T'-$MoTe_2$.[1]

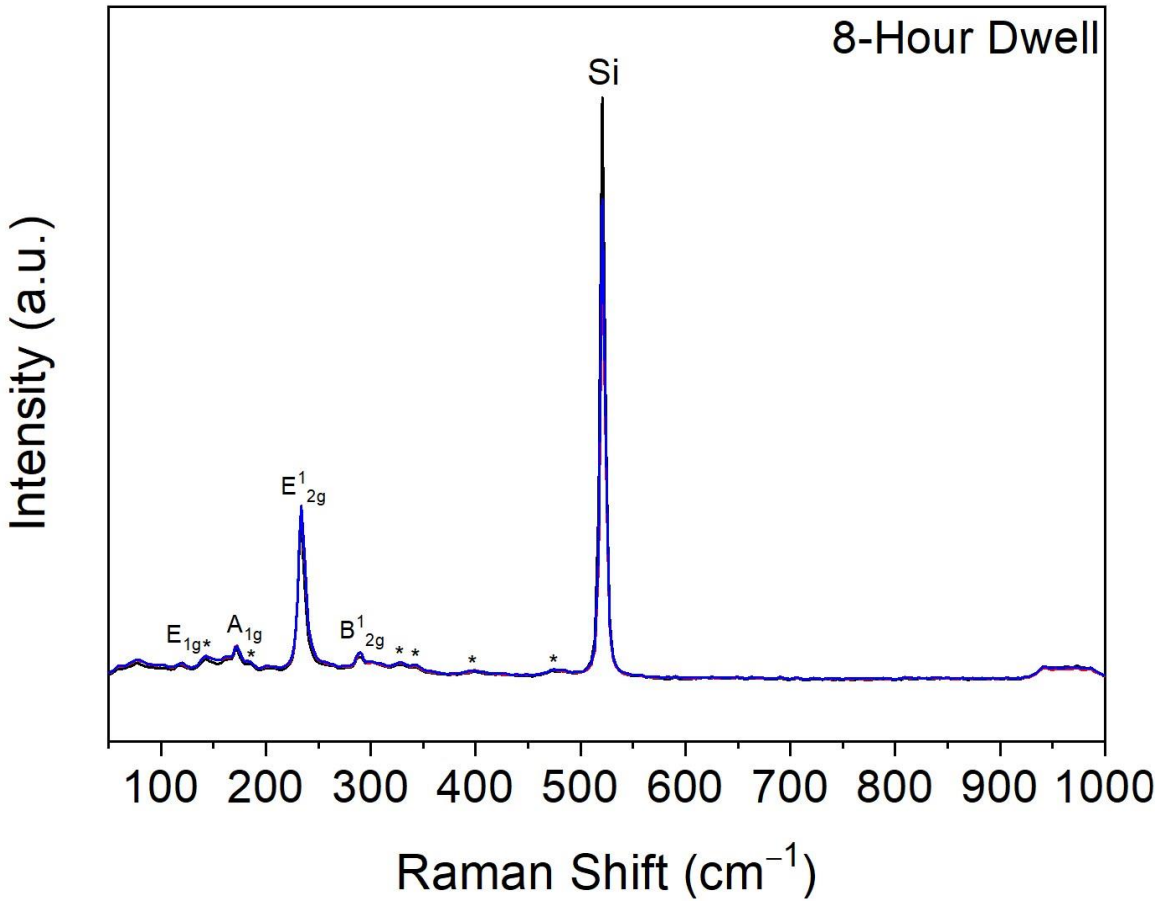

Figure 4-11: 532 nm Raman spectra obtained from a 2H-$MoTe_2$ film converted from a 3 nm $MoO_3/SiO_2/Si$ film with $FeTe_2$ at 650 °C with an 8-hour dwell.

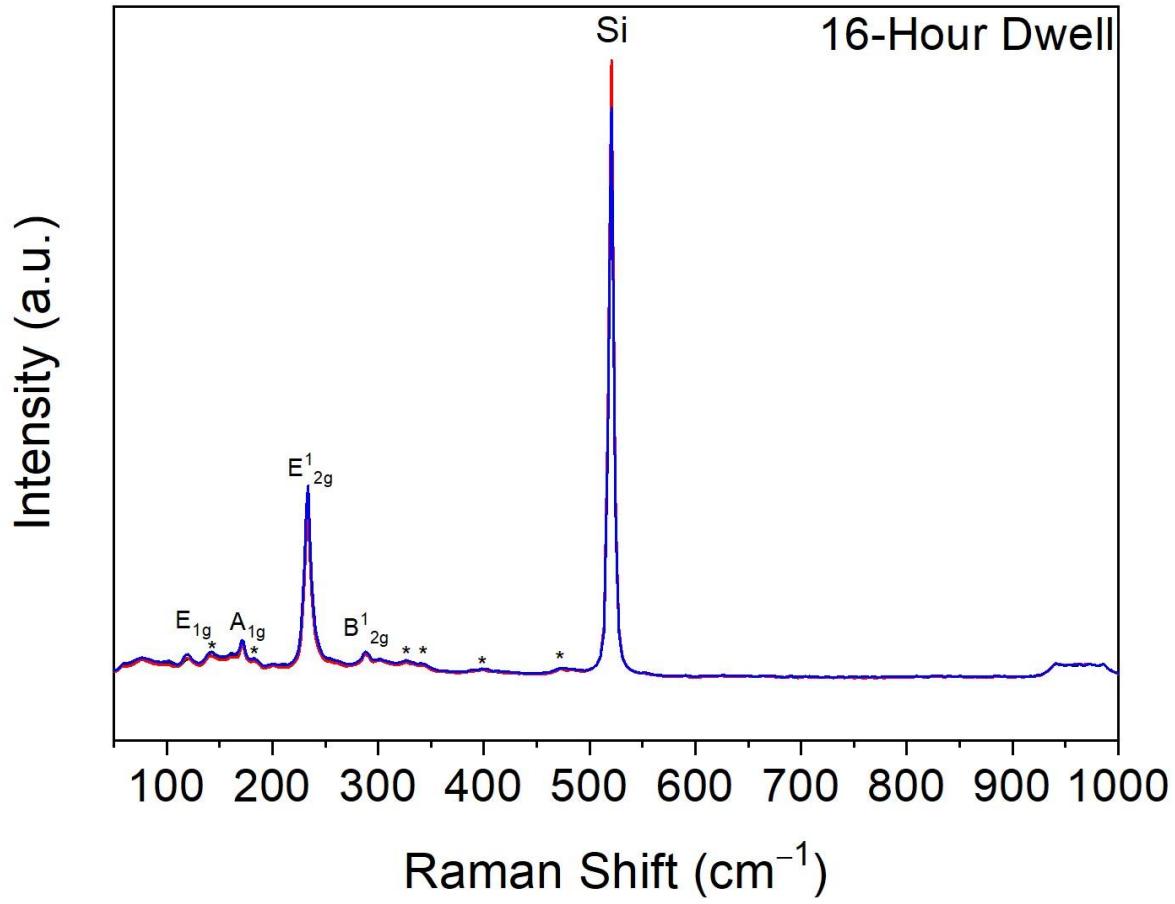

Figure 4-12: 532 nm Raman spectra obtained from a 2H-$MoTe_2$ film converted from a 3 nm MoO_3/SiO_2/Si film with $FeTe_2$ at 650 °C with a 16-hour dwell.

Although the films produced from 8- and 16-hour dwells display the same Raman modes as the 4-hour dwell film, the intensities are very clearly reduced. This observation is confirmed by plotting the peak area of the most intense mode of 2H-$MoTe_2$ (E^1_{2g}, 234 cm^{-1}) divided by the peak area of the silicon peak against dwell time (Figure 4-13). The plot illustrates that a 4-hour dwell time is optimal for the deposition of 2H-$MoTe_2$ using $FeTe_2$ in the flow CVD setup, with a E^1_{2g}/Si peak area ratio of ~1 that is consistent across the entirety of the film. It is interesting that this ratio drops sharply for dwell times of 8- and 16-hours, as this was not the case for the 1T'-$MoTe_2$ films. Once again, the mass lost from the $FeTe_2$ pellets was recorded for these reactions and plotted against dwell time (Figure 4-14), the mass lost from the pellets used in the deposition of 1T'-$MoTe_2$ are also shown in this plot. The values of mass lost for both sets of reactions are consistent with the exception of the MoO_3 16-hour dwell, where an error in pellet position may have caused less Te vapour than expected. This may explain why the 2H-$MoTe_2$ film produced from the 16-hour dwell has a lower E^1_{2g}/Si ratio than the film produced from an 8-hour dwell. Consequently, from the two series of reactions it is evident that the variation in molybdenum precursor influences the phase of the product $MoTe_2$ film, in line with the observations made by Zhou *et al.*[1]

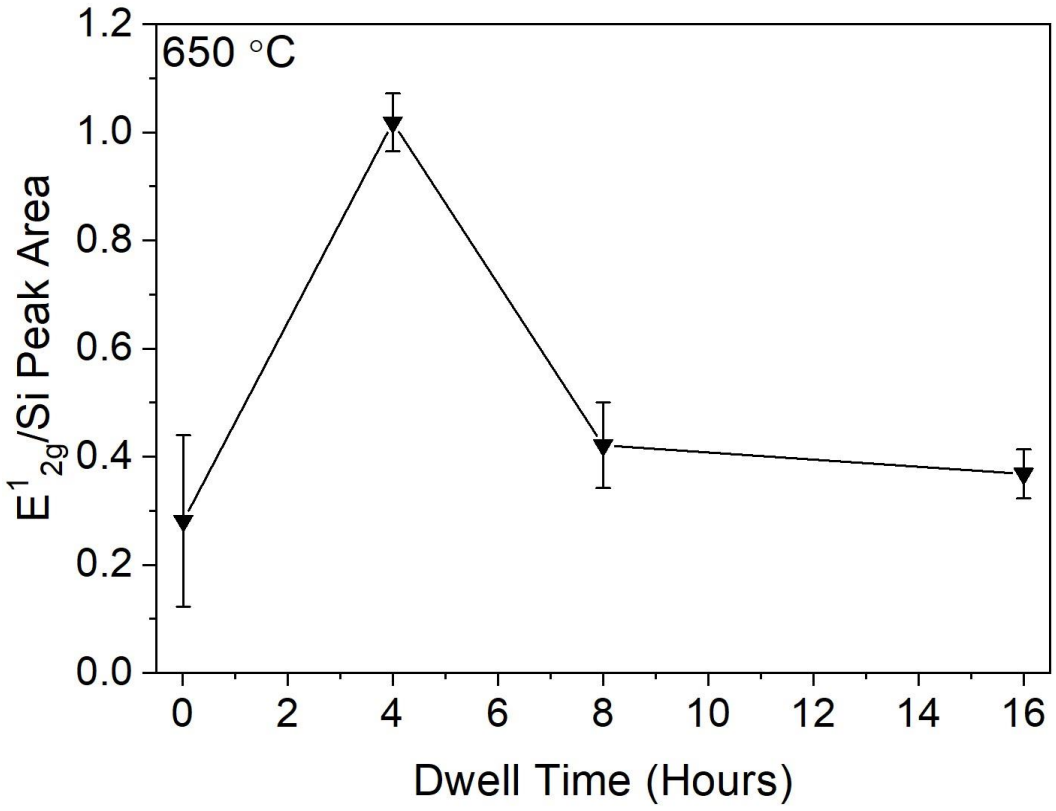

Figure 4-13: Plot of the E^1_{2g} (234 cm^{-1}) peak area divided by the Si peak area against the dwell time of the CVD reactions for MoO_3 films reacted at 650 °C with $FeTe_2$.

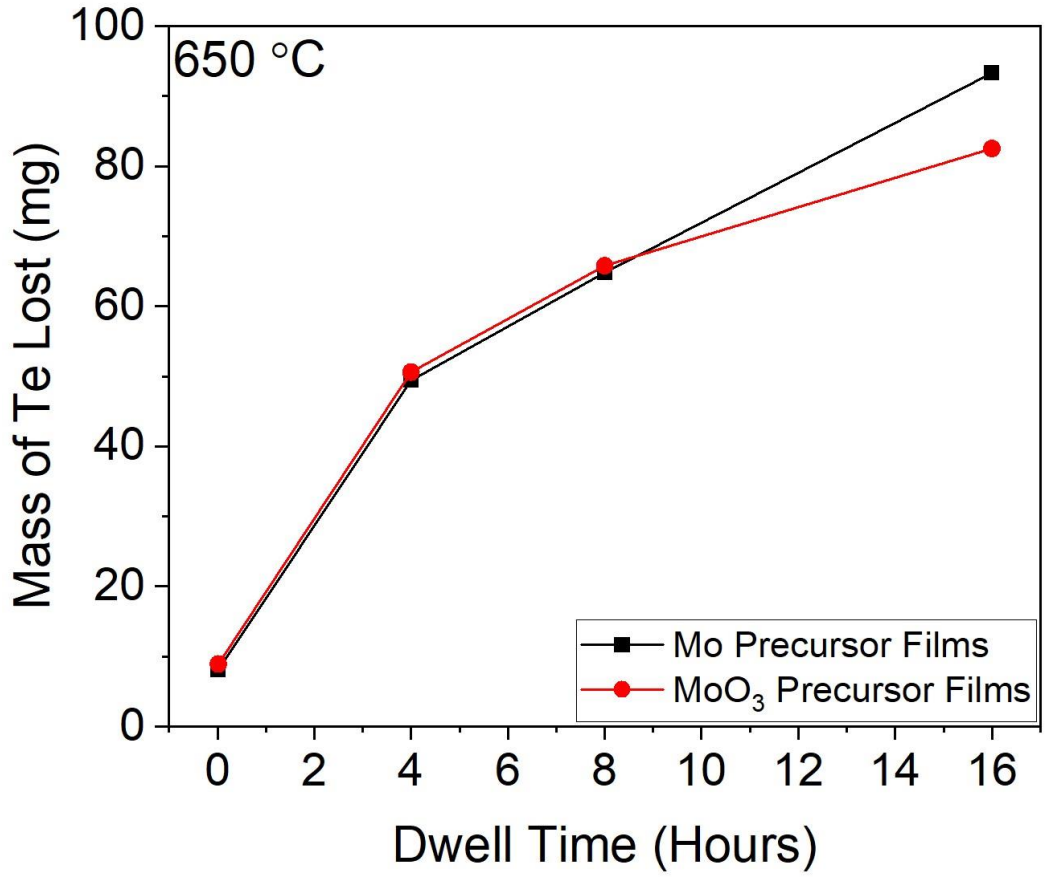

Figure 4-14: Plot of the mass lost from the $FeTe_2$ precursor pellets against the dwell time of the CVD reactions for Mo and MoO_3 films reacted at 650 °C.

4.3.3. CVD Using Elemental Tellurium with Molybdenum Precursor Films

In order to compare $FeTe_2$ to the commonly used elemental Te precursor, experiments were conducted using tellurium pellets. Furthermore, the impact that Te vapour pressure has on the reaction outcome was studied by varying the position of the Te pellet in the furnace. This allows for a comparison to be made between the masses lost from the Te and $FeTe_2$ pellets and the $MoTe_2$ films produced under these conditions. For consistency, an initial experiment was conducted using identical parameters to the first $FeTe_2$ reaction, utilising a dwell time of 4 hours (Figure 4-15).

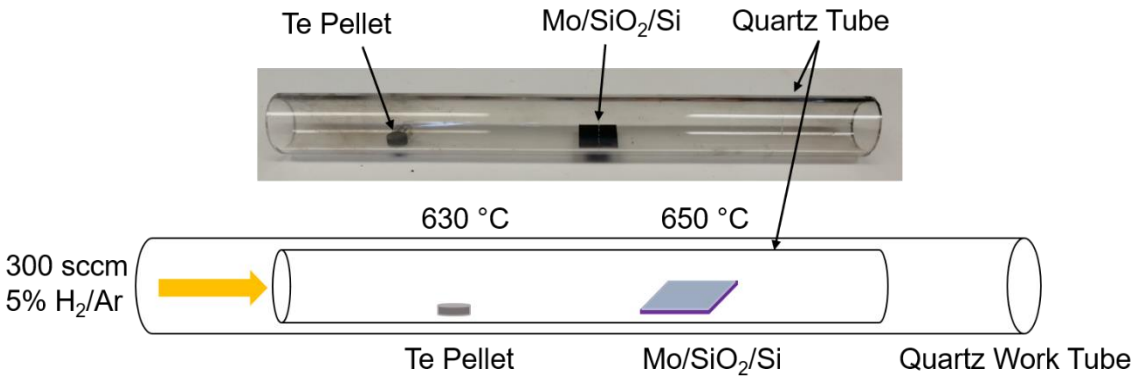

Figure 4-15: Photograph and schematic illustrating the flow CVD reactor setup for Mo films reacted with Te at 650 °C.

Upon retrieval of the film, it was found that the Te pellet had evaporated completely and this coupled with an optical image (Figure 4-16) showing the film to be patchy and discontinuous would imply that the Te supply ran out before the end of the dwell period. The Raman spectra from the film (Figure 4-17) indicates that it is of a mixed phase nature. Peaks associated with 1T'-$MoTe_2$ are present at ~76, ~109, 126, ~161, ~188 and ~257 cm^{-1}, whilst weak peaks that indicate the presence of 2H-$MoTe_2$ can be found at ~171 and ~234 cm^{-1}, respectively. The mixed nature of the film would imply that there was an insufficient amount of Te to fully convert to 2H-$MoTe_2$ and that the dwell time was too long to favour pure 1T'-$MoTe_2$.[3,10,11] Therefore, it was decided to trial a dwell period of 1-hour to see if it was possible to isolate phase pure 1T'-$MoTe_2$ using elemental tellurium as the precursor.

Figure 4-16: An optical image of the $MoTe_2$ film produced from $Mo/SiO_2/Si$ with Te at 650 °C with a 4-hour dwell.

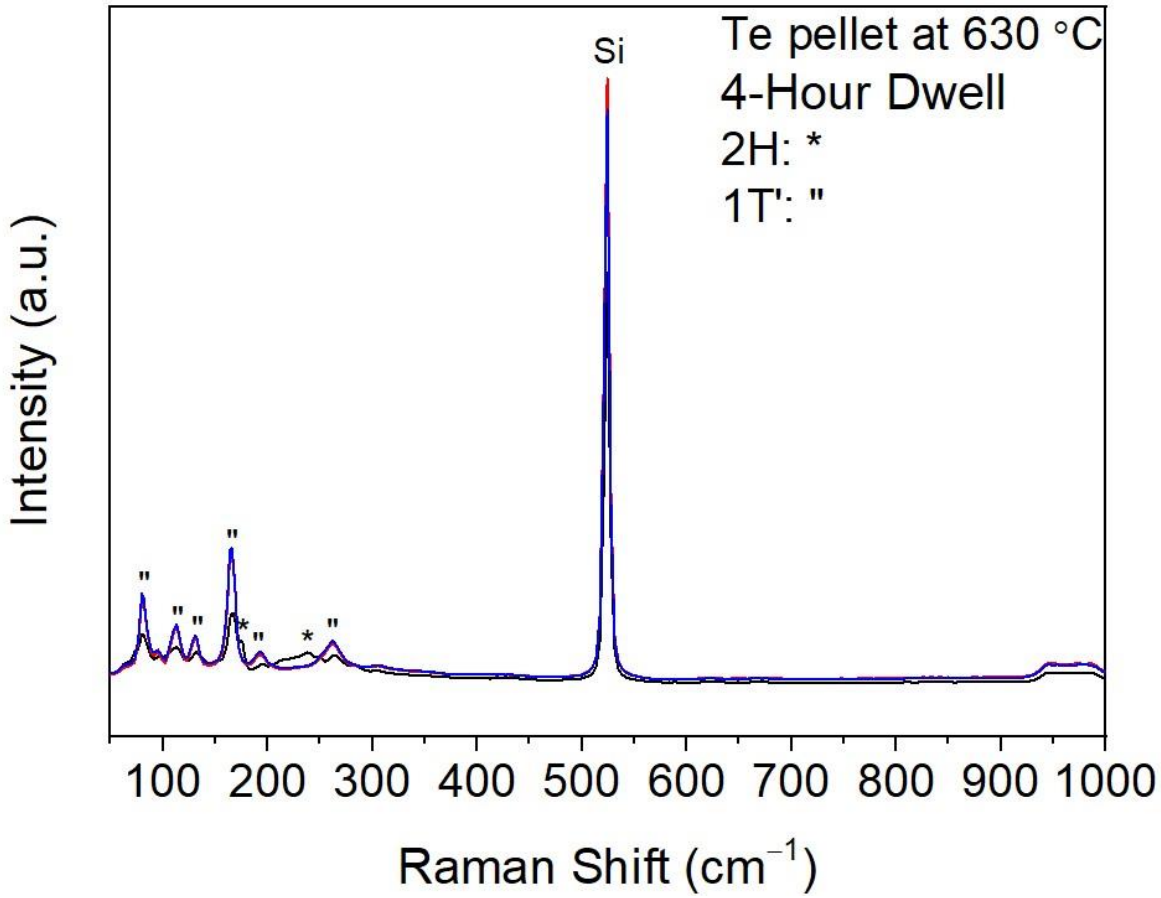

Figure 4-17: Raman spectra recorded from the $MoTe_2$ film produced from Mo/SiO_2/Si with Te at 650 °C with a 4-hour dwell.

Utilising the same conditions, except reducing the dwell period to 1-hour clearly results in the formation of phase pure 1T'-$MoTe_2$, as evident from the Raman spectra collected across the film (Figure 4-18). A_g modes are present at ~76, ~108, 126, ~161, and 262 cm^{-1}, whilst a single B_g mode is visible at ~189 cm^{-1} confirming that 1T'-$MoTe_2$ formed. Also, the Te pellet was not completely consumed and as such the mass lost from the pellet could be recorded.

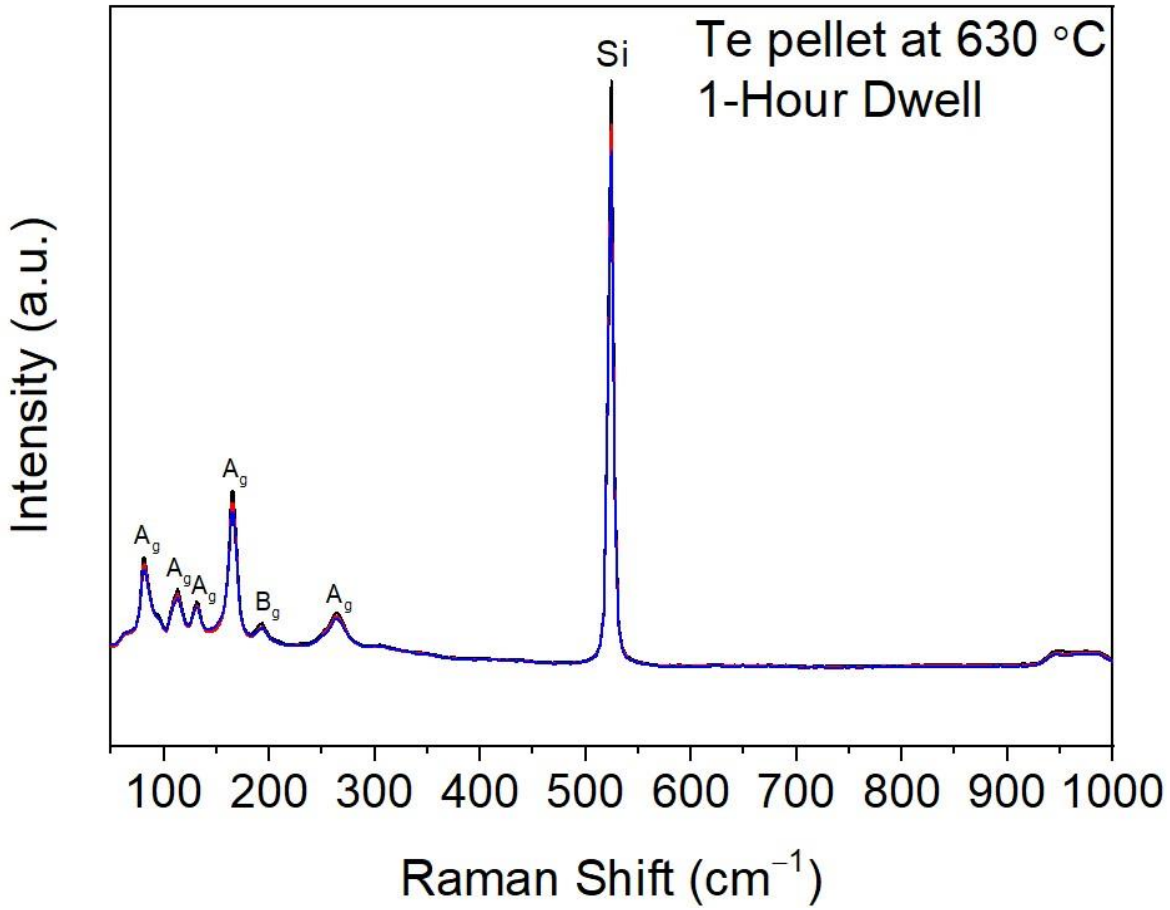

Figure 4-18: Raman spectra recorded from the $MoTe_2$ film produced from Mo/SiO_2/Si with Te at 630 °C with a 1-hour dwell.

Efforts were then made to vary the tellurium vapour pressure for several depositions by changing the position of the Te pellet in the furnace, with the aim of achieving a similar vapour pressure to that produced by $FeTe_2$ to compare the results. The pellets were positioned in such a way that their dwell temperatures would be 585 °C, 535 °C and 485 °C whilst the substrate remained at 650 °C. As the previous reaction (with Te pellet at 630 °C) resulted in phase pure 1T'-$MoTe_2$, a reduction in dwell temperature for the Te pellet should still result in the formation of 1T'-$MoTe_2$ but of declining quality. However, this is not the case for the film produced where the Te pellet is at 585 °C. From the optical image (Figure 4-19) it is possible to make out two very distinct areas of the film, one much lighter in colour than the other. Raman spectra obtained from these two areas (Figure 4-20) reveal that they correspond to the different phases of $MoTe_2$. The lighter areas were found to be 2H-$MoTe_2$ with peaks present at ~119, ~171, ~234 and ~289 cm^{-1} whilst the darker sections are 1T'-$MoTe_2$ with peaks at ~76, ~108, ~126, ~161, ~187 and ~257 cm^{-1}. This type of in-plane homojunction of the two $MoTe_2$ phases is something that has been observed by several other groups and utilised in the fabrication of all $MoTe_2$ based field effect transistors.[10,12,13] However, this method does not allow for precise spatial control over the phases, unlike the

method highlighted in Chapter 3, but it does only require access to one molybdenum precursor.

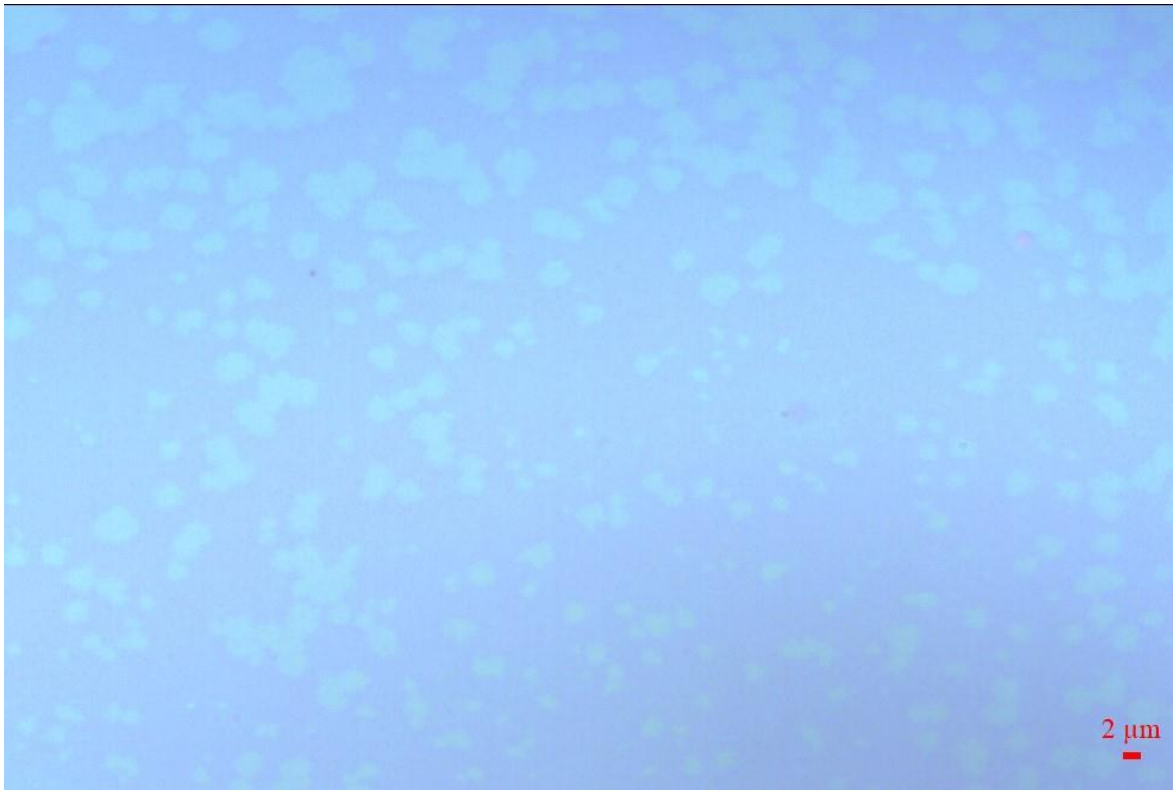

Figure 4-19: An optical image of the $MoTe_2$ film produced from $Mo/SiO_2/Si$ with Te pellet at 585 °C with a 1-hour dwell. Raman spectroscopy reveals that the lighter areas correspond to 2H-$MoTe_2$, whilst the darker sections of the film are 1T'-$MoTe_2$.

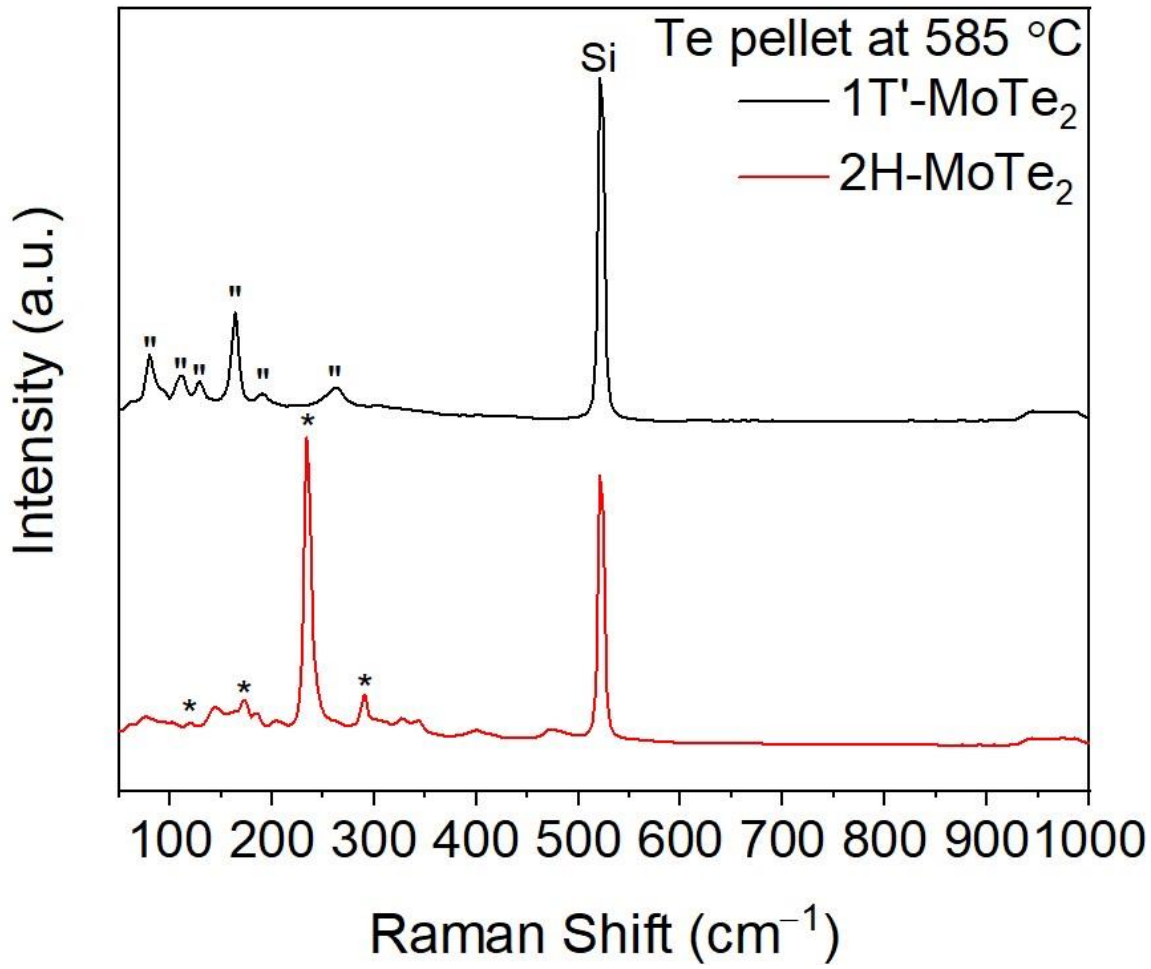

*Figure 4-20: Raman spectra recorded from different areas of the same $MoTe_2$ film produced from $Mo/SiO_2/Si$ with Te pellet at 585 °C with a 1-hour dwell. Peaks belonging to 1T'-$MoTe_2$ are marked with " and were obtained from a darker area of the film shown in Figure 4-19. Peaks belonging to 2H-$MoTe_2$ are marked with * and were obtained from a lighter area of the film shown in Figure 4-19.*

Further reductions of Te vapour pressure were then tested by setting the dwell temperatures of the Te pellet to 535 °C and 485 °C respectively. Raman spectra collected from these films are displayed in Figures 4-21 and 4-22. From these spectra it is clear that these films are mixed phase $MoTe_2$, but they do not show the in-plane homojunctions observed in Figure 4-19. Interestingly, the film converted with the lowest Te vapour pressure (Te pellet at 485 °C) produces a mixed phase film that contains a higher proportion of 2H-$MoTe_2$ than the film converted with a slighter higher Te vapour pressure (Te pellet at 535 °C). This result is surprising and contradicts literature observations. One such study by Yoo et al tested a similar range of Te vapour pressures and found that a high vapour pressure would form phase pure 2H-$MoTe_2$ from a molybdenum precursor film, reducing the vapour pressure would then lead to the visible in-plane 1T'-2H homojunctions. Phase pure 1T'-$MoTe_2$ would be favoured upon reducing the vapour pressure further and finally at the lowest Te vapour pressure, 1T'-$MoTe_2$ would still form but of significantly lower quality.[10] Their results

suggest that the phase obtained when using elemental tellurium is less dependent on the type of molybdenum precursor used compared to $FeTe_2$. However, work performed in this chapter has found that there is clearly more optimisation required when using elemental Te, as varying the Te flux did not produce similar results.

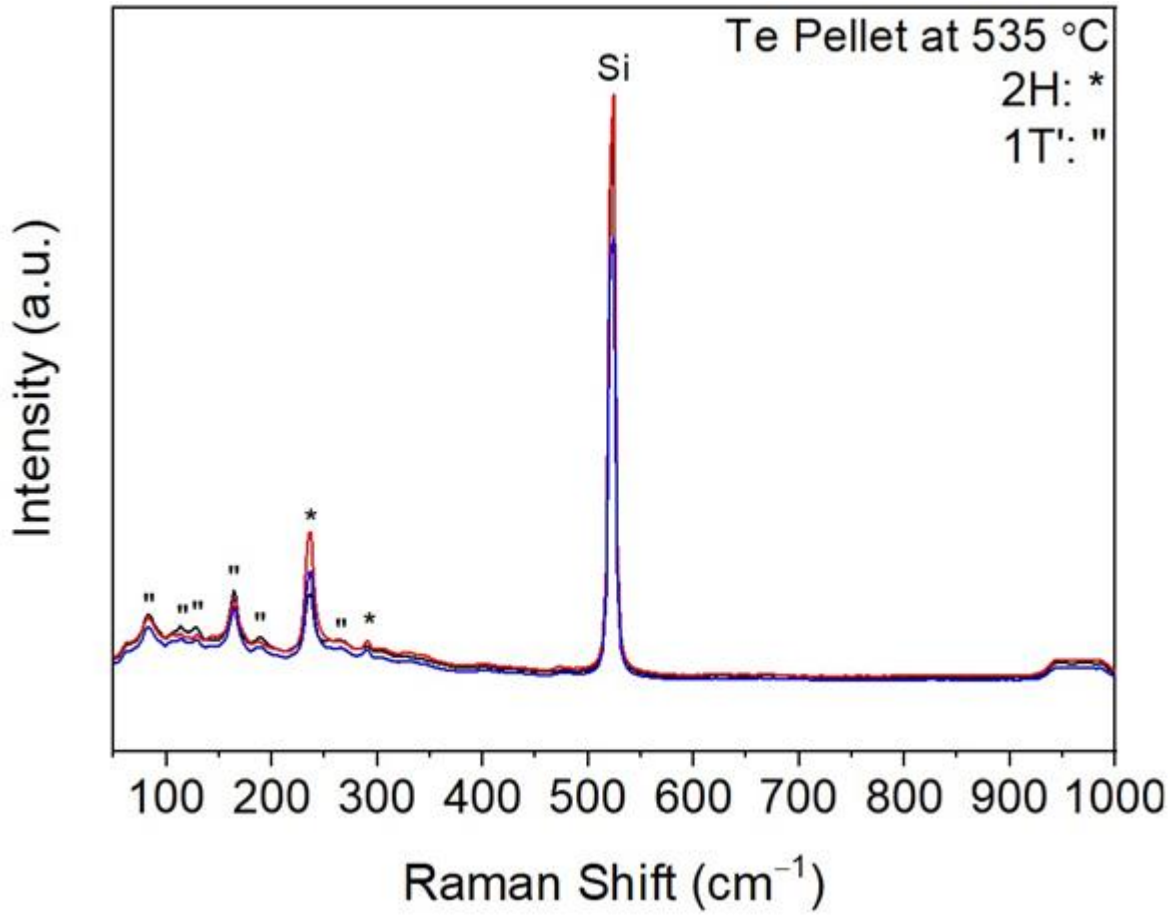

*Figure 4-21: Raman spectra recorded from the $MoTe_2$ film produced from $Mo/SiO_2/Si$ with Te pellet at 535 °C with a 1-hour dwell. Peaks belonging to 1T'-$MoTe_2$ are marked with " whilst those belonging to 2H-$MoTe_2$ are marked with *.*

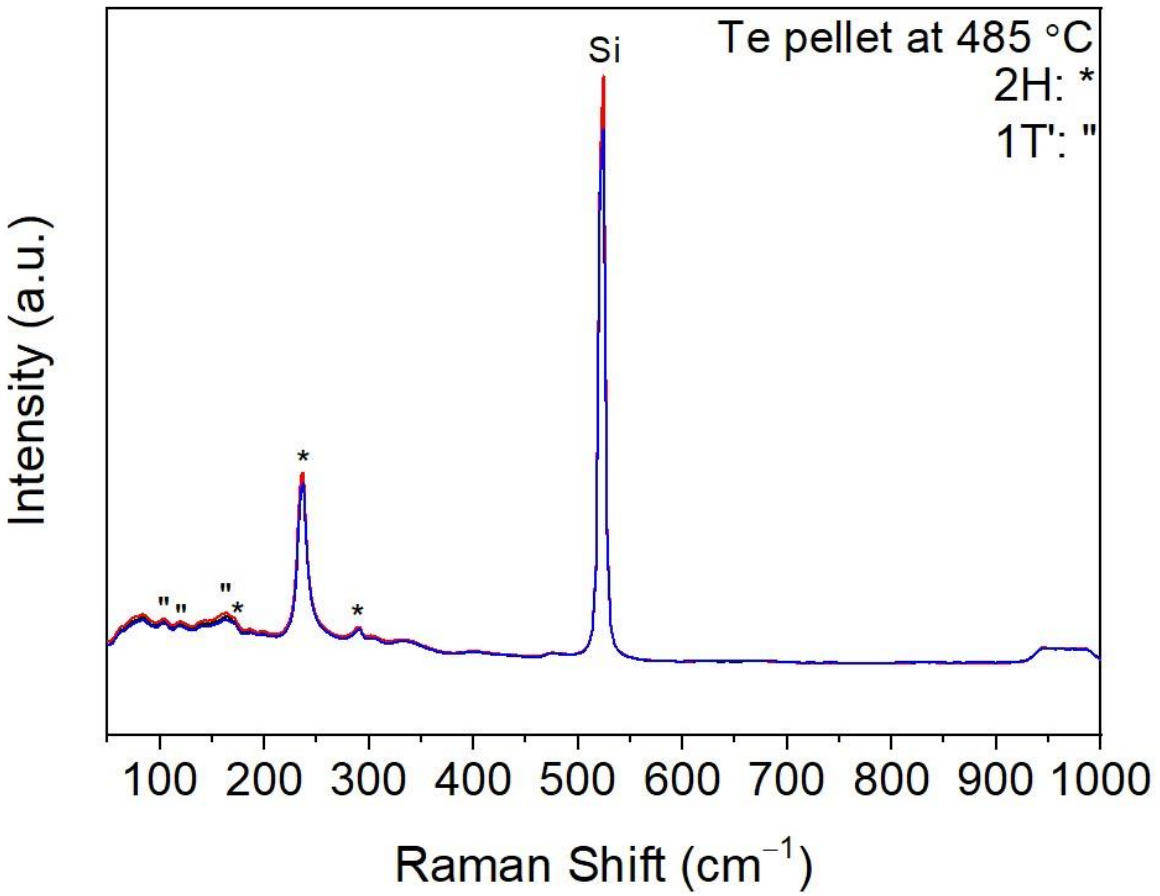

*Figure 4-22: Raman spectra recorded from the $MoTe_2$ film produced from Mo/SiO_2/Si with Te pellet at 485 °C with a 1-hour dwell. Peaks belonging to 1T'-$MoTe_2$ are marked with " whilst those belonging to 2H-$MoTe_2$ are marked with *.*

4.3.4. CVD Using Elemental Tellurium with Molybdenum Trioxide Precursor Films

The experiments from the previous section were then repeated using MoO_3 precursor films in order to investigate the impact of changing the molybdenum precursor when using elemental tellurium. Again, 3 nm MoO_3/SiO_2/Si films were utilised with the other parameters remaining the same. Furthermore, the effect of varying the Te vapour on the reaction outcome was again tested by changing the position of the Te pellet. The first reaction performed had the Te pellet positioned so that it would experience a dwell temperature of 630 °C. The Raman spectra recorded from the resultant $MoTe_2$ film are shown in Figure 4-22. The spectra contain two A_g mode belonging to 1T'-$MoTe_2$ at ~125 and ~161 cm^{-1} although they are extremely weak. This is in stark contrast to the result obtained using a molybdenum film and elemental tellurium (Raman spectra in Figure 4-18) under the same reaction conditions. In that instance 1T'-$MoTe_2$ was also formed but the modes in the Raman spectra appear much more intense. It is possible in the case of MoO_3 and Te that the high dwell temperature of the Te pellet coupled with the reduction of MoO_3 to MoO_2 before

conversion to $MoTe_2$ means there was insufficient Te vapour pressure to fully form 1T'-$MoTe_2$.

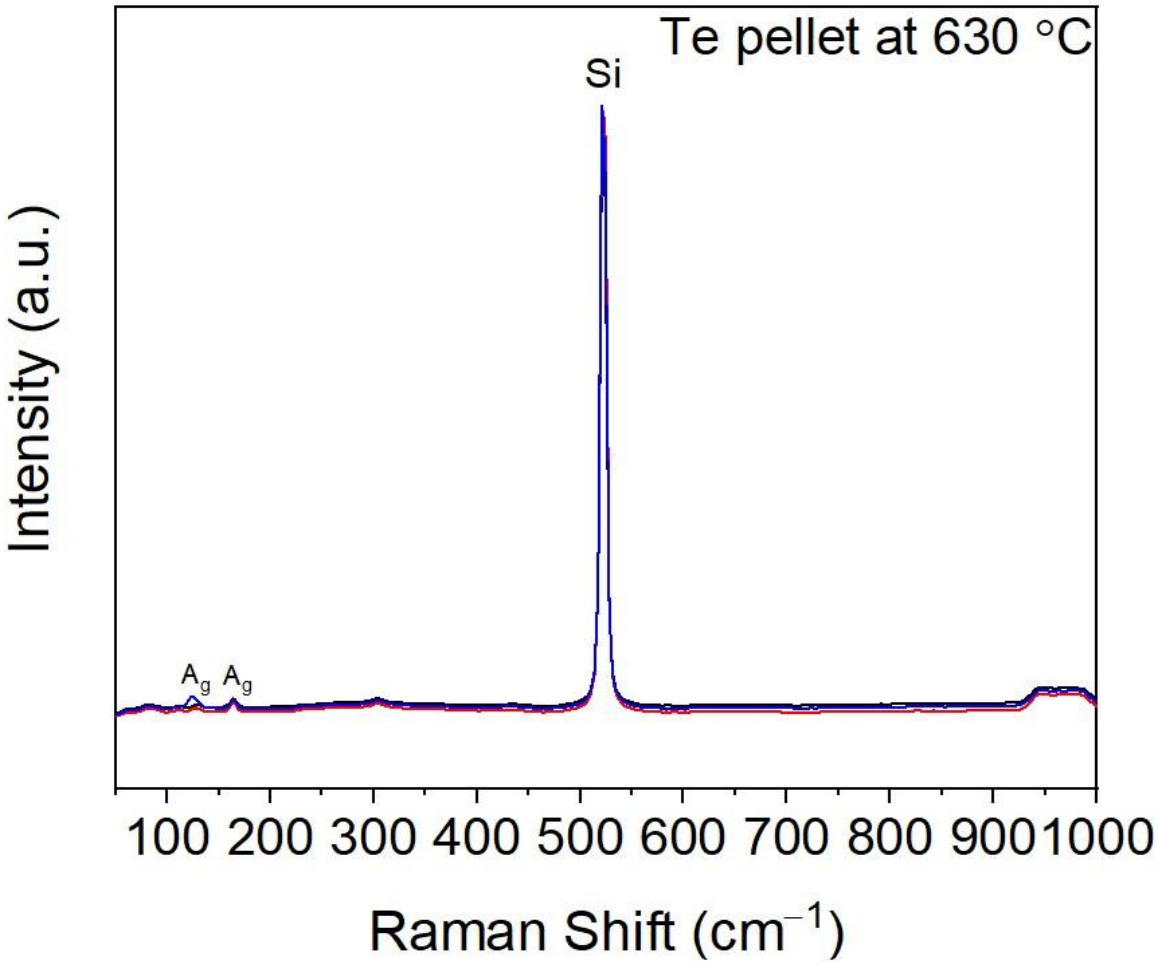

Figure 4-22: Raman spectra recorded from the $MoTe_2$ film produced from $MoO_3/SiO_2/Si$ with Te pellet at 630 °C with a 1-hour dwell.

It is therefore plausible that a reduction in the Te pellet dwell temperature would result in slower evaporation of Te leading to the formation of a higher quality 1T'-$MoTe_2$ film when using MoO_3 as the precursor film. A deposition was carried out with the Te pellet positioned so it would experience a dwell temperature of 585 °C whilst the other parameters remained constant. The Raman spectra obtained from the film (Figure 4-23) contain several peaks belonging to 1T'-$MoTe_2$ all of which are of an increased intensity compared to the previous film synthesised with the Te pellet at 630 °C.

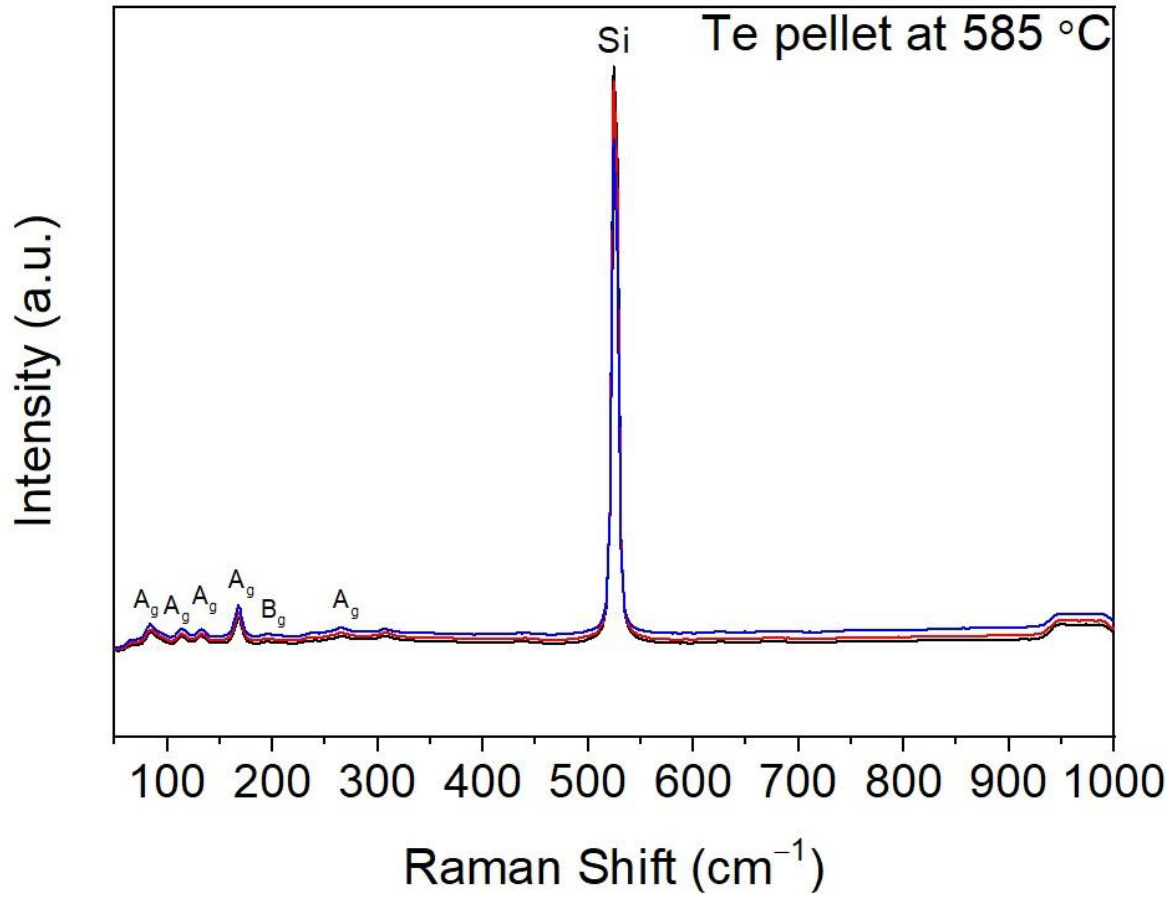

Figure 4-23: Raman spectra recorded from the $MoTe_2$ film produced from $MoO_3/SiO_2/Si$ with Te pellet at 585 °C with a 1-hour dwell.

Subsequent reductions in the Te pellet dwell temperatures to 535 °C and 485 °C respectively also provide interesting reaction outcomes. The Raman spectra from the remaining two films (Figures 4-24 and 4-25) reveal that they are both mixed phase films with the E^1_{2g} mode of 2H-$MoTe_2$ at ~234 cm^{-1} and the main A_g mode of 1T'-$MoTe_2$ present in both spectra at ~161 cm^{-1}. It once again appears that the film produced from the Te pellet at 485 °C contains a higher proportion of 2H-$MoTe_2$ compared to the one produced with the Te pellet at 535 °C, this was also the case when Mo precursor films were reacted with Te. Perhaps this can be attributed to the slower evaporation of Te at this temperature meaning that there was a higher vapour pressure by the time MoO_3 had been reduced to MoO_2 to begin conversion to $MoTe_2$.

It is clear that the Raman peaks of the films converted from Mo and Te are of much higher intensity than those converted from MoO_3 and Te. Work in Chapter 3 revealed that a film produced from 1 nm Mo would result in a ~6 layered $MoTe_2$ film, whilst the $MoTe_2$ film converted from 3 nm MoO_3 was thicker at ~7 layers. Therefore, the differences in Raman intensity are not because the films produced from MoO_3 are inherently thinner. It is apparent that the combination of MoO_3 and Te in this experimental set up is not ideal and is in stark

contrast to the results obtained using MoO_3 and $FeTe_2$ as precursors which consistently produced 2H-$MoTe_2$.

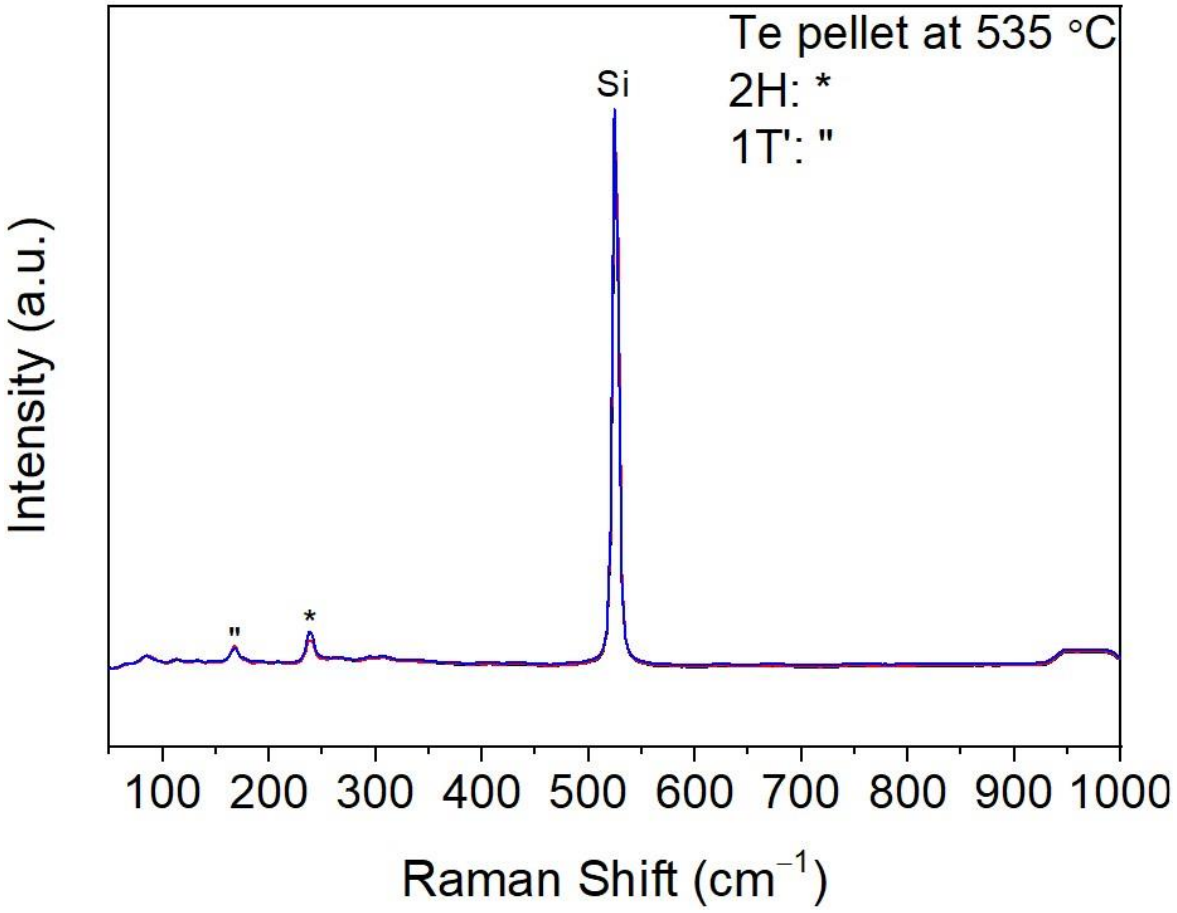

Figure 4-24: Raman spectra recorded from the $MoTe_2$ film produced from $MoO_3/SiO_2/Si$ with Te pellet at 535 °C with a 1-hour dwell.

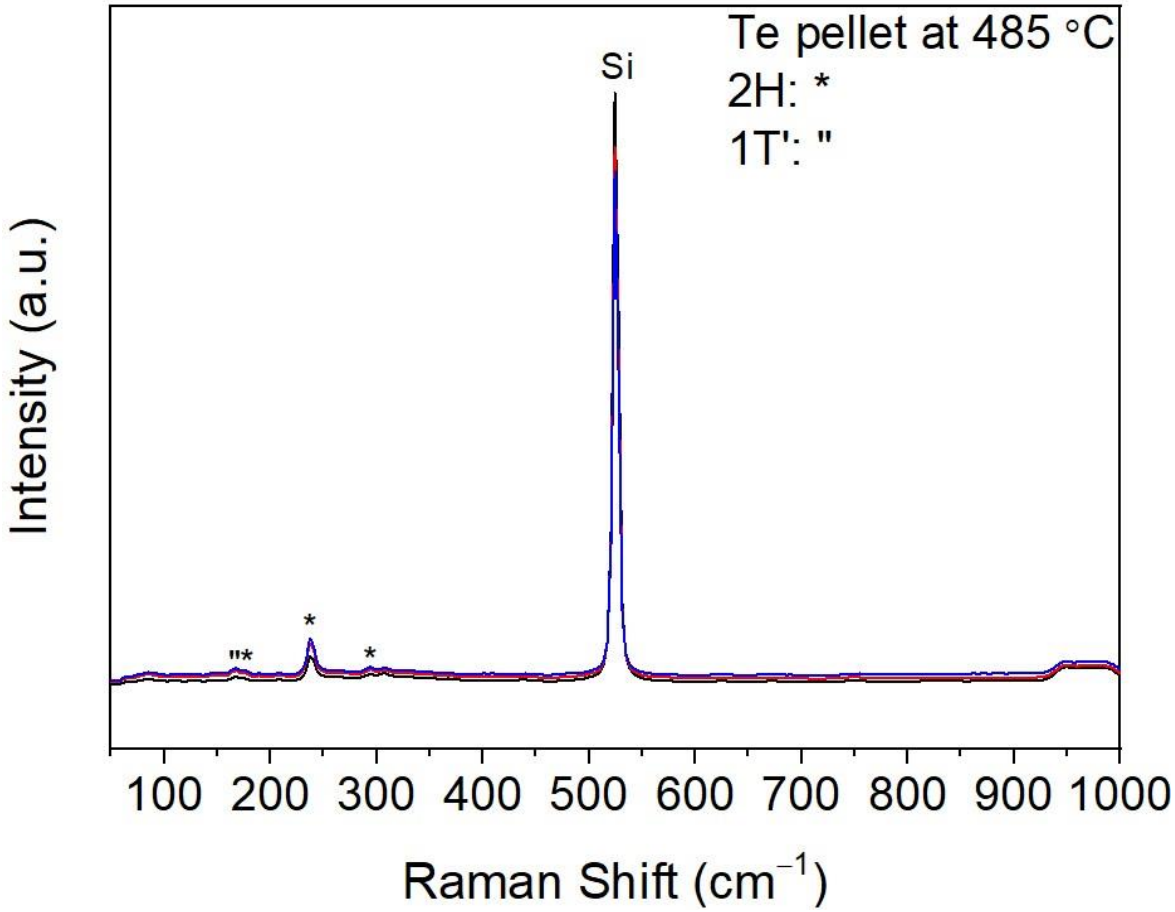

Figure 4-25: Raman spectra recorded from the MoTe2 film produced from $MoO_3/SiO_2/Si$ with Te pellet at 485 °C with a 1-hour dwell.

The procedure of recording the mass of the Te pellets before and after the deposition process was carried out in the same manner as for the $FeTe_2$ pellets earlier in the chapter. Figure 4-26 shows how the mass lost from the Te pellets varies with their dwell temperature for the reactions conducted with Mo and MoO_3 precursor films. It is clear that the discrepancies in the quality of the films produced from Mo and MoO_3 when using elemental Te do not arise due to major differences in Te vapour pressure, with both sets of experiments consuming almost identical amounts of Te for their respective dwell temperatures. Therefore, it is likely due to the reduction of MoO_3 to MoO_2 before conversion to $MoTe_2$.

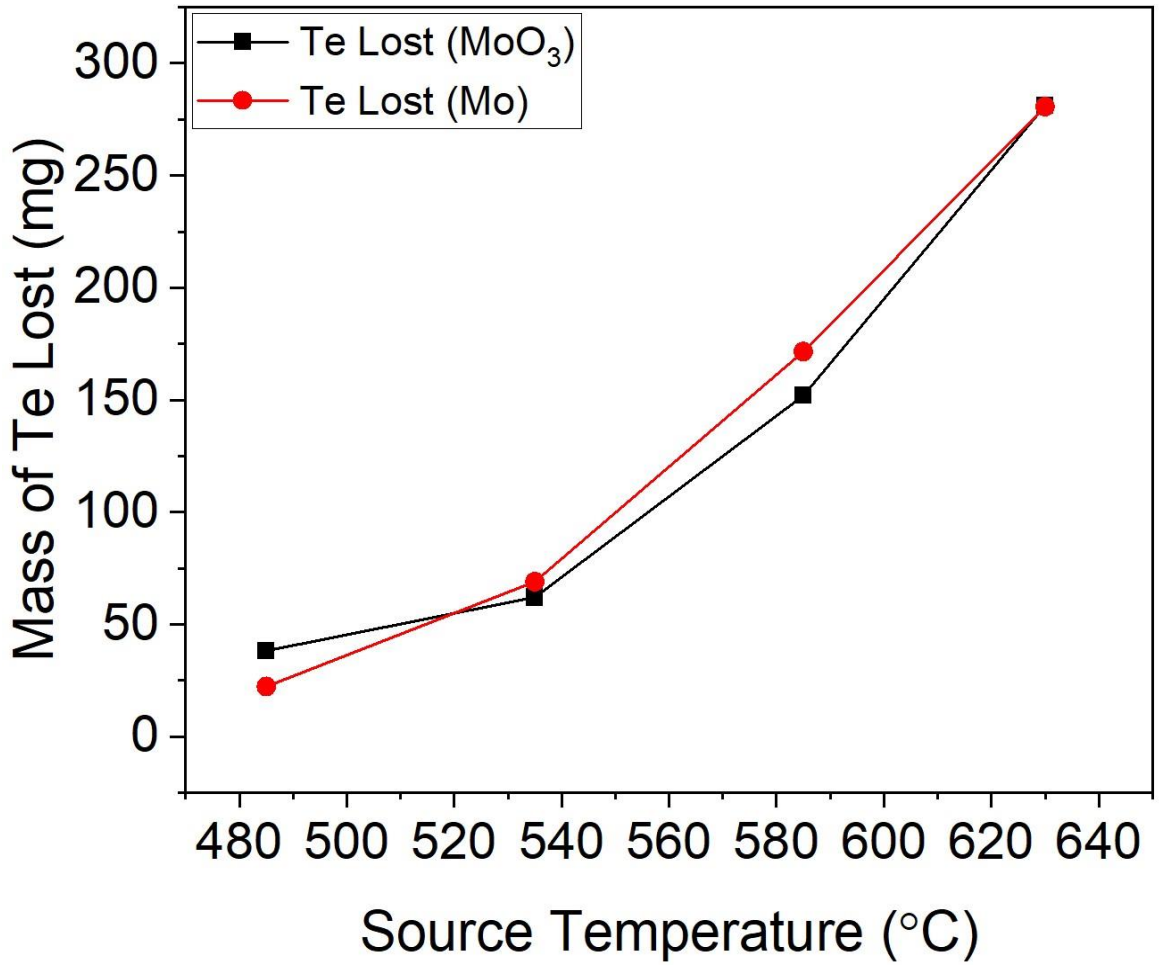

Figure 4-26: A plot of the masses lost from the 300 mg Te pellets used in the conversion of Mo and MoO_3 precursor films at the various dwell temperatures tested.

4.4. Conclusions

In this chapter the $FeTe_2$ precursor was applied in a traditional flow CVD setup and the experimental conditions for the phase pure synthesis of 1T'- and 2H-$MoTe_2$ were determined. Furthermore, the impact of varying dwell duration was studied, finding that when using $FeTe_2$ the dwell duration appears largely irrelevant in determining the phase of the product $MoTe_2$ film, which from several literature examples is not the case for elemental Te. The phase of the resultant $MoTe_2$ film was dictated by the type of molybdenum precursor used, with MoO_3 forming 2H-$MoTe_2$ and Mo forming 1T'-$MoTe_2$, respectively. Additionally, elemental Te was trialled as the precursor in the same setup, where it was discovered that long dwell times are not suitable due to the low evaporation temperature meaning it becomes depleted rapidly, which leads to evaporation of the $MoTe_2$ film. Therefore, the effect that varying the Te flux has on the reaction outcome was studied by positioning the Te pellet at different dwell temperatures for both Mo and MoO_3 precursors. It was discovered that in this setup MoO_3 is not a good choice of precursor as the quick evaporation of Te coupled with the reduction of MoO_3 to MoO_2 before conversion to $MoTe_2$ led to poor quality films being formed, as evident from the weak Raman spectra. This was not the case for Mo, although it was not possible to isolate phase pure 2H-$MoTe_2$, with the resultant films either being mixed phase or 1T'-$MoTe_2$. Therefore, it seems like both $FeTe_2$ and Te can be suitable precursors depending on the molybdenum sources available. If Mo and MoO_3 are both available, then $FeTe_2$ appears the best choice as phase pure 1T'- and 2H-$MoTe_2$ thin films can be synthesised. However, if only Mo is available, then Te would be better suited as a precursor as 1T'-$MoTe_2$ can be synthesised and with further optimisation of reaction conditions it is more than likely that pure 2H-$MoTe_2$ could be isolated as well.

Finally, it should be noted that the different reactor geometries employed in Chapter 3 and this chapter resulted in different $MoTe_2$ phases forming from a particular precursor layer. For example, in the closed CVD reactor Mo precursor films preferentially converted to 2H-$MoTe_2$, whereas in the flow setup Mo converted to 1T'-$MoTe_2$. Likewise, MoO_3 converted to 1T'-$MoTe_2$ in the closed setup and 2H-$MoTe_2$ is the flow system. This result was somewhat surprising but given the small energy difference between the two phases it is plausible that such a significant change to the setup was the cause of these variations. Furthermore, it appears that the $FeTe_2$ precursor is also key to the phase selectivity. In the flow setup the dwell time was varied extensively, but it was not possible to force Mo to convert to 2H-$MoTe_2$ even with extended dwell times. This is in contrast to elemental Te with several literature reports showing that increased dwell times when using Te favour the formation of 2H-$MoTe_2$. Also, when using Te in the flow setup it was possible to obtain 1T'-

$MoTe_2$ and mixed phase films from Mo precursor films which was not achievable when using $FeTe_2$. It is also apparent that the choice of molybdenum precursor is incredibly important for determining the phase of the product $MoTe_2$ film, something that was also observed in the literature procedures shown in Tables 3-1 and 3-2.

Overall, when looking at a single reactor setup in isolation it is apparent that both the choice of molybdenum precursor and the $FeTe_2$ precursor used are incredibly important for dictating the phase of the $MoTe_2$ film. Although altering the reactor geometry clearly has an influence on the phase of the product films it does not appear to be as important as the choice of Mo precursor or the use of $FeTe_2$.

4.5. References

1. Zhou, L., Xu, K., Zubair, A., Liao, A. D., Fang, W., Ouyang, F., Lee, Y-H., Ueno, K., Saito, R., Palacios, T., Kong, J. & Dresselhaus, M. S. Large-Area Synthesis of High-Quality Uniform Few-Layer $MoTe_2$. *J. Am. Chem. Soc.* **137**, 11892–11895 (2015).

2. Zhou, L., Zubair, A., Wang, Z., Zhang, X., Ouyang, F., Xu, K., Fang, W., Ueno, K., Li, J., Palacious, T., Kong, J. & Dresselhaus, M. S. Synthesis of High-Quality Large-Area Homogenous 1T′ $MoTe_2$ from Chemical Vapor Deposition. *Adv. Mater.* **28**, 9526–9531 (2016).

3. Park, J. C. Yun, S. J., Kim, H., Park, J-H., Chae, S. H., An, S.-J., Kim, J.-G., Kim, S. M., Kim, K. K. & Lee, Y. H. Phase-Engineered Synthesis of Centimeter-Scale 1T′- and 2H-Molybdenum Ditelluride Thin Films. *ACS Nano* **9**, 6548–6554 (2015).

4. Zhu, X., Li, A., Wu, D., Zhu, P., Xiang, H., Liu, S., Sun, J., Ouyang, F., Zhou, Y. & Xiong, X. Tunable large-area phase reversion in chemical vapor deposited few-layer $MoTe_2$ films. *J. Mater. Chem. C* **7**, 10598–10604 (2019).

5. Zhou, L., Huang, S., Tatsumi, Y., Wu, L., Guo, H., Bie, Y.-Q., Ueno, K., Yang, T., Zhu, Y., Kong, J., Saito, R. & Dresselhaus, M. S. Sensitive Phonon-Based Probe for Structure Identification of 1T′ $MoTe_2$. *J. Am. Chem. Soc.* **139**, 8396–8399 (2017).

6. Jin, Y. & Shen, P. K. Nanoflower-like metallic conductive MoO_2 as a high-performance non-precious metal electrocatalyst for the hydrogen evolution reaction. *J. Mater. Chem. A* **3**, 20080–20085 (2015).

7. Wang, T., Li, J. & Zhao, G. Synthesis of MoS_2 and MoO_3 hierarchical nanostructures using a single-source molecular precursor. *Powder Technol.* **253**, 347–351 (2014).

8. Yamamoto, M., Wang, S. T., Ni, M., Lin, Y.-F., Li, S.-L., Aikawa, S., Jian, W.- B., Ueno, K., Wakabayashi, K. & Tsukagoshi, K. Strong Enhancement of Raman Scattering from a Bulk-Inactive Vibrational Mode in Few-Layer $MoTe_2$. *ACS Nano* **8**, 3895–3903 (2014).

9. Guo, H., Yang, T., Yamamoto, M., Zhou, L., Ishikawa, R., Ueno, K., Tsukagoshi, K., Zhang, Z., Dresselhaus, M. S. & Saito, R. Double resonance Raman modes in monolayer and few-layer $MoTe_2$. *Phys. Rev. B - Condens. Matter Mater. Phys.* **91**, 205415 (2015).

10. Yoo, Y., DeGregorio, Z. P., Su, Y., Koester, S. J. & Johns, J. E. In-Plane 2H-1T′

$MoTe_2$ Homojunctions Synthesized by Flux-Controlled Phase Engineering. *Adv. Mater.* **29**, 1605461 (2017).

11. Sun, L., Ding, M., Li, J., Yang, L., Lou, X., Xie, Z., Zhang, W. & Chang, H. Phase-controlled large-area growth of $MoTe_2$ and $MoTe_{2-x}O_x/MoTe_2$ heterostructures for tunable memristive behavior. *Appl. Surf. Sci.* **496**, 143687 (2019).

12. Ma, R., Zhang, H., Yoo, Y., Degregorio, Z. P., Jin, L., Golani, P., Azadani, J. G., Low, T., Johns, J. E., Bendersky, L. A., Davydov, A. V. & Koester, S. J. $MoTe_2$ Lateral Homojunction Field-Effect Transistors Fabricated using Flux-Controlled Phase Engineering. *ACS Nano* **13**, 8035–8046 (2019).

13. Zhang, X., Jin, Z., Wang, L., Hatchtel, J. A., Vilarreal, E., Wang, Z., Ha, T., Nakanishi, Y., Tiwary, C. S., Lai, J., Dong, L., Tang, J., Vajtai, R., Ringe, E., Idrobo, J. C., Yakobson, B. I., Lou, J., Gambin, V., Koltun, R. & Ajayan, P. M. Low Contact Barrier in 2H/1T′ $MoTe_2$ In-Plane Heterostructure Synthesized by Chemical Vapor Deposition. *ACS Appl. Mater. Interfaces* **11**, 12777–12785 (2019).

5. Applications of $MoTe_2$ Thin Films

5.1. $MoTe_2$ Thin Films as HER Catalysts

5.1.1. Introduction

The renewable energy capacity of the United Kingdom is projected to more than double by the year 2030, from ~46.7 gigawatts in 2020 to ~ 110 gigawatts in 2030.[1] However, the intermittent nature of these renewable sources poses issues for grid balancing. Therefore, ways of storing the electricity produced by renewable sources will become ever more important as the capacity increases over the coming decade. One method of storing excess energy generated by renewables is the production of hydrogen through the electrolysis of water. The hydrogen generated through electrolysis can be stored as a gas and used when required to produce electricity in a hydrogen fuel cell, or in other applications such as providing heat for buildings, refuelling fuel cell vehicles and even as a feedstock for the chemical industry.[2]

5.1.1.1. Hydrogen Evolution Reaction Catalysts.

Currently, platinum and its alloys are still the most efficient hydrogen evolution reaction (HER) electrocatalysts, but the high cost and low natural abundance of these noble metals has motivated a great deal of research into finding cheaper, earth abundant alternatives.[3] The excellent electrochemical activity of platinum is in part attributed to its near zero free energy change for hydrogen absorption, following the Sabatier principle which states that optimal catalyst surfaces exhibit moderate binding energies for reaction intermediates, which is hydrogen adsorption for the HER. This has focused the search for new HER catalysts to earth abundant materials which possess a similarly small Gibbs free energy of hydrogen absorption (ΔG_H).

Presently, it is relatively straightforward to calculate this value using DFT and was first performed by Nørskov *et al.* in 2005 where they developed a simple model effective for homogeneous materials.[4] However, for heterogenous materials containing different elements, defects or further structural variations a detailed model of the whole system is ideal, but these models become decidedly more complicated and are therefore not often investigated. To simplify the models, it is common to only report the most highly active adsorption sites, however this does not necessarily give a good representation of the total activity, resulting in disagreement between theoretical models and experimental data.[5] In this regard the 2D TMDCs are particularly interesting for fundamental research and present an excellent opportunity to test the validity of computational models against experimentally obtained results. Due to their layered structure, the location of active sites on the basal plane

and edges can be modelled with impressive accuracy as it is only the 001 surface that has to be taken into consideration.[6] For example, a recent computational study by Ekspong *et al.* illustrated this to impressive effect, with current densities able to be determined from ΔG_H obtained using DFT. Their model combines the activity of all adsorption sites to calculate total activity meaning that any atomic variations like doping, vacancies and distortions in the material can be included. The authors used this model to study the heterogeneous structure of MoS_2 and were able to include both the basal plane and edge active sites into the calculations. Furthermore, they were able to test structures with differing proportions of these active sites, effectively modelling the common experimental strategy of nano structuring, with the calculated overpotentials matching well with experimental observations.[5] Incidentally, MoS_2 has been one of the most heavily studied, experimentally and computationally, transition metal dichalcogenides for use as a hydrogen evolution catalyst.

5.1.1.2. Molybdenum Disulfide

Hinnemann *et al.* calculated that MoS_2 has a similar free energy change to that of platinum and therefore predicted it would be a promising catalytic material (Figure 5-1). This result was somewhat surprising as it had previously been reported that bulk MoS_2 is a poor electrocatalyst for the HER.[7]

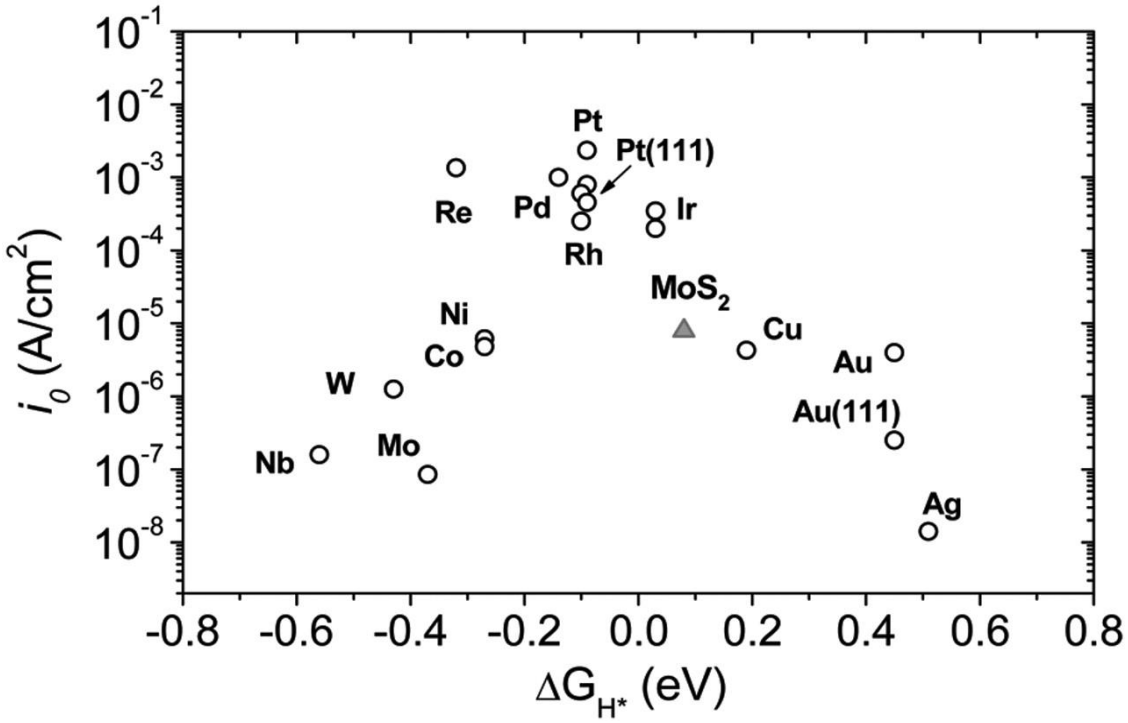

Figure 5-1: Volcano plot of exchange current densities as a function of the calculated Gibbs free energy of hydrogen adsorption for various noble and transition metals, as well as MoS_2 nanoparticles.[8]

Naturally occurring MoS_2 exists in bulk form as the semiconducting, hexagonal 2H-phase, with S-Mo-S layers held together through van der Waals forces. The layered structure gives rise to two possible active sites for the HER, the edge sites and the basal plane sites. The theoretically predicted potential of MoS_2 was realised experimentally by Jaramillo *et al.* whilst also identifying the edge sites as responsible for the catalytic performance and that the basal plane sites can be considered catalytically inactive.[8] Molybdenum disulfide's layered structure means that it is largely made of inert basal planes and its catalytic activity is determined by the concentration and reactivity of the edge sites. Therefore, a common strategy to improve the catalytic performance of 2H-MoS_2 has been to synthesise nanostructured materials which feature a high concentration of edge sites and has subsequently been applied to several other TMDC electrocatalysts.[9–13] A comparison of the overpotentials required to achieve a current density of 10 mA cm^{-2} for several of the leading 2H-MoS_2 electrocatalysts are shown in Table 5-1. Although these materials achieve promisingly low overpotentials, 2H-MoS_2 is limited due to its semiconducting nature with poor electrical transport and inefficient electrical contact to the substrate.[10]

Table 5-1: Comparison of the overpotentials required to achieve a current density of 10 mA cm^{-2} for 2H-MoS_2 electrocatalysts.

Catalyst	**Overpotential (V) at 10 mA cm^{-2}**	**Reference**
MoS_2 nanoparticles	-0.17	8
Double-gyroid MoS_2 bicontinuous network	-0.28	9
MoS_2 on reduced graphene oxide	-0.16	14
Amorphous MoS_2	-0.20	15
Mesoporous MoS_2 nanosheets	-0.22	16

However, as with many other TMDCs, MoS_2 can exist in several polymorphs where subtle structural changes can vastly affect the electronic properties of the material. As mentioned above, MoS_2 exists naturally in the thermodynamically favoured, semiconducting 2H phase, characterised by two S-Mo-S layers constructed from edge-sharing MoS_6 trigonal prisms. In contrast, 1T-MoS_2 is characterised by a single S-Mo-S layer formed from edge-sharing MoS_6 octahedra and due to the change in crystal structure exhibits metallic conductivity, meaning it has vastly different catalytic properties to 2H-MoS_2 (Figure 5-2).[17,18] 1T-MoS_2 is only metastable and can often only be synthesised *via* complex, multistep procedures. One of the most common methods to obtain 1T-MoS_2 from 2H-MoS_2 is through chemical

exfoliation utilising lithium intercalation.[19] The phase transition is a result of electron transfer from the intercalated lithium, which destabilises the thermodynamically favourable trigonal prismatic structure and favours octahedral coordination of Mo.[20] However, due to its limited thermodynamic stability the reverse transition can occur and isolation of genuinely phase pure metallic MoS_2 remains a considerable challenge.[21] Nevertheless, MoS_2 has proved an efficient and noble-metal free electrocatalyst for the HER and furthered interest in other TMDC materials as potential HER electrocatalysts including WS_2, $MoSe_2$ and WSe_2.[22–24]

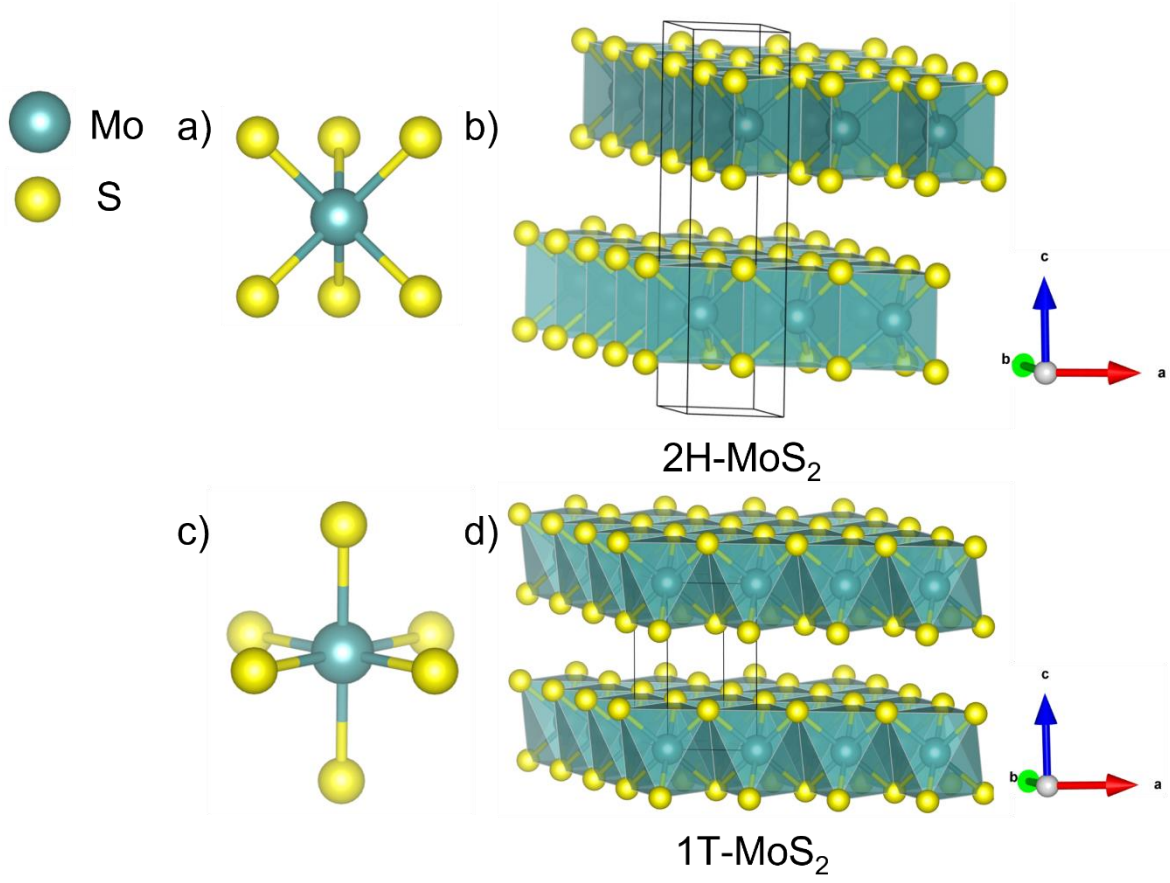

Figure 5-2: Depiction of the trigonal prismatic coordination of Mo by S in 2H-MoS_2 (a); corresponding crystal crystal structure of 2H-MoS_2 showing the unit cell (b); the octahedral coordination of Mo by S in 1T-MoS_2 (c); and corresponding crystal structure showing the unit cell (d). Mo atoms are represented by teal spheres, whilst S atoms are represented by yellow spheres.

5.1.1.3. Molybdenum Ditelluride

Compared to its sulfide and selenide counterparts, $MoTe_2$ has been relatively unexplored as an HER electrocatalyst. $MoTe_2$ possesses a distinct advantage over MoS_2 and $MoSe_2$ in that it can crystallise in the metallic 1T'-phase in the bulk form. Furthermore, both the 2H- and 1T'-phases can be synthesised directly *via* a simple solid-state method with varying the dwell

temperature enough to give control over the product phase due to the extremely small difference in ground state energy between the two.[25–27] Initial research into the HER activity of $MoTe_2$ was conducted by Seok *et al.*, who synthesised single crystal 2H- and 1T'-$MoTe_2$ and tested their electrocatalytic activity. The authors found that the semiconducting phase is catalytically inactive, whilst the metallic phase shows an intrinsic activity similar to that of platinum. Furthermore, they found that as hydrogen is adsorbed onto the surface of 1T'-$MoTe_2$ a lattice distortion, known as Peierls distortion, occurs enhancing the activity of the material (Figure 5-3). It involves in-plane Mo atoms moving closer together forming a chain and is thought to be driven by electron doping on the basal plane, altering the lattice structure and lowering the Gibbs free energy of hydrogen adsorption.[28,29]

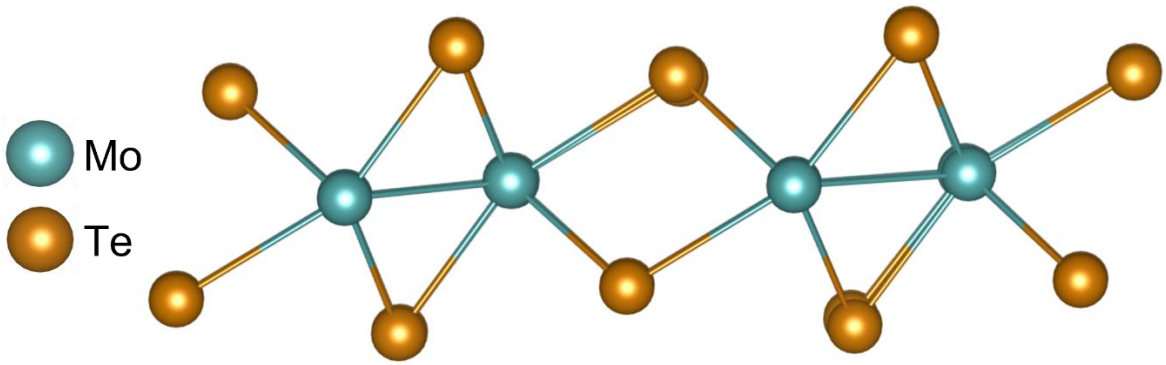

Figure 5-3: Depiction of the Peierls distortion in 1T'-$MoTe_2$ illustrating the formation of Mo-Mo bonds when hydrogen is adsorbed onto the surface.

This research was furthered by McGlynn *et al* who utilised bulk 2H- and 1T'-$MoTe_2$ powders synthesised using a simple sealed ampoule method. Their findings echoed those of Seok *et al*, showing that 1T'-$MoTe_2$ could act as an efficient electrocatalyst for the HER, whilst 2H-$MoTe_2$ showed poor catalytic performance.[27] The authors then followed this work with a report on the electrochemical activation of 1T'-$MoTe_2$ when held at a cathodic bias, interestingly this activation was found to be reversible and occurs without any changes to morphology or composition. The impressive activation resulted in a reduction in overpotential required to achieve a current density of 10 mA cm^{-2} from 0.32 to 0.18 V (Figure 5-4). They concluded that the activation could be attributed to hydrogen adsorption on specific Te active sites, driving a distortion in the structure of 1T'-$MoTe_2$ resulting in a more active catalyst. It was discerned that the enhancement did not occur at the sparse edge sites, but on the basal plane of the catalyst, therefore offering an effective way to enhance the performance of $MoTe_2$ and possibly other TMDC materials as well.[30]

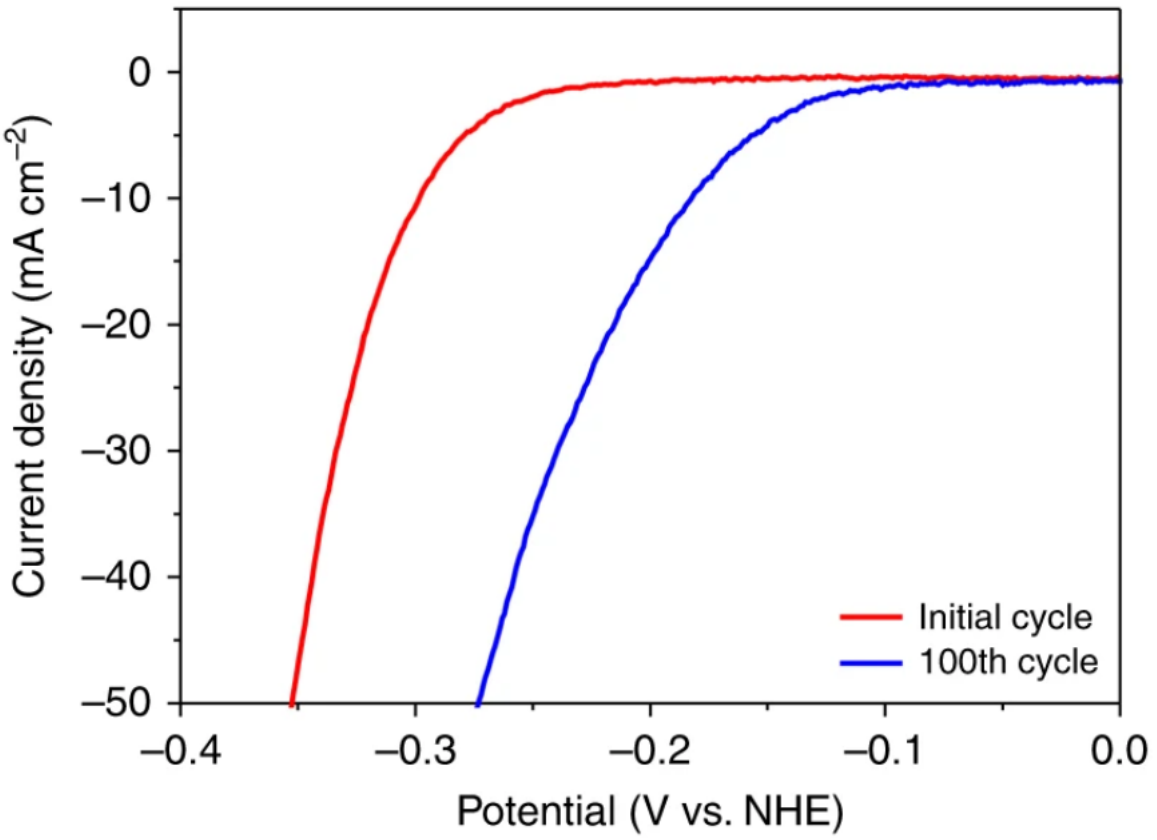

Figure 5-4: CV scans from the work of McGlynn et al. showing the impressive electrochemical activation of their 1T'-$MoTe_2$ HER catalyst, showing a reduction in overpotential of 0.14 V between the initial and 100th cycle.[30]

The three previously mentioned literature reports suggested that the HER activity of 1T'-$MoTe_2$ was due to the active sites situated on the basal plane rather than the edge sites that are responsible for the activity of MoS_2. Therefore, it would seem that a promising strategy to increase the performance of 1T'-$MoTe_2$ would be to structure the catalyst in such a way to increase the density of basal plane sites, similarly done for MoS_2 and edge sites.[9] Thin films of $MoTe_2$ tend to grow in such a manner that they stack along the *c* axis, with their basal planes parallel to the substrate. As such $MoTe_2$ thin films would offer a large concentration of basal plane sites compared to edge sites and at the time of undertaking the following research there were no reports of $MoTe_2$ thin films being utilised as HER catalysts. Moreover, utilising chemical vapour deposition as the production method would allow for the deposition of large area catalyst films, only limited by the size of the reactor.

5.1.2. Aims

The aims of this section involve investigating the potential application of $MoTe_2$ thin films, as electrocatalysts for the production of hydrogen from water. Both 1T'- and 2H-$MoTe_2$ will be produced using CVD from predeposited precursor films with a variety of thicknesses and characterised using Raman spectroscopy. The films will then be tested for their catalytic activity using linear sweep voltammetry and compared to the performance of their bulk powder counterparts.

5.1.3. Results and Discussion

5.1.3.1. $MoTe_2$ Thin Films as HER Catalysts

In order to test $MoTe_2$ thin films as HER catalysts, Mo and MoO_3 were deposited *via* electron beam physical vapour deposition and thermal deposition on bare silicon substrates before conversion to 2H- and 1T'-$MoTe_2$. This allowed for these substrates to be used directly as the working electrode in the electrochemical setup. Firstly, 2H-$MoTe_2$ was synthesised through conversion of 5, 20, 50 and 100 nm Mo/Si precursor films in the same CVD setup utilised in Chapter 3. By depositing a range of thicknesses, rudimentary testing of catalyst loading was able to be conducted.

Raman spectroscopy was again used to confirm the phase of the CVD produced films. The spectra obtained (Figure 5-5) confirm that all thicknesses of Mo were successfully converted to 2H-$MoTe_2$ with all characteristic modes present at ~119, ~171, ~234 and ~289 cm^{-1} in the films converted from 20 and 50 nm Mo respectively. In the case of the 5 nm film, it is difficult to make out any peaks other that the main E^1_{2g} mode at ~234 cm^{-1}. This may be due to the lack of oxide on the substrate meaning the 520 cm^{-1} silicon peak is far more intense, dwarfing the peaks of 2H-$MoTe_2$. Subsequently, the B^1_{2g} mode at ~289 cm^{-1} does not appear in the spectrum of the 100 nm film, suggesting this film is sufficiently thick to be considered bulk 2H-$MoTe_2$ as this mode is not active in bulk samples.[31]

For the synthesis of 1T'-$MoTe_2$ films the procedure was repeated, except MoO_3 precursor layers with thicknesses of 5, 20, 50 and 100 nm were deposited onto the silicon substrates. The Raman spectra from these films (Figure 5-6) confirm that 1T'-$MoTe_2$ has indeed been synthesised with each film displaying peaks corresponding to this phase at ~79, ~109, ~126, ~161, ~189 and ~259 cm^{-1}.

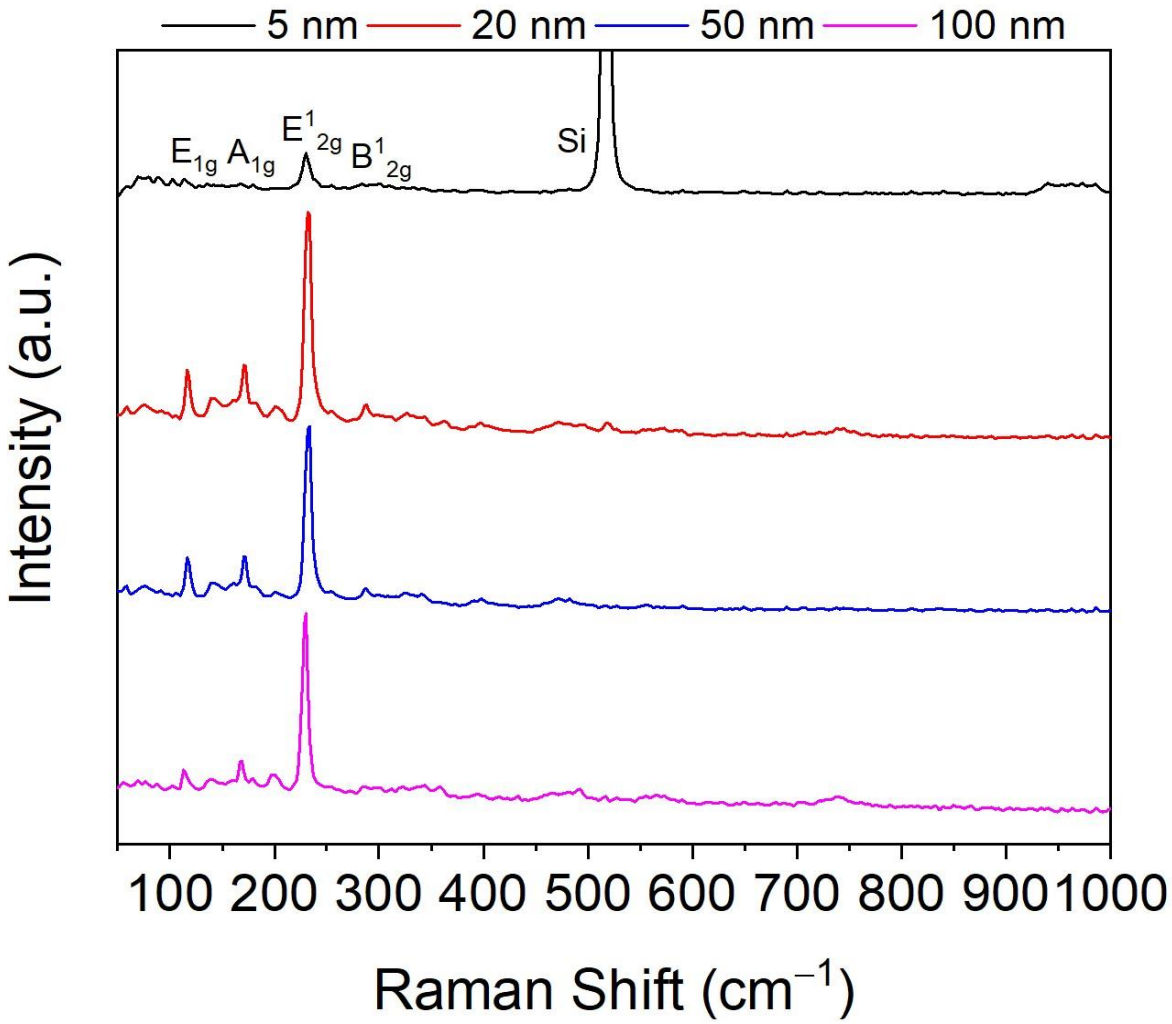

Figure 5-5: Raman spectra of 2H-$MoTe_2$ converted from 5, 20, 50 and 100 nm Mo/Si precursor films.

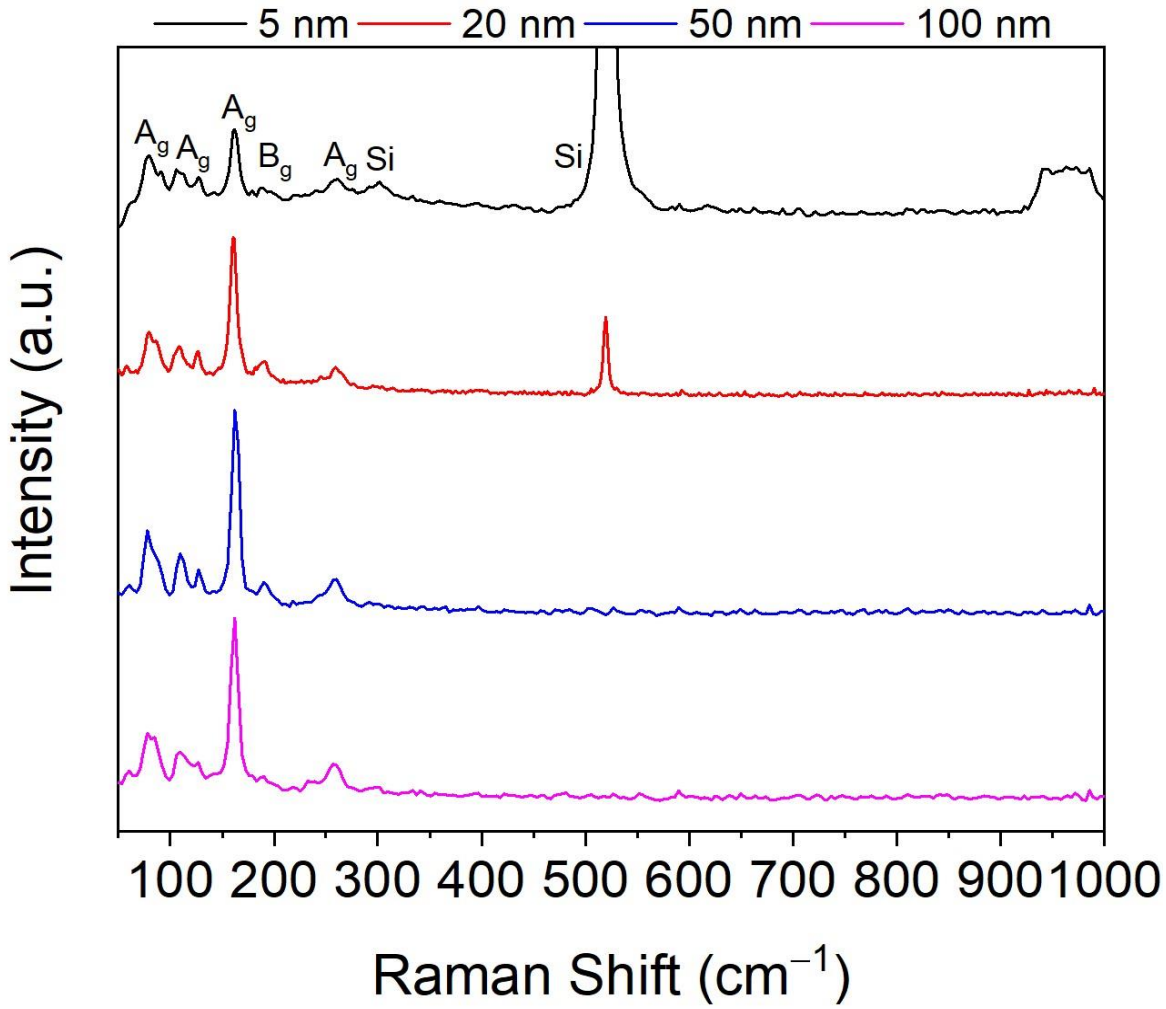

Figure 5-6: Raman spectra of 1T'-$MoTe_2$ converted from 5, 20, 50 and 100 nm MoO_3/Si precursor films.

$MoTe_2$ films converted from 5 nm Mo and MoO_3 precursor films were characterised using X-ray diffraction to investigate whether they orientate themselves with the basal plane parallel to the substrate, which would maximise the number of active sites. Figure 5-7 shows the obtained XRD patterns for 1T'- and 2H-$MoTe_2$ films, with only peaks from the *(00l)* family present for both phases. This confirms that the films grow stacked in the *c* direction with their basal planes parallel to the substrate. It should be noted that the peaks of 1T'-$MoTe_2$ are weaker than those of 2H-$MoTe_2$. This is most probably due to the 1T' film being thinner as there is less expansion when converting from MoO_3 to $MoTe_2$ compared to converting Mo to $MoTe_2$ and the same thickness of both precursor layers was used.

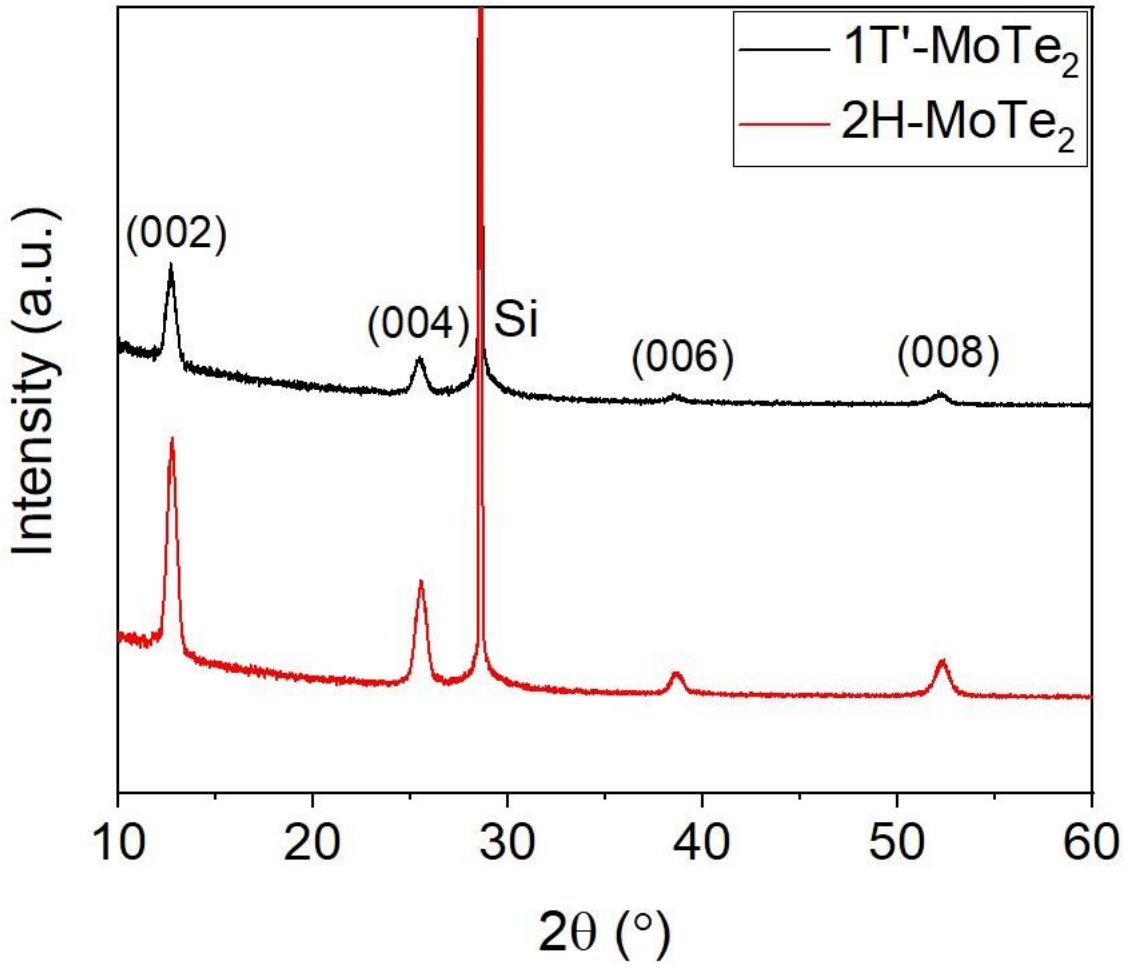

Figure 5-7: XRD patterns of 1T'- and 2H-$MoTe_2$ converted from 5 nm MoO_3 and Mo, respectively.

The films were then tested for their ability to catalyse the hydrogen evolution reaction using linear sweep voltammetry, with the potential required to achieve a current density of 10 mA cm^{-2} taken as the figure of merit. This value is often quoted for potential HER catalysts as it corresponds to the current density required for a 12.3% efficient solar to hydrogen device, which is the minimum efficiency required to make photoelectrochemical water splitting cost competitive.[15,32] Furthermore, normalising material performance to the electrode area allows for the easy comparison of catalysts tested under differing conditions. It is evident from the LSV scans in Figure 5-8 that the three thinnest 2H-$MoTe_2$ do not perform well at all, with each unable to reach a current density of 10 mA cm^{-2} even when large potentials are applied. Interestingly, the thickest film and the bulk powder, tested as a reference point, have nearly identical overpotentials (- 0.63 vs - 0.65 V) at 10 mA cm^{-2}. This suggests that catalyst loading may have been an issue for the thinner films, with an insufficient amount of 2H-$MoTe_2$ present to reach higher current densities. The overpotentials for the tested materials are summarised in Table 5-2.

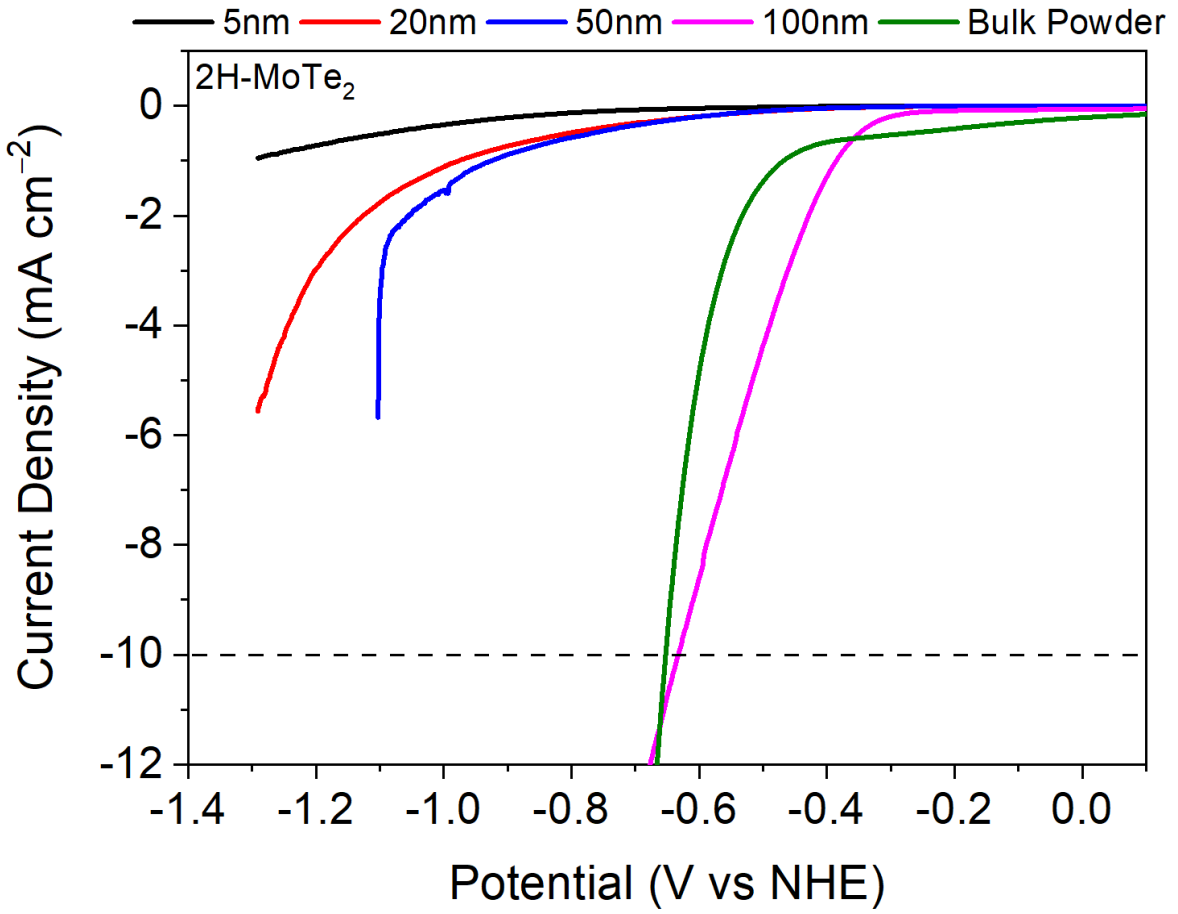

Figure 5-8: Linear sweep voltammetry of 2H-$MoTe_2$ films of varying thicknesses and bulk powder. The thicknesses refer to the precursor Mo layer thickness.

Table 5-2: Summary of overpotentials required to achieve a current density of 10 mA cm^{-2} for 2H-$MoTe_2$ films of varying thicknesses and bulk powder.

Catalyst	**Precursor Thickness (nm)**	**Overpotential (V) at 10 mA cm^{-2}**
2H-$MoTe_2$ film	5	-
2H-$MoTe_2$ film	20	-
2H-$MoTe_2$ film	50	-
2H-$MoTe_2$ film	100	- 0.63
2H-$MoTe_2$ powder	-	- 0.65

Subsequently, the 1T'-$MoTe_2$ films and bulk powder were tested in the same manner (Figure 5-9). In this case all of the films are able to achieve a current density of 10 mA cm^{-2}, although this value was only reached at very high overpotentials, which are summarised in Table 5-3. The increased conductivity of the 1T' phase compared to the 2H phase may explain why the 1T'-$MoTe_2$ films are able to attain higher current densities than 2H-$MoTe_2$ even when supplied with the same potential.[33] Once again there is a clear trend between increasing thickness and increasing performance of the catalyst film with a decrease in overpotential of 0.45 V observed between the films converted from 5 and 100 nm MoO_3, respectively. In research conducted by McManus *et* al. they also witnessed this thickness dependent

performance. The authors found that their electrodeposited films became rougher as they increased in thickness and as such had a higher porosity, resulting in a higher surface area and more active sites.[34] The results from the group are also summarised in Table 5-2, the method used involved electrodeposition of Te onto a precursor Mo layer before thermally assisted conversion to $MoTe_2$, which produces incredibly rough films. The R_q values for the films are significantly larger than their respective thicknesses, and their catalytic performance surpasses that of the CVD produced films in this work. However, their best performing film still possesses a higher overpotential than the bulk powder tested, suggesting that other methods are required for improving the performance of thin film $MoTe_2$ electrocatalysts. Unfortunately, the atomic force microscope was not available when these thin film catalysts were synthesised. As such the reason for the catalytic improvement with increasing thickness cannot definitely be attributed to increasing surface roughness, but from the literature reports on thin film $MoTe_2$ electrocatalysts this explanation seems highly likely.

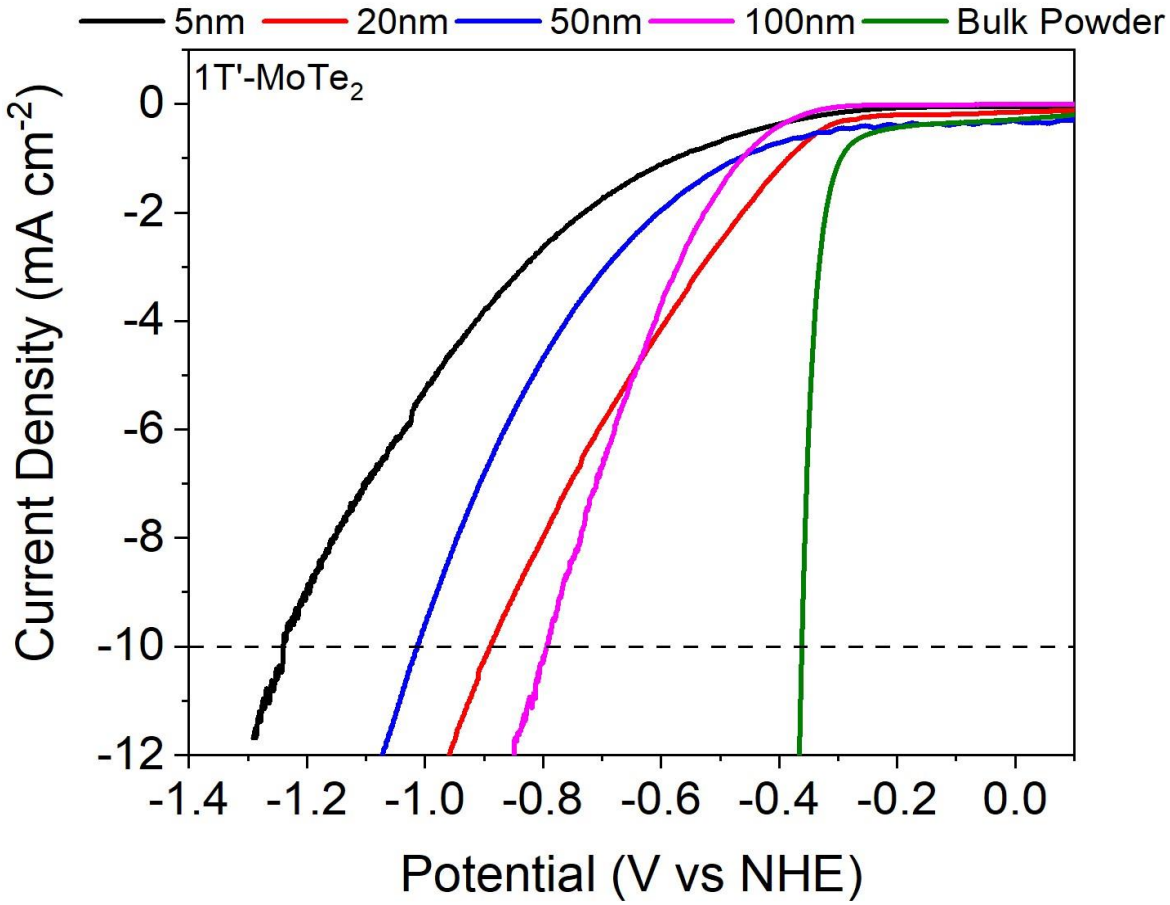

Figure 5-9: Linear sweep voltammetry of 1T'-$MoTe_2$ films of varying thicknesses and bulk powder. The thicknesses refer to the precursor MoO_3 layer thickness.

Table 5-3: Summary of overpotentials required to achieve a current density of 10 mA cm^{-2} for 1T'-$MoTe_2$ films of varying thicknesses and bulk powder. Also shown are the results obtained by McManus et al. revealing the relationship between film thickness, surface roughness (R_q) and the overpotential.[34]

Catalyst	**Precursor Thickness (nm)**	**Overpotential (V) at 10 mA cm^{-2}**
1T'-$MoTe_2$ film	5	-1.24
1T'-$MoTe_2$ film	20	- 1.01
1T'-$MoTe_2$ film	50	- 0.89
1T'-$MoTe_2$ film	100	- 0.79
1T'-$MoTe_2$ powder	-	- 0.36
1T'-$MoTe_2$ film (McManus *et al.*)	5 (R_q = 29 nm)	- 0.62
1T'-$MoTe_2$ film (McManus *et al.*)	30 (R_q = 56 nm)	- 0.50
1T'-$MoTe_2$ film (McManus *et al.*)	50 (R_q = 65 nm)	- 0.46

Disappointingly, the thickest 1T'-$MoTe_2$ film was outperformed by the 1T'-$MoTe_2$ powder with an overpotential difference of 0.43 V between the two, in contrast to 2H-$MoTe_2$. One possible explanation for this is the lack of stability observed for the 1T'-$MoTe_2$ films during electrochemical testing. Figure 5-10 shows a photograph of the thickest 2H- and 1T'-$MoTe_2$ films after LSV measurements, the 2H film looks identical before and after cycling. Whilst the 1T' film is heavily discoloured and looks visibly rougher than it did before the measurement. Although 1T'-$MoTe_2$ powder has been shown to be a very stable electrocatalyst, this is perhaps not the case for CVD grown films of 1T'-$MoTe_2$.[27,30]

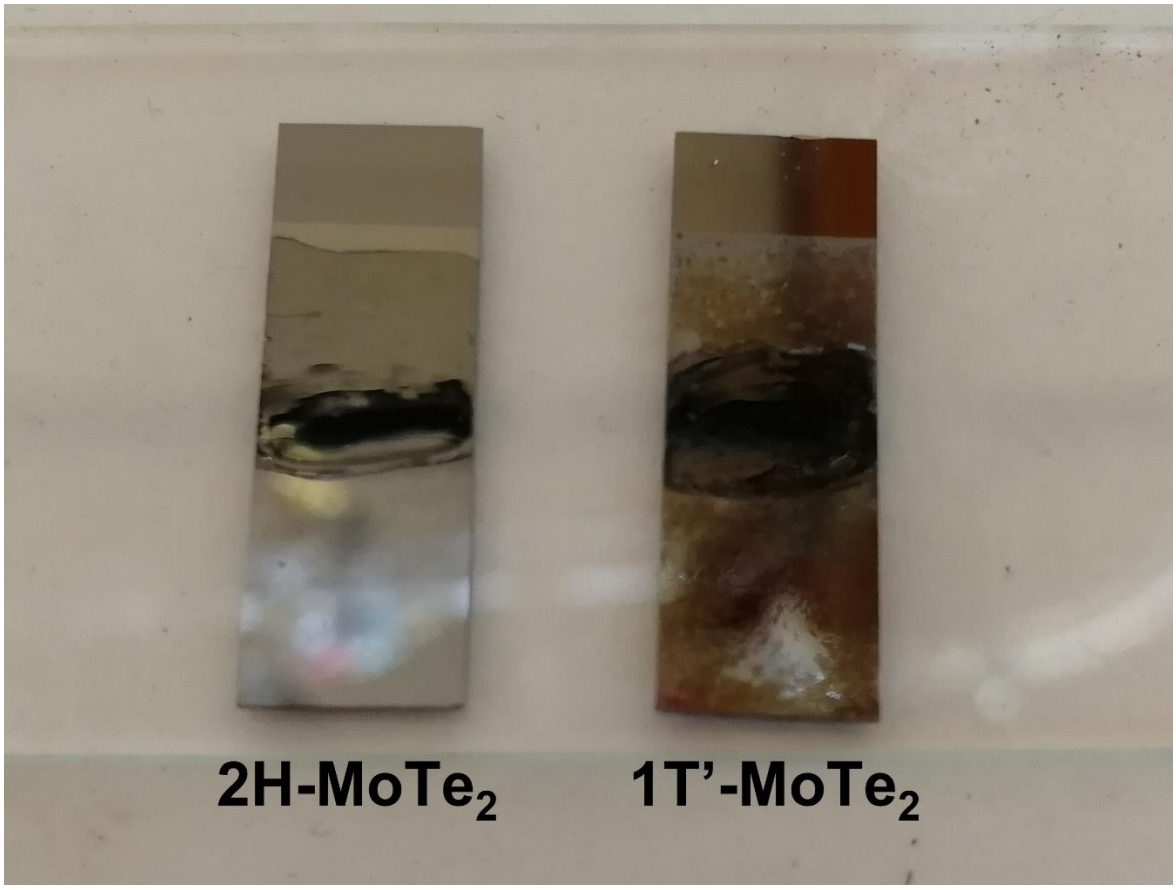

Figure 5-10: A photograph of the thickest 2H- and 1T'-$MoTe_2$ films after LSV measurements.

The poor electrocatalytic performance of CVD grown 1T'-$MoTe_2$ films was also observed by Zhuang *et al.* Their 1T'-$MoTe_2$ film, also converted from 5 nm Mo, was only able to achieve a current density of 4 mA cm^{-2} at an overpotential of - 0.94 V, a similar result to the 5 nm film in this work. In order to increase the performance, they used a gallium focused ion beam to selectively pattern defects into their films. For example, by patterning 40 line defects (200 μm × 1 μm) into their 1T' film they were able to increase the current density achieved to 15 mA cm^{-2} at an overpotential of - 0.57 V. They attribute this performance boost to the increased density of edge sites exposed, enhancing the conductivity of the film and reducing the charge transfer resistance. Taking this concept further the group tested different defect shapes, finding that covering the film in 180 nm hexagonal nanopores could drastically increase performance with a current density of 10 mA cm^{-2} achieved at an overpotential as low as -0.23 V.[35] This literature work highlighted how important the edge sites are to catalytic activity in the case of $MoTe_2$ thin films. Due to the extremely low surface roughness of the films produced by the CVD method used, previously shown in Chapter 3, it would be expected that basal plane active sites would make up the vast majority of active sites for the films employed in this work. This may explain the poor performance of the

unmodified CVD grown films. Table 5-4 compares the overpotentials achieved at 10 mA cm^{-2} for $MoTe_2$ prepared *via* various synthesis methods.

Table 5-4: HER performance of $MoTe_2$ synthesised by various methods.

Catalyst	**Synthesis Method**	**Overpotential (V) at 10 mA cm^{-2}**	**Reference**
1T'-$MoTe_2$ film	Thermally assisted conversion of electrodeposited precursors	- 0.46	[34]
1T'-$MoTe_2$	Solid-state synthesis	- 0.35	[27]
1T'-$MoTe_2$ with electrochemical activation	Solid-state synthesis	- 0.18	[30]
1T'-$MoTe_2$ with FIB engineered defects	CVD	- 0.23	[35]
2H-$MoTe_2$ single crystal	Flux method	- 0.65	[36]
1T'-$MoTe_2$ single crystal	Flux method	- 0.36	[36]
$MoTe_2$ nanosheets	Liquid phase exfoliation	- 0.31	[37]
1T'-$MoTe_2$ on porous carbon cloth	CVD	- 0.23	[38]
Ultrathin $MoTe_2$ nanowires	Templated hydrothermal synthesis followed by annealing	-0.41	[39]

The only CVD produced materials in Table 5-4 rely on defect engineering or a highly porous substrate to give good HER performance, meaning that the films produced by the CVD method developed in Chapter 3 are not ideal candidates as HER catalysts due to their low surface roughness and limited stability in the electrolyte. A potential solution would be to replace the precursor films with an electrodeposited precursor, with MoO_3 being successfully electrodeposited with great control over the morphology of the product film.[40] As the CVD process used for the production of $MoTe_2$ films in this work retains the morphology of the precursor film after deposition, conversion of a rough, porous electrodeposited MoO_3 film would offer a route to rough, high surface area 1T'-$MoTe_2$.

5.1.4. Conclusions

Both phase pure 1T'- and 2H-$MoTe_2$ thin films were grown on pure silicon substrates from varying thicknesses of precursor layers, with their phase confirmed by Raman spectroscopy. Their electrocatalytic performance towards the HER was then tested using linear sweep voltammetry, finding that performance improved for each phase with increasing thickness and with thin film 2H-$MoTe_2$ having an almost identical overpotential to its bulk powder. However, 1T'-$MoTe_2$ performed far worse than its bulk powder, possibly due to the lack of stability of the film, but it was in line with the literature performance of a pristine 1T' film. Despite the poor performance, there does seem to be methods for improving the catalytic ability of the films, such as engineering defects through ion-beam etching or by starting from rough electrodeposited precursors, resulting in films with much higher surface areas and therefore a greater density of active sites.

It is difficult to offer a direct comparison between the electrocatalytic performances of the molybdenum based dichalcogenides due to the variety of production methods used in the synthesis of the catalysts such as nanostructuring, defect engineering or the use of porous substrates/supports. However, $MoTe_2$ does have a distinct advantage over MoS_2 and $MoSe_2$ in that its metallic 1T'-phase is not metastable and can be synthesised directly, making it attractive for fundamental studies and testing computational models.

5.2. 1T'-$MoTe_2$ as a Substrate for Surface Enhanced Raman Spectroscopy

5.2.1. Introduction

Surface enhanced Raman spectroscopy (SERS) is an ultrasensitive and non-invasive analytical technique that has found widespread use in a variety of fields such as explosives detection, biosensing, monitoring environmental contaminants and bioimaging.[41–44] A wide array of materials have been explored for SERS applications mainly involving noble metals and two dimensional materials as well as their composites and heterostructures. Each having their own advantages and drawbacks.

5.2.1.1. Noble Metal Based SERS Substrates

Noble metal based SERS substrates offer highly efficient enhancement of the Raman signal of analyte molecules, with enhancement factors on the order of 10^{15} which is sufficient for single molecule detection.[45] The enhancement from these materials can be attributed to the enhanced local electromagnetic field due to the resonant excitation of plasmons in the metallic surface by the incident Raman laser. In turn this causes an increase in polarisation of the adsorbed analyte, enhancing its Raman signal.[46] This mechanism is known as the electromagnetic enhancement mechanism (EM).

Gold and silver nanoparticles are some of the most commonly used materials for SERS substrates as their surface plasmon resonance frequencies lie in the visible and near infrared regions, where several wavelengths of laser routinely used for Raman spectroscopy exist.[47] Despite their impressive enhancement factors, noble metal substrates do have several drawbacks, namely their expense, limited stability, strong spectral backgrounds and the often complicated fabrication processes used to generate the nanostructures.[48] Therefore, there has been significant effort to find non-metallic, plasmon free materials for SERS application.

5.2.1.2. 2D Material Based SERS Substrates

This search for noble-metal free SERS substrates led to a great deal of interest in 2D materials, such as graphene and the TMDCs, for applications in surface enhanced Raman spectroscopy. These materials do not provide Raman signal enhancement through the EM mechanism as their plasmon resonances are not typically in the visible range, graphene for example has a plasmon resonance in the terahertz range.[49] Instead, they give enhancement through what is termed the chemical mechanism (CM), which is mainly induced through charge transfer (CT) between the SERS substrate and analyte molecules, impacting the polarisability of the molecules and thus, increasing the Raman cross-section and Raman signal.[46] The CM can be further broken down into a subset of three different mechanisms

which include: (i) a molecular resonance mechanism where the incident beam is resonant with a molecular excitation, (ii) a CT mechanism due to resonance of the incident beam with an excitation from the substrate to the adsorbed analyte, and (iii) non-resonant enhancement due to chemical bonding between the adsorbed analyte and substrate.[46] The enhancement factors achieved tend to be lower for the CM compared to EM enhancement, although, recently limits of detection (LODs) for some typical Raman probe molecules on 2D material SERS substrates are approaching those achieved on noble metals.[50,51]

The interaction between the SERS substrate and probe molecule plays a crucial role in the CM derived Raman enhancement. Atomically flat surfaces allow for the uniform chemisorption of analyte molecules, required for good enhancement and can facilitate the acquirement of stable and reproducible Raman signals.[48] Furthermore, alignment of the band structures of the molecule-surface interface and the available energy levels of the SERS material should be favourable for charge transfer processes.[52] In this regard, the metallic and semi-metallic transition metal dichalcogenides like, 2H-NbS_2, 1T'-WTe_2, 1T'-$MoTe_2$, 1T'-ReS_2 and 1T-$NbTe_2$ have attracted enormous attention for SERS applications, with their chemical stability, biocompatibility and atomically flat surfaces being particularly advantageous.[53] Several of them possess a high density of states near the Fermi level, suggesting they can provide strong analyte-substrate coupling and facilitate effective charge transfer.[54] In addition, chemical vapour deposition has been shown to be a suitable method for the production of large-area, few-layered TMDCs with atomically flat surfaces, allowing for relatively straight forward large scale production of these materials.[55]

Table 5-5 offers a comparison for the LODs achieved by various 2D materials for common Raman probes. The performance of 1T'-WTe_2 is particularly impressive in the work of Tao *et al.* with detection of R6G possible at concentrations as low as 10^{-13} M. The authors were able to improve the LOD even further by integrating WTe_2 flakes with a distributed Bragg reflector, making detection of R6G possible at femtomolar levels.[50] The table also shows the vast differences in performance between the metallic and semiconducting TMDCs with Song *et al.* observing a difference of three orders of magnitude between the LODs on metallic 1T-MoS_2 and semiconducting 2H-MoS_2. This was attributed to the increased efficiency of charge transfer from the Fermi level of the 1T-phase to the highest occupied molecular orbital of the probe molecule over that from the top of the valence band of 2H-MoS_2.[51] This result was in agreement with a similar study previously conducted by Yin *et al.*[56]

Table 5-5: A comparison of LODs achieved by various 2D material SERS substrates for several common Raman probes.

SERS Substrate	**Analyte**	**LOD**	**Reference**
1T'-WTe_2	Rhodamine 6G	10^{-13} M	50
	Crystal Violet	10^{-13} M	
	Rhodamine B	10^{-12} M	
NbS_2	Methylene Blue	10^{-12} M	51
1T-MoS_2	Methylene Blue	10^{-6} M	
2H-MoS_2	Methylene Blue	10^{-3} M	
Mechanically exfoliated graphene	Rhodamine 6G	10^{-9} M	57
	Protoporphyrin	10^{-7} M	
N-doped graphene	Rhodamine B	10^{-11} M	52
	Rhodamine 6G	10^{-8} M	
	Protoporphyrin	10^{-8} M	
1T-MoS_2	Rhodamine 6G	10^{-8} M	56
1T-$MoSe_2$	Rhodamine 6G	10^{-8} M	
1T'-ReS_2	Rhodamine 6G	10^{-9} M	58
	Methylene Blue	10^{-9} M	
	Crystal Violet	10^{-8} M	
	Rhodamine B	10^{-8} M	
$NbTe_2$	Rhodamine 6G	10^{-9} M	59
1T-$HfTe_2$	Uric Acid	10^{-4} M	60

Although there has been a significant amount of research into the application of TMDCs as SERS substrates, the analytes used have tended to be a limited range of model Raman dyes. This is sufficient for fundamental studies and is useful for bench marking the performance of previously untested materials but the full potential of TMDCs as SERS substrates can only be realised by testing clinically relevant analytes in real world scenarios.

5.2.2. Aims

The aims of this section are to conduct a preliminary study into the application of 1T'-$MoTe_2$ thin films as SERS substrates. Initially, rhodamine 6G will be used as an analyte due to the extensive research conducted in conjunction with TMDC SERS substrates. Furthermore, the layer dependent SERS performance of 1T'-$MoTe_2$ will be investigated by utilising few-layer and many-layer films as substrates before a simple concentration dependent study is performed. Subsequently, a more in-depth study of 1T'-$MoTe_2$ as a SERS substrate will be conducted with the CVD produced thin films characterised extensively *via* Raman spectroscopy, AFM and water contact angle (WCA) measurements. Then the films will be investigated for their SERS performance for a clinically relevant molecule, β-sitosterol, with extensive SERS measurements carried out to determine their performance, stability and recyclability. Finally, efforts will be made to characterise any complex formed between the analyte and 1T'-$MoTe_2$ with techniques including, UV-vis and IR spectroscopy as well as electrochemical measurements and allowing for the mechanism of Raman enhancement to be discerned.

5.2.3. Results and Discussion

5.2.3.1. A Preliminary Study of 1T'-$MoTe_2$ as a SERS Substrate

Previous research has found that two dimensional materials can act effectively as SERS substrates. Interestingly, they exhibit layer-dependent performance, typically thinner films perform better than their bulk counterparts.[50,56–58,61–65] Therefore, a preliminary study was conducted in the use of 1T'-$MoTe_2$ as a SERS substrate for the detection of the dye molecule Rhodamine 6G, the structure of which is displayed in Figure 5-11.

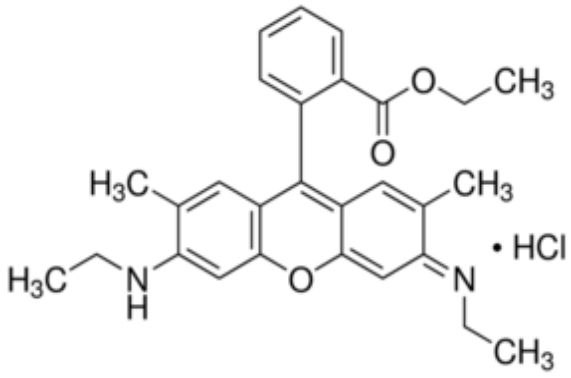

Figure 5-11: The structure of Rhodamine 6G.

Rhodamine 6G was chosen as an analyte as extensive research has been conducted using it for SERS measurements with 2D materials and its Raman peaks are found between 600-1800 cm^{-1} meaning that the Raman peaks of 1T'-$MoTe_2$ will not interfere, allowing unambiguous assignments to be made.[50,56–58,62,63] For the initial test, a solution of rhodamine 6G with a concentration of 500 nM was dropcast onto a bare SiO_2/Si substrate, an 11-layer 1T'-$MoTe_2$ film and a 5-layer 1T'-$MoTe_2$ film. The Raman spectra recorded are shown in Figure 5-12.

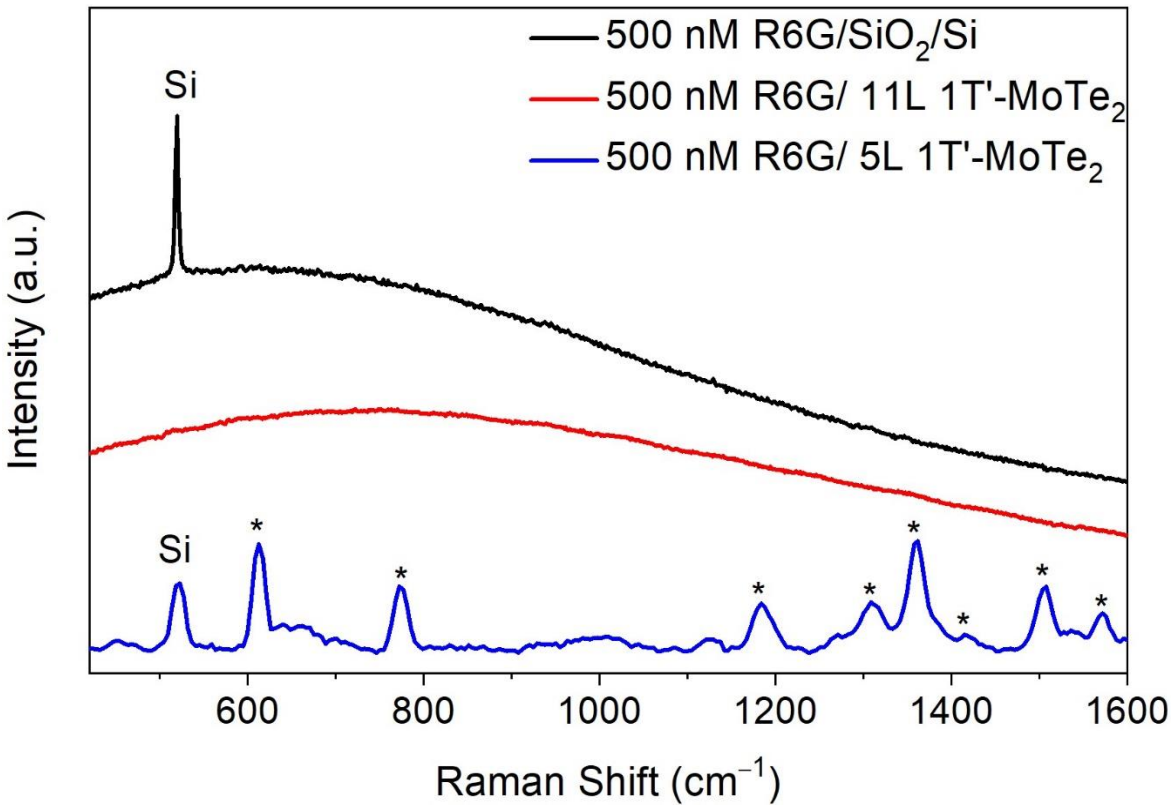

Figure 5-12: 532 nm Raman spectra of 500 nM solution of Rhodamine 6G drop cast on bare SiO_2/Si, 11-layer 1T'-$MoTe_2$ and 5-layer 1T'-$MoTe_2$. Peaks belonging to R6G are marked with "" and those belonging to the SiO_2/Si substrate are denoted "Si".*

Interestingly, there are no Raman signals resulting from the R6G deposited on the SiO_2/Si substrate or 11-layer 1T'-$MoTe_2$ film, with both spectra dominated by large fluorescence backgrounds. In contrast to this, the fluorescence is massively suppressed by the 5-layer 1T'-$MoTe_2$ film and Raman modes of the dye, labelled with "*", are clearly visible. The suppression of fluorescence is thought to arise through efficient charge transfer between the $MoTe_2$ film and R6G dye, which decreases the fluorescence cross section and subsequently causes fluorescence quenching.[50] The dramatic difference in performance between the 5-layer and 11-layer 1T'-$MoTe_2$ films has also been observed in other 2D material systems where the intensity of the Raman dye signal decreases with the increasing thickness of the SERS substrate.[50,63,66,67] Potential reasons for this include, the layer dependent nature of the band structures of 2D materials, substrate induced doping, or the varying chemisorption abilities of films with different thicknesses.[63,67] It should be noted that in the case of R6G on 11-layer 1T'-$MoTe_2$ that there is no peak corresponding to the silicon substrate in the Raman spectrum. It seems unlikely that the thickness of the $MoTe_2$ film is the cause of this as it is only around 8nm thick. It is possible that the dropcasting method used in the deposition of the R6G solution resulted in the agglomeration of R6G molecules on the surface and therefore formed a thicker layer than expected, masking the signal from the silicon substrate.

In future SERS studies spincoating could be used for the deposition of the analyte to irradicate this potential issue.

A wide-ranging Raman spectrum of R6G on 5-layer 1T'-$MoTe_2$ (Figure 5-13) clearly shows that the Raman peaks of 1T'-$MoTe_2$ do not interfere with those of the R6G dye. Interfering Raman peaks can sometimes be an issue for trace level detection of organic molecules on noble metal-based SERS substrates, limiting their usefulness.[68]

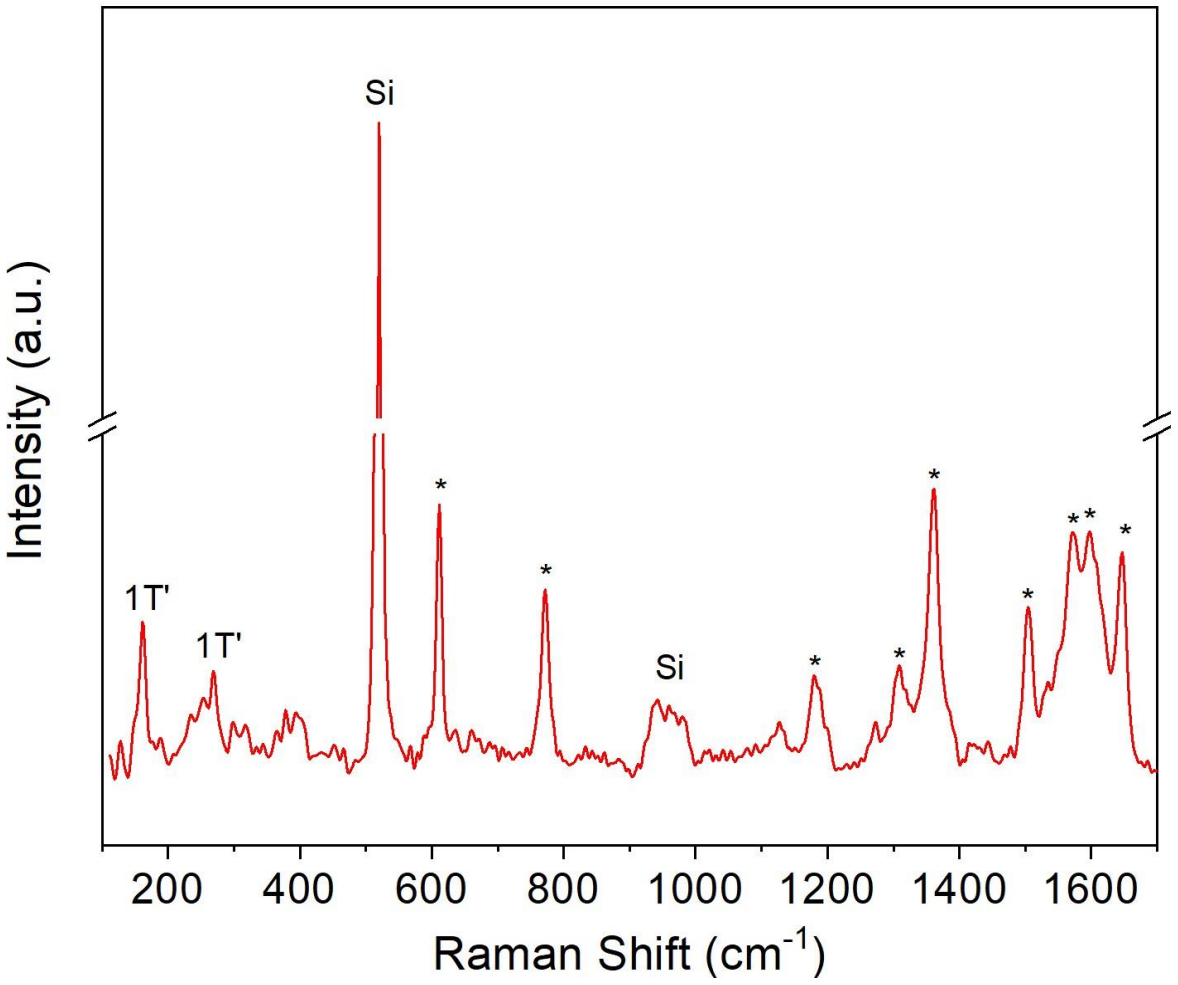

Figure 5-13: Wide ranging 532 nm Raman spectrum of 500 nM Rhodamine 6G solution drop cast on the surface of a 5-layer 1T'-$MoTe_2$ film on SiO_2/Si. The peaks of 1T'-$MoTe_2$ marked as "1T'", the most intense peaks of Rhodamine 6G are marked with "" and peaks belonging to the substrate are denoted "Si".*

As SERS is a technique used routinely to probe trace amounts of molecules, the sensitivity of 1T'-$MoTe_2$ as a SERS substrate was tested. Solutions of R6G with concentrations ranging from 0.5-500 nM were dropcast onto 5-layer 1T'-$MoTe_2$ and their Raman spectra recorded. In Figure 5-14 it is possible to observe the characteristic Raman peaks of R6G for the 500 and 50 nM solutions at 612, 773, 1184, 1308, 1360,1508, 1569, 1602 and 1646 cm^{-1}, consistent with literature spectra.[57,69] However, below these concentrations, at 5 nM for instance, it is only possible to distinguish the peaks at 612, 773 and 1360 cm^{-1} from the

background, whilst those in the range of 1569-1646 cm^{-1} exhibit a significant broadening to the extent that it is not possible to identify them individually. It is not possible to distinguish any peaks in the spectrum recorded from the 0.5 nM solution.

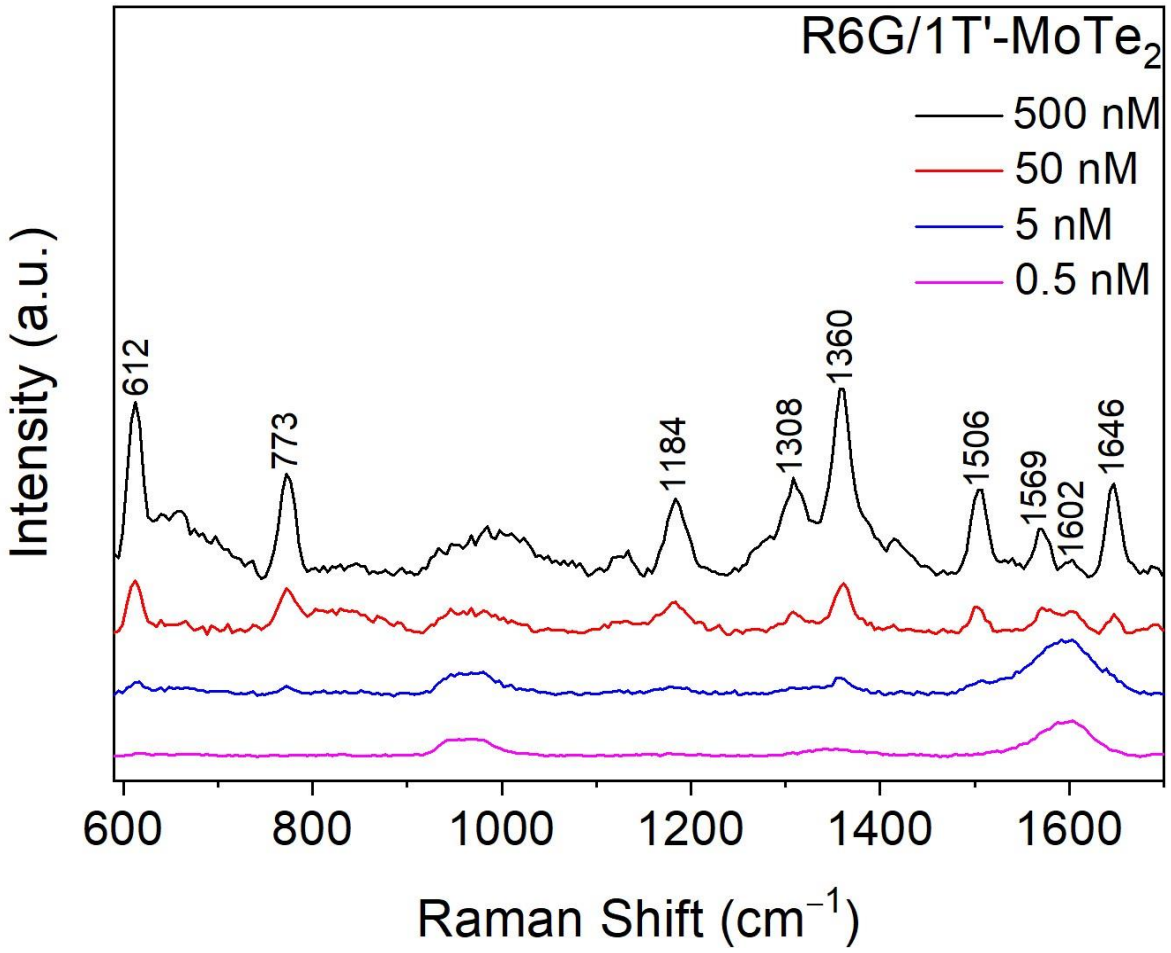

Figure 5-14: 532 nm Raman spectra recorded from R6G solutions with concentrations ranging from 0.5-500 nM dropcast on 5-layer 1T'-$MoTe_2$/SiO_2/Si. Peaks corresponding to R6G are labelled with their respective Raman shift.

Tao *et al.* were able to detect R6G at concentrations as low as 4×10^{-14} M using CVD grown flakes of 3-layer 1T'-WTe_2, significantly outperforming the 1T'-$MoTe_2$ films employed in this work. It is possible that the number of layers of WTe_2 used is crucial to this impressive performance as with increasing thickness the performance of WTe_2 drops off.[50] This suggests that by depositing thinner films of 1T'-$MoTe_2$ the SERS performance towards R6G could be improved. Nonetheless, the results obtained from this brief study were encouraging enough to further investigate the application of 1T'-$MoTe_2$ as a SERS substrate.

5.2.3.2. 1T'-$MoTe_2$ as a SERS Substrate for β-Sitosterol

The majority of studies using TMDCs as SERS substrates have utilised dye molecules like rhodamine 6G, rhodamine B or crystal violet and in this regard, it is important to expand the library of analytes studied to truly understand the potential of TMDCs as SERS substrates. Therefore, β-sitosterol was chosen as an analyte for a more in-depth study. β-sitosterol is an interesting target for investigation as it is a lipophilic marker for type 1 diabetes, coronary artery disease and cardiovascular disease, the structure of the molecule is shown in Figure 5-15.[70]

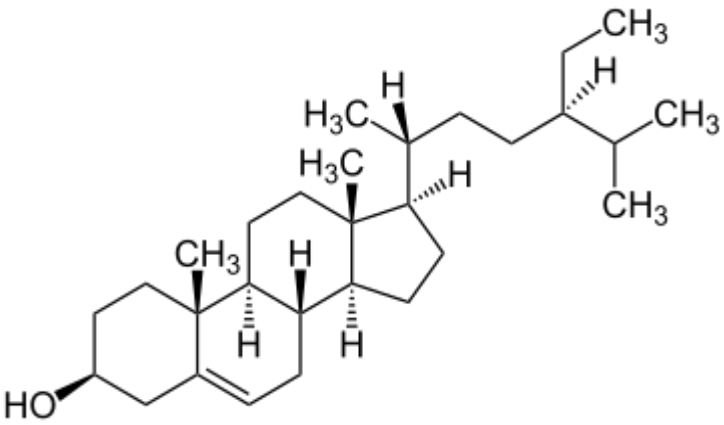

Figure 5-15: Structure of β-sitosterol.

The detection of β-sitosterol on noble-metal SERS platforms is hampered by low levels of detectable signals. Some successful research in this area has shown that it is possible to detect β-sitosterol in mM concentrations using grafted gold surfaces adorned with lipophilic functional groups.[68] Unfortunately, overlapping Raman peaks of the lipophilic functional groups and β-sitosterol make trace sensing extremely difficult. In this regard, the 2D transition metal tellurides, with their hydrophobic surfaces and lack of interfering Raman peaks, may potentially be useful as sensing platforms for trace level detection of β-sitosterol.[55,71]

5.2.3.2.1. Characterisation of 1T'-$MoTe_2$ Films to be used as SERS Substrates

To investigate the applicability of 1T'-$MoTe_2$ films as SERS substrates for β-sitosterol, films were converted, using the method and the CVD setup discussed in Chapter 3.3.4, from MoO_3 precursor layers with thicknesses of 1.5, 3, 4.5 and 6 nm. This resulted in the formation of 1T'-$MoTe_2$ films with thicknesses corresponding to 5, 7, 8 and 10 layers, respectively. AFM was used to determine the thicknesses of these 1T'-$MoTe_2$ films, and the images are shown in Figures 5-16 and 5-17. To confirm their phase as 1T'-$MoTe_2$, the films were characterised by Raman spectroscopy. Figure 5-18 shows the spectra recorded from the films, A_g modes

at ~109, ~127, ~161 and ~257 and a B_g mode at ~189 cm^{-1} confirm the films are all phase pure 1T'-$MoTe_2$.

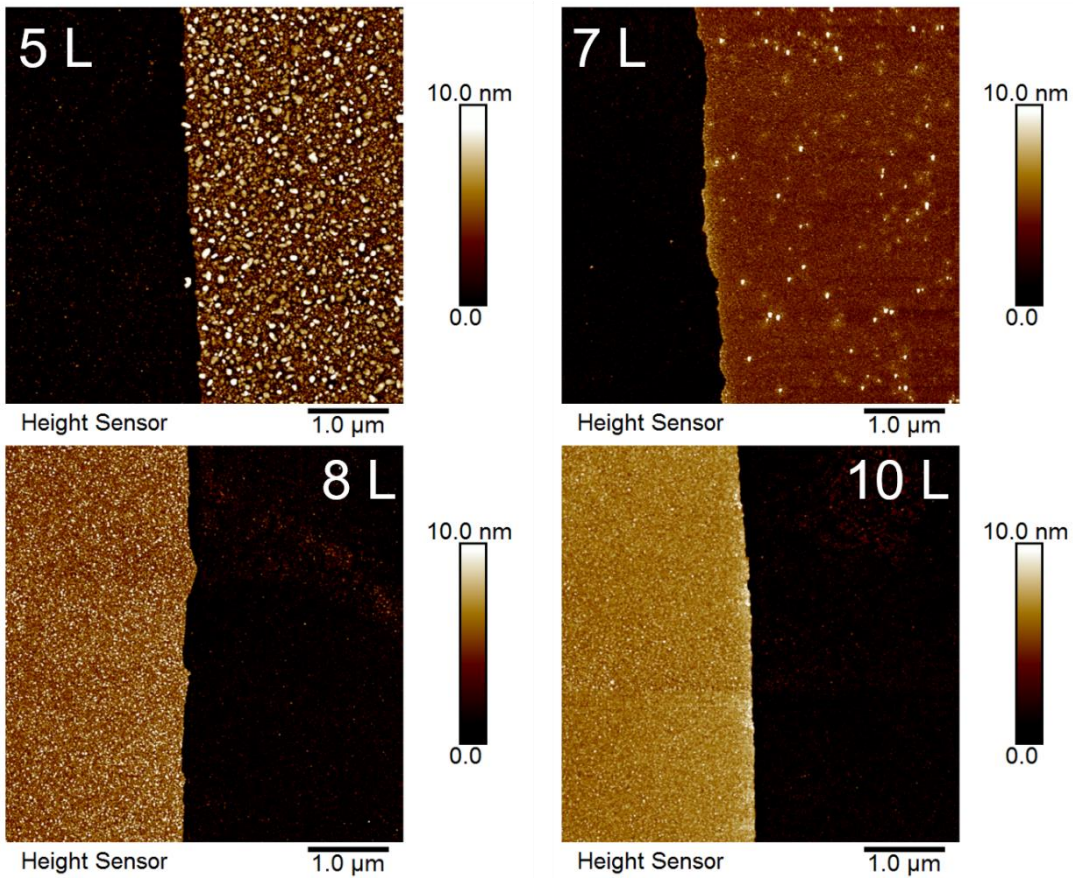

Figure 5-16: 2D topographic profiles of the interface between few-layered 1T'-$MoTe_2$ films ranging from 5-10 layers in thickness and SiO2/Si substrates.

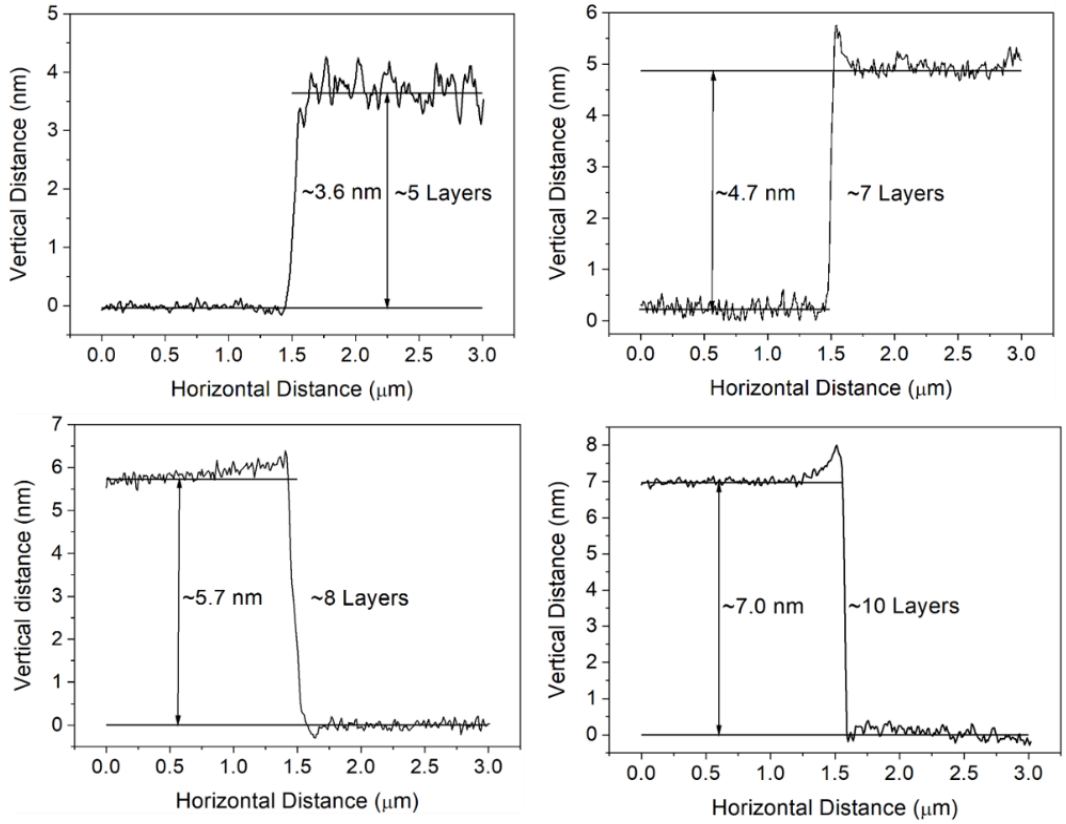

Figure 5-17: The variation in height between 1T'-MoTe2 films (corresponding to images in Figure 3-33) and their substrates from AFM measurements.

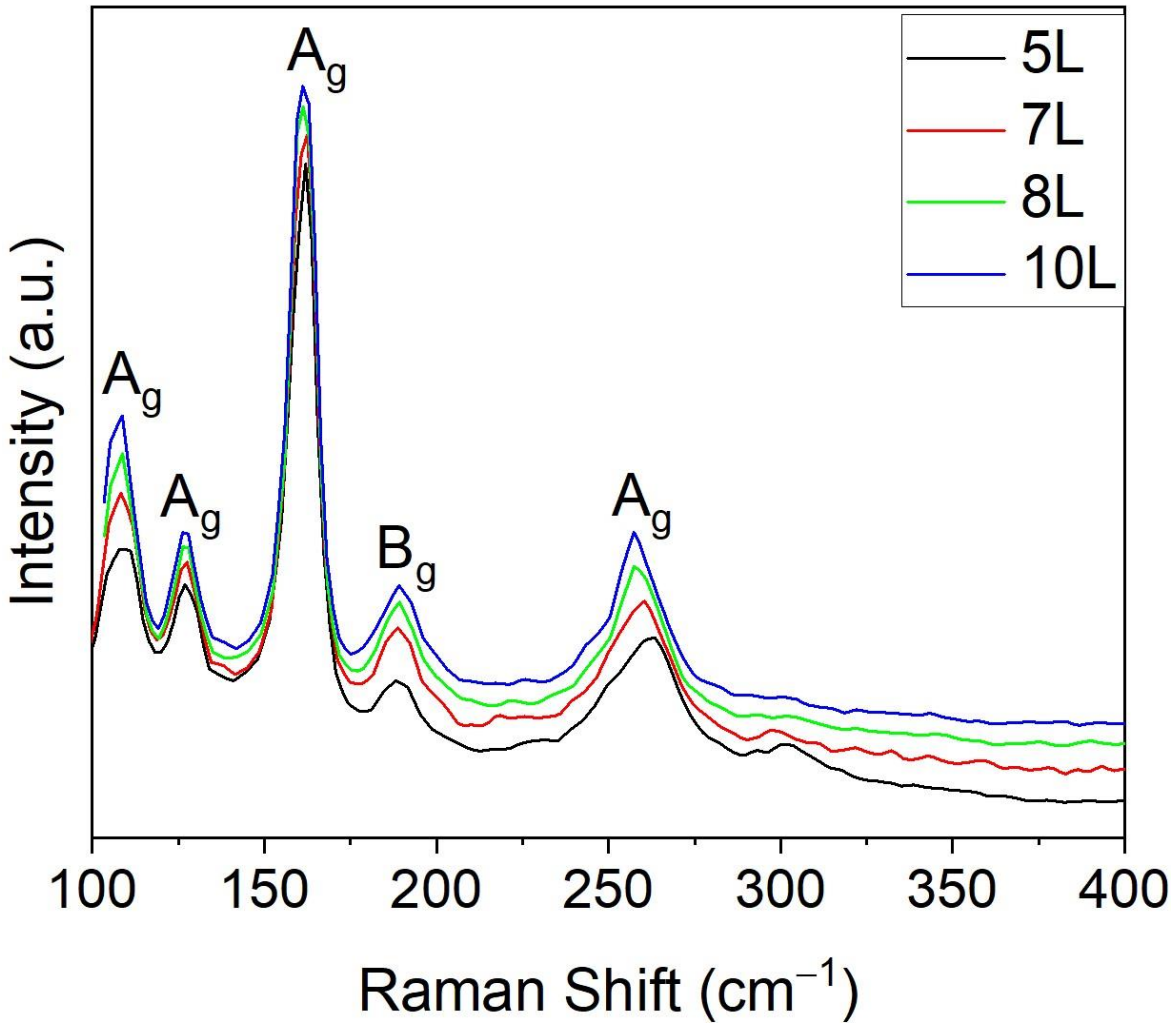

Figure 5-18: 532 nm Raman spectra of 1T'-$MoTe_2$ films of varying thicknesses used as SERS substrates.

As well as measuring the films thicknesses, AFM was also used to determine the surface roughness of the 1T'-$MoTe_2$ films. The values of root mean square surface roughness (R_q) for each film are highlighted in Table 5-6 and the corresponding 2D topographic profiles of the 5×5 μm^2 areas from where these values were obtained are shown in Figure 5-19 The measured R_q values indicate that the films are all smooth and uniform with every film having an R_q value below 1 nm. There is no trend between increasing thickness and increasing roughness of the films, meaning that any differences in SERS performance between the films cannot be attributed to differences in surface roughness.

Table 5-6: Surface roughness values of 1T'-$MoTe_2$ films of varying thicknesses used as SERS substrates.

Number of 1T'-$MoTe_2$ Layers	**R_q (nm)**
5	0.580
7	0.569
8	0.572
10	0.606

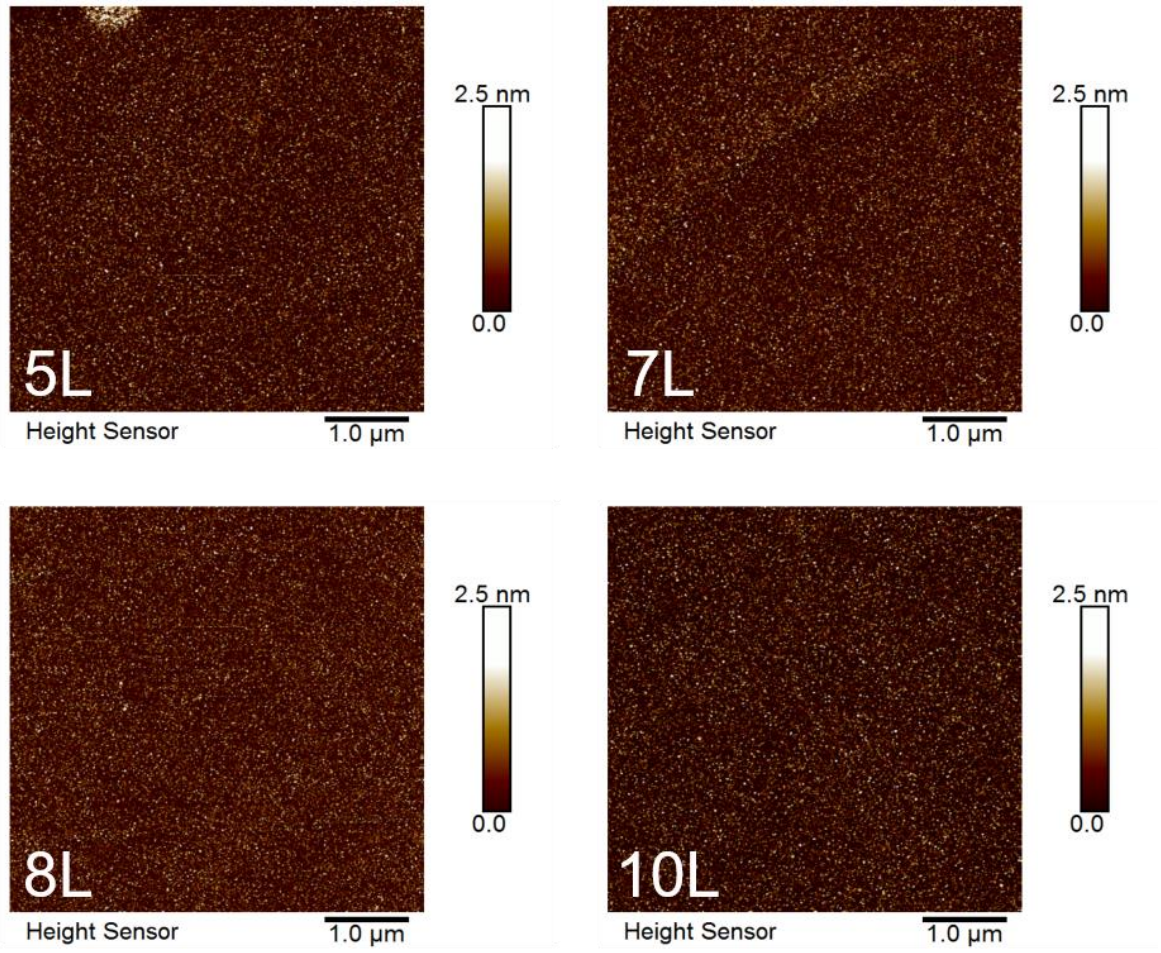

Figure 5-19: 2D topographic profiles of 5×5 µm^2 areas of 1T'-$MoTe_2$ with varying numbers of layers used as SERS substrates.

As β-sitosterol, the chosen analyte, is a lipophilic molecule it was decided to investigate the hydrophobicity of the 1T'-$MoTe_2$ films by performing water contact angle measurements. Figure 5-20 highlights the contact angles of the films and how they vary with increasing thickness. There is little difference between the contact angles of the 5- and 7-layered films, with both displaying contact angles of around 90°, indicating that they are both hydrophobic. An increase in the thickness of the films results in a drastic reduction in the water contact angle with the 10-layered film having a contact angle of around 65°, meaning that the thicker

films are much more hydrophilic in nature than the 5- and 7-layered films. Therefore, it is likely that the thinner films will allow for a more homogeneous distribution of the analyte due to the lipophilic nature of β-sitosterol. This should also lead to enhanced surface-analyte interactions for the thinner films, resulting in improved surface distribution and adsorption compared to the hydrophilic thicker films.

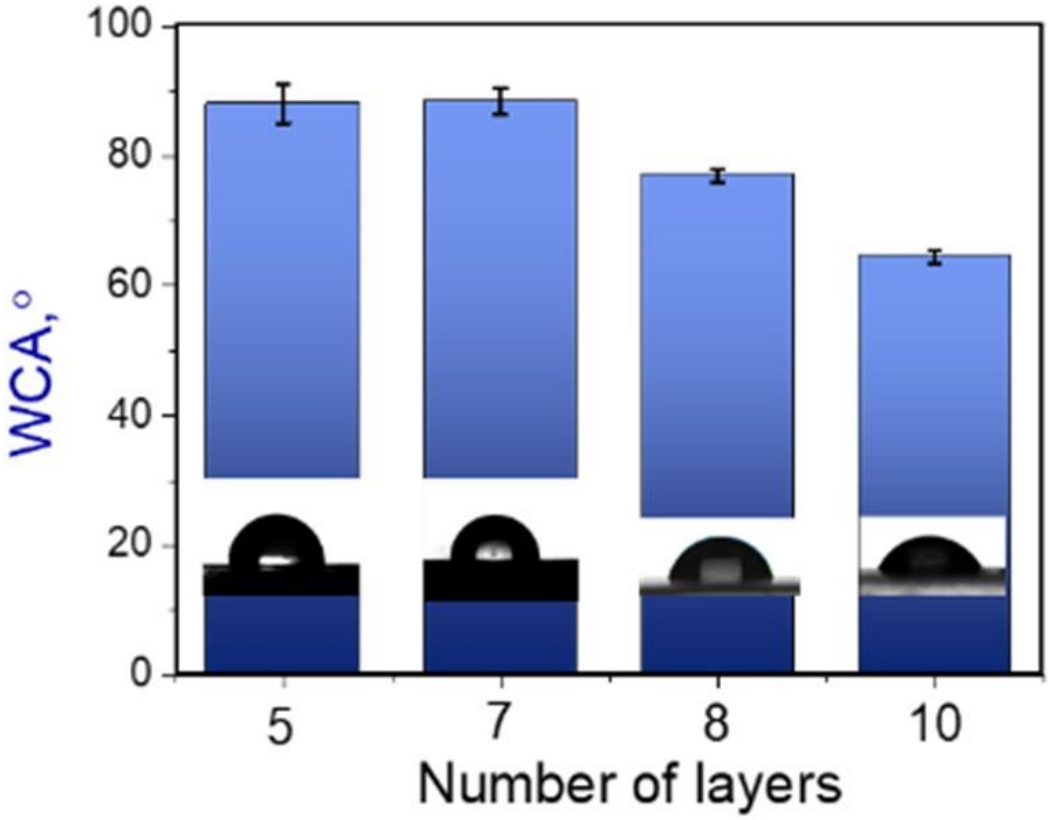

Figure 5-20: Water contact angles measured on 5, 7, 8 and 10 layered 1T'-$MoTe_2$ films, inset with the images of the water droplets on the films.

A decrease in WCA with increasing thicknesses of two-dimensional materials has been observed before by several groups. Gaur *et al.* found that increasing the thickness of their CVD grown MoS_2 resulted in a decrease in WCA, similarly Jaiswal *et al.* obtained the same result, again with MoS_2.[72,73] In their study Jaiswal *et al.* also investigated the impact that defect concentration has on the water contact angle, finding that an increased number of defects led to a decrease in WCA. Therefore, it is plausible that the decrease in WCA observed with increasing thickness of the 1T'-$MoTe_2$ films is related to an increase in the number defects for these thicker films.

5.2.3.2.2. β-Sitosterol SERS Measurements on 1T'-$MoTe_2$

Firstly, efforts were made to determine the effect that varying the number of layers of 1T'-$MoTe_2$ has on the sensing of β-sitosterol. β-sitosterol solutions (1:2 water/ethanol) in concentrations of 10^{-5}, 10^{-6} and 10^{-7} M were spin-coated onto the 1T'-$MoTe_2$ films and Raman spectra recorded. Figure 5-21 shows how the intensity of the main characteristic peak of β-sitosterol (~1668 cm^{-1}) varies with the number of layers of 1T'-$MoTe_2$ and the concentration of the analyte solutions used.

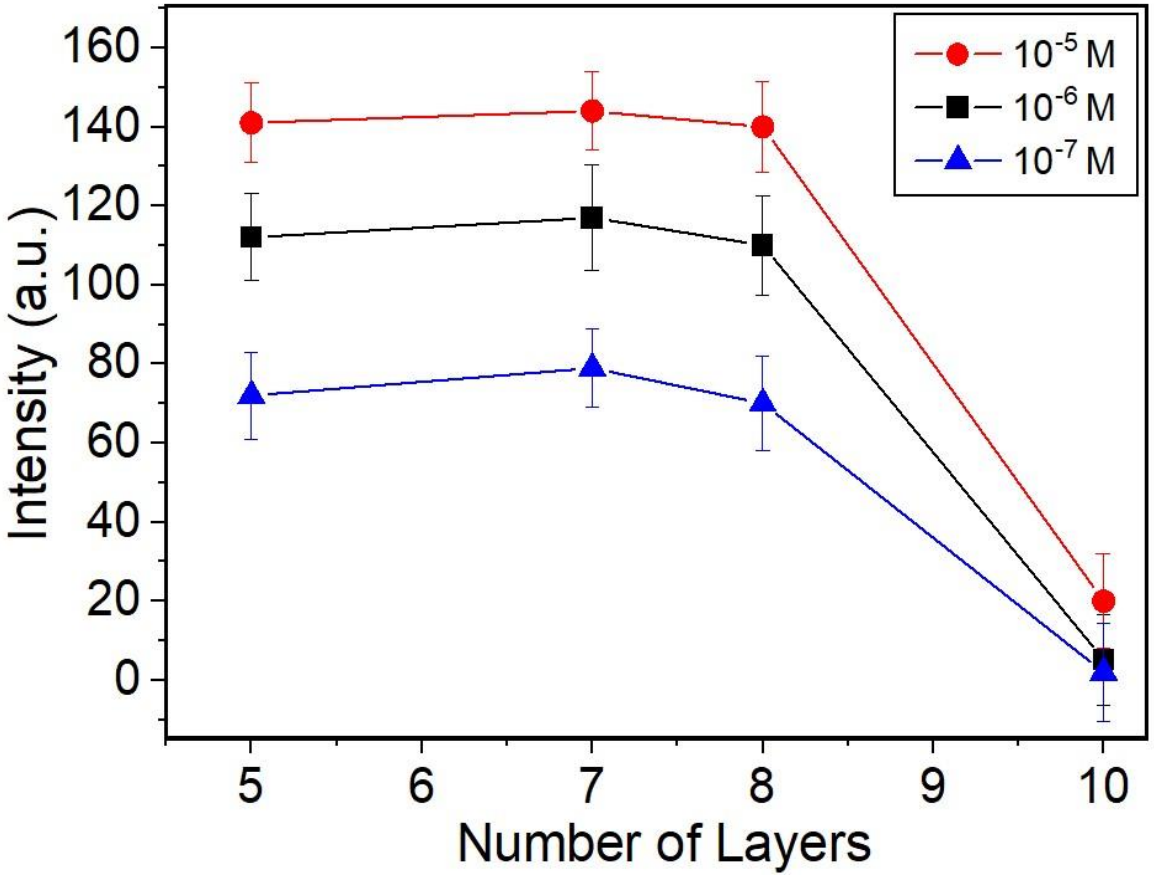

Figure 5-21: A plot showing how the intensity of the 1668 cm^{-1} Raman peak of β-Sitosterol varies with the number of layers of 1T'-$MoTe_2$ SERS substrates for various concentrations of β-Sitosterol solutions.

It is evident that there is little difference in the intensities achieved when using the 5- or 7-layer 1T'-$MoTe_2$ films as SERS substrates, whilst an increase in the thickness results in a slight drop off in intensity for the 8-layered film. For the thickest 10-layer film, the main peak of β-sitosterol becomes almost indistinguishable from the background for the 10^{-6} and 10^{-7} M solutions mirroring the results obtained earlier when using R6G as an analyte.

To investigate the homogeneity of β-sitosterol deposition on the 7- and 10-layered 1T'-$MoTe_2$ films Raman mapping was employed. The variation in intensity of the 1668 cm^{-1} peak on the 7-layer film (Figure 5-22a) reveals excellent homogeneity across the mapped area (1.4 mm × 0.8 mm), with a mean square roughness of 0.52. Conversely, mapping β-

sitosterol deposited on a 10-layer film reveals a much more inhomogeneous distribution of the analyte with a mean square roughness of 41.6 (Figure 5-22b). Although the 10-layered film had a greater surface roughness than the 7-layered film it is not considerable enough to cause such a significant increase to the inhomogeneity of analyte distribution.

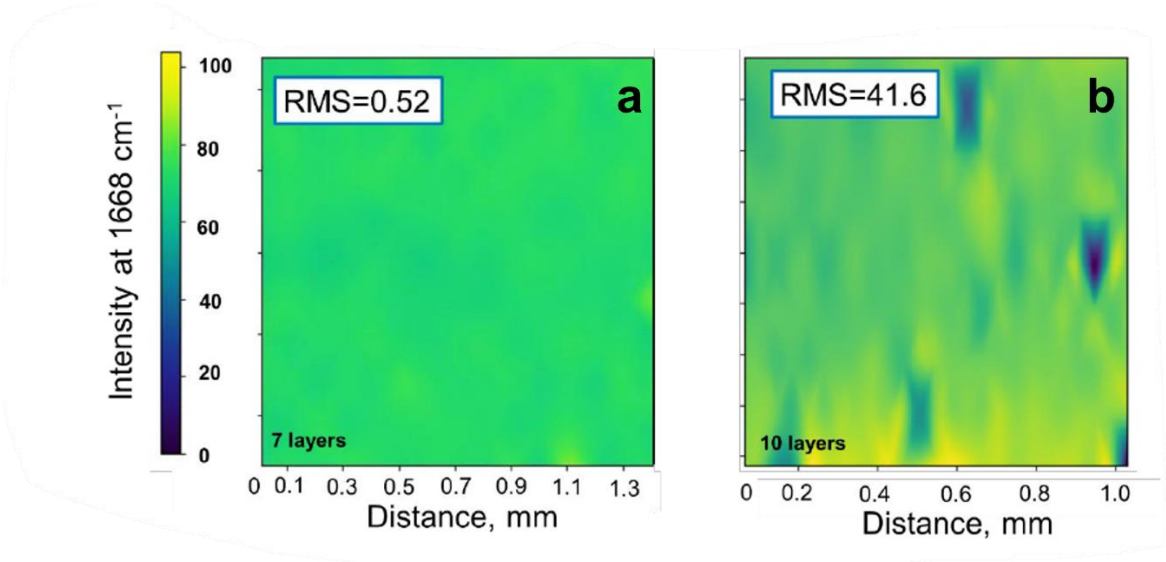

Figure 5-22: Raman maps of the intensity of the 1668 cm^{-1} peak of β-sitosterol deposited on 7-layer 1T'-$MoTe_2$ (a) and 10-layer 1T'-$MoTe_2$ (b).

As the 7-layered 1T'-$MoTe_2$ film achieved the highest intensities for each of the solutions measured in Figure 5-20 it was decided to use this thickness of film to try and determine the limit of detection for β-sitosterol on 1T'-$MoTe_2$. Solutions of β-sitosterol with concentrations ranging from of 10^{-4} to 10^{-9} M were deposited onto 7-layer 1T'-$MoTe_2$ and Raman spectra recorded. Figure 5-23 shows the spectra obtained from the solutions with concentrations of 10^{-4}, 10^{-6}, 10^{-8} and 10^{-9} M, respectively. The characteristic Raman peaks of β-sitosterol at ~889 and ~1668 cm^{-1} are clearly distinguishable for all concentrations tested. Furthermore, a plot of the intensity of the 1668 cm^{-1} peak against the logarithm of β-sitosterol concentration reveals an excellent linear correlation between the two with an R^2 value of 0.99879 (Figure 5-24).

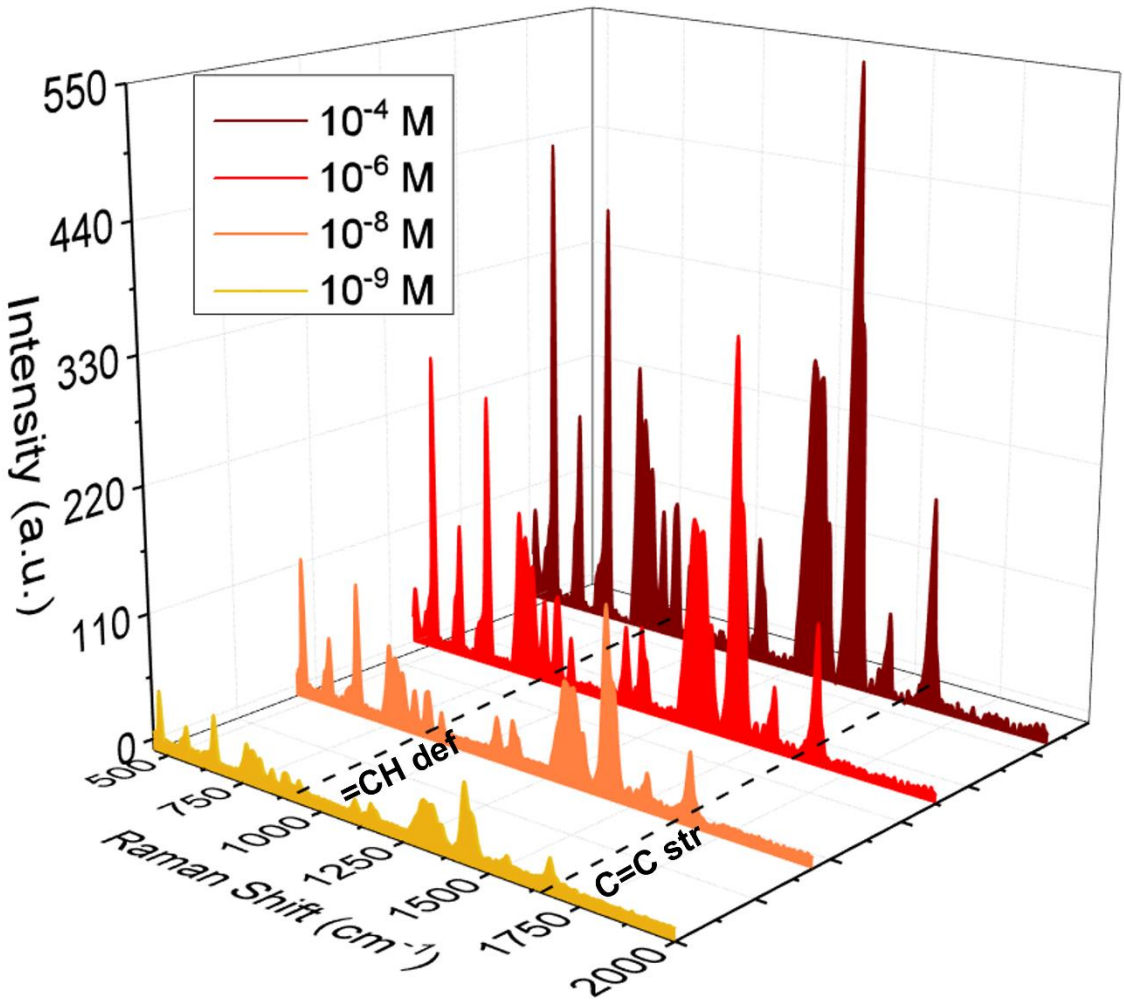

Figure 5-23: Raman spectra recorded for β-sitosterol deposited on 7-layer 1T'-$MoTe_2$ in concentrations of 10^{-4}, 10^{-6}, 10^{-8} and 10^{-9} M. The main characteristic peaks at 889 and 1668 cm^{-1} are marked.

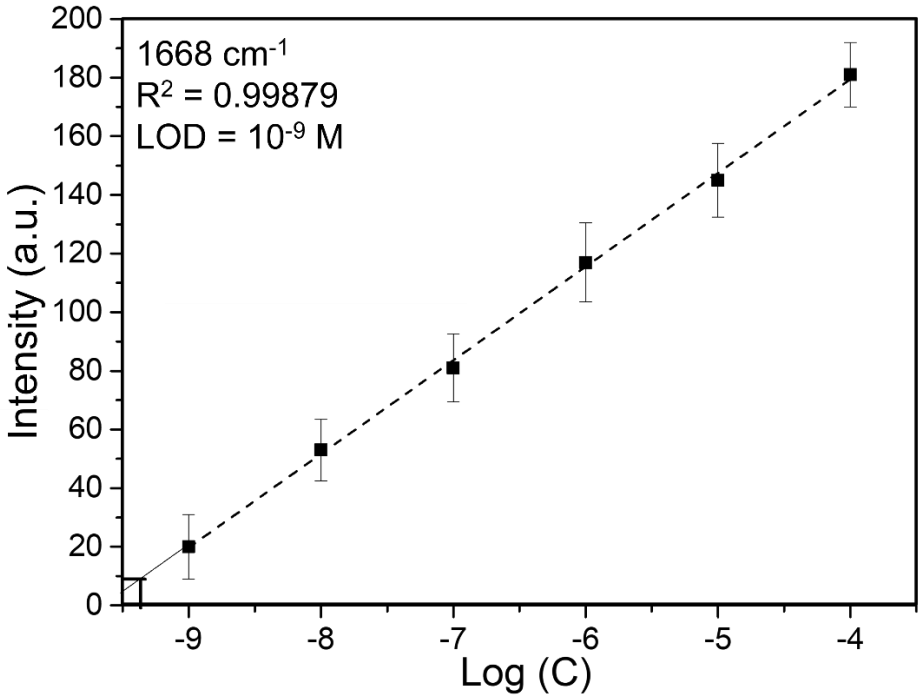

Figure 5-24: Plot of 1668 cm^{-1}peak intensity against the logarithm of β-sitosterol concentration.

The limit of detection was then calculated using the signal-to-noise approach as recommended by IUPAC.[74] In these guidelines the minimal concentration where the signal-to-noise relation is equal to three is considered as the limit of detection. The standard deviation in background noise was calculated using 20 spectra gathered from 7-layered 1T'-$MoTe_2$ using the following equation:

$$SD = \sqrt{\frac{\sum |x - \overline{x}|}{N}}$$

Where x is the intensity of the 1668 cm^{-1} peak, $\bar{x}$ is the mean of the intensities and N is the number of spectra used resulting in a standard deviation of 3.2. Therefore, the minimally acceptable signal intensity must be three times greater than this value meaning the intensity of the 1668 cm^{-1} peak must have an absolute value of 9.6. This intensity is highlighted in Figure 5-24 and corresponds to a β-sitosterol concentration of $10^{-9.3}$ M. Excitingly, the calculated LOD of 10^{-9} M is one of the lowest reported so far for the detection of sterol-like lipophilic molecules using SERS. Table 5-7 highlights some literature examples of the LODs achieved for other SERS substrates used for the sensing of lipophilic molecules.

Table 5-7: Literature LODs achieved for the SERS detection of sterol-like, lipophilic molecules.

SERS Substrate	**Analyte**	**LOD**	**Reference**
Au grating modified w/ alkylaryl moieties	Sitosterol & squalene	10^{-6} M	[68]
Au nanoparticles w/ alkanethiol monolayers	1,2-dimyristoyl-*sn*-glycero-3-phosphocholine	10^{-6} M	[75]
Au nanoparticles w/octanthiol	Canola oil	3 % Vol.	[76]
Ag nanoparticles	Okadaic acid, dinophysistoxin-1 & dinophysistoxin-2	10^{-6} M	[77]
Au nanoparticles modified w/ 16-mercaptohexadecanoic acid	Cholesterol oxidase	0.5 mg/ml	[78]
Anti-estrogen aptamers and complementary DNA modified gold−silver nanoparticles	Steroid estrogens	10^{-9} M	[79]
7-layer 1T'-$MoTe_2$	β-sitosterol	10^{-9} M	This work ([80])

The stability of the SERS substrates is an important factor for the analytical and clinical applications of surface enhanced Raman spectroscopy.[81] Therefore, the stability of the 1T'-$MoTe_2$ films was tested by measuring the Raman spectra of deposited β-sitosterol at intervals over a 45-day period in storage and monitoring the intensities of the 889 and 1668 cm^{-1} peaks. Figure 5-25 reveals that the intensities of the two characteristic peaks only decrease by around 15 % over the course of the 45-day storage period, indicating that 1T'-$MoTe_2$ does not cause irreversible damage to the analyte.

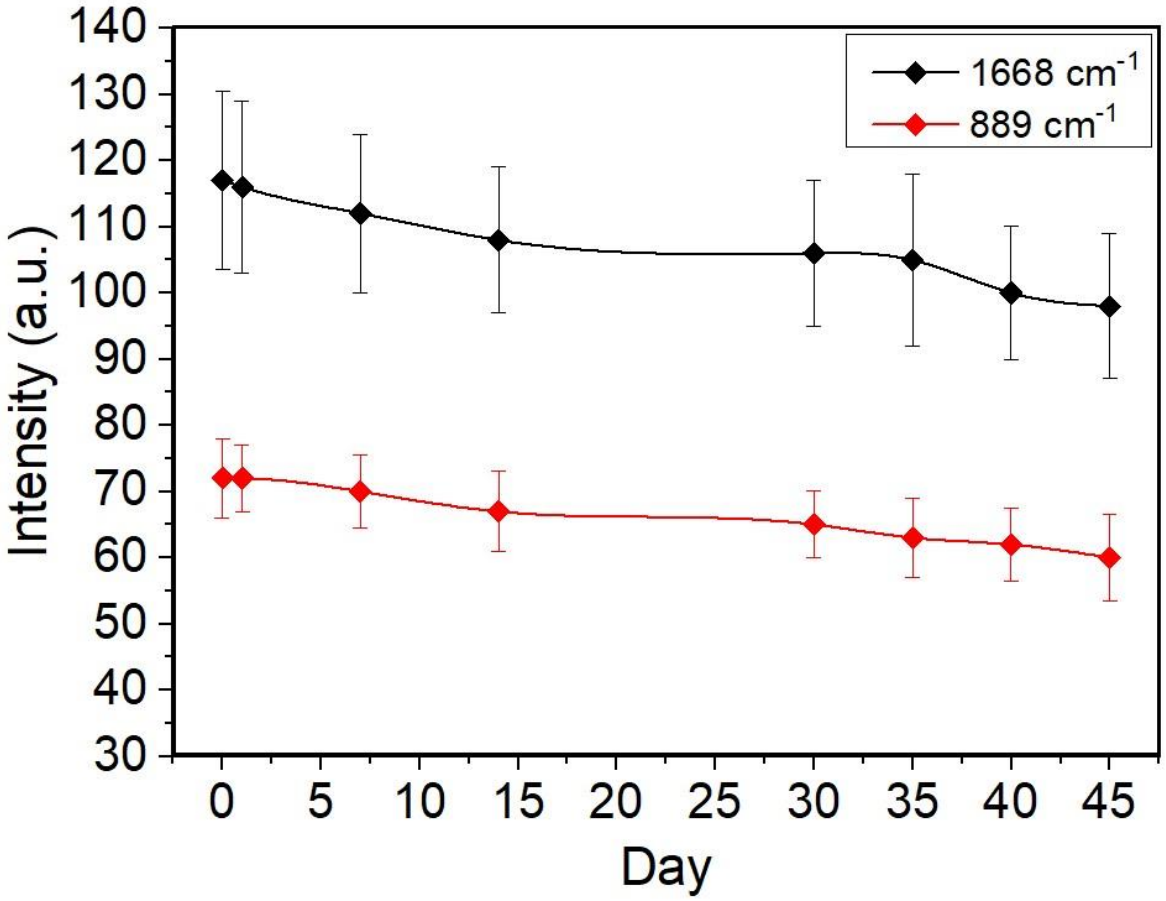

Figure 5-25: Plot showing how the intensities of 889 and 1668 cm^{-1} change with time once deposited on 1T'-$MoTe_2$.

In addition to testing the stability of the 1T'-$MoTe_2$ substrate, the potential for regeneration of the film after β-sitosterol sensing was investigated. A 10^{-6} M β-sitosterol solution was deposited on 7-layer 1T'-$MoTe_2$ and a Raman spectrum recorded, this substrate was then immersed in ethanol and sonicated for a period of 30 minutes to remove the β-sitosterol. Once this process was complete another Raman spectrum was then obtained. Figure 5-26 shows how the intensity of the 1668 cm^{-1} peak varies when β-sitosterol is applied to the substrate versus when it has been washed off for a series of 5 cycles. There is around an 18% drop in intensity between the first and second sensing step, but it then remains stable for the subsequent sensing steps. There is also a slight increase in measurement uncertainty with an increasing number of cycles. Figure 5-27 shows Raman spectra obtained during steps 5 and 6 of the utilisation/regeneration cycles. It is evident from the spectrum recorded on step 5 that there is no β-sitosterol on the 1T'-$MoTe_2$ film, indicating the success of the sonication cleaning procedure. Then after reapplication of β-sitosterol on step 6, the spectrum clearly shows peaks associated with the analyte at ~657, ~889, ~1105, ~1153, ~1308, ~1430 and 1668 cm^{-1}, respectively.[68,82] These experiments suggest that it is feasible to reuse a 1T'-

$MoTe_2$ film for repeated SERS measurements especially considering the minimal losses in signal intensity and the simplicity of the analyte deposition and removal procedures.

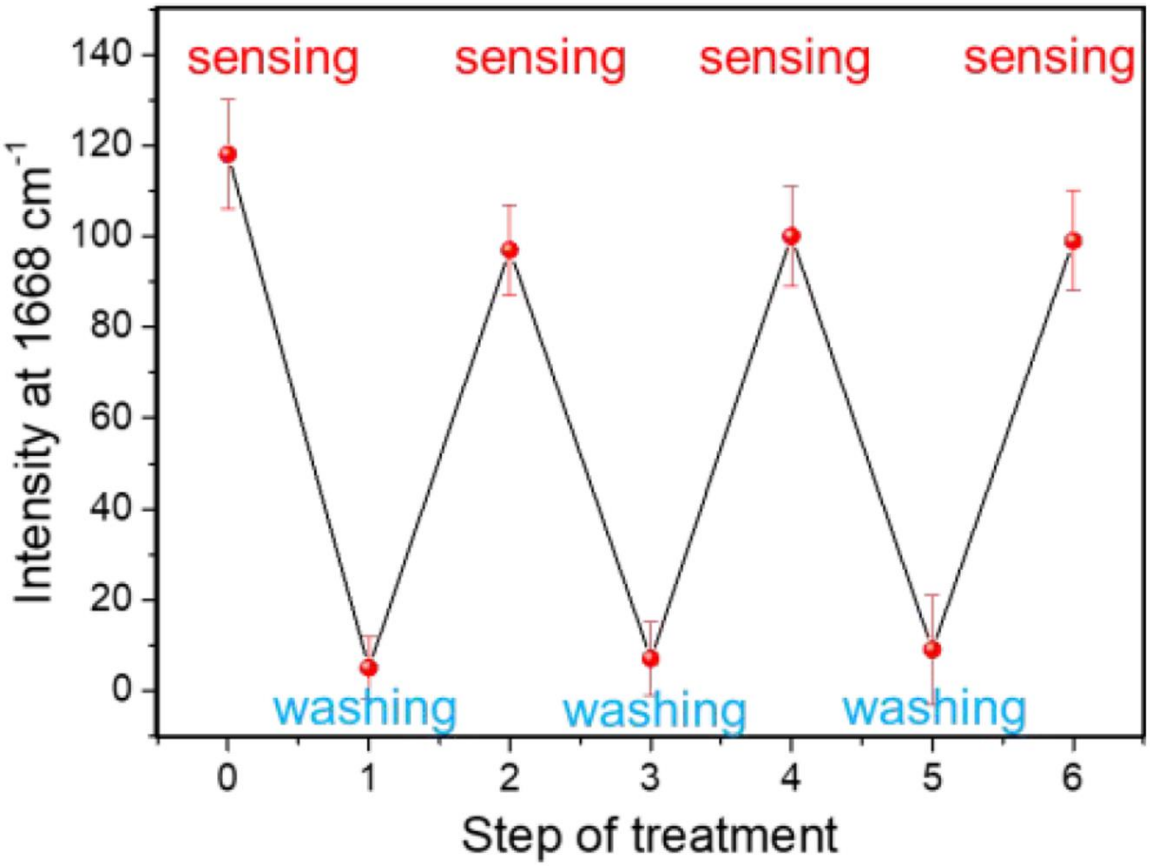

Figure 5-26: Dependence of β-sitosterol 1668 cm^{-1} peak intensity as a function of 1T'-$MoTe_2$ utilisation/regeneration steps.

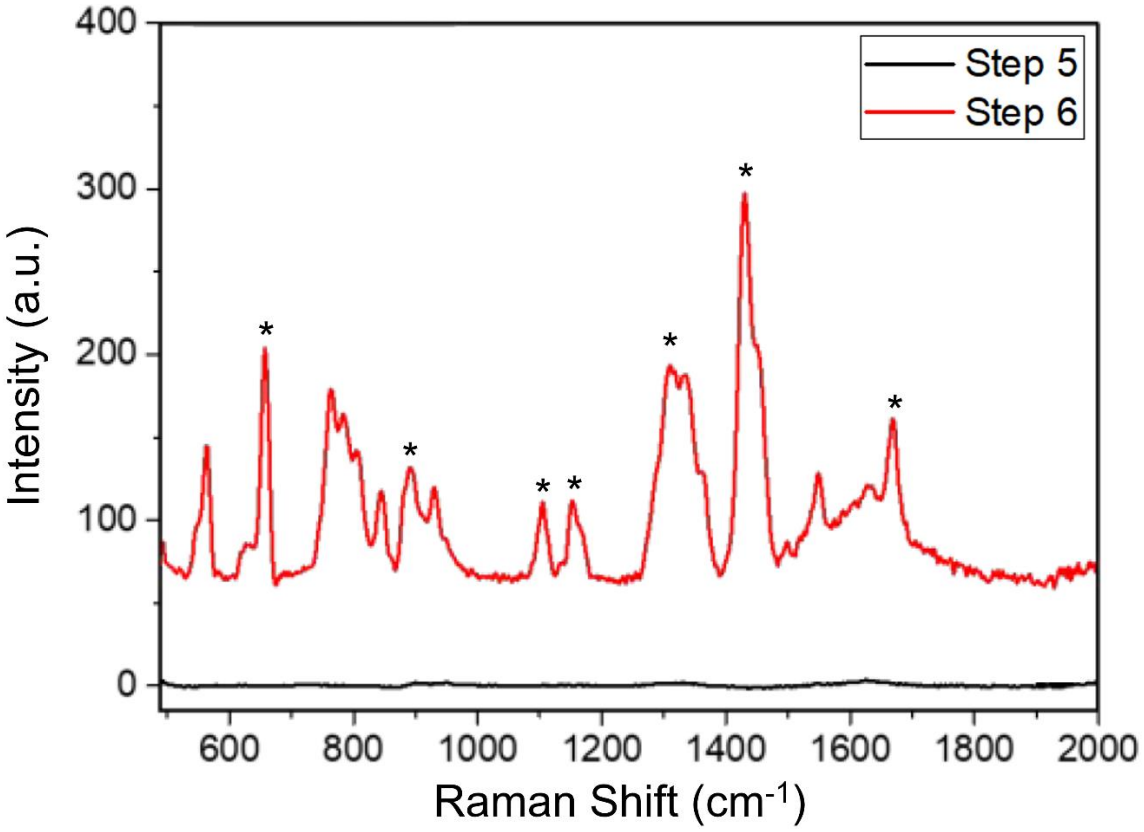

Figure 5-27: Raman spectra recorded on Step 5, after washing β-sitosterol of off 1T'-$MoTe_2$ and Step 6, after the redeposition of β-sitosterol.

The previous testing of 1T'-$MoTe_2$ as a SERS substrate for the detection of β-sitosterol has been conducted under ideal conditions, with no other competing biomolecules present. Therefore, the sensing of β-sitosterol in the presence of a biological matrix was trialled, as this can significantly complicate SERS detection. A fetal bovine serum (FBS) cell culture medium was chosen as it is commonly used in studies featuring interactions between cells and disease causing markers.[83,84] Consequently, a 10^{-4} M solution of β-sitosterol in FBS was spin coated onto 1T'-$MoTe_2$ and Raman spectra recorded. Figure 5-28 shows the Raman spectra obtained from β-sitosterol in FBS/1T'-$MoTe_2$ and β-sitosterol/1T'-$MoTe_2$, where fingerprint peaks are clearly identifiable even in the presence of the culture medium. Interestingly, although there are other biomolecules present in the biomatrix at much higher concentrations than β-sitosterol, it is predominantly the peaks of β-sitosterol that are enhanced. This implies that 1T'-$MoTe_2$ has some kind of selectivity towards β-sitosterol, and it is the chemical enhancement mechanism and the formation of a surface complex that is responsible for the observed enhancement in Raman signal.

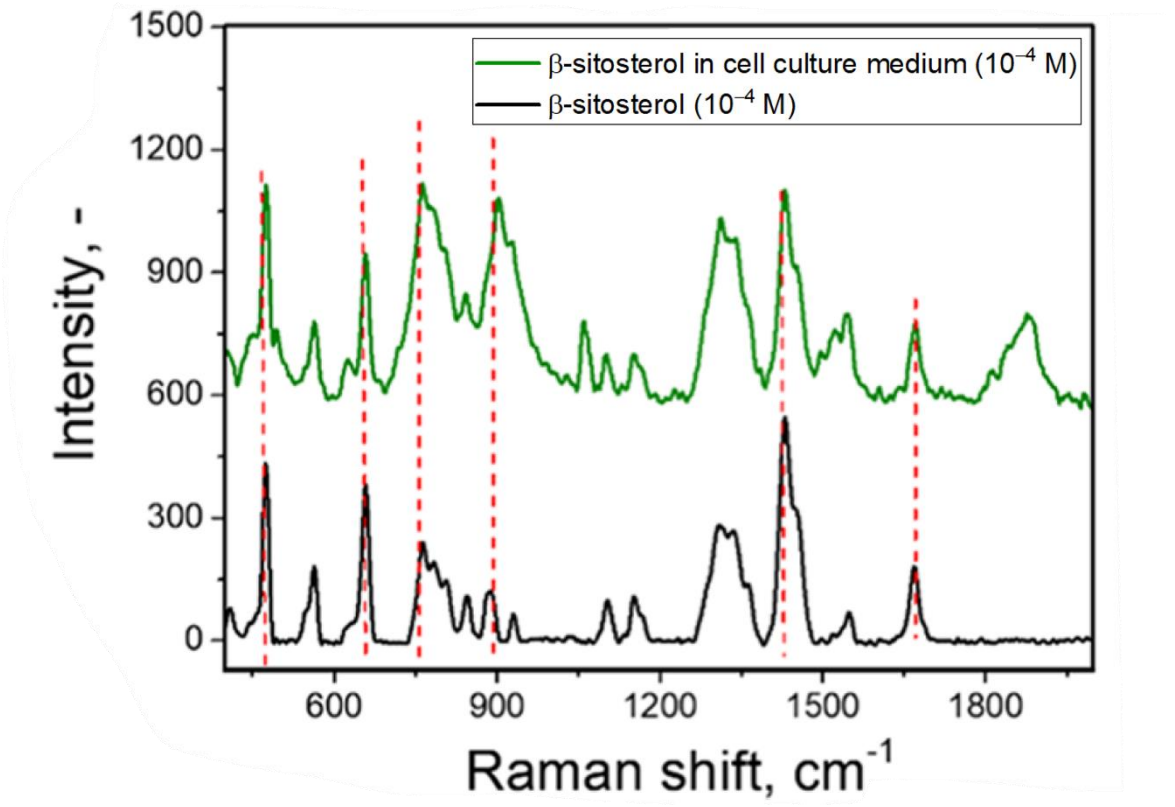

Figure 5-28: Raman spectra obtained from β-sitosterol in FBS/1T'-$MoTe_2$ and β-sitosterol/1T'-$MoTe_2$. The characteristic Raman peaks of β-sitosterol are marked.

5.2.3.2.3. Determination of the Mechanism of Raman Enhancement

The work conducted previously in this chapter has shown that 1T'-$MoTe_2$ can be a promising alternative to the commonly used noble-metal SERS substrates. Therefore, it is important to try and determine the mechanism by which the Raman enhancement witnessed for β-sitosterol occurs. Atomically flat, smooth surfaces are known to be unable to support the large surface plasmons that are required for the electromagnetic mechanism of enhancement to occur and therefore this mechanism can be ruled out for 1T'-$MoTe_2$.[85] That would leave the chemical enhancement mechanism as being responsible, but there are still differing possibilities under the umbrella of chemical enhancement. These include, a charge transfer mechanism due to resonance of the incident beam with an excitation from the substrate to the adsorbed analyte, a molecular resonance mechanism where the incident beam is resonant with a molecular excitation and finally, enhancement due to non-resonant interactions between the surface and the adsorbed analyte.[46] It should be noted that it is often challenging to determine exactly which of the three aforementioned mechanisms are responsible for any observed enhancement.

To investigate the molecular resonance mechanism, density functional theory (DFT) calculations were employed to determine the highest occupied molecular orbital (HOMO)

and lowest unoccupied molecular orbital (LUMO) of β-sitosterol. DFT reveals that the HOMO-LUMO levels of the molecule are located at -6.16 and 0.77 eV, resulting in a band gap of 5.39 eV respectively (Figure 5-29). The band gap of β-sitosterol far exceeds the excitation wavelength of the Raman laser used for the measurements (785 nm, 1.53 eV), meaning that the enhancement mechanisms relying on molecular resonance effects can be discounted. Incidentally, the HOMO-LUMO gap of rhodamine 6G is 2.3 eV meaning that a 532 nm laser would cause molecular excitation as this wavelength corresponds to an energy of 2.3 eV.[50]

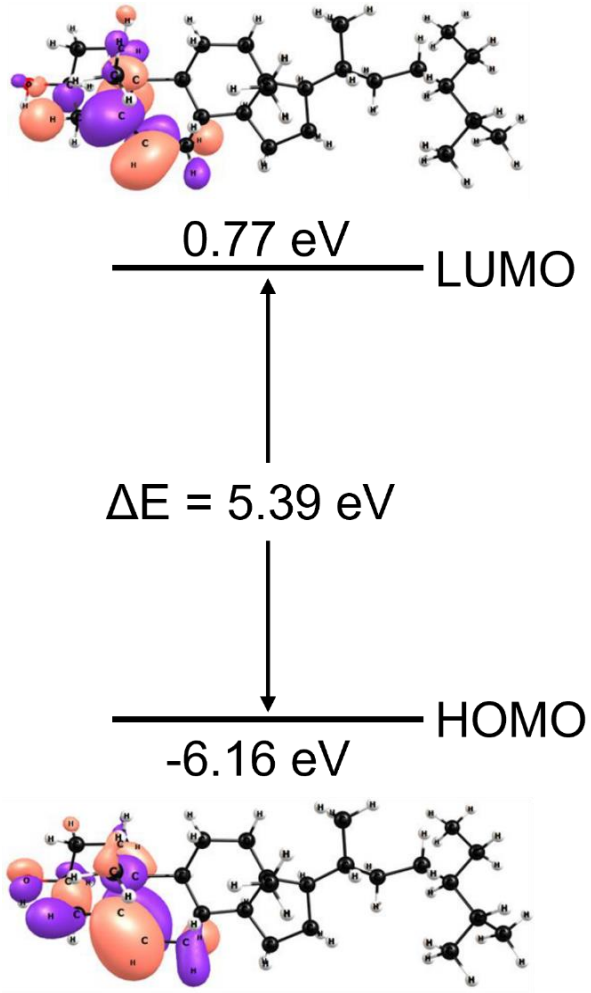

Figure 5-29: HOMO-LUMO energy band diagram of β-sitosterol with values calculated by DFT. A visual representation of the location of the HOMO and LUMO for β-sitosterol are also shown.

UV-vis absorption spectroscopy was utilised to confirm the conclusions arrived at based upon the DFT calculations. Spectra were obtained for 7-layer 1T'-$MoTe_2$ deposited on sapphire, β-sitosterol and rhodamine 6G. From Figure 5-30 it is evident that the maximum absorption of β-sitosterol is between 200-225 nm, whilst 1T'-$MoTe_2$ shows almost zero absorbance around 785 nm. This confirms that the enhancement witnessed when using the 785 nm Raman laser is not due to molecular resonance effects. Resonance could be induced

by using a laser in the range of 200-225 nm but wavelengths this short cause strong photoluminescence in organic molecules which can then mask the Raman peaks.[86] Rhodamine 6G shows strong absorbance around 532 nm meaning that the enhancement witnessed for R6G on 1T'-$MoTe_2$ is likely somewhat caused by molecular resonance with the incident laser.

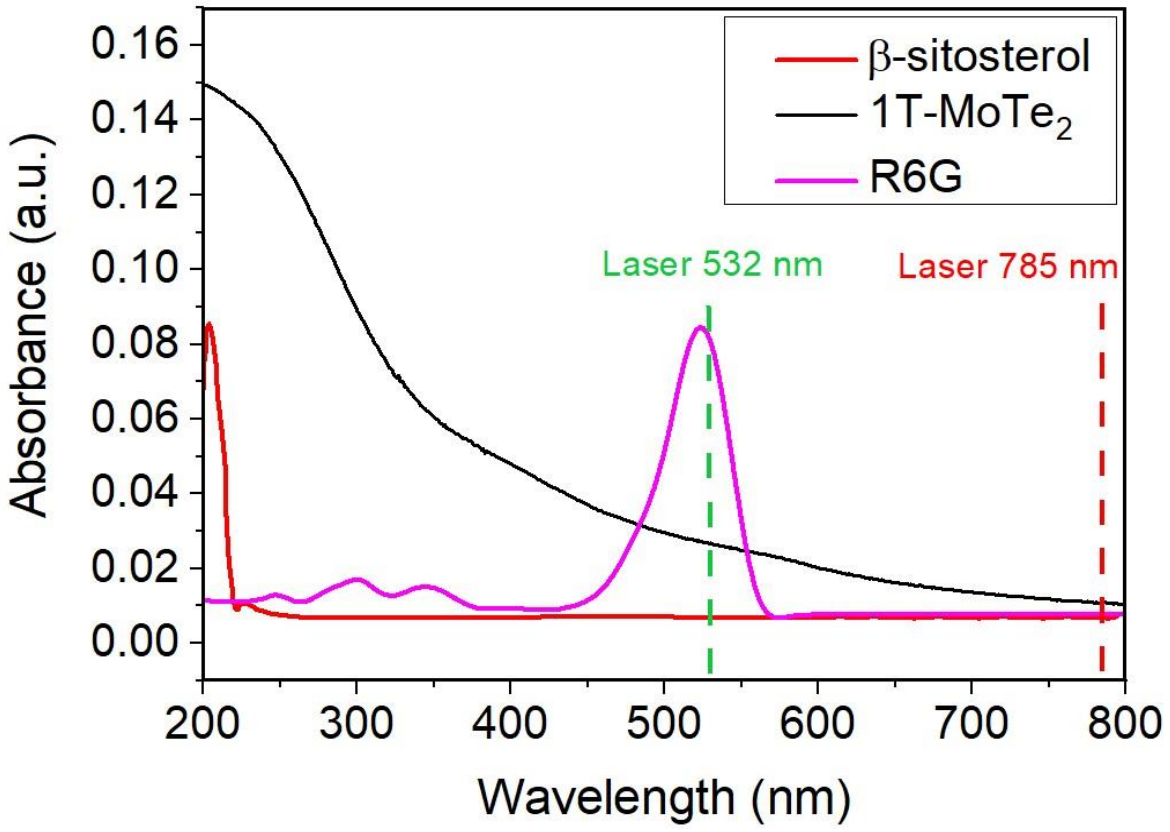

Figure 5-30: UV-Vis absorption spectra of 1T'-$MoTe_2$, β-sitosterol and rhodamine 6G.

After determining that molecular resonance is not responsible for the observed enhancement, attention was turned to proving that an analyte-substrate complex was formed. Once again UV-vis absorption spectroscopy was used to probe the possible formation of a surface complex with spectra obtained for β-sitosterol deposited on 1T'-$MoTe_2$ in this instance. Figure 5-31a reveals the appearance of low-intensity absorption bands for β-sitosterol/1T'-$MoTe_2$ at ~580 nm (Figure 5-31b) and ~910 nm (Figure 5-31c), which do not appear in the spectra obtained from β-sitosterol solution or β-sitosterol/sapphire. The appearance of these bands can be attributed to the formation of a surface complex.[87,88]

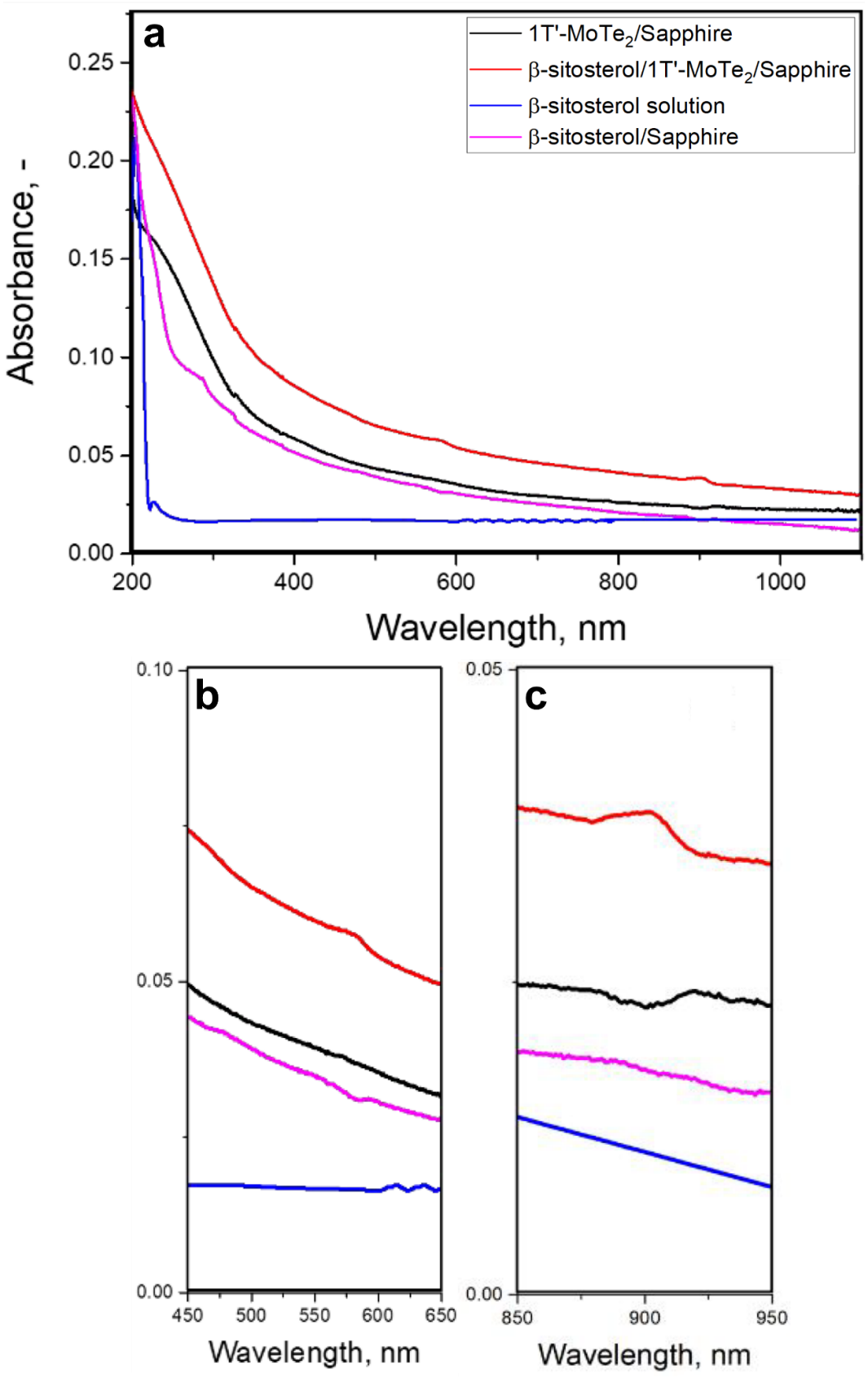

Figure 5-31: UV-vis spectra of 1T'-$MoTe_2$, β-sitosterol/1T'-$MoTe_2$, β-sitosterol solution and β-sitosterol/sapphire (a). The presence of absorption bands at ~580 nm (b) and ~ 910 nm (c) in the spectrum from β-sitosterol/1T'-$MoTe_2$ indicate the formation of a surface complex.

In addition to UV-vis spectroscopy, Fourier-transform infra-red (FTIR) spectroscopy was performed on β-sitosterol deposited on 1T'-$MoTe_2$, β-sitosterol deposited on SiO_2/Si and 1T'-$MoTe_2$ (Figure 5-32).

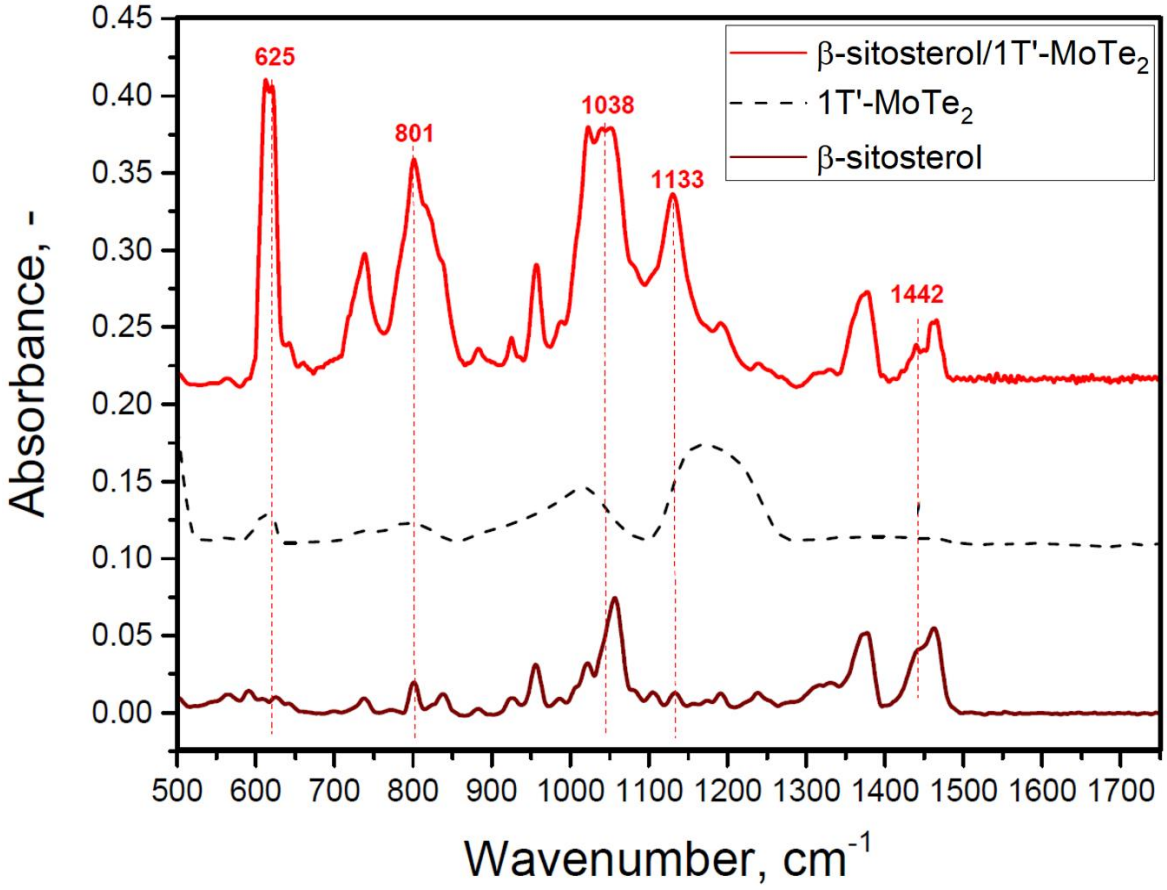

Figure 5-32: FTIR spectra obtained for β-sitosterol/1T'-$MoTe_2$, 1T'-$MoTe_2$ and β-sitosterol.

It is immediately clear that the spectra obtained from β-sitosterol/1T'-$MoTe_2$ and β-sitosterol/SiO_2/Si are vastly different with enhanced peak intensities observed for several of the characteristic bands of β-sitosterol when deposited on 1T'-$MoTe_2$. Peaks associated with the hydroxyl group and the carbon-carbon double bond are particularly effected, with large increases in intensity witnessed for the bands at ~1133 cm^{-1} (C-O stretch), ~1038 cm^{-1} (CH_2 out of plane (C=C)), ~801 cm^{-1} (CH_2 out of plane (C=C)) and ~625 cm^{-1} (-OH out of plane).[89] The fact that peaks belonging to the hydroxy group were majorly impacted suggests that β-sitosterol forms a complex to 1T'-$MoTe_2$ through the polar part of the molecule. Similarly, the changes to the peaks corresponding to the unsaturated C=C bond and the location of the HOMO of β-sitosterol (Figure 5-29) suggest that this area of the molecule also participates in the formation of a surface complex.

Finally, cyclic voltammetry was used to study the β-sitosterol/1T'-$MoTe_2$ system. CV scans of β-sitosterol deposited on 7L-1T'-$MoTe_2$ and a standard glassy carbon substrate were obtained (Figure 5-33). Currently, there are no electrochemical studies directly on β-sitosterol and as such analysis of other lipophilic molecules with similar structures was used to assign the observed peaks to oxidation of the C=C bond and/or oxidation of the hydroxyl group.[90] On the carbon electrode an oxidation peak can be observed at E_{ox} = 1.78 and appears to be due to irreversible oxidation of the analyte. Interestingly, the measurement on the $MoTe_2$ substrate shows a noticeable peak shift to E_{ox} = 1.67 V, coupled with a large increase to the peak height. The shift in E_{ox} indicates that chemical absorption has occurred and a surface complex between β-sitosterol and 1T'-$MoTe_2$ has formed.

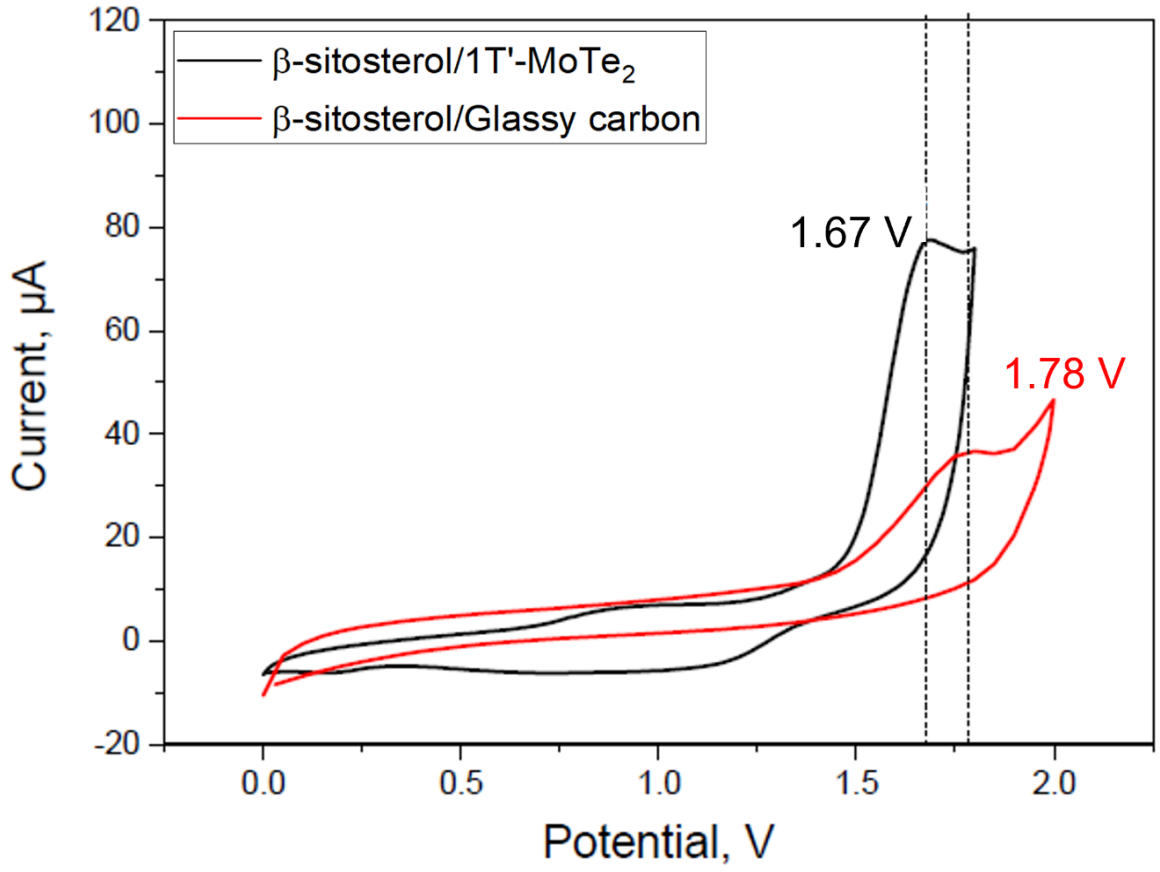

Figure 5-33: Cyclic voltammograms measured on 1T'-$MoTe_2$ and glassy carbon in an ethanol solution of β-sitosterol.

To further investigate this, cyclic voltammetry in conjunction with laser irradiation was performed (Figure 5-34). In the case of β-sitosterol deposited on 1T'-$MoTe_2$ there was no change to E_{ox} and only a negligible increase to peak intensity when irradiated with a 532 nm laser compared to the CV scan obtained with no laser irradiation. Conversely, when irradiated with 785 nm light there is a distinct shift of E_{ox} = 1.67 V to E_{ox} = 1.58 V, coupled with a clear increase to the peak intensity. This result suggests that the use of the 785 nm

Raman laser helps to facilitate charge transfer processes in the β-sitosterol-1T'-$MoTe_2$ complex.

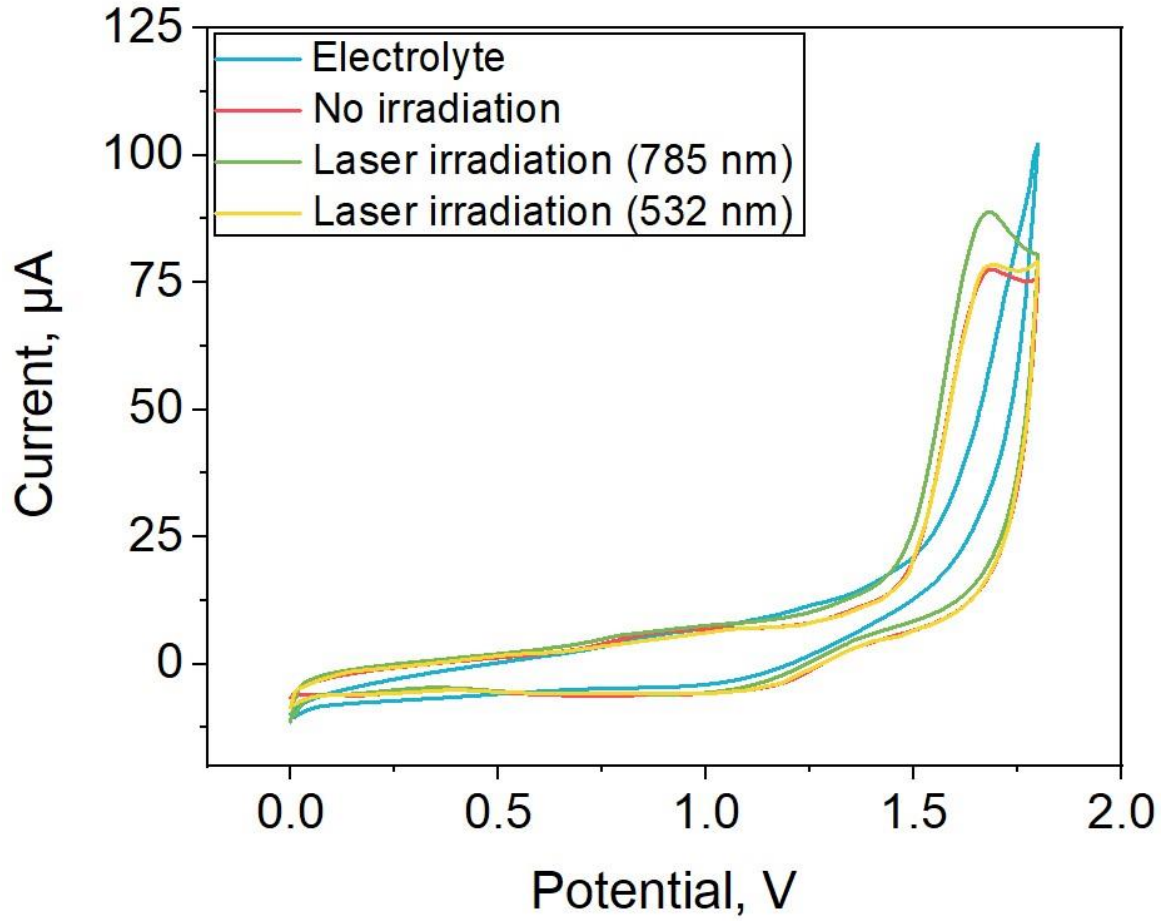

Figure 5-34: CV scans of the electrolyte, β-sitosterol/1T'-$MoTe_2$ with no irradiation, under 532 nm irradiation and under 785 nm irradiation.

Due to the mismatch in the energy of the incident 785 nm Raman laser and HOMO-LUMO gap of β-sitosterol, as calculated by DFT and experimentally confirmed by UV-vis, the molecular resonance mechanism of enhancement was discounted. Therefore, it is probable that the enhancement is due to ground-state chemical interactions between the analyte and the surface. The formation of a surface complex when 1T'-$MoTe_2$ is used as a substrate was confirmed by the UV-vis, FTIR and CV measurements. Furthermore, the results of the CV measurements under 785 nm irradiation suggest that, unlike free β-sitosterol, the surface complex could resonate with this excitation wavelength, due to changes in the excitation energy of the surface complex.[91] Unfortunately, the in-depth computational calculations required to fully discern the important role that the excitation wavelength plays is beyond the scope of this work due to the dynamic nature of the surface complex.

5.2.4. Conclusions

In conclusion, few-layered 1T'-$MoTe_2$ was found to be a promising noble-metal free SERS substrate for both a model Raman probe (R6G) as well as a clinically relevant biomolecule in β-sitosterol. The relationship between the thickness of the CVD grown films and the intensity of the SERS signal showed that enhancement deteriorates rapidly as the number of layers increases, while nanomolar detection of β-sitosterol was achievable on a relatively thick 1T'-$MoTe_2$ film. Moreover, the detection of β-sitosterol in a complex cell culture was realised, highlighting that the sensing ability of 1T'-$MoTe_2$ can go beyond using simple model solutions in ideal conditions. The stability and recyclability of the surfaces was addressed with a minimal loss of signal intensity from the analyte when stored over a period of 45 days. A simple washing procedure showed that the substrate could be cleaned and reused for sensing for at least five cycles, again with minimal losses of performance. Furthermore, the formation of a surface complex between β-sitosterol and 1T'-$MoTe_2$ was investigated and confirmed through UV-vis, IR spectroscopy and cyclic voltammetry.

The mechanism of Raman enhancement was found not to involve molecular resonance with the incident laser due to a mismatch in energy between the two which was confirmed through DFT calculations. Unfortunately, the computational calculations required to discern to what extent either a CT mechanism due to resonance of the incident beam with an excitation from the substrate to the adsorbed analyte or non-resonant enhancement due to chemical bonding between the adsorbed analyte and substrate are responsible for the observed Raman enhancement are beyond the scope of this work.

Finally, the SERS performance of 1T'-$MoTe_2$ coupled with the simple and highly scalable CVD production method makes it a promising material in the design of future SERS platforms for the detection of clinically relevant molecules.

5.3. References

1. United Kingdom Power Market Outlook to 2030, Update 2021 - Market Trends, Regulations, and Competitive Landscape. https://store.globaldata.com/report/gdpe2222icr--united-kingdom-power-market-outlook-to-2030-update-2021-market-trends-regulations-and-competitive-landscape/.

2. International Renewable Energy Agency, T. Renewable Power-to-Hydrogen Innovation Landscape Brief. (2019).

3. Seh, Z. W., Kibsgaard, J., Dickens, C. F., Chorkendorff, I., Nørskov, J. K. & Jaramillo, T. F. Combining theory and experiment in electrocatalysis: Insights into materials design. *Science* **355**, 6321 (2017).

4. Nørskov, J. K., Bligaard, T., Logadottir, A., Kitchin, J. R., Chen, J. G., Pandelov, S. & Stimming, U. Trends in the exchange current for hydrogen evolution. *J. Electrochem. Soc.* **152**, J23–J26 (2005).

5. Ekspong, J., Gracia-Espino, E. & Wågberg, T. Hydrogen Evolution Reaction Activity of Heterogeneous Materials: A Theoretical Model. *J. Phys. Chem. C* **124**, 20911–20921 (2020).

6. Pandey, M., Vojvodic, A., Thygesen, K. S. & Jacobsen, K. W. Two-Dimensional Metal Dichalcogenides and Oxides for Hydrogen Evolution: A Computational Screening Approach. *J. Phys. Chem. Lett.* **6**, 1577–1585 (2015).

7. Tributsch, H. & Bennett, J. C. Electrochemistry and photochemistry of MoS_2 layer crystals. I. *J. Electroanal. Chem. Interfacial Electrochem.* **81**, 97–111 (1977).

8. Jaramillo, T. F., Jørgensen, K. P., Bonde, J., Nielsen, J. H., Horch, S. & Chorkendorff, I. Identification of Active Edge Sites for Electrochemical H_2 Evolution from MoS_2 Nanocatalysts. *Science* **317**, 100-102 (2007).

9. Kibsgaard, J., Chen, Z., Reinecke, B. N. & Jaramillo, T. F. Engineering the surface structure of MoS_2 to preferentially expose active edge sites for electrocatalysis. *Nat Mater* **11**, 963–969 (2012).

10. Voiry, D., Yamaguchi, H., Li, J., Silva, R., Alves, D. C. B., Fujita, T., Chen, M., Asefa, T., Shenoy, V. B., Eda, G. & Chhowalla, M. Enhanced catalytic activity in strained chemically exfoliated WS_2 nanosheets for hydrogen evolution. *Nat. Mater.*

12, 850–855 (2013).

11. Merki, D., Fierro, S., Vrubel, H. & Hu, X. Amorphous molybdenum sulfide films as catalysts for electrochemical hydrogen production in water. *Chem. Sci.* **2**, 1262–1267 (2011).

12. Karunadasa, H. I., Montalvo, E., Sun, Y., Majda, M., Long, J. R. & Chang, C. J. A Molecular MoS_2 Edge Site Mimic for Catalytic Hydrogen Generation. *Science* **335**, 698–702 (2012).

13. Vrubel, H., Merki, D. & Hu, X. Hydrogen evolution catalyzed by MoS_2 and MoS_2 particles. *Energy Environ. Sci.* **5**, 6136–6144 (2012).

14. Li, Y., Wang, H., Xie, L., Liang, Y., Hong, G. & Dai, H. MoS_2 Nanoparticles Grown on Graphene: An Advanced Catalyst for the Hydrogen Evolution Reaction. *J. Am. Chem. Soc.* **133**, 7296–7299 (2011).

15. Benck, J. D., Chen, Z., Kuritzky, L. Y., Forman, A. J. & Jaramillo, T. F. Amorphous Molybdenum Sulfide Catalysts for Electrochemical Hydrogen Production: Insights into the Origin of their Catalytic Activity. *ACS Catal.* **2**, 1916–1923 (2012).

16. Yin, Y., Han, J., Zhang, Y., Zhang, X., Xu, P., Yuan, Q., Samad, L., Wang, X., Wang, Yi., Zhang, Z., Zhang, P., Cao, X., Song, B. & Jin, S. Contributions of Phase, Sulfur Vacancies, and Edges to the Hydrogen Evolution Reaction Catalytic Activity of Porous Molybdenum Disulfide Nanosheets. *J. Am. Chem. Soc.* **138**, 7965–7972 (2016).

17. Manzeli, S., Ovchinnikov, D., Pasquier, D., Yazyev, O. V & Kis, A. 2D transition metal dichalcogenides. *Nat. Rev. Mater.* **2**, 17033 (2017).

18. Kertesz, M. & Hoffmann, R. Octahedral vs. trigonal-prismatic coordination and clustering in transition-metal dichalcogenides. *J. Am. Chem. Soc.* **106**, 3453–3460 (1984).

19. Lukowski, M. A., Daniel, A. S., Meng, F., Forticaux, A., Li, L. & Jin, S. Enhanced Hydrogen Evolution Catalysis from Chemically Exfoliated Metallic MoS_2 Nanosheets. *J. Am. Chem. Soc.* **135**, 10274–10277 (2013).

20. Py, M. A. & Haering, R. R. Structural destabilization induced by lithium intercalation in MoS_2 and related compounds. *Can. J. Phys.* **61**, 76–84 (1983).

21. Eda, G., Fujita, T., Yamaguchi, H., Voiry, D., Chen, M. & Chhowalla, M. Coherent Atomic and Electronic Heterostructures of Single-Layer MoS_2. *ACS Nano* **6**, 7311–7317 (2012).

22. Mahler, B., Hoepfner, V., Liao, K. & Ozin, G. A. Colloidal Synthesis of 1T-WS_2 and 2H-WS_2 Nanosheets: Applications for Photocatalytic Hydrogen Evolution. *J. Am. Chem. Soc.* **136**, 14121–14127 (2014).

23. Tang, H., Dou, K., Kaun, C.-C., Kuang, Q. & Yang, S. $MoSe_2$ nanosheets and their graphene hybrids: synthesis, characterization and hydrogen evolution reaction studies. *J. Mater. Chem. A* **2**, 360–364 (2014).

24. Wang, H., Kong, D., Johanes, P., Cha, J. J., Zheng, G., Yan, K., Liu, N. & Cui, Y. $MoSe_2$ and WSe_2 Nanofilms with Vertically Aligned Molecular Layers on Curved and Rough Surfaces. *Nano Lett.* **13**, 3426-3433 (2013).

25. Kumar, A. & Ahluwalia, P. K. Electronic structure of transition metal dichalcogenides monolayers 1H-MX_2 (M = Mo, W; X = S, Se, Te) from ab-initio theory: new direct band gap semiconductors. *Eur. Phys. J. B* **85**, 186 (2012).

26. Sung, J. H., Heo, H., Si, S., Kim, Y. H., Noh, H. R., Song, K., Kim, J., Lee, C.-S., Seo, S.-Y., Kim, D.-H., Kim, H.-K., Yeom, H. W., Kim, T.-H., Choi, S.-Y., Kim, J. S., Jo, M.-H. Coplanar semiconductor-metal circuitry defined on few-layer $MoTe_2$ via polymorphic heteroepitaxy. *Nat. Nanotechnol.* **12**, 1064–1070 (2017).

27. McGlynn, J. C., Cascallana-Matias, I., Fraser, J. P., Roger, I., McAllister, J., Miras, H. N., Symes, M. D. & Ganin, A. Y. Molybdenum Ditelluride Rendered into an Efficient and Stable Electrocatalyst for the Hydrogen Evolution Reaction by Polymorphic Control. *Energy Technol.* **6**, 345–350 (2018).

28. Seok, J., Lee, J.-H., Cho, S., Ji, B., Kim, H. W., Kwon, M., Kim, D., Kim, Y.-M., Oh, S. H., Kim, S. W., Lee, Y. H., Son, Y.-W. & Yang, H. Active hydrogen evolution through lattice distortion in metallic MoTe 2. *2D Mater.* **4**, 25061 (2017).

29. Tsai, C., Chan, K., Nørskov, J. K. & Abild-Pedersen, F. Theoretical insights into the hydrogen evolution activity of layered transition metal dichalcogenides. *Surf. Sci.* **640**, 133–140 (2015).

30. McGlynn, J. C., Dankwort, T., Kienle, L., Bandeira, N. A. G., Fraser, J. P., Gibson, E. K., Cascallana-Matías, I., Kamarás, K., Symes, M. D., Miras, H. N. & Ganin, A. Y. The rapid electrochemical activation of $MoTe_2$ for the hydrogen evolution

reaction. *Nat. Commun. 2019 101* **10**, 4916 (2019).

31. Yamamoto, M., Wang, S. T., Ni, M., Lin, Y.-F., Li, S.-L., Aikawa, S., Jian, W.- B., Ueno, K., Wakabayashi, K. & Tsukagoshi, K. Strong Enhancement of Raman Scattering from a Bulk-Inactive Vibrational Mode in Few-Layer $MoTe_2$. *ACS Nano* **8**, 3895–3903 (2014).

32. Walter, M. G., Warren, E. L., McKone, J. R., Boettcher, S. W., Mi, Q., Santori, E. & Lewis, N. S. Solar Water Splitting Cells. *Chem. Rev.* **110**, 6446–6473 (2010).

33. Tang, Q. & Jiang, D. Mechanism of Hydrogen Evolution Reaction on 1T-MoS_2 from First Principles. *ACS Catal.* **6**, 4953–4961 (2016).

34. McManus, J. B., Cunningham, G., McEvoy, N., Cullen, C. P., Gity, F., Schmidt, M., McAteer, D., Mullarkey, D., Shvets, I. V., Hurley, P. K., Hallan, T. & Duesbery, G. S. Growth of 1T′ $MoTe_2$ by Thermally Assisted Conversion of Electrodeposited Tellurium Films. *ACS Appl. Energy Mater.* **2**, 521–530 (2019).

35. Zhuang, P., Sun, Y., Dong, P., Smith, W., Sun, Z., Ge, Y., Pei, Y., Cao, Z., Ajayan, P. M. Shen, J. & Ye, M. Revisiting the Role of Active Sites for Hydrogen Evolution Reaction through Precise Defect Adjusting. *Adv. Funct. Mater.* **29**, 1901290 (2019).

36. Seok, J., Lee, J.-H., Cho, S., Ji, B., Kim, H. W., Kwon, M., Kim, D., Kim, Y.-M., Oh, S. H., Kim, S. W., Lee, Y. H., Son, Y.-W. & Yang, H. Active hydrogen evolution through lattice distortion in metallic $MoTe_2$. *2D Mater.* **4**, 025061 (2017).

37. Qiao, H., Huang, Z., Liu, S., Liu, Y., Li, J. & Qi, X. Liquid-exfoliated molybdenum telluride nanosheets with superior electrocatalytic hydrogen evolution performances. *Ceram. Int.* **44**, 21205–21209 (2018).

38. Lu, D., Ren, X., Ren, L., Xue, W., Liu, S., Liu, Y., Chen, Q., Qi. & Zhong, J. Direct Vapor Deposition Growth of 1T′ $MoTe_2$ on Carbon Cloth for Electrocatalytic Hydrogen Evolution. *ACS Appl. Energy Mater.* **3,** 3212-3219 (2019)

39. Mao, J., Zhou, L., Li, Y., Tao, Y., Chai, K., Shi. Y. & Xu, W. Synthesis of $MoTe_2$ nanowire as an efficient hydrogen evolution reaction material. *Mater. Lett.* **290**, 129471 (2021).

40. Yao, D. D., Ou, J. Z., Latham, K., Zhiuykov, S., O'Mullane, A. P. & Kalantar-zadeh, K. Electrodeposited α- and β-Phase MoO_3 Films and Investigation of Their Gasochromic Properties. *Cryst. Growth Des.* **12**, 1865–1870 (2012).

41. Dasary, S. S. R., Singh, A. K., Senapati, D., Yu, H. & Ray, P. C. Gold Nanoparticle Based Label-Free SERS Probe for Ultrasensitive and Selective Detection of Trinitrotoluene. *J. Am. Chem. Soc.* **131**, 13806–13812 (2009).

42. Tripp, R., Dluhy, R. & Zhao, Y. Novel nanostructures for SERS biosensing. *Nano Today* **3**, 31–37 (2008).

43. Dutta, S., Ray, C., Sarkar, S., Pradhan, M., Negishi, Y. & Pal, T. Silver Nanoparticle Decorated Reduced Graphene Oxide (rGO) Nanosheet: A Platform for SERS Based Low-Level Detection of Uranyl Ion. *ACS Appl. Mater. Interfaces* **5**, 8724–8732 (2013).

44. Zavaleta, C. L., Smith, B. R., Walton, I., Doering, W., Davis, G., Shojaei, B., Natan, M. J., Gambhir, S. S. Multiplexed imaging of surface enhanced Raman scattering nanotags in living mice using noninvasive Raman spectroscopy. *Proc. Natl. Acad. Sci.* **106**, 13511 LP – 13516 (2009).

45. Qian, X.-M. & Nie, S. M. Single-molecule and single-nanoparticle SERS: from fundamental mechanisms to biomedical applications. *Chem. Soc. Rev.* **37**, 912–920 (2008).

46. Schlücker, S. Surface-Enhanced Raman Spectroscopy: Concepts and Chemical Applications. *Angew. Chemie Int. Ed.* **53**, 4756–4795 (2014).

47. Ding, S. Y., Yi, J., Li, J.-F., Ren, B., Wu, D.-Y., Panneerselvam, R., &Tian, Z.-Q. Nanostructure-based plasmon-enhanced Raman spectroscopy for surface analysis of materials. *Nature Reviews Materials* **1**, 16021 (2016).

48. Karthick Kannan, P., Shankar, P., Blackman, C. & Chung, C. Recent Advances in 2D Inorganic Nanomaterials for SERS Sensing. *Adv. Mater.* **31**, 1803432 (2019).

49. Rana, F. Graphene terahertz plasmon oscillators. *IEEE Trans. Nanotechnol.* **7**, 91–99 (2008).

50. Tao, L., Chen, K., Chen, Z., Cong, C., Qiu, C., Chen, J., Wang, X., Chen, H., Yu, T., Xie, W., Deng, S. & Xu, J.-B. 1T′ Transition Metal Telluride Atomic Layers for Plasmon-Free SERS at Femtomolar Levels. *J. Am. Chem. Soc.* **140**, 8696–8704 (2018).

51. Song, X. Wang, Y., Zhao, F., Li, Q., Ta, H. Q., Rummeli, M. H., Tully, C. G., Li, Z., Y, W.-J., Yang, L., Lee, K.-B., Yang, J., Bozkurt, I., Liu, S., Zhang, W. &

Chhowalla. M. Plasmon-Free Surface-Enhanced Raman Spectroscopy Using Metallic 2D Materials. *ACS Nano* **13**, 8312–8319 (2019).

52. Feng, S., Dos Santos, M . C., Carvalho, B. R., Lv, R., Li, Q., Fujisawa, K., Elias, A. L., Lei, Y., Perea-Lopez, N., Endo, M., Pan, M., Pimenta, M. A. & Terrones, M. Ultrasensitive molecular sensor using N-doped graphene through enhanced Raman scattering. *Sci. Adv.* **2**, e1600322 (2016).

53. Chen, M., Liu, D., Du, X., Lo, K. H., Wang, S., Zhou, & Pan, H. 2D materials: Excellent substrates for surface-enhanced Raman scattering (SERS) in chemical sensing and biosensing. *TrAC Trends Anal. Chem.* **130**, 115983 (2020).

54. Chhowalla, M., Shin, H. S., Eda, G. Li, L.-J., Loh, K. K. & Zhang, H. The chemistry of two-dimensional layered transition metal dichalcogenide nanosheets. *Nat Chem* **5**, 263–275 (2013).

55. Samadi, M., Sarikhani, N., Zirak, M., Zhang, H., Zhang, H.-L. & Moshfegh, A. Z. Group 6 transition metal dichalcogenide nanomaterials: Synthesis, applications and future perspectives. *Nanoscale Horizons* vol. 3 90–204 (2018).

56. Yin, Y., Miao, P., Zhang, Y., Han, J., Zhang, X., Gong, Y., Gu, L., Xu, C., Yao, T., Xu, P., Wang, Y., Song, B. & Jin, S. Significantly Increased Raman Enhancement on MoX_2 (X = S, Se) Monolayers upon Phase Transition. *Adv. Funct. Mater.* **27**, 1606694 (2017).

57. Ling, X., Xie, L., Fang, Y., Xu, H., Zhang, H., Kong, J., Dresselhaus, M. S., Zhang, J. & Liu, Z. Can Graphene be used as a Substrate for Raman Enhancement? *Nano Lett.* **10**, 553–561 (2010).

58. Miao, P., Qin, J.-K., Shen, Y., Su, H., Dai, J., Song, B., Du, Y., Sun, M., Zhang, W., Wang, H.-L. Xu, C.-Y. & Xu, P. Unraveling the Raman Enhancement Mechanism on 1T'-Phase ReS_2 Nanosheets. *Small* **14**, e1704079 (2018).

59. Wang, K., Guo, Z., Li, Y., Guo, Y., Liu, H., Zhang, W., Zou, Z., Zhang, Y. & Liu, Z. Few-Layer $NbTe_2$ Nanosheets as Substrates for Surface-Enhanced Raman Scattering Analysis. *ACS Appl. Nano Mater.* **3**, 11363–11371 (2020).

60. Li, Y., Chen, H., Guo, Y., Wang, K., Zhang, Y., Lan, P., Guo, J., Zhang, W., Zhong, H., Guo, Z., Zhuang, Z. & Liu, Z. Lamellar hafnium ditelluride as an ultrasensitive surface-enhanced Raman scattering platform for label-free detection of uric acid. *Photonics Res.* **9**, 1039–1047 (2021).

61. Ling, X., Fang, W., Lee, Y.-H., Araujo, P. T., Zhang, X., Rodriguez-Nieva, J. F., Lin, Y., Zhang, J., Kong, J., Dresselhaus, M. S. Raman enhancement effect on two-dimensional layered materials: Graphene, h-BN and MoS_2. *Nano Lett.* **14**, 3033–3040 (2014).

62. Deng, S., Xu, W., Wang, J., Ling, X., Wu, J., Xie, L., Kong, J., Dresselhaus, M. S. Direct measurement of the Raman enhancement factor of rhodamine 6G on graphene under resonant excitation. *Nano Res.* **7**, 1271–1279 (2014).

63. Lee, Y., Kim, H., Lee, J., Yu, S. H., Hwang, E., Lee, C., Ahn, J.-H. & Cho, J. H. Enhanced Raman Scattering of Rhodamine 6G Films on Two-Dimensional Transition Metal Dichalcogenides Correlated to Photoinduced Charge Transfer. *Chem. Mater.* **28**, 180–187 (2016).

64. Qiu, C., Zhou, H., Yang, H., Chen, M., Guo, Y. & Sun, L. Investigation of n-layer graphenes as substrates for Raman enhancement of crystal violet. *J. Phys. Chem. C* **115**, 10019–10025 (2011).

65. Ling, X., Wu, J., Xie, L. & Zhang, J. Graphene-thickness-dependent graphene-enhanced Raman scattering. *J. Phys. Chem. C* **117**, 2369–2376 (2013).

66. Qiu, C., Zhou, H., Yang, H., Chen, M., Guo, Y. & Sun, L. Investigation of *n* -Layer Graphenes as Substrates for Raman Enhancement of Crystal Violet. *J. Phys. Chem. C* **115**, 10019–10025 (2011).

67. Ling, X., Wu, J., Xie, L. & Zhang, J. Graphene-Thickness-Dependent Graphene-Enhanced Raman Scattering. *J. Phys. Chem. C* **117**, 2369–2376 (2013).

68. Guselnikova, O., Kalachyova, Y., Hrobonova, K., Trusova, M., Barek, J., Postnikov, P., Svorcik, V. & Lyutakov. SERS platform for detection of lipids and disease markers prepared using modification of plasmonic-active gold gratings by lipophilic moieties. *Sensors Actuators, B Chem.* **265**, 182–192 (2018).

69. Ling, X., Fang, W., Lee, Y.-H., Araujo, P. T., Zhang, X., Rodriguez-Nieva, J. F., Lin, Y., Zhang, J., Kong, J., Dresselhaus, M. S. Raman Enhancement Effect on Two-Dimensional Layered Materials: Graphene, h-BN and MoS_2. *Nano Lett.* **14**, 3033–3040 (2014).

70. Semova, I., Levenson, A. E., Krawczyk, J., Bullock, K., Williams, K. A., Wadwa, R. P., Shah, A. S., Khoury, P. R., Kimball, T. R., Urbina, E. M., de Ferranti, S. D., Bishop, F. K., Maahs, D. M., Dolan, L. M., Clish, C. B. & Biddinger, S. B. Type 1

diabetes is associated with an increase in cholesterol absorption markers but a decrease in cholesterol synthesis markers in a young adult population. *J. Clin. Lipidol.* **13**, 940–946 (2019).

71. Wang, L., Ge, L., Rufford, T. H. & Zhu, Z. H. in *Nanotubes and Nanosheets: Functionalization and Applications of Boron Nitride and Other Nanomaterials* (ed. Chen, Y.) 223–229 (CRC Press, 2015).

72. Gaur, A. P. S., Sahoo, S., Ahmadi, M., Dash, S. P., Guinel, M. J.-F. & Katiyar, R. S. Surface energy engineering for tunable wettability through controlled synthesis of MoS_2. *Nano Lett.* **14**, 4314–4321 (2014).

73. Jaiswal, M. K., Singh, K. A., Lokhande, G. & Gaharwar, A. K. Superhydrophobic states of 2D nanomaterials controlled by atomic defects can modulate cell adhesion. *Chem. Commun.* **55**, 8772–8775 (2019).

74. *International Conference on Harmonisation of Technical Requirements for Registration of Pharmaceuticals for Human Use Ich Harmonised Tripartite Guidline Validation of Analytical Procedures: Text and Methodology Q2(R1)*.

75. Kundu, J., Levin, C. S. & Halas, N. J. Real-time monitoring of lipid transfer between vesicles and hybrid bilayers on Au nanoshells using surface enhanced Raman scattering (SERS). *Nanoscale* **1**, 114–117 (2009).

76. Driver, M., Li, Y., Zheng, J., Decker, E., McClements, D. J. & He, L. Fabrication of lipophilic gold nanoparticles for studying lipids by surface enhanced Raman spectroscopy (SERS). *Analyst* **139**, 3352–3355 (2013).

77. Pinzaru, S. C., Muller, C., Ujevic, I., Venter, M. M., Chis, V. & Glamuzina. Lipophilic marine biotoxins SERS sensing in solutions and in mussel tissue. *Talanta* **187**, 47–58 (2018).

78. Wojnarowska, R., Polit, J., Broda, D., Gonchar, M. & Sheregii, E. M. Surface enhanced Raman scattering as a probe of the cholesterol oxidase enzyme. *Appl. Phys. Lett.* **106**, 103701 (2015).

79. Liu, S., Chen, Y., Wang, Y. & Zhao, G. Group-Targeting Detection of Total Steroid Estrogen Using Surface-Enhanced Raman Spectroscopy. *Anal. Chem.* **91**, 7639–7647 (2019).

80. Fraser, J. P., Postnikov, P., Miliutina, E., Kolska, Z., Valiev, R., Švorčík, V.,

Lyutakov, O., Ganin, A. Y. & Guselnikova, O. Application of a 2D molybdenum telluride in SERS-detection of biorelevant molecules. *ACS Appl. Mater. Interfaces* **15**, 54 (2020).

81. Kalachyova, Y., Mareš, D., Jeřábek, V., Elashnikov, R., Švorčík, V. & Lyutakov, O. Longtime stability of silver-based SERS substrate in the environment and (bio)environment with variable temperature and humidity. *Sensors Actuators, A Phys.* **285**, 566–572 (2019).

82. Sosińska, E., Przybylski, R., Hazendonk, P., Zhao, Y. Y. & Curtis, J. M. Characterisation of non-polar dimers formed during thermo-oxidative degradation of β-sitosterol. *Food Chem.* **139**, 464–474 (2013).

83. Dumont, E., De Bleye, C., Cailletaud, J., Sacré, P.-Y., Van Lerberghe, P.-B., Rogister, B., Rance, G. A., Aylott, J. W., Hubert, P. & Ziemons, E. Development of a SERS strategy to overcome the nanoparticle stabilisation effect in serum-containing samples: Application to the quantification of dopamine in the culture medium of PC-12 cells. *Talanta* **186**, 8–16 (2018).

84. Sun, F., Zhang, P., Bai, T., Galvan, D. D., Hung, H.-C., Zhou, N., Jiang, S. & Yu, Q. Functionalized plasmonic nanostructure arrays for direct and accurate mapping extracellular pH of living cells in complex media using SERS. *Biosens. Bioelectron.* **73**, 202–207 (2015).

85. Morton, S. M. & Jensen, L. Understanding the molecule-surface chemical coupling in SERS. *J. Am. Chem. Soc.* **131**, 4090–4098 (2009).

86. Jones, R. R., Hooper, D. C., Zhang, L., Wolverson, D. & Valev, V. K. Raman Techniques: Fundamentals and Frontiers. *Nanoscale Research Letters* vol. 14 1–34 (2019).

87. Pérez León, C., Kador, L., Peng, B. & Thelakkat, M. Characterization of the adsorption of Ru-bpy dyes on mesoporous TiO_2 films with UV-Vis, Raman, and FTIR spectroscopies. *J. Phys. Chem. B* **110**, 8723–8730 (2006).

88. Jiang, L., You, T., Yin, P., Shang, Y., Zhang, D., Guo, L. & Yang, S. Surface-enhanced Raman scattering spectra of adsorbates on Cu_2O nanospheres: Charge-transfer and electromagnetic enhancement. *Nanoscale* **5**, 2784–2789 (2013).

89. Socrates, G. Infrared and Raman Characteristic Group Frequencies: Tables and Charts. in 50, 68, 94 (John Wiley & Sons Ltd, 2004).

90. Ziyatdinova, G. K. & Budnikov, H. C. Evaluation of the antioxidant properties of spices by cyclic voltammetry. *J. Anal. Chem.* **69**, 990–997 (2014).

91. Furtak, T. E. & Roy, D. Nature of the active site in surface-enhanced Raman scattering. *Phys. Rev. Lett.* **50**, 1301–1304 (1983).

6. Synthesis and Investigation of Mo_3Sb_7 and $Mo_3Sb_{7-x}Te_x$

6.1. Introduction

Despite the numerous potential applications of $MoTe_2$, it of course is not the perfect material. For instance, the semiconducting 2H-phase is attractive for optoelectronic applications due to its direct bandgap of around 1.1 eV in the monolayer.[1] Especially in the field of silicon photonics, which have potential to become a key part of modern communications networks. This is because silicon itself is not a highly efficient light emitting material due to its indirect bandgap and as such a gain material must be used to deliver strong emission.[2] Recent work has shown that 2H-$MoTe_2$ can be integrated and utilised as a gain material but to achieve the required power densities it must be thinned down to just a couple of layers. This increases the band gap compared to the bulk material (~1→~1.1 eV) whereas an ideal gain material would have a bandgap lower than 1 eV to emit at the relevant communication wavelengths of 1310 or 1550 nm.[2–4]

One possible strategy for tuning the bandgap of 2H-$MoTe_2$ is to dope this material. Unfortunately, replacing tellurium results in a widening of the bandgap (if replaced by other chalcogens, S or Se) or a change in crystal structure (if replaced by Sb for example).[5,6] Doping on the Mo site, therefore seems like the only strategy, however, there are very few examples of this in the literature. Moreover, access to the Raman spectroscopy setup was disrupted from June 2020 until March 2021 due to building improvement works. This meant losing access to the most powerful characterisation tool for $MoTe_2$, as it can easily distinguish between the 2H- and 1T'-phases and can even be used to gauge the number of layers in a sample, as shown in Chapter 3. Therefore, it was decided to investigate Mo_3Sb_7 and doping tellurium into this system to explore $Mo_3Sb_{7-x}Te_x$ compounds as this would be feasible to monitor using PXRD. Furthermore, there are no reports on the chemical vapour deposition of Mo_3Sb_7 or $Mo_3Sb_{7-x}Te_x$ thin films and so the opportunity to apply the previously developed CVD setup to an unexplored chemical system was deemed exciting.

6.1.1. Structure and Properties of Mo_3Sb_7 and $Mo_3Sb_{7-x}Te_x$

Mo_3Sb_7 is the only known compound in the Mo-Sb binary system and exhibits a body-centred cubic Ir_3Ge_7-type crystal structure (Figure 6-1).[7]

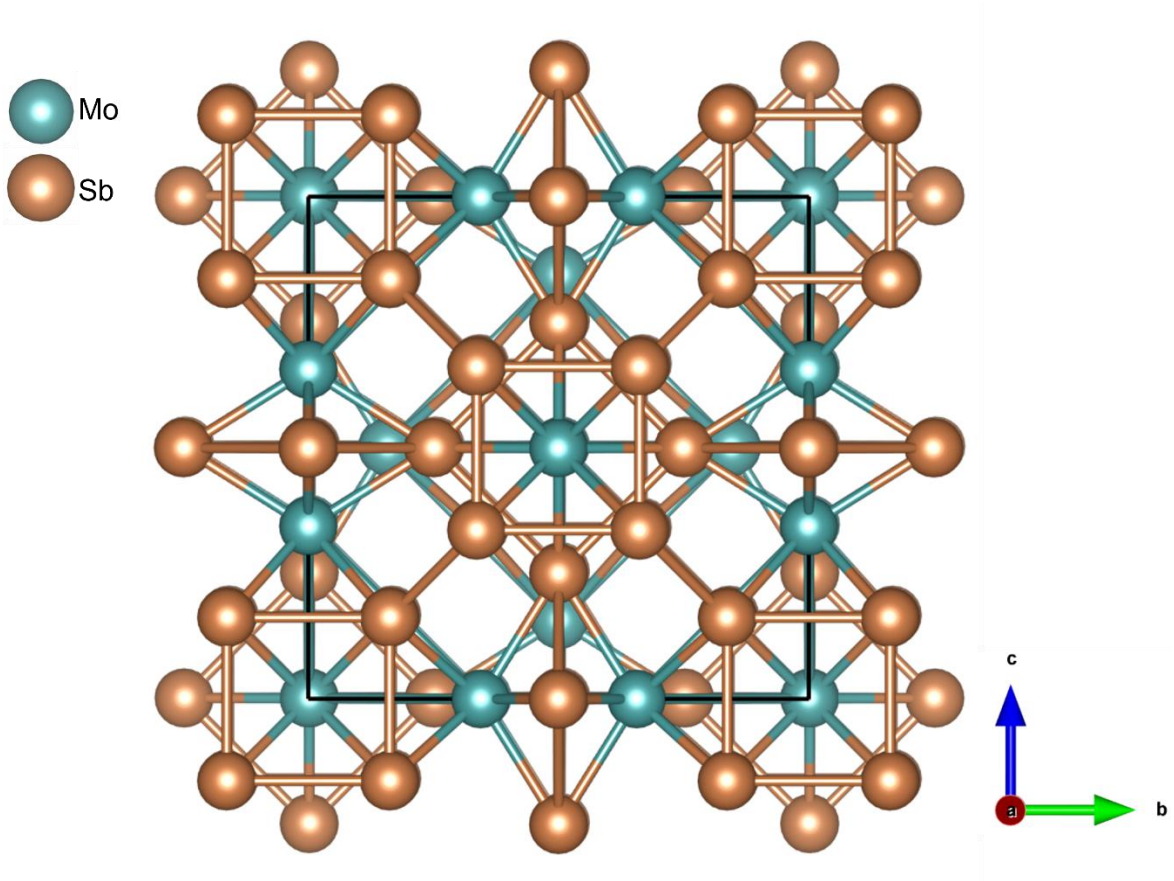

Figure 6-1: Extended unit cell of Mo_3Sb_7, viewed along the x-axis.

The structure consists of two antiprisms, which share a square face formed by Sb atoms with Mo atoms found at the center of these building blocks (Figure 6-2a). The $MoSb_8$ square antiprisms are connected *via* Sb-Sb bonds between neighbouring pairs forming infinite chains. This connection results in the formation of an empty Sb_8 cube, a feature that makes the intercalation of metal cations into this structure possible (Figure 6-2b).[8] Due to the 45° rotation angle between the two square faces there are two inequivalent positions for Sb. The Sb1 atoms form the face in the center of two $MoSb_8$ square antiprisms whilst Sb2 atoms form the cube.

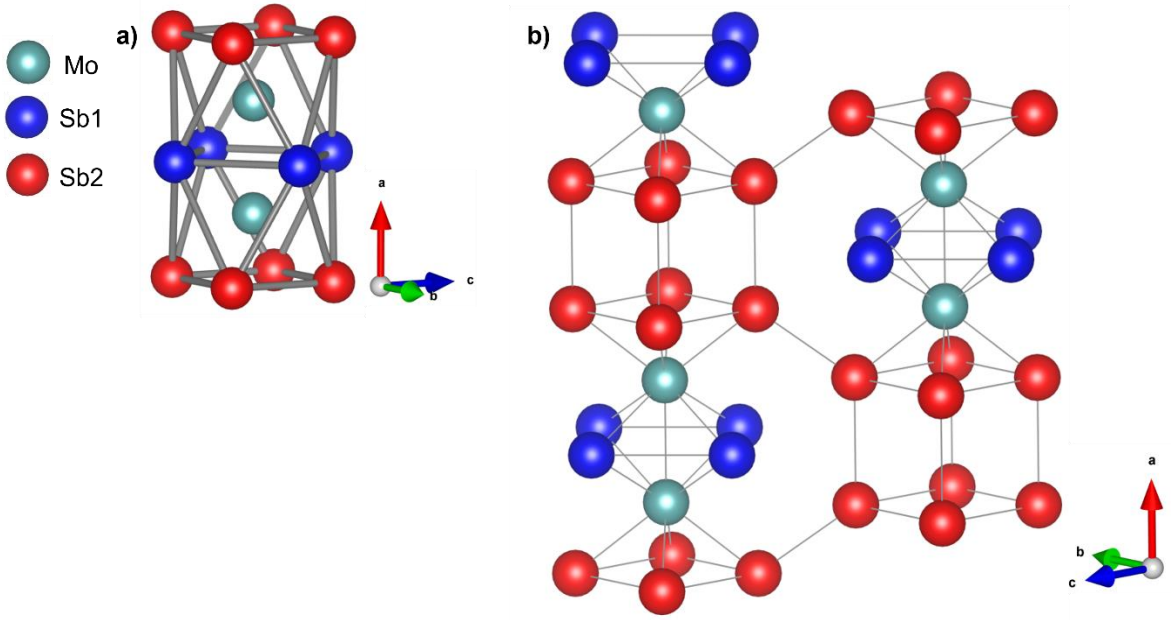

Figure 6-2: An antiprism formed by four Sb1 atoms (blue) and eight Sb2 atoms (red). Mo atoms (teal) sit in the centre of the prism (a); Two parallel chains of $MoSb_8$ antiprisms, highlighting the cubes formed by Sb2 atoms (b).

Mo_3Sb_7 exhibits metallic conductivity and has mostly been investigated for use as a thermoelectric material. Thermoelectric materials can either generate electricity from heat (Seebeck effect) or vice versa (Peltier effect) and are useful for power generation and refrigeration applications.[9] An ideal thermoelectric material should have a large Seebeck coefficient, S, high electrical conductivity, σ, and a low thermal conductivity, κ. Comparisons between thermoelectric materials can be made using the dimensionless figure of merit *z*T, which can be defined as:

$$zT = \frac{S^2\sigma}{\kappa}T$$

A common strategy for improving the thermoelectric properties of a material is to reduce its thermal conductivity. An interesting approach to this in the case of Mo_3Sb_7 was to attempt to fill the cubic voids with smaller cations, which reduce thermal conductivity by vibrating in their void, a phenomenon referred to as rattling. This is also observed in the filled skutterudites class of thermoelectrics such as $LaFe_3CoSb_{12}$.[10–12]

Typically, metals are poor thermoelectric materials due to their low Seebeck coefficients, however the Mo_3Sb_7 system was still of interest due to theoretical calculations that indicated that substituting Te for Sb (adding valence electrons) would result in a crossover from metallic to semiconducting behaviour.[13] Seebeck coefficients of semiconductors are typically two orders of magnitude higher than those of metals.[14] This change in conduction behaviour was subsequently confirmed experimentally with $Mo_3Sb_{7-x}Te_x$ materials showing

promising thermoelectric performance, with a zT = 0.51 for $Mo_3Sb_{5.2}Te_{1.8}$ at 850 K compared to Mo_3Sb_7 which exhibited zT = 0.09 at the same temperature.[15]

In regards to the structure of $Mo_3Sb_{7-x}Te_x$ there are of course two inequivalent Sb sites on which Te could reside. A joint computational and neutron diffraction study by Candolfi *et al*. determined that Te preferentially replaces Sb1 in the structure of $Mo_3Sb_{7-x}Te_x$ (Figure 6-3). They attribute this to the Sb1 site being more favourable for accommodating more electrons when substituting Sb for the more electronegative Te.[16]

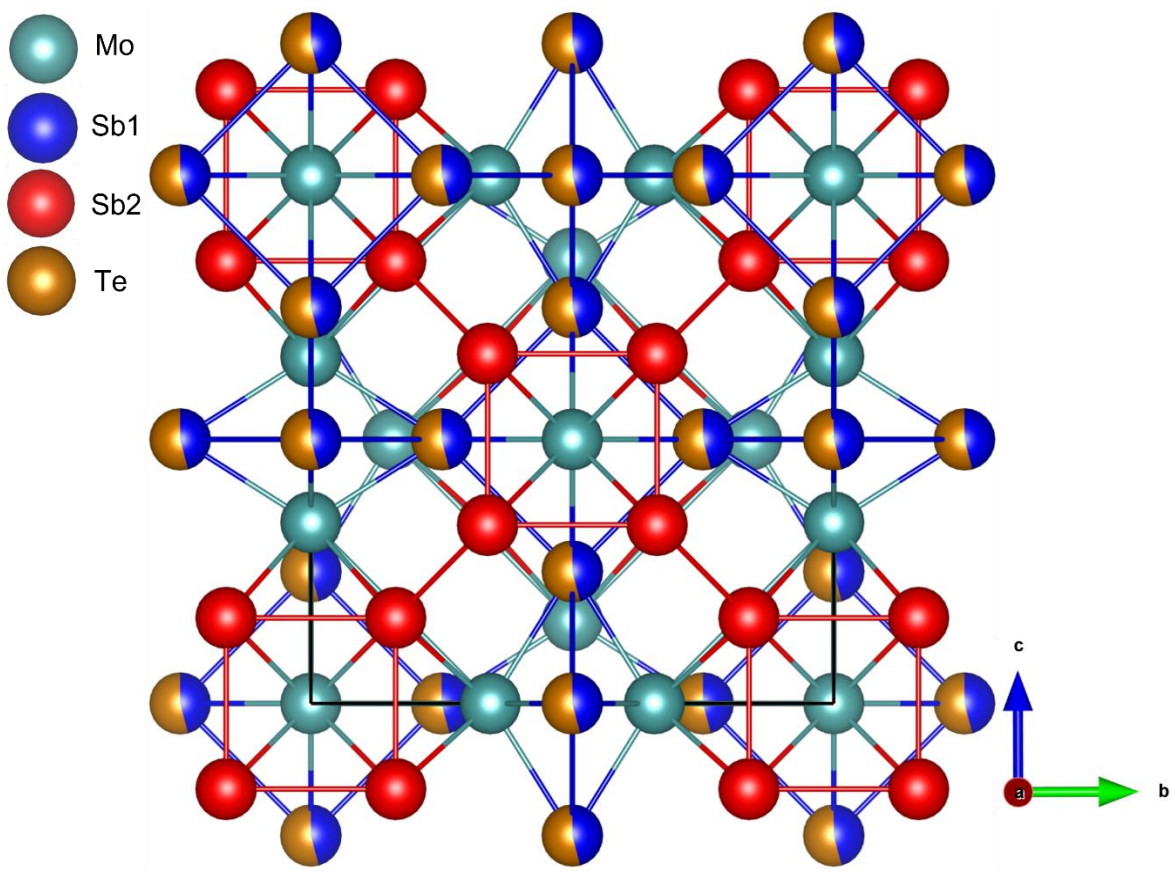

Figure 6-3: Extended unit cell of $Mo_3Sb_{5.4}Te_{1.6}$ as viewed along the x-axis. Te atoms (orange) preferentially replace Sb1 atoms (blue) in the structure whilst Mo (teal) and Sb2 atoms (red) are unaffected.

Aside from its application as a thermoelectric material Mo_3Sb_7 has also been investigated for its superconductivity and as an anode for lithium and sodium ion batteries.[17,18] However, there have been no accounts of Mo_3Sb_7 being utilised as an HER electrocatalyst, most probably due to the reported inactivity of Sb towards the HER.[19,20] The ability to add tellurium to this system without changing the structure offers an interesting opportunity to test the impact this has on the electrocatalytic behaviour of these materials. Furthermore, $Mo_3Sb_5Te_2$ is reported to have a narrow bandgap of 0.5 eV, with a decrease in Te concentration causing bandgap widening to a maximum value of 0.9 eV, making $Mo_3Sb_{7-x}Te_x$ potentially interesting for far-infrared optoelectronic applications.[6]

6.2. Aims

The aims of this section are to first synthesise Mo_3Sb_7 and $Mo_3Sb_{7-x}Te_x$ materials with varying levels of tellurium concentrations as bulk powders. Subsequently the materials will be characterised with PXRD and Rietveld refinements performed to ensure the materials are phase pure. The morphology and composition of the materials will be probed with a combination of SEM/EDX before being tested as electrocatalysts for the production of hydrogen from water. Finally chemical vapour deposition of Mo_3Sb_7 and $Mo_3Sb_{7-x}Te_x$ thin films will be attempted which again will be characterised by PXRD.

6.3. Results and Discussion

6.3.1. Synthesis and Characterisation of Bulk Mo_3Sb_7 and $Mo_3Sb_{7-x}Te_x$ Powders

Initially, Mo_3S_7 was synthesised using a modified version of the literature procedure reported by Dashjav *et al.* where stoichiometric amounts of elemental Mo and Sb powders were ground together using a pestle and mortar before being loaded into a quartz ampoule and sealed under vacuum. The sealed ampoule was then heated to a temperature of 700 °C for a dwell period of 100 hours before cooling to room temperature naturally.[6] The resulting powder was then reground and analysed using PXRD and Rietveld refinement used to ensure the material was phase pure. Rietveld refinement allows for the monitoring of shifts in atomic positions meaning it can be used to observe changes in Mo-Sb/Te bond length as Te is substituted for Sb. As it is not possible to distinguish directly between Sb and Te using XRD due to their similar electron density, the ability to monitor the substitution of Te for Sb by observing changes in bond length gives Rietveld refinement an advantage over other refinement methods such as Le Bail. The crystal structure data of Mo_3Sb_7 published by Dashjav *et al.* was used as a model for the refinement which is shown in Figure 6-4.[6]

The refinement of Mo_3Sb_7 achieved a reasonable match between the experimental and simulated profile, with each experimental peak described by the calculated pattern suggesting that the sample is single-phased and free from impurities. However, there are some discrepancies in the intensities of the experimental and calculated peaks. This may possibly be attributed to the quality of PXRD data, as it was not sufficient to refine Uiso values (attempts to refine the Uiso led to unrealistic negative values) that were fixed at neutron data and caused issues with peak intensities. Nevertheless, the unit cell parameter obtained from the refinement of a = 9.5651 (1) Å is close to the value of a = 9.5692 Å obtained by Okabe *et al.*[21]

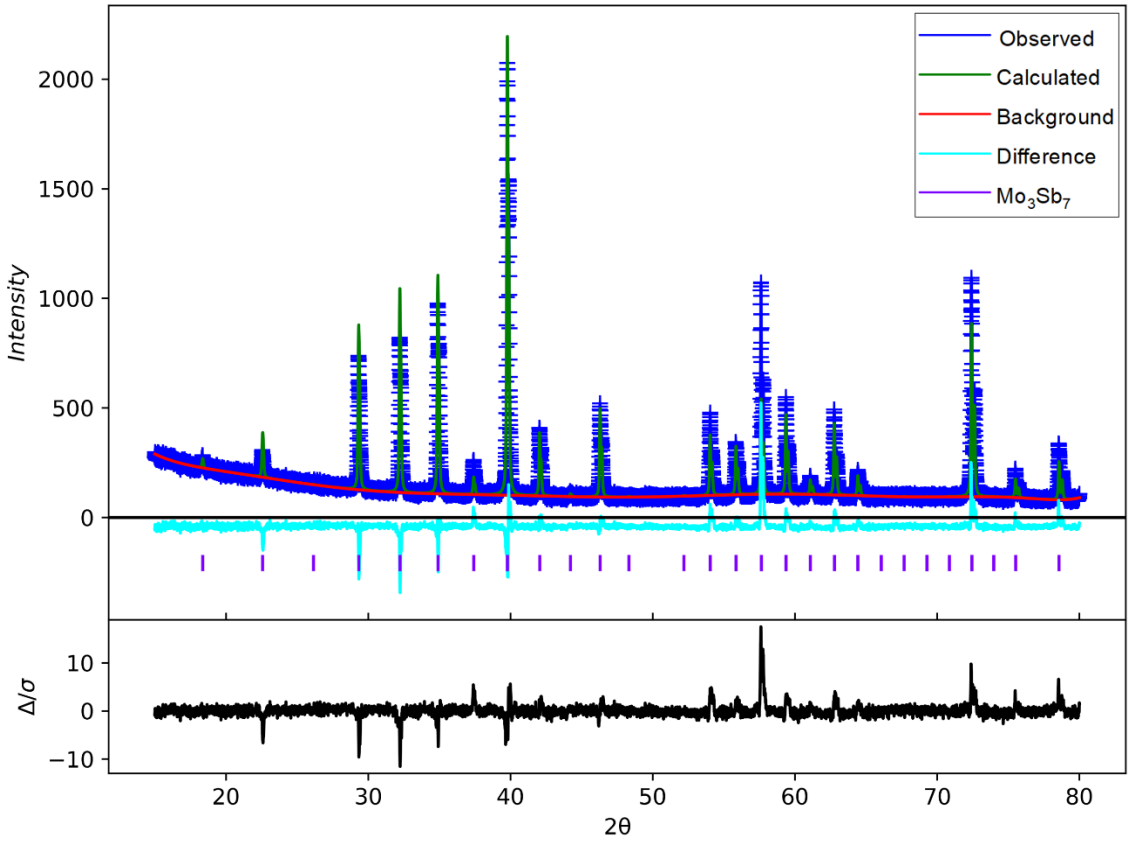

Figure 6-4: Rietveld refinement of Mo_3Sb_7 with observed (blue), calculated (green), background (red), difference (cyan) and peak position (purple) plots shown.

In the case of $Mo_3Sb_{7-x}Te_x$, two materials of differing tellurium concentration were synthesised using the same procedure for both, a modified version of the method previously reported by Dashjav *et al.*[6] Stoichiometric amounts of Mo, Sb and Te powders to result in compositions of Mo_3Sb_6Te, $Mo_3Sb_{5.4}Te_{1.6}$ and $Mo_3Sb_5Te_2$ were ground together in a pestle and mortar and loaded into quartz ampoules which were subsequently sealed under vacuum. For these materials the ampoules were heated to 750 °C for 100 hours before cooling naturally to room temperature. PXRD patterns of the synthesised powders were recorded, followed by Rietveld refinement using published crystal structure data of $Mo_3Sb_{5.4}Te_{1.6}$ reported by Candolfi *et al.* as a model.[16] The refinements of Mo_3Sb_6Te, $Mo_3Sb_{5.4}Te_{1.6}$ and $Mo_3Sb_5Te_2$ are shown in Figures 6-5, 6-6 and 6-7, respectively.

Regarding Mo_3Sb_6Te, the refinement again produced a reasonable fit, with each experimental peak described by the calculated pattern indicating the synthesised material is phase pure Mo_3Sb_6Te. As was the case for Mo_3Sb_7, there is also a disagreement between some of the intensities of the observed and calculated peaks which unfortunately, could not be resolved. Again, this was probably a result of the quality of the PXRD data obtained. The obtained unit cell parameter, a = 9.5598 (1) Å is marginally smaller compared to Mo_3Sb_7,

which can be understood from the differences in atomic radii of Sb and Te. As tellurium has a smaller atomic radius than antimony, incorporation of it into the structure will lead to a decrease in the lattice parameter.[15]

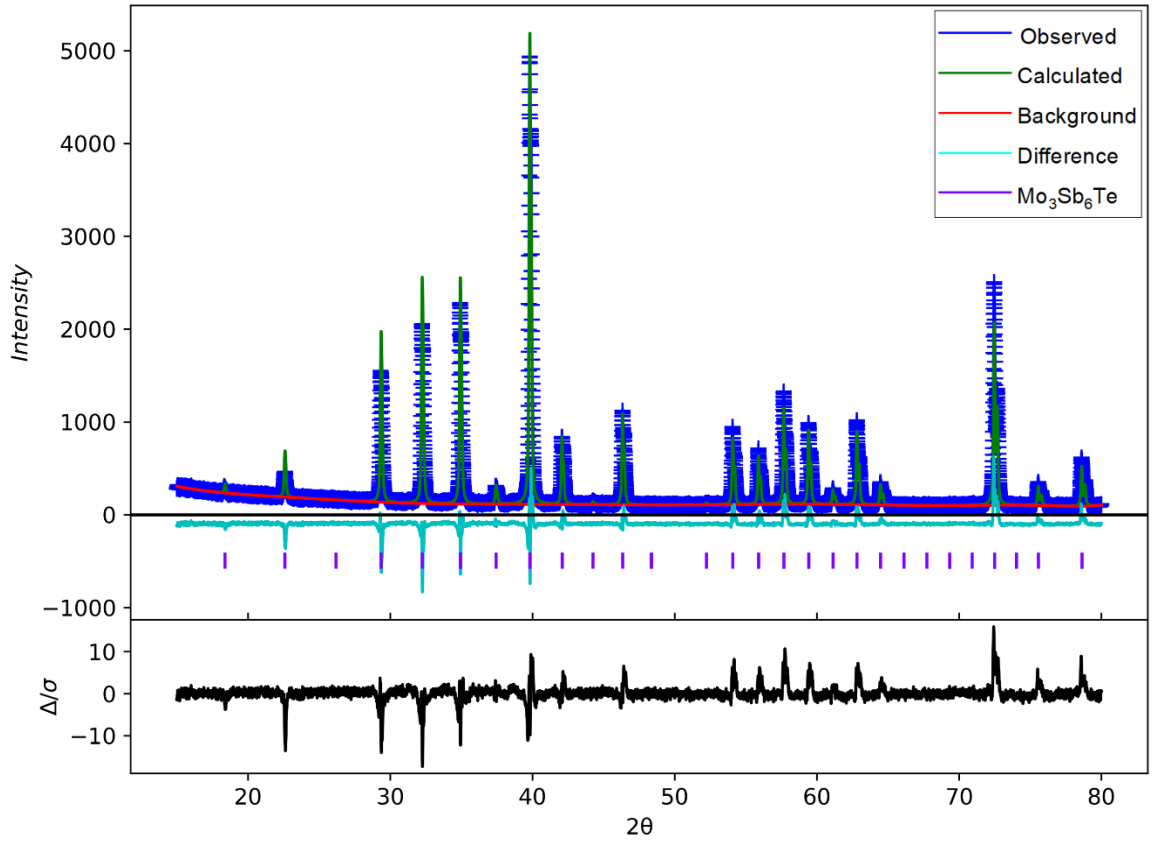

Figure 6-5: Rietveld refinement of Mo_3Sb_6Te with observed (blue), calculated (green), background (red), difference (cyan) and peak position (purple) plots shown.

The refinement of $Mo_3Sb_{5.4}Te_{1.6}$, once again provided a good fit whilst the discrepancy between observed and calculated intensity witnessed in the other two compounds was again present. Each experimental peak is described by the calculated pattern indicating that the material is phase pure. The obtained unit cell parameter of a = 9.5579 (6) Å is slightly smaller compared the value reported in a literature report of 9.5632 Å. With the incorporation of more Te into the structure the lattice parameter decreases slightly compared to Mo_3Sb_6Te.

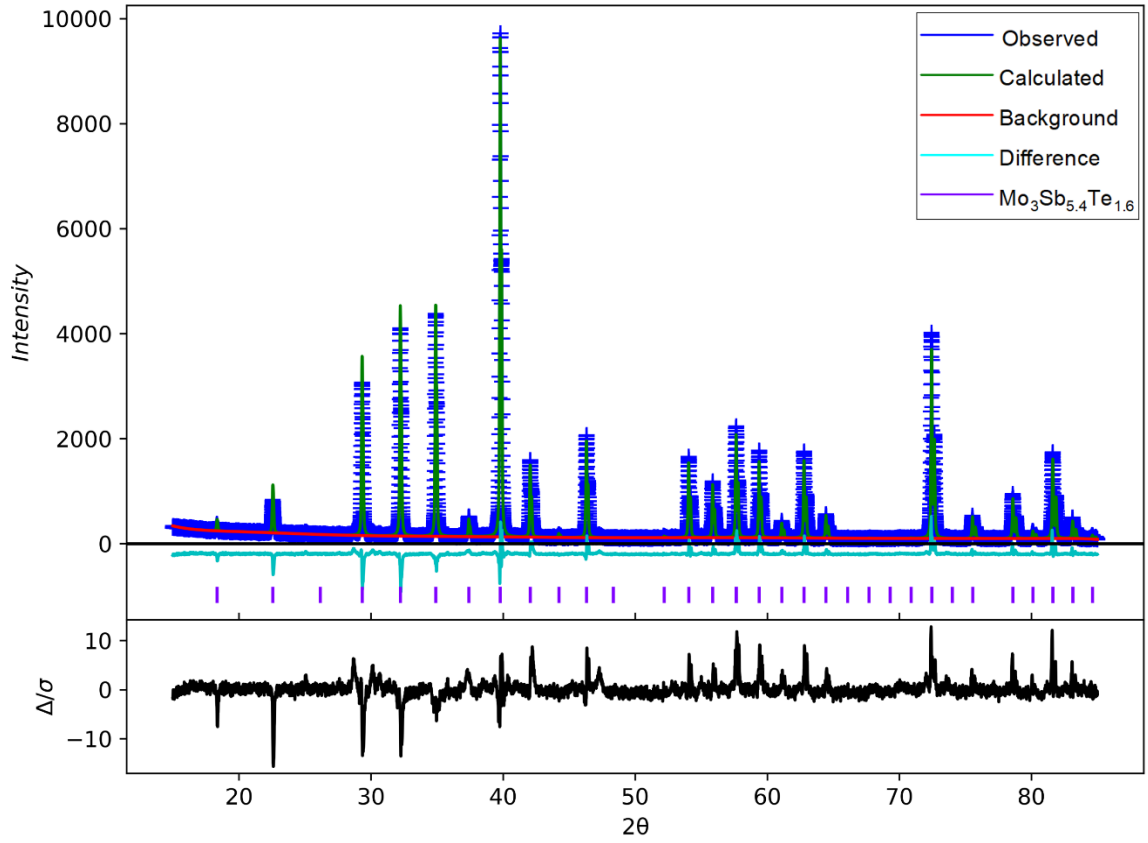

Figure 6-6: Rietveld refinement of $Mo_3Sb_{5.4}Te_{1.6}$ with observed (blue), calculated (green), background (red), difference (cyan) and peak position (purple) plots shown.

The further addition of Te in the case of $Mo_3Sb_5Te_2$ unfortunately results in the formation of 2H-$MoTe_2$ as an impurity, which is immediately clear from the refinement of this material (Figure 6-7). This is in line with the observations of Shi *et al.* and Xu *et al*. who found that the maximum amount of Te that can be substituted for Sb without the formation of $MoTe_2$ as an impurity is around 1.8.[11,15] The unit cell parameter, *a*, for $Mo_3Sb_5Te_2$ was found to be 9.5575 (3) Å, the smallest of the four compounds, which is to be expected since it should have the highest Te content. The lattice parameters of each compound are plotted against their Te content in Figure 6-8 to illustrate this clearly. The unit cell parameters, weighted profile R-factor (R_{wp}) and goodness of fit (GoF) factor from the Rietveld refinements are summarised in Table 6-1.

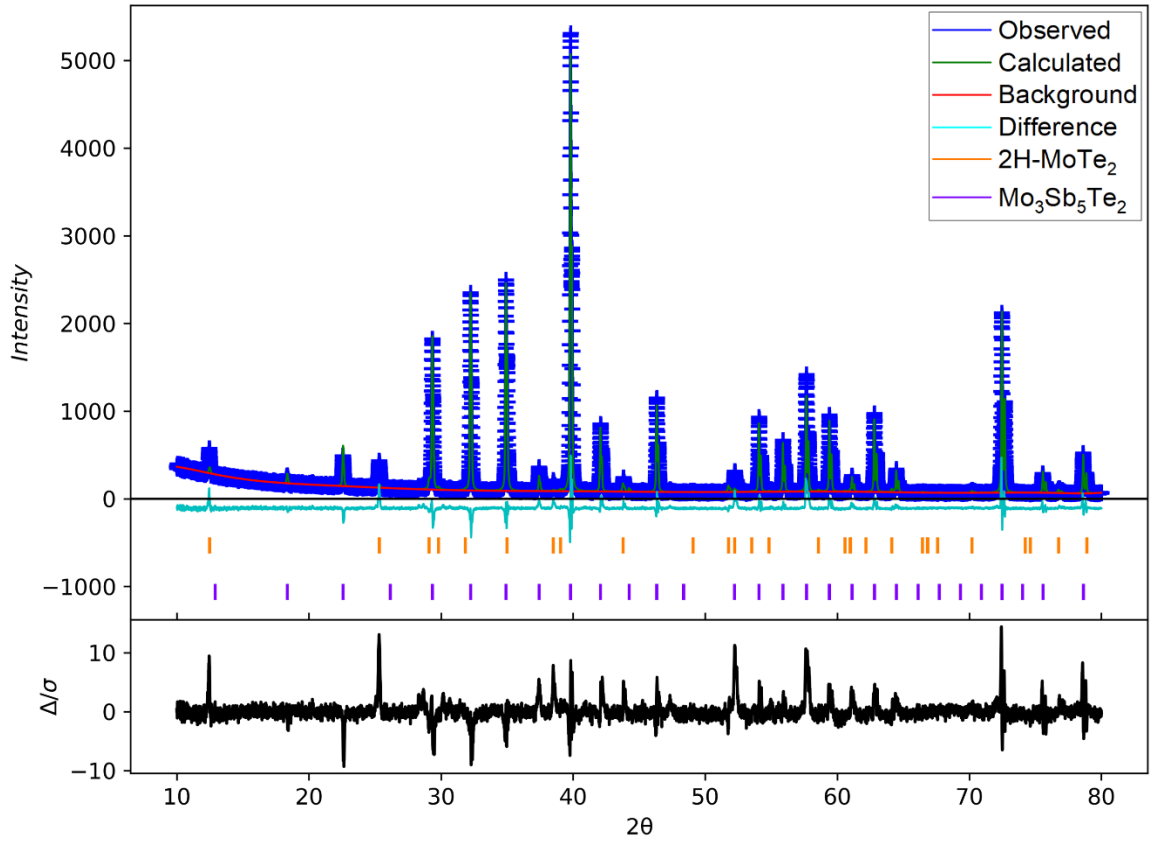

Figure 6-7: Rietveld refinement of $Mo_3Sb_5Te_2$ with observed (blue), calculated (green), background (red), difference (cyan) and peak positions of 2H-$MoTe_2$ (orange) and $Mo_3Sb_5Te_2$ (purple) plots shown.

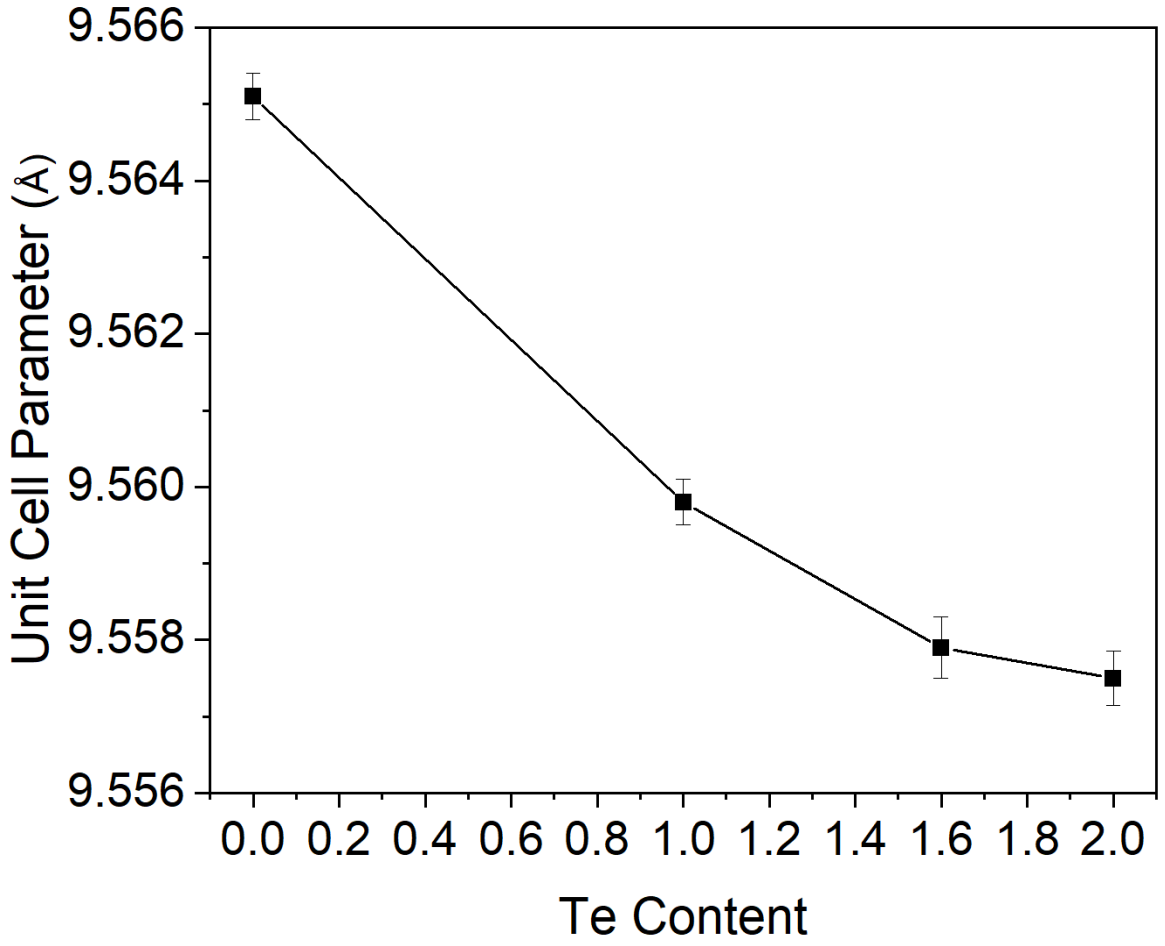

Figure 6-8: Plot revealing how the unit cell parameter, a, varies with increasing Te concentration in $Mo_3Sb_{7-x}Te_x$, where X = 0, 1, 1.6 & 2.

Table 6-1: A summary of the summary of the unit cell dimensions, R_{wp} and GoF values obtained for $Mo_3Sb_{7-x}Te_x$ where X = 0, 1, 1.6 & 2 from their respective Rietveld refinements.

Compound	**Unit Cell dimensions, *a* (Å)**	**R_{wp} (%)**	**GoF**
Mo_3Sb_7	9.5651(1)	10.72	1.29
Mo_3Sb_6Te	9.5598 (1)	12.54	1.79
$Mo_3Sb_{5.4}Te_{1.6}$	9.5579 (6)	11.82	1.84
$Mo_3Sb_5Te_2$	9.5575 (3)	12.77	1.63

6.3.2. Morphology and Composition of Bulk Mo_3Sb_7 and $Mo_3Sb_{7-x}Te_x$

Morphology can have a huge impact on the performance of electrocatalysts, with nano-structuring a common technique employed to improve catalytic performance, through increasing surface area, increasing the density of active sites or even improving electron transfer in the catalyst material.[22] Therefore, scanning electron microscopy was used to image the different materials to ensure that there were no significant disparities in morphology and subsequently, any differences in catalytic performance cannot be attributed to this. $Mo_3Sb_5Te_2$ was not examined *via* SEM due to the presence of the $MoTe_2$ impurity meaning the catalytic activity of this material cannot be solely attributed to $Mo_3Sb_5Te_2$. The three materials have broadly similar morphologies (Figure 6-9) with cubic crystallites interspersed in more agglomerated material. Interestingly, the cubic microcrystals of Mo_3Sb_7 (Figure 6-9a) appear significantly larger than those found in either Mo_3Sb_6Te (Figure 6-9b) or $Mo_3Sb_{5.4}Te_{1.6}$ (Figure 6-9c) with an edge length of ~20 µm compared to between ~8-10 µm for the Te doped materials.

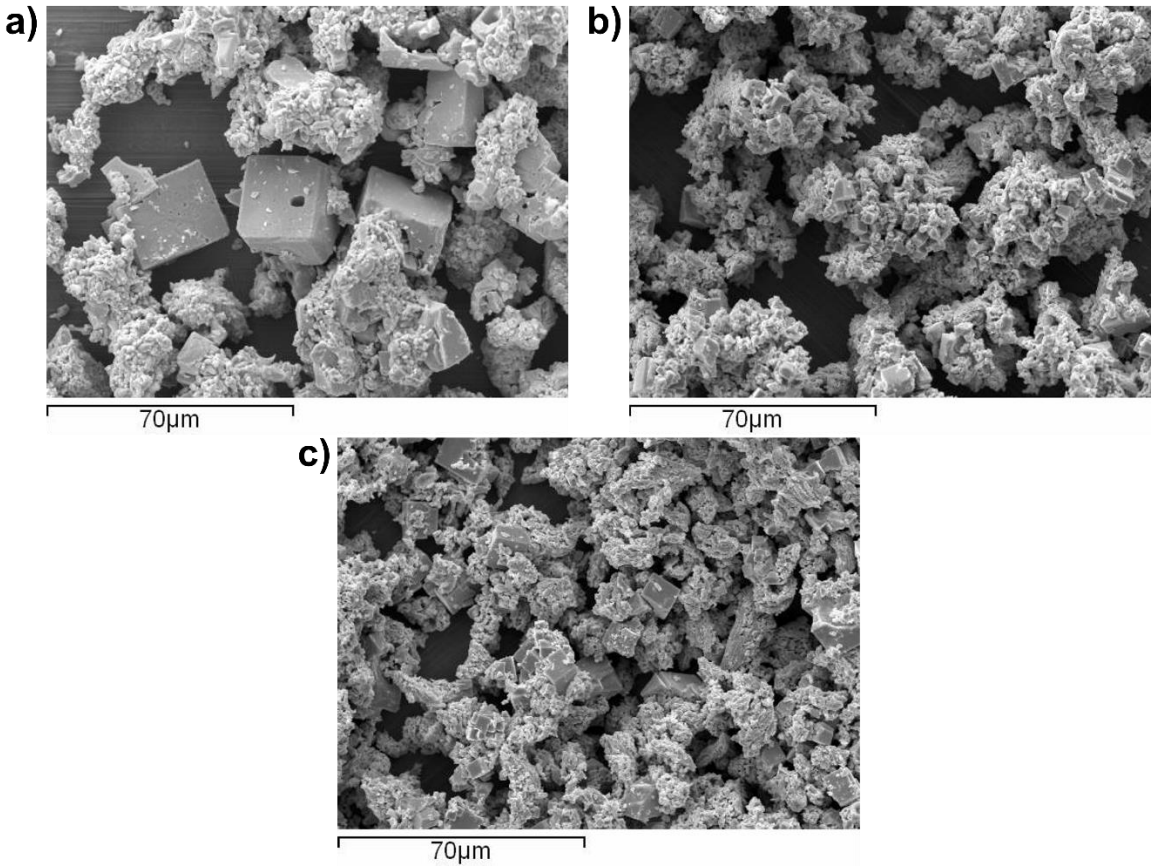

Figure 6-9: SEM images at 800x magnification of Mo_3Sb_7 (a); Mo_3Sb_6Te (b) and $Mo_3Sb_{5.4}Te_{1.6}$ (c).

Additionally, energy dispersive X-ray spectroscopy was performed to determine the elemental composition of the materials. Three spectra were recorded for each material and averaged to give the atomic percentage composition, which are summarised in Table 6-2.

Table 6-2: EDX analysis showing the experimental atomic % composition of Mo_3Sb_7, Mo_3Sb_6Te and $Mo_3Sb_{5.4}Te_{1.6}$ compared to theoretical values.

	Mo_3Sb_7 at. %		**Mo_3Sb_6Te at. %**			**$Mo_3Sb_{5.4}Te_{1.6}$ at. %**		
Element	Mo	Sb	Mo	Sb	Te	Mo	Sb	Te
Experimental	29.67 ± 1.02	71.33 ± 1.02	29.24 ± 1.07	59.88 ± 1.07	10.88 ± 1.07	29.87 ± 0.55	56.74 ± 0.55	13.39 ± 0.55
Theoretical	30	70	30	60	10	30	54	16

It is evident that the compositions of Mo_3Sb_7 and Mo_3Sb_6Te are close to the ideal theoretical values within experimental error. However, $Mo_3Sb_{5.4}Te_{1.6}$ appears to have a significant tellurium deficiency with an atomic percentage of ~13% as opposed to the theoretical value of 16%. Nevertheless, there is still sufficient variation in tellurium doping concentration to test the impact that this has on electrocatalytic performance.

6.3.3. Electrocatalytic Activity of Mo_3Sb_7 and $Mo_3Sb_{7-x}Te_x$ Towards the HER

In order to test the bulk Mo_3Sb_7 and $Mo_3Sb_{7-x}Te_x$ materials as electrocatalysts they were first made into catalyst inks that were subsequently drop cast onto glassy carbon working electrodes using a method reported by Gao *et al*.[23] The inks consisted of 10 mg of the respective catalyst dispersed in a mixture of 0.8 ml dimethylformamide and 50 µL Nafion followed by sonication for 20 minutes. Nafion is a sulfonated tetrafluoroethylene-based fluoropolymer-copolymer that has seen extensive use in proton exchange membrane electrolysers due to its stability under the harsh acidic conditions within the electrolyser and its high proton conductivity.[24] In this case Nafion was used to act as a conductive binder to the substrate. After sonication, 30 µL of the ink suspension was dropcast onto the glassy carbon electrode with a surface area of 0.071 cm^2, before being allowed to dry for several hours, resulting in a catalyst loading of 5.3 mg cm^{-2}. This ink formulation resulted in a visually smooth catalyst layer, with full coverage of the bare glassy carbon (Figure 6-10).

Figure 6-10: Photograph of dried catalyst inks on glassy carbon working electrodes.

Cyclic voltammetry was employed to test the electrocatalytic ability of the three materials, with the potential required to achieve a current density of 10 mA cm^{-2} again taken as the figure of merit. Mo_3Sb_7 performs poorly requiring an overpotential of -0.570 V to achieve a current density of 10 mA cm^{-2} (Figure 6-11). The material also displays a veritable lack of stability with the current densities achieved in subsequent scans dropping rapidly. On the second cycle a current density of 14 mA cm^{-2} is achieved at -0.6 V, but on the 20th cycle a current density of 7.4 mA cm^{-2} is only able to be reached at the same potential. Interestingly, Mo_3Sb_7 has a lower overpotential, by 50 mV, on the 2nd cycle compared to the bulk 2H-$MoTe_2$ powder tested in Chapter 5, despite the inactivity of antimony towards the HER, suggesting that its metallic conductivity aids performance in this case.[19,20]

With the addition of tellurium into the structure of Mo_3Sb_7 the conductivity changes from metallic to semiconducting, which typically is not ideal for hydrogen evolution catalysts.[25] However, the activity of Te towards the HER has been reported and replacing inactive Sb with Te may compensate for this change in electronic behaviour.[26] The CV scans from Mo_3Sb_6Te suggest that this amount of Te doping is not sufficient, with the compound having a higher overpotential by around 25 mV compared to Mo_3Sb_7 (Figure 6-12). Although, Mo_3Sb_6Te shows much improved stability with only a 4 mV reduction in overpotential between the 2nd and 20th cycles.

A further increase in tellurium doping does, however, result in improved electrocatalytic performance (Figure 6-13). The overpotential required by $Mo_3Sb_{5.4}Te_{1.6}$ to achieve a current density of 10 mA cm^{-2} is -0.511 V for the 2nd cycle and -0.514 V for the 20th cycle, once again illustrating the superior stability of the Te doped materials. Furthermore, the current densities achieved by $Mo_3Sb_{5.4}Te_{1.6}$ are slightly higher those achieved by Mo_3Sb_7 suggesting that the level of Te doping in this case is sufficient to overcome the limitations of its semiconducting nature. $Mo_3Sb_{5.4}Te_{1.6}$ also shows far superior catalytic performance to the bulk 2H-$MoTe_2$ powder tested as a control in Chapter 5, exhibiting a 0.14 V reduction in overpotential compared to the TMDC material. The overpotentials of the three materials tested are summarised in Table 6-3.

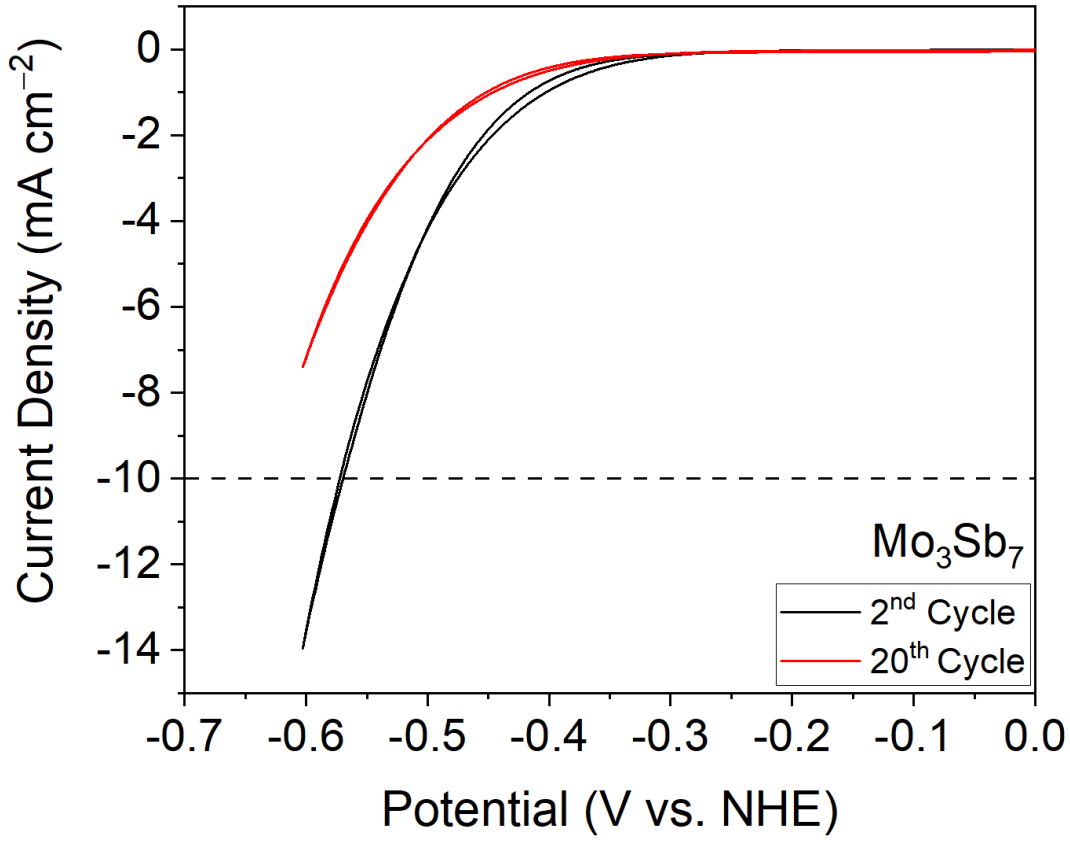

Figure 6-11: CV scans showing the 2nd and 20th cycles for Mo_3Sb_7.

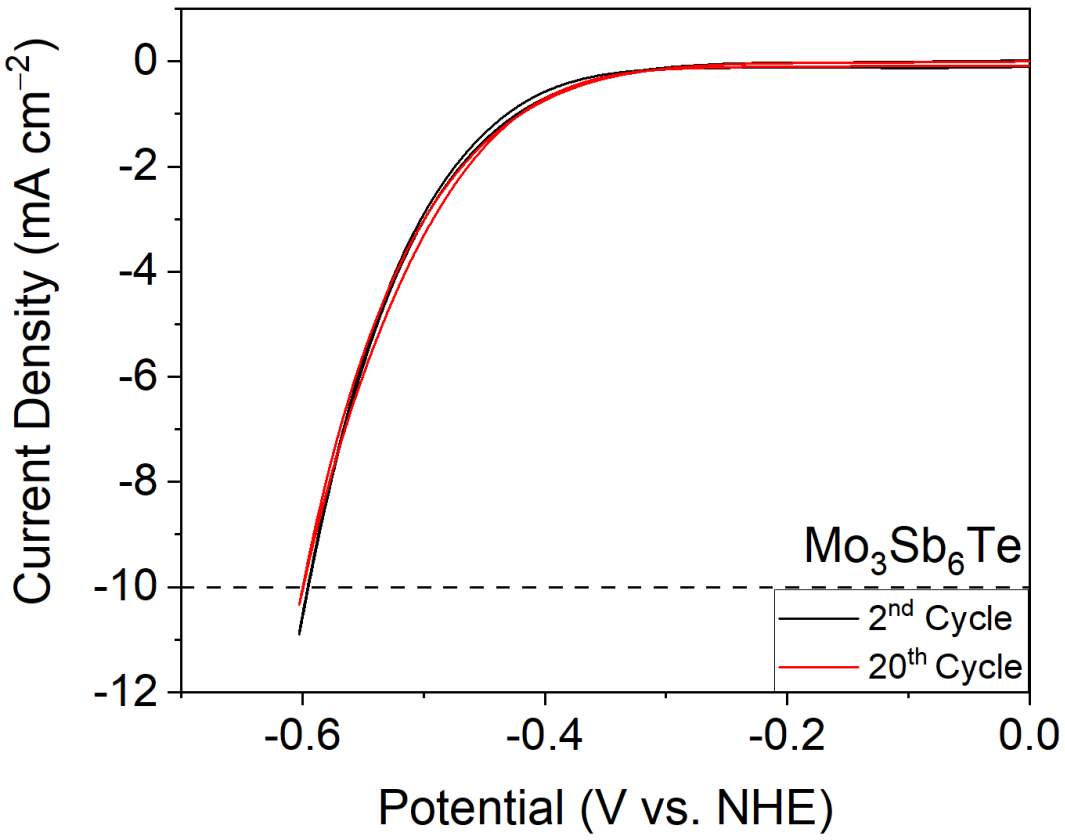

Figure 6-12: CV scans showing the 2nd and 20th cycles for Mo_3Sb_6Te.

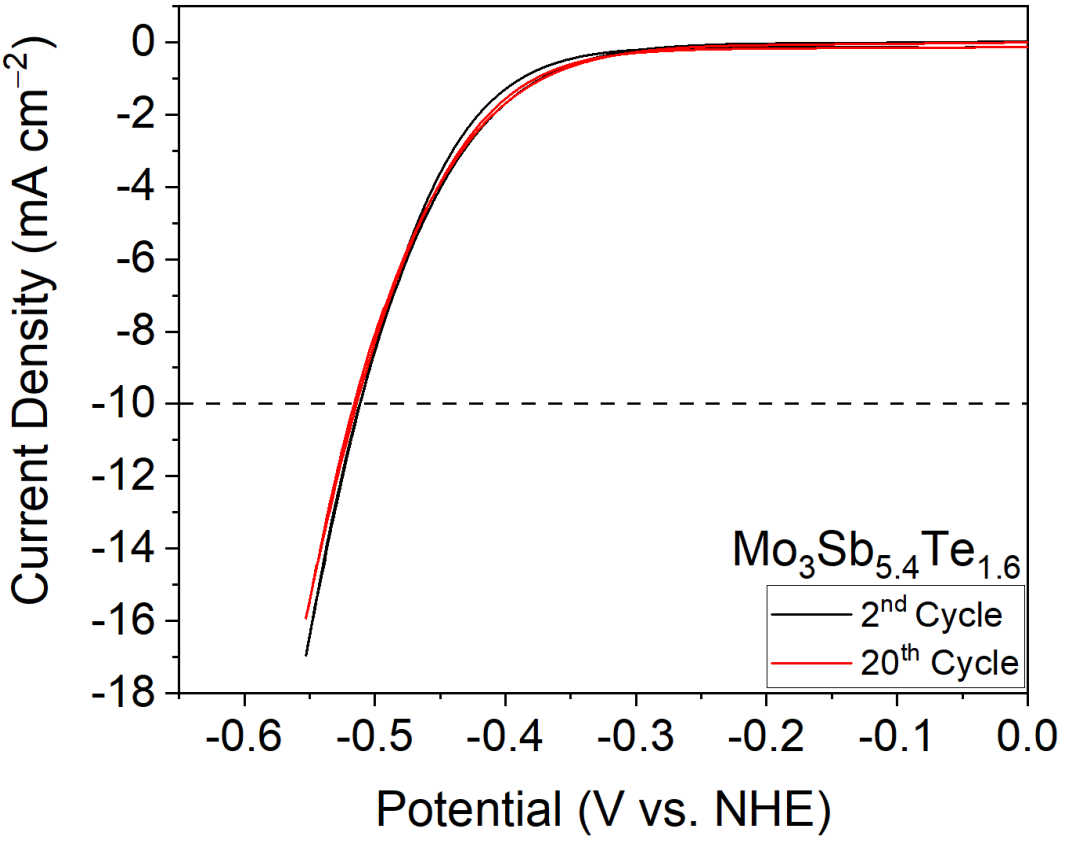

Figure 6-13: CV scans showing the 2nd and 20th cycles for $Mo_3Sb_{5.4}Te_{1.6}$.

Table 6-3: A summary of the overpotentials required to achieve a current density of 10 mA cm^{-2} on the 2nd and 20th cycles for Mo_3Sb_7 and $Mo_3Sb_{7-x}Te_x$ compounds.

Material	Overpotential (V) at 10 mA cm^{-2} 2nd Cycle	Overpotential (V) at 10 mA cm^{-2} 20th Cycle
Mo_3Sb_7	-0.570	-
Mo_3Sb_6Te	-0.595	-0.599
$Mo_3Sb_{5.4}Te_{1.6}$	-0.511	-0.514

Tafel analysis was used to gain a further insight into the catalytic activity of Mo_3Sb_7 and $Mo_3Sb_{7-x}Te_x$. Tafel plots are obtained by calculating the logarithm of the current density, which is subsequently plotted on the x-axis against the overpotential on the y-axis. The gradient of the resultant plot gives the Tafel slope, which is a measure of the voltage required the increase the current density by an order of magnitude. An efficient electrocatalyst should ideally have a low Tafel slope and achieve the highest current density at the lowest possible overpotential. For example, platinum electrocatalysts typically exhibit Tafel slopes of around 30 mV per decade.[27] The mechanism of hydrogen production can also be inferred by the value of the Tafel slope. There are three reaction pathways that can occur during the electrochemical production of hydrogen, known as the Volmer, Heyrovsky and Tafel reactions, which are illustrated in Table 6-4

Table 6-4: Description of the three reaction that can occur during the electrochemical production of hydrogen.

Volmer Reaction	$H_3O^+ + e^- \rightarrow H_{ads} + H_2O$	Discharge step
Heyrovsky Reaction	$H_{ads} + H_3O^+ + e^- \rightarrow H_2 + H_2O$	Electrochemical desorption step
Tafel Reaction	$H_{ads} + H_{ads} \rightarrow H_2$	Recombination step

The hydrogen evolution reaction on platinum proceeds *via* the Volmer-Tafel mechanism, which involves the initial adsorption of hydrogen onto the catalyst surface (Volmer) followed by the rate-limiting recombination step. In contrast, TMDC electrocatalysts are thought to produce hydrogen *via* the Volmer-Heyrovsky mechanism, with electrochemical desorption (Heyrovsky) being rate limiting.[28,29]

The 20th CV cycle for each material was used to calculate their respective Tafel slopes which are shown in Figure 6-14. Unsurprisingly, the values of the Tafel slopes for the compounds mirrors their general catalytic performance. For instance, Mo_3Sb_7 has the poorest catalytic performance after 20 cycles and subsequently has the largest Tafel slope of 167.5 ± 0.6 mV

dec^{-1}, which is higher than that of Mo_3Sb_6Te (153.6 ± 0.7 mV dec^{-1}) and $Mo_3Sb_{5.4}Te_{1.6}$ (136.2 ± 0.5 mV dec^{-1}). The values of Tafel slopes obtained for these materials suggest that the kinetics of the HER are limited due to inefficient adsorption of hydrogen on the catalyst surface.[28] As well as outperforming bulk 2H-$MoTe_2$ in terms of overpotential $Mo_3Sb_{5.4}Te_{1.6}$ also has a lower Tafel slope, which for 2H-$MoTe_2$ was found to be 159 ± 6 mV dec^{-1} by McGlynn *et al.*[30]

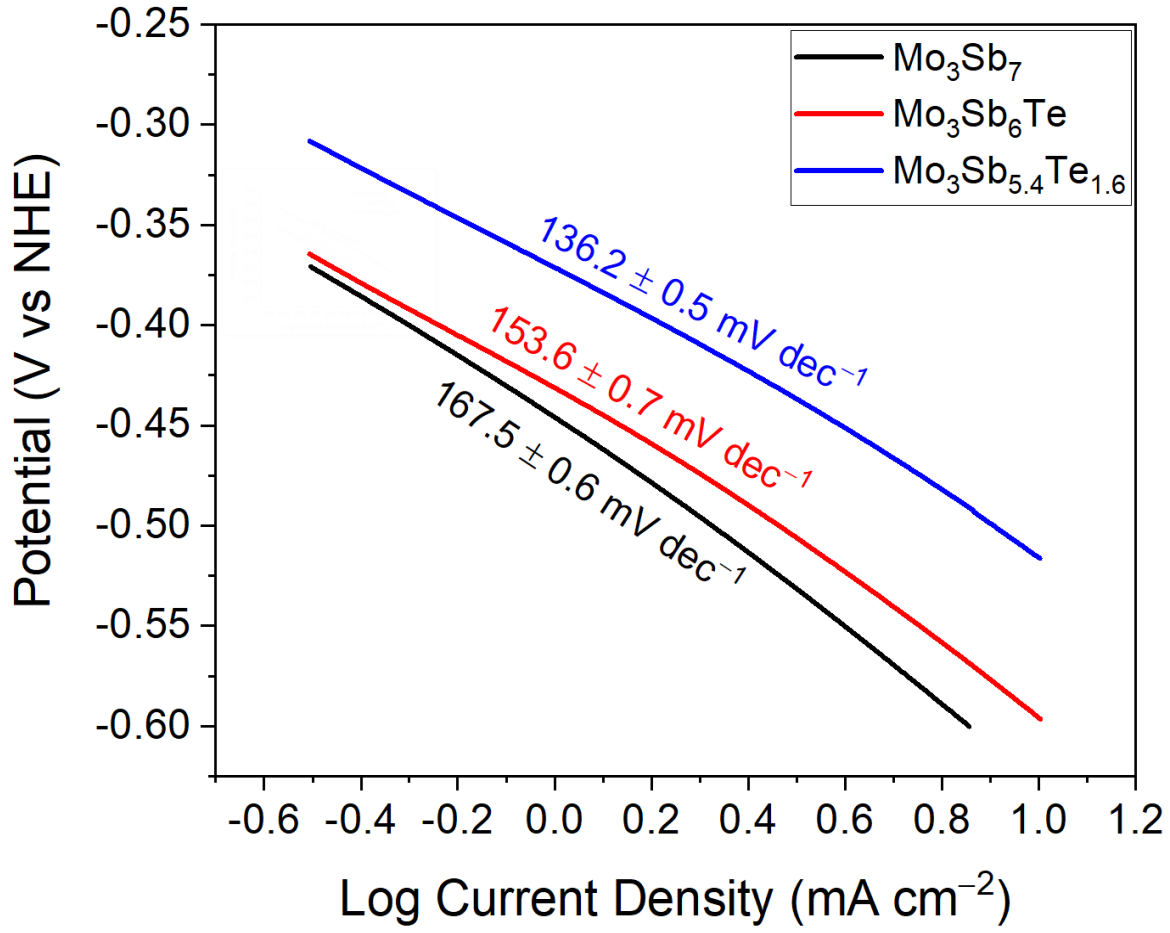

Figure 6-14: Tafel slopes obtained for Mo_3Sb_7, Mo_3Sb_6Te and $Mo_3Sb_{5.4}Te_{1.6}$.

The brief electrochemical testing of $MoSb_7$, Mo_3Sb_6Te and $Mo_3Sb_{5.4}Te_{1.6}$ found them to be poor electrocatalysts for the hydrogen evolution reaction with large overpotentials, high Tafel slopes and incredibly poor stability in the case of Mo_3Sb_7. Due to the inactivity of Sb-sites towards the HER, this was to be expected. Nevertheless, they provide an interesting system to study the impact of doping Te into this system, which dramatically improved performance for $Mo_3Sb_{5.4}Te_{1.6}$ as well as improving the stability. Further increasing the tellurium concentration may improve performance further but it should be noted that Te fractions of above 1.8 result in the formation of $MoTe_2$ as an impurity.[15]

6.3.4. Attempted Chemical Vapour Deposition of Mo_3Sb_7 and $Mo_3Sb_{7-x}Te_x$ Thin Films

In parallel with the solid-state route, attempts were made at synthesising Mo_3Sb_7 and $Mo_3Sb_{7-x}Te_x$ thin films through chemical vapour deposition using the same flow setup used in Chapter 4. With no literature reports on the CVD of Mo_3Sb_7, a similar approach to the CVD of $MoTe_2$ was taken with some modifications. Due to the higher melting point of antimony compared to tellurium, the Sb shot used as a precursor was placed in the hot zone of the CVD furnace at a temperature of 750 °C, with the $Mo/SiO_2/Si$ substrate placed 9 cm downstream at a temperature of 650 °C (Figure 6-15). As the only characterisation method available for monitoring the outcome of these reactions was XRD, a 20 nm Mo precursor film was used in the hope it would result in thick enough product films and their XRD peaks could be observed and not overwhelmed by those belonging to the silicon substrate.

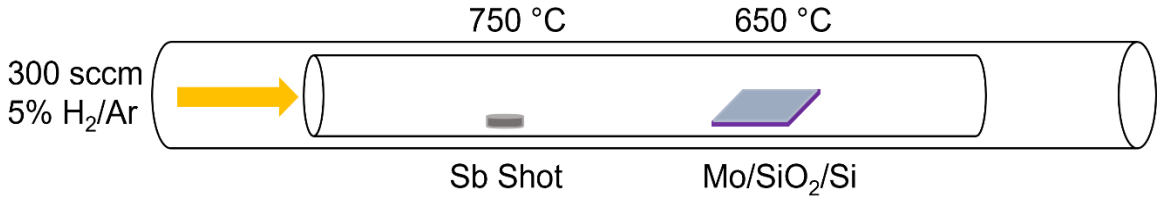

Figure 6-15: CVD setup and parameters used in the attempted deposition of Mo_3Sb_7.

For the first attempt a dwell time of 4 hours was used and the same 5% H_2/Ar carrier gas at a flow rate of 300 sccm was utilised. The XRD pattern obtained from the product film was compared to that obtained from a bare SiO_2/Si substrate and is shown in Figure 6-16.

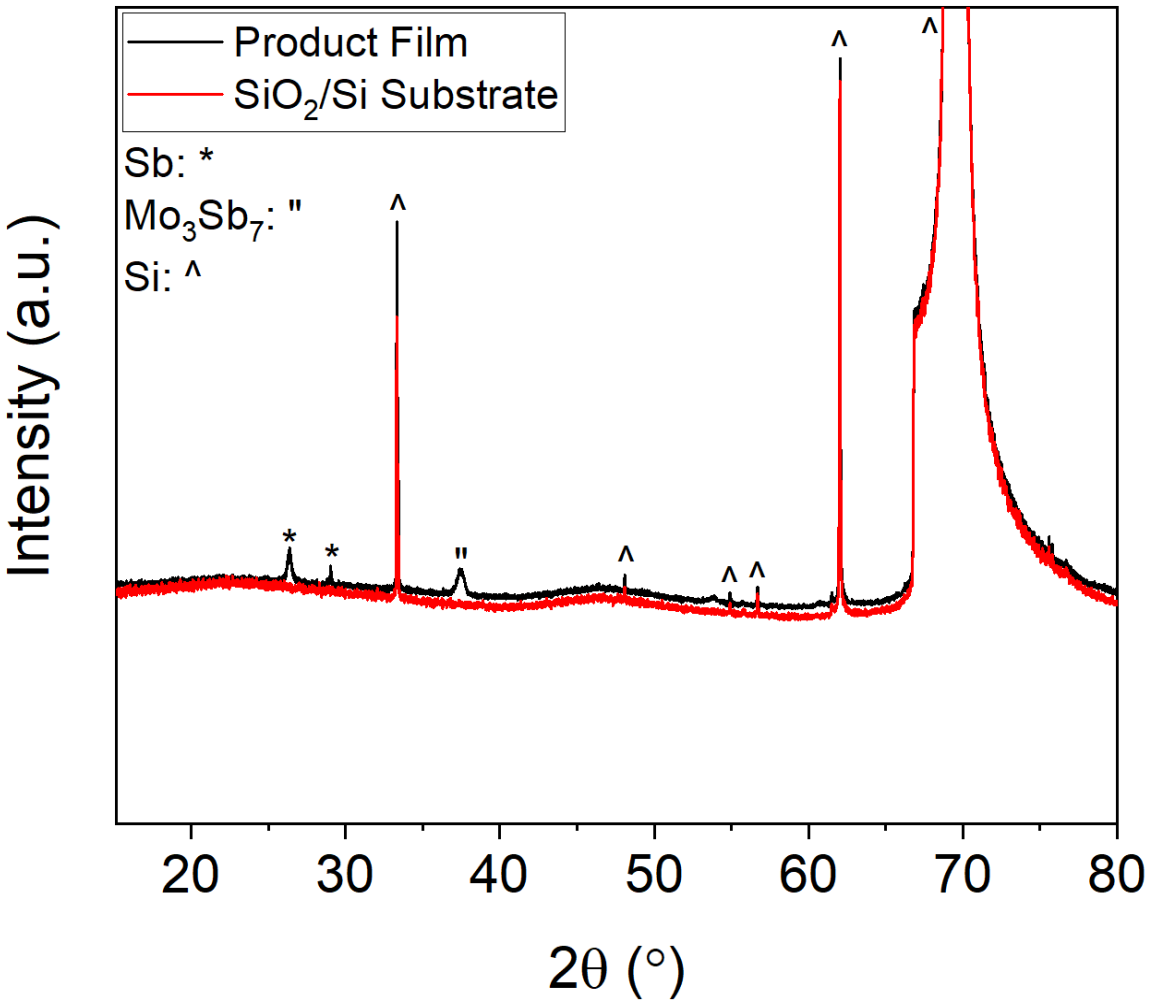

Figure 6-16: XRD patterns with Intensity on a log scale, obtained from the CVD produced film and a bare SiO_2/Si substrate.

Aside from the peaks that clearly belong to the substrate there are peaks that belong to both elemental Sb at ~26° and ~29° and Mo_3Sb_7 at ~37°. The peaks of both Sb and Mo_3Sb_7 are weak in comparison to those belonging to the substrate, possibly due to incomplete conversion of the precursor Mo layer. In order to test this longer dwell times of 8 and 16 hours were trialled and the XRD patterns of the resulting films are shown in Figure 6-17.

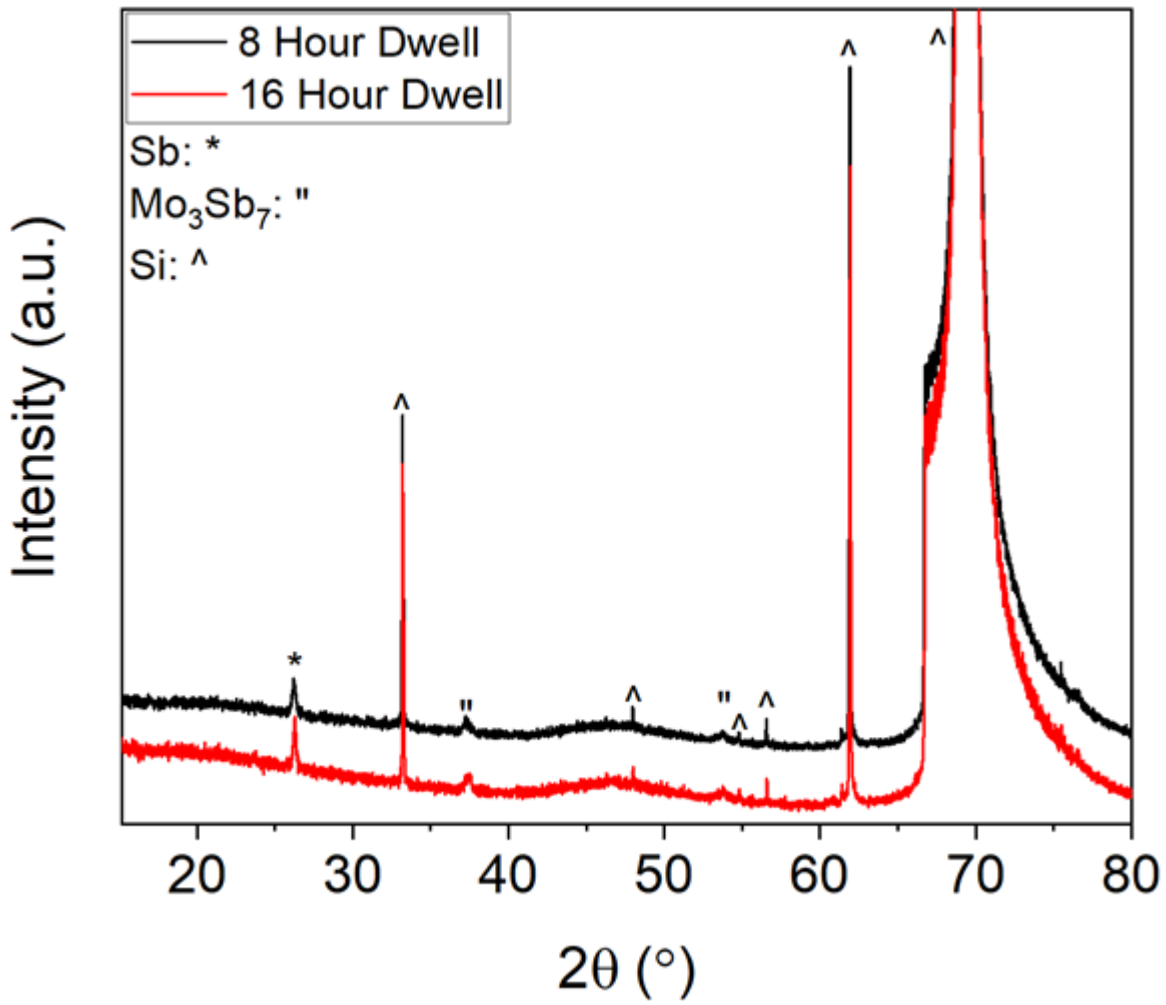

Figure 6-17: XRD patterns with Intensity on a log scale, obtained from CVD produced films with dwell times of 8 and 16 hours.

The outcomes of these reactions were similar to that of the 4-hour dwell, with small peaks belonging to elemental Sb at ~26° and Mo_3Sb_7 at ~37° and ~54°, whilst peaks belonging to the silicon of the substrate feature heavily in the obtained pattern.

It was thought that elemental Sb may be condensing on the substrate due to the temperature differential of around 100 °C between the source and the substrate. Therefore, the substrate was moved closer to the source so that its dwell temperature was around 700 °C. A dwell period of 4 hours was trialled for this reaction due to the minor impact that increasing the dwell time to 8 and 16 hours had. The XRD pattern of this film (Figure 6-18) is broadly identical to the previously obtained patterns, with peaks belonging to elemental Sb at ~26°, Mo_3Sb_7 at ~37° and ~54° and silicon again featuring heavily. Even with the increased dwell temperature of the substrate the elemental Sb is still present.

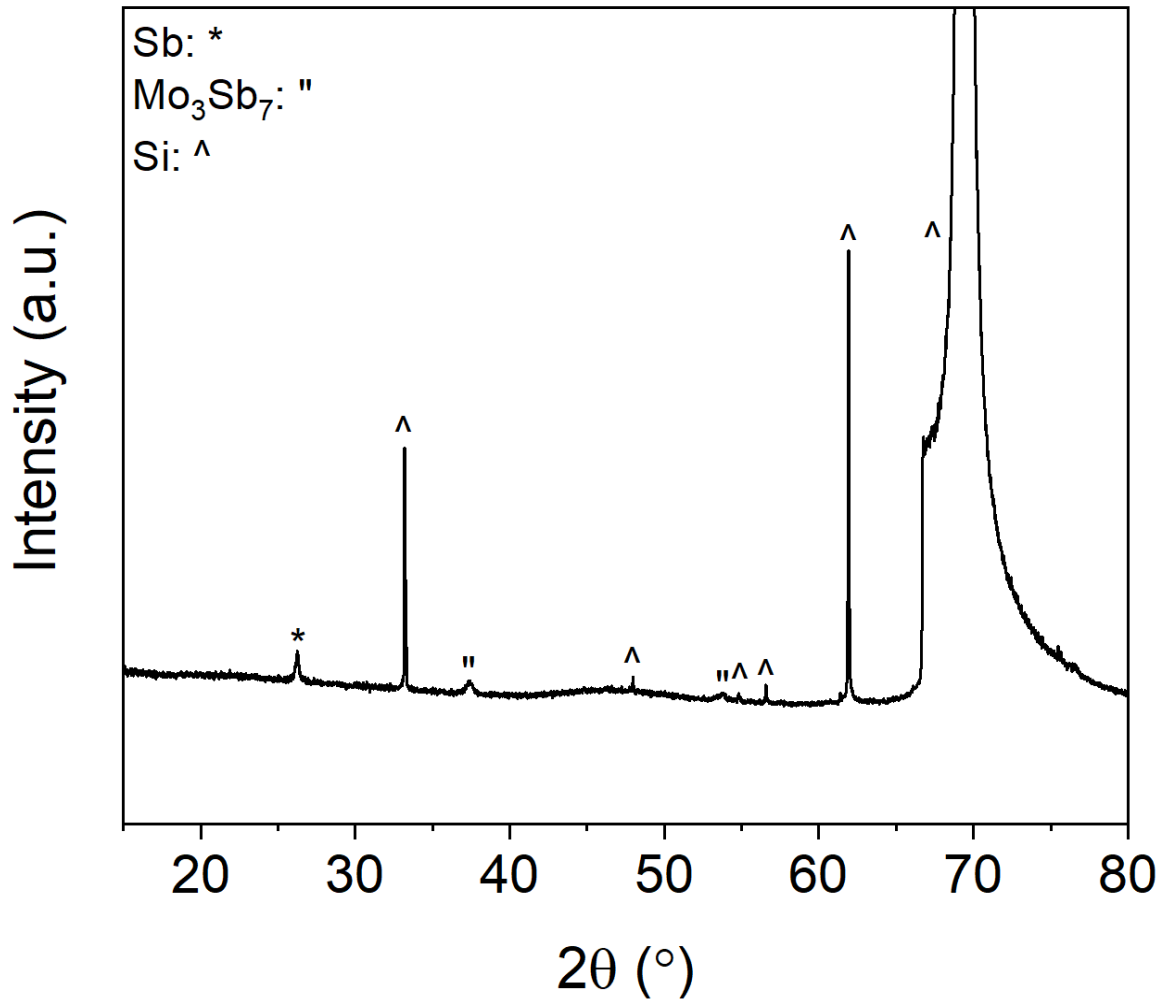

Figure 6-18: XRD pattern obtained from the CVD produced film which experienced a dwell temperature of 700 °C instead of 650 °C.

Due to the lack of intensity and the limited number of peaks corresponding to Mo_3Sb_7 compared to the silicon substrate it was not possible to perform Rietveld refinements on the obtained XRD patterns.

To investigate the possibility of depositing tellurium doped Mo_3Sb_7 films it was decided to react a previously synthesised $MoTe_2$ film with elemental Sb, rather than starting from an Mo precursor film and Te and Sb precursors. Due to the differences in melting points of Te and Sb it would be difficult to get them to their required temperatures at the same time.

The $MoTe_2$ film was converted from 100 nm MoO_3 in the hope that the resulting film would be sufficiently thick enough to somewhat survive a second CVD reaction. The parameters used for the CVD of Mo_3Sb_7 films were utilised again with a dwell of 8 hours chosen. The XRD patterns of the $MoTe_2$ film before and then the film reacted with Sb immediately show that a reaction has taken place (Figure 6-19). The family of (*00l*) peaks that were present in the pattern of $MoTe_2$ have all completely disappeared and have been replaced by numerous other peaks. Interestingly, the peak at ~33°, which corresponds to the silicon substrate is

very weak in the initial $MoTe_2$ pattern, due to the thickness of this film. However, it becomes the most intense peak after the CVD reaction suggesting that some of the initial film may have evaporated during the process.

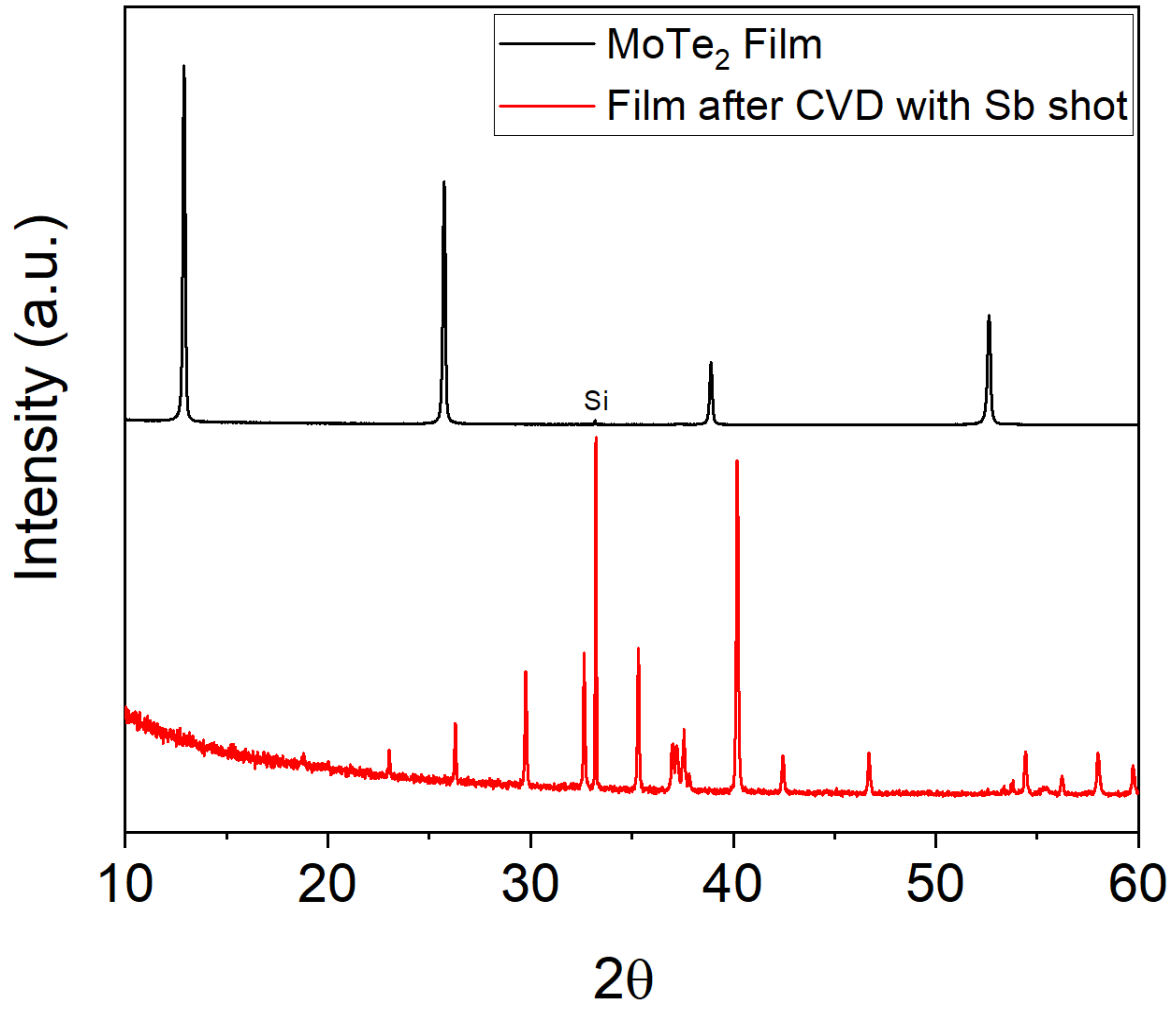

Figure 6-19: XRD patterns of an $MoTe_2$ film and of the same film after it underwent a second CVD reaction with Sb shot in an attempt to form an $Mo_3Sb_{7-x}Te_x$ film.

In an attempt to verify that these peaks belonged to $Mo_3Sb_{7-x}Te_x$, Rietveld refinement was performed (Figure 6-20). The refinement clearly shows that the vast majority of peaks in the pattern belong to Mo_3Sb_7 or an $Mo_3Sb_{7-x}Te_x$ species. However, the quality of the refinement is hampered by several unknown peaks, particularly at ~26° and the cluster between ~37-37.5°. Efforts were made to determine their origin, but they do not belong to elemental Mo, Sb or Te, nor either phase of $MoTe_2$ or any antimony telluride species such as SbTe or Sb_2Te_3. Finally, oxides of any of the above elements were also ruled out. Out of interest the unit cell parameter was refined which resulted in a = 9.5682 (3) Å, larger than would be expected for $Mo_3Sb_{7-x}Te_x$ and more in line with Mo_3Sb_7.[15]

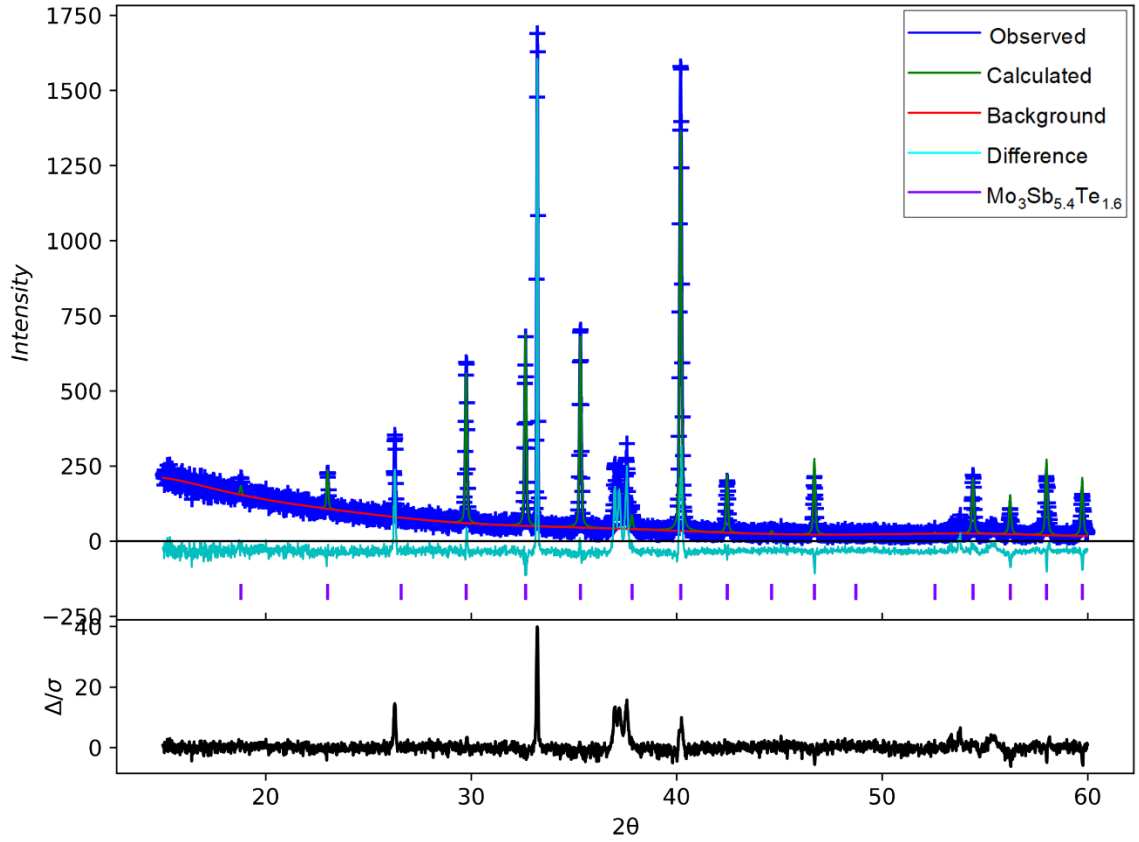

Figure 6-20: Rietveld refinement of the product film produced via a CVD reaction between an $MoTe_2$ film and Sb shot with observed (blue), calculated (green), background (red), difference (cyan) and peak position (purple) plots shown.

Therefore, the film was studied by EDX analysis to try and determine if there was any tellurium present, the results are summarised in Table 6-5. Unfortunately, there was no Te detected by EDX from any of the five areas studied across the film, in agreement with the Rietveld refinement. Moreover, the distribution of Mo and Sb across the films varies wildly suggesting that it is very inhomogeneous. These results coupled with the Rietveld refinement indicate that the film is actually Mo_3Sb_7 with tellurium seemingly evaporating from the $MoTe_2$ precursor film.

Table 6-5: EDX atomic percentages obtained from 5 locations across the $Mo_3Sb_{7-x}Te_x$ film.

Element	Area 1	Area 2	Area 3	Area 4	Area 5
Mo (at. %)	40.69	4.32	38.58	28.18	27.18
Sb (at. %)	59.31	33.36	61.42	45.63	41.04
Te (at. %)	0.00	0.00	0.00	0.00	0.00
O (at. %)	0.00	62.32	0.00	26.19	31.77
Totals	100	100	100	100	100

However, difficulty in acquiring the required thickness of MoO_3 precursor films for conversion to $MoTe_2$ meant that this method could not be investigated further. The results were promising nonetheless with varying CVD parameters like reducing dwell time or substrate dwell temperature worth testing to try and suppress Te evaporation from the $MoTe_2$ film, hopefully resulting in an $Mo_3Sb_{7-x}Te_x$ thin film.

6.4. Conclusions

Due to lack of access to the Raman instrument between June 2020 and March 2021 making characterising $MoTe_2$ extremely difficult the $Mo_3Sb_{7-x}Te_x$ (where x = 0, 1, 1.6 and 2) system was explored. Bulk powders of these materials were synthesised using a solid-state sealed ampoule method and Rietveld refinements carried out on the obtained PXRD patterns. This confirmed three compounds were phase pure and free from impurities whilst in $Mo_3Sb_5Te_2$, 2H-$MoTe_2$ was formed as an impurity. The refinements also revealed that the unit cell parameter, *a*, decreased with increasing Te concentration, due to the smaller atomic radius of Te compared to Sb. Furthermore, the morphologies of the materials were studied using SEM, revealing that they were broadly similar.

This presented an opportunity to test how the tellurium concentration impacted the performance of these materials as HER electrocatalysts, since the structure and morphologies were near identical any disparities in performance would be related to the level of tellurium doping. This revealed that increased levels of Te doping led to increased catalytic performance, confirmed through cyclic voltammetry and Tafel analysis.

Finally, efforts were made to synthesise Mo_3Sb_7 and $Mo_3Sb_{7-x}Te_x$ in thin film form using chemical vapour deposition. In the case of Mo_3Sb_7, the difficulty of characterising the product films and issues with elemental antimony condensing on the films meant that this area of research was not pursued any further. To try and synthesise $Mo_3Sb_{7-x}Te_x$ thin films, Sb shot was reacted with an $MoTe_2$ thin film. The XRD patterns of the $MoTe_2$ film and the product film after reaction with Sb made it immediately clear that a reaction had occurred. A Rietveld refinement was performed, and it showed that the majority of the XRD peaks belonged to $Mo_3Sb_{7-x}Te_x$, but the refined unit cell parameter was larger than expected for $Mo_3Sb_{7-x}Te_x$ and was more in line with Mo_3Sb_7. Subsequently, EDX revealed an absence of tellurium across the film, in agreement with the Rietveld refinement indicating that the film is actually Mo_3Sb_7. This result was somewhat promising and offers the opportunity for this area to be explored in future work.

6.5. References

1. Lezama, I. G., Ubaldini, A., Longobardi, M., Giannini, E., Renner, C., Kuzmenko, A. B. & Morpurgo, A. F. Surface transport and band gap structure of exfoliated 2H-$MoTe_2$ crystals. *2D Mater.* **1**, 21002 (2014).

2. Liu, D.-S., Wu, J., Xu, H. & Wang, Z. Emerging Light-Emitting Materials for Photonic Integration. *Adv. Mater.* **33**, 2003733 (2021).

3. Fang, H., Liu, J., Lin, Q., Su, R., Wei, Y., Krauss, T. F., Li, J., Wang, Y. & Wang, X. Laser-Like Emission from a Sandwiched $MoTe_2$ Heterostructure on a Silicon Single-Mode Resonator. *Adv. Opt. Mater.* **7**, 1900538 (2019)

4. Reeves, L., Wang, Y. & Krauss, T. F. 2D Material Microcavity Light Emitters: To Lase or Not to Lase? *Adv. Opt. Mater.* **6**, 1800272 (2018)

5. Susarla, S., Kutana, A., Hachtel, J. A., Kochat, V., Apte, A., Vajtai, R., Idrobo, J. C., Yakobson, B. I., Tiwary, C. S. & Ajayan, P. M. Quaternary 2D Transition Metal Dichalcogenides (TMDs) with Tunable Bandgap. *Adv. Mater.* **29**, 1702457 (2017).

6. Dashjav, E., Szczepenowska, A. & Kleinke, H. Optimization of the thermopower of the antimonide Mo_3Sb_7 by a partial SB/Te substitution. *J. Mater. Chem.* **12**, 345–349 (2002).

7. Jensen, P. & Kjekshus, A. The Crystal Structure of Mo_3Sb_7. *Acta Chem. Scand.* **20**, (1966).

8. Soheilnia, N., Dashjav, E. & Kleinke, H. Band-gap tuning by solid-state intercalations of Mg, Ni, and Cu into Mo_3Sb_7. *Can. J. Chem.* **81**, 1157–1163 (2003).

9. Snyder, G. J. & Toberer, E. S. Complex thermoelectric materials. *Nat. Mater.* **7**, 105–114 (2008).

10. Zhang, H., He, J., Zhang, B., Su, Z., Tritt, T. M., Soheilnia, N. & Kleinke, H. Thermoelectric properties of $Mo_3Sb_{5.4}Te_{1.6}$ and $Ni_{0.06}Mo_3Sb_{5.4}Te_{1.6}$. *J. Electron. Mater.* **36**, 727–731 (2007).

11. Xu, H., Kleinke, K. M., Holgate, T., Zhang, H., Su, Z., Tritt, T. M. & Kleinke, H. Thermoelectric performance of $Ni_yMo_3Sb_{7-x}Te_x$ ($y \leq 0.1$, $1.5 \leq x \leq 1.7$). *J. Appl. Phys.* **105**, 53703 (2009).

12. Sales, B. C., Mandrus, D. & Williams, R. K. Filled skutterudite antimonides: A new class of thermoelectric materials. *Science* **272**, 1325–1328 (1996).

13. Häussermann, U., Elding-Pontén, M., Svensson, C. & Lidin, S. Compounds with the Ir_3Ge_7 Structure Type: Interpenetrating Frameworks with Flexible Bonding Properties. *Chem. – A Eur. J.* **4**, 1007–1015 (1998).

14. Markov, M., Hu, X., Liu, H.-C., Liu, N., Poon, S. J., Esfarjani, K. & Zebarjadi, M. Semi-metals as potential thermoelectric materials. *Sci. Rep.* **8**, 9876 (2018).

15. Shi, X., Pei, Y., Snyder, G. J. & Chen, L. Optimized thermoelectric properties of $Mo_3Sb_{7-x}Te_x$ with significant phonon scattering by electrons. *Energy Environ. Sci.* **4**, 4086–4095 (2011).

16. Candolfi, C., Lenoir, B., Dauscher, A. & Tobola, J. Neutron Diffraction and Ab initio Studies of Te Site Preference in $Mo_3Sb_{7-x}Te_x$. *Chem. Mater.* **20**, 6556–6561 (2008).

17. Candolfi, C., Lenoir, B., Dauscher, A., Bellouard, C., Hejtmanek, J., Santava, E. & Tobola, J. Spin Fluctuations and Superconductivity in Mo_3Sb_7 *Phys. Rev. Lett.* **99**, 37006 (2007).

18. Baggetto, L., Allcorn, E., Unocic, R. R., Manthiram, A. & Veith, G. M. Mo_3Sb_7 as a very fast anode material for lithium-ion and sodium-ion batteries. *J. Mater. Chem. A* **1**, 11163–11169 (2013).

19. Nan, H., Liu, Y., Li, Q., Shen, P. & Chu, K. A Janus antimony sulfide catalyst for highly selective N_2 electroreduction. *Chem. Commun.* **56**, 10345–10348 (2020).

20. Liu, X., Jang, H., Li, P., Wang, J., Qin, Q., Kim, M. G., Li, G. & Cho, J. Antimony-Based Composites Loaded on Phosphorus-Doped Carbon for Boosting Faradaic Efficiency of the Electrochemical Nitrogen Reduction Reaction. *Angew. Chemie Int. Ed.* **58**, 13329–13334 (2019).

21. Okabe, H., Yano, S., Muranaka, T. & Akimitsu, J. Magnetic and structural phase transitions in Mo_3Sb_7. *J. Phys. Conf. Ser.* **150**, 52196 (2009).

22. Wan, H., Liu, X., Wang, H., Ma, R. & Sasaki, T. Recent advances in developing high-performance nanostructured electrocatalysts based on 3d transition metal elements. *Nanoscale Horizons* **4**, 789–808 (2019).

23. Gao, S., Lin, Y., Jiao, X., Sun, Y., Luo, Q., Zhang, W., Li, D., Yang, J. & Xie, Y. Partially oxidized atomic cobalt layers for carbon dioxide electroreduction to liquid fuel. *Nature* **529**, 68–71 (2016).

24. Carmo, M., Fritz, D. L., Mergel, J. & Stolten, D. A comprehensive review on PEM

water electrolysis. *Int. J. Hydrogen Energy* **38**, 4901–4934 (2013).

25. Li, H., Jia, X., Zhang, Q. & Wang, X. Metallic Transition-Metal Dichalcogenide Nanocatalysts for Energy Conversion. *Chem* **4**, 1510–1537 (2018).

26. Ibraheem, S., Li, X., Shah, S. S. A., Najam, T., Yasin, G., Iqbal, R., Hussain, S., Ding, W. & Shahzad, F. Tellurium Triggered Formation of Te/Fe-NiOOH Nanocubes as an Efficient Bifunctional Electrocatalyst for Overall Water Splitting. *ACS Appl. Mater. Interfaces* **13**, 10972–10978 (2021).

27. Gomez, R., Fernandez-Vega, A., Feliu, J. M. & Aldaz, A. Hydrogen evolution on platinum single crystal surfaces: effects of irreversibly adsorbed bismuth and antimony on hydrogen adsorption and evolution on platinum (100). *J. Phys. Chem.* **97**, 4769–4776 (1993).

28. Tsai, C., Chan, K., Nørskov, J. K. & Abild-Pedersen, F. Theoretical insights into the hydrogen evolution activity of layered transition metal dichalcogenides. *Surf. Sci.* **640**, 133–140 (2015).

29. Tang, Q. & Jiang, D. Mechanism of Hydrogen Evolution Reaction on 1T-MoS_2 from First Principles. *ACS Catal.* **6**, 4953–4961 (2016).

30. McGlynn, J. C., Cascallana-Matías, I., Fraser, J. P., Roger, I., McAllister, J., Miras, H. N., Symes, M. D. & Ganin, A. Y. Molybdenum Ditelluride Rendered into an Efficient and Stable Electrocatalyst for the Hydrogen Evolution Reaction by Polymorphic Control. *Energy Technol.* **6**, 345–350 (2018).

7. Conclusions and Outlook

In conclusion, this work saw the successful implementation of a CVD system that allowed for the depsition of both 2H- and 1T'-$MoTe_2$ thin films, through the direct tellurisation of a precursor layer using a novel $FeTe_2$ precursor in place of elemental Te. The phase selectivity was revealed to be dependent on the choice of molybdenum precursor layer, with Mo converting preferentially to 2H-$MoTe_2$ and MoO_3 converting to 1T'-$MoTe_2$. The produced films were then characterised using techniques such as Raman spectroscopy, AFM, XPS and TEM. The characterisation showed the films to be phase pure and homogeneous over the whole substrate and revelaed that the morphology of the precursor films dictated the morpology of the $MoTe_2$ product films. XPS also revealed that both Mo and MoO_3 precursor films are completely converted into $MoTe_2$ whilst TEM/SAED showed both phases to be polycrystalline in nature. Furthermore, by varying the the thickness of the precursor layers it was possible to control the number of layers in the resultant $MoTe_2$ films, with 5 layers the minimum thickness achieved. AFM was then used to measure the thickness of the films and Raman spectroscopy and optical microscopy were assessed as complimetnary methods to rapidly guauge the thickness of subsequently produced films. As the phase slectivity was achieved through the use of two separate molybdenum precursors, it was possible to deposit both on a single substrate, allowing for the formation of 1T'- and 2H-$MoTe_2$ on the same substrate from a single CVD reaction. This method may offer a simple route for the production of 1T'-2H homojunctions.

The conditions used for the successful deposition of 1T'- and 2H-$MoTe_2$ were then applied to a more conventional CVD setup in order to discern if $FeTe_2$ was still a suitable precursor. Again, it was possible to depostit both phase pure 1T'- and 2H-$MoTe_2$ with selectivty achieved through the use of two different molybdenum precursor layers. Furthermore, the impact of varying dwell time on the reaction outcome was studied using Raman spectroscopy, finding that increased dwell times were not sufficient in overcoming the phase selectivity caused by the choice of molybdenum precursor when $FeTe_2$ was used. The same experiments were then conducted using elemental Te in place of $FeTe_2$. However, Te was not suited to long dwell times due to the complete exhaustion of the source for dwell times of 4 hours or longer. Efforts were then made to reproduce literature work which claimed that phase selectivity could be achieved through varying the dwell temperature of the elemental Te source. Unfortunately, this was ultimately unsuccessful.

The CVD deposited $MoTe_2$ thin films were then applied in two different applications. Initially, both 2H- and 1T'-$MoTe_2$ films deposited on conductive silicon substrates were

trialled as electrocatalyts for the production of hydrogen from water. Films of both phases with varying thicknesses were deposited to study the impact of film thickness on catalytic performance. In the case of 2H-$MoTe_2$ it was discovered that the thicker the film the lower the overpotential achieved (better performance), with a 2H film converted from 100 nm Mo having slighty improved performance compared to 2H bulk powder. The thickness dependent performance was also observed for 1T'-$MoTe_2$, however a lack of stability in the films meant that the performance was significantly worse than bulk 1T'-$MoTe_2$ powder tested as a comparison. Ultimately, the 1T' films showed weak adhesion to the silicon substrate and this was most likely the cause of the poor performance.

Subsequently, 1T'-$MoTe_2$ films were trialed as substrates for surface enhanced Raman spectroscopy. An initial brief study was conducted using the model dye, rhodamine 6G, as an analyte. Enhancement of the Raman signal was achieved on 5-layer 1T'-$MoTe_2$ whilst even a small increase in the thickness to an 11-layer film resulted in a loss of the Raman enhancement. This result was consistent with other 2D material SERS substrates. Various concentrations of R6G were then tested, finding that the lowest concentration detectable was 50 nM. This may be further improved by producing thinner 1T'-$MoTe_2$ films, as this has been shown to be an effective strategy for other 2D materials.

To truly realise the potential of the TMDCs as SERS substrates, analytes other than common dyes should be invesitgated. Subsequently, a throrough investigation into the suitability of 1T'-$MoTe_2$ films as SERS substrates for β-sitosterol was conducted. β-sitosterol is a lipophilic, sterol-like molecule that is a marker for several coronary dieseases. 1T'-$MoTe_2$ films ranging from 5- to 10-layers in thickness were produced and characterised by Raman spectroscopy and AFM. Thickness-dependent SERS measurements were completed which concluded that the 5- and 7-layer films performed significantly better than their thicker counterparts. Following on from this, concentration dependent measurements were conducted finding that the limit of detection of β-sitosterol on 1T'-$MoTe_2$ was 10^{-9} M. This is one of the lowest LODs reported so far for sterol-like molecules, as well as outperforming several noble metal based SERS substrates. The stability of 1T'-$MoTe_2$ as a SERS substrate was also investigated. β-sitosterol on 1T'-$MoTe_2$ was stored in ambient conditions over a period of 45 days, with Raman spectra recorded periodically, which revealed minimal losses of Raman peak intensity over the duration of storage. The possibility of recycling the SERS substrates was addressed using a simple washing procdure to remove any traces of β-sitosterol from 1T'-$MoTe_2$, with Raman spectroscopy used to confirm this was successful. Then more β-sitosterol was applied and measured before being removed again. This process

was repeated for a total of three cycles with minimal losses of Raman signal intensity observed over the course of the process, indictaing that recycling the substrates is possible. Efforts were then made at determining the mechanism of Raman enhancement. DFT calculations and UV-vis spetroscopy revealed that the Raman enhancement was not due to excitement of the analyte caused by the incident Raman laser. Therefore, it was concluded that the formation of a surface complex between β-sitosterol and 1T'-$MoTe_2$ was responsible. A variety of charactersiation techniques such as infrared spectroscopy, UV-vis spectroscopy and cyclic voltammetry were subsequently used to prove the existance of this surface complex.

Finally, the $Mo_3Sb_{7-x}Te_x$ (where x = 0, 1, 1.6 & 2) group of compounds were synthesised through a solid-state method. Rietveld refinements were used to ensure that the materials were phase pure and they revealed that $MoTe_2$ forms as an impurity when x = 2. Moreover, the unit cell parameter, *a*, was shown to decrease slightly with increasing tellurium concentration, indicating the successful incorporation of Te into the structure. Due to the minimal structural changes upon the addition of Te, these compounds provide an opportunity to observe the impact that increasing the Te content has upon their electrocatalytic activity. As such the morphology and composition of the materials were probed by SEM/EDX to ensure that the only differences were their tellurium concentration. Increasing Te content was shown to increase the catalytic performance of these materials as well as their stability. Due to lack of literature reports of the chemical vapour deposition of Mo_3Sb_7 and $Mo_3Sb_{5.4}Te_{1.6}$ efforts were made to utilise the previously developed CVD system to deposit these materials. This was somewhat successful, however difficulty in characterising the product films and getting the required precursor materials ultimately meant that this line of research was not persued further.

In terms of outlook there is still much that could be investigated in the areas that this thesis delved into. For example, the deposition of monolayers of both 1T'- and 2H-$MoTe_2$ was not possible due to limitations in the deposition systems used to provide the required precursor Mo and MoO_3 layers. It is hoped that a monolayer of MoO_3 would convert into a monolayer of $MoTe_2$ and therefore deposition methods that are capable of producing this, such as ALD, are worthy of being explored. Expanding the library of SERS analytes tested with $MoTe_2$ as the substrate is another important avenue of research that could be further explored to demonstrate the capabilities of the TMDCs in this area. Finally, methods of reducing the bandgap of few-layer 2H-$MoTe_2$ to suit potential optoelectronic applciations, such as doping, could be explored in bulk powders and then in thin film form.